Investigations on Molecular Organization and Physical Properties of Asymmetric Bent-core Liquid Crystals

by

DEEPSHIKA MALKAR

A thesis submitted to

JAWAHARLAL NEHRU UNIVERSITY

for the award of the degree

of

DOCTOR OF PHILOSOPHY

DEPARTMENT OF SOFT CONDENSED MATTER PHYSICS
RAMAN RESEARCH INSTITUTE
BANGALORE 560080

MARCH 2020

I dedicate this thesis to my beloved parents

DECLARATION

I, hereby, declare that this thesis is composed independently by me at the Raman Research Institute, Bangalore, India, under the supervision of Dr. Arun Roy. The subject matter presented at this thesis has not previously formed the basis for the award of any degree, diploma, membership, associateship, fellowship or any other similar title of any other university or institution. I also declare that I have run it through the Turnitin plagiarism software.

Dr. Arun Roy
(Thesis Supervisor)
Soft Condensed Matter Physics
Raman Research Institute
Bangalore 560080
India

Deepshika Malkar

THESIS CERTIFICATE

This is to certify that the thesis entitled ***Investigations on Molecular organization and physical properties of asymmetric bent-core liquid crystals***, submitted by **Deepshika Malkar**, for the award of the degree of **Doctor of Philosophy** of Jawaharlal Nehru University, Delhi, India is her original work. This has not been published or submitted elsewhere for the award of any degree or diploma.

Prof. Ravi Subrahmanyan
Director
Raman Research Institute
Bangalore 560080
India

Dr. Arun Roy
Thesis Supervisor
Soft Condensed Matter Physics
Raman Research Institute
Bangalore 560080
India

Date: 19th March 2020

ACKNOWLEDGEMENTS

First and foremost, I want to thank my supervisor, Dr. Arun Roy. It has been an honour to be his first Ph.D. student. I appreciate all his contributions of time and ideas to make my Ph.D. experience productive and stimulating. The joy and enthusiasm he has for his research were contagious and motivational for me, even during tough times in the Ph.D. He always motivated me by giving positive examples from his life. I hope that I could be as lively, enthusiastic, and energetic as him. He has been supportive and has given me the freedom to pursue various projects without objection. He has always provided great insights into my research work.

I am also very grateful to have Prof. Pramod A Pullarkat and Prof. Sandeep Kumar as my advisory committee members and for giving me invaluable suggestions during the annual reviews.

I thank the SAAC members, Prof. Sadiq Rangwala, Prof. V.A Raghunathan, Prof Shiv Sethi, Dr. Dibyendu Roy, for their helpful career advice and suggestions in general.

I also thank my collaborators, Prof. Veena Prasad and Prof. B.K. Sadashiva, for providing me liquid crystal samples for studies during my Ph.D.

I thank Mrs. Vasudha K. N, Mr. Yateendran, Mr. Dasan for technical assistance. I especially thank Mrs. Vasudha for helping me with DSC and XRD studies. I thank Mr. Mani, who helped me to design an experimental setup, make coverslips and glass items that were necessary for my experiments. I am thankful to RRI workshop staff for their help and support.

I also thank Dr. Harsha Mohan Paroor and Dr. Anand Kumar for their personal and professional guidance during these years. I thank all the present lab members Subhadip, Vishnu, Swarnak, Saichand, Dipak for their company and support. I thank

my past lab members, Jacintha, Prashant, Aditi, Soham, Bhagyashree, Dr. Harsha Mohan, Elizabeth, for their help with the experiments, useful discussions, and pleasant company.

I thank my friends at RRI, especially Ranjana, Anjali, Mahesh, Manohar, Prutha, Subhash, Prabhakaran, Divya, Intezar, Dr. Pramod, Sanjay, Sreeja, Santanu, Irla, Alakananda, Anu Vasistha and Neha for making my stay enjoyable here.

I especially thank M. Sumanth Kumar for his help and support in learning LabVIEW, Mathematica, and MATLAB. I thank him for providing me a pleasant environment and helpful suggestions during my thesis writing. I appreciate all the library staff, especially Manjunath, for their help and support.

I thank the SCM group secretary, Mr. Radhakrishna, for his help with all the official work. I sincerely thank Raja and Murali for their support on a daily basis. I thank the director, Prof. Ravi Subrahmanyan, for his help with various academic issues. I want to thank the administrative officer Mr. CSR Murthy and assistant administrative officer Mr. Naresh, for their assistance with countless administrative matters.

I express my sincere gratitude to all the administrative staff, especially Mrs. Marisa, Mrs. K. Radha and Mrs. Vidhyamani for their help and support in these years. I thank the computer department staff for their continuous support. I acknowledge the canteen staff, hostel staff, and everyone at RRI for their cooperation and encouragement.

I will forever be thankful for my former college research advisors Prof. V.K. Rastogi, and Prof. Beerpal for providing me invaluable advice during my graduate school career. Their enthusiasm and love for teaching are contagious. I especially thank Dr. Jyant Teotia and Dr. Manoj Kumar for their encouragement and motivation during my college time, which helped me decide to pursue higher education. I thank my school teacher Rajkumar Singh who first introduced me to physics.

I want to thank especially Mrs. Supreeti Roy for her love and support in these past years. I cannot forget the day when I met her for the first time in our hostel,

and she became an essential part of my life. Because of her, I found another home in Bangalore. She always provided me a home environment even in the hostel. Her personal and professional suggestions were beneficial during my Ph.D. I cannot forget the delicious food, especially mango payasam, which she used to make for me. I also thank my little friends Sushmit and Anusha, who are like my younger siblings. I really enjoyed their company in these years. It is difficult to express my feeling here in words for such good people.

A special thanks to my family. Words cannot express how grateful I am to my parents for all the sacrifices that they made for my well-being. I would also like to thank my beloved sisters Jyoti Malkar and Pooja Malkar. I thank them for supporting me in everything, and especially for encouraging me throughout this journey. To my beloved brother Prabhat Kumar Malkar, I would like to express my thanks for being so supportive always and cheering me up.

Synopsis

A typical bent-core (BC) banana-shaped molecule consists of a relatively rigid bent-core part which has two rod-like arms joined end to end with an angle of about 120 degrees between them. In addition, flexible aliphatic chains usually are attached to one or both ends of the rigid core of the molecule. Based on the rigid-arms and associated chain lengths, BC molecules can be classified into two categories: symmetric and asymmetric BC molecules. In a symmetric BC banana-shaped molecule, both the arms and the chains are the same, giving rise to C_{2V} point symmetry of the molecule. However, in a asymmetric BC molecule, the asymmetry can be introduced either by using different chain lengths and linkage groups in the symmetric BC banana-shaped molecule or using rigid arms of different lengths. A bent-core hockey-stick shaped (BCHS) molecule is formed when one of the arms is relatively shorter than the other arm. The BCHS molecule can be considered to have an intermediate shape between the bent-core banana-shaped and the rod-like molecules as shown in Figure 1.

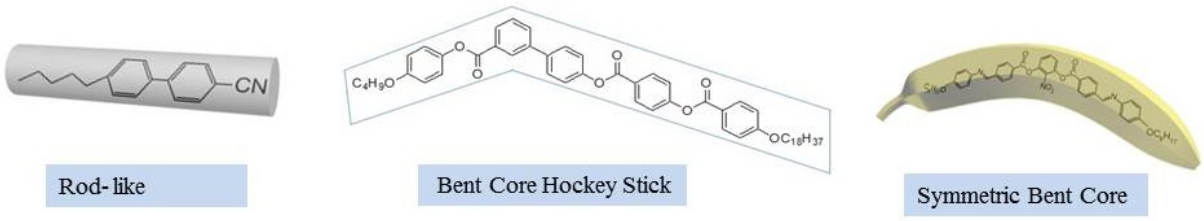

Figure 1: Molecular structure of a bent-core hockey-stick shaped molecule which lies between a rod-like and symmetric bent-core banana-shaped molecules.

The BC banana-shaped molecules are known to exhibit a polar order in their tilted smectic phases due to their transverse shape anisotropy. On the other hand, rod-like molecules in their tilted smectic phases rotate almost freely about their long axes giving rise to almost uniaxial layers. As BCHS molecules have an intermediate shape, it is interesting to investigate the phase behavior and the molecular organization in their

liquid crystal (LC) phases. Only a few studies had been reported on the LC phases exhibited by BCHS molecules. The present thesis consists of experimental studies on LC phases exhibited by pure compounds consisting of BCHS molecules and on the binary mixtures of rod-like and BCHS molecules. We also developed theoretical models to account for the observed LC phases and electro-optic effects on their smectic phases. The motivation of this thesis is to decipher the self aggregated molecular organization and physical properties of LC phases exhibited by such molecules with non-conventional shape. This thesis is divided into six chapters.

Chapter 1

This chapter deals with the basic introduction of liquid crystals along with details of their physical properties and classifications.

Chapter 2

This chapter contains the methodologies and experimental techniques which had been utilized during this thesis work. The physical properties of BC liquid crystals were characterized using a variety of experimental techniques such as differential scanning calorimetry (DSC), polarizing optical microscopy (POM), X-ray diffraction (XRD), polarization reversal switching current measurement, dielectric constant measurements, electro-optic studies. POM is a simple and powerful tool to examine LC textures and phase transitions. In this chapter, we described a home-built electro-optic experimental setup which was used to measure dielectric constant and transmitted optical intensity simultaneously as a function of temperature and applied voltage. The electro-optic setup was interfaced to a computer using a LabVIEW program. The birefringence of a planar-aligned sample can be obtained from the measured optical intensity. The setup was calibrated using a well studied commercially available LC sample 4'-(Octyloxy)-4-biphenylcarbonitrile (8OCB). Our experimental measurements for the birefringence and dielectric anisotropy (Figure 2) showed good agreement with literature values.

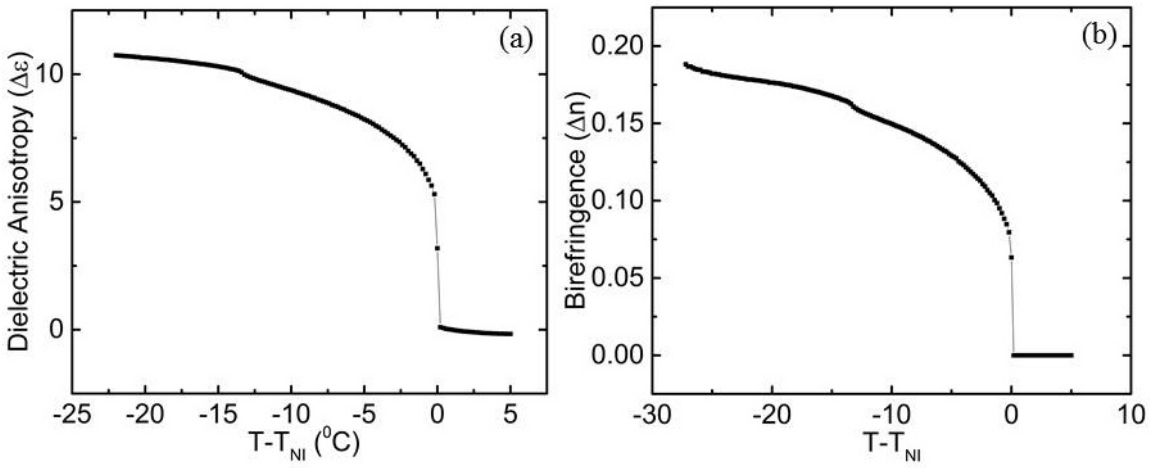

Figure 2: (a) Measured dielectric anisotropy and (b) birefringence of a planar-aligned sample as a function of relative temperature for a compound 8OCB.

Chapter 3

In this chapter, we describe the experimental studies on two compounds consisting of BCHS molecules. In the first part, we describe the experimental studies on a compound 4-n butyloxyphenyl 4-(4-n-octadecyloxybenzoyloxy-4-benzoyloxy) biphenyl-3-carboxylate which is abbreviated as 4OC18. In the second part, we present experimental results on a different compound 4-(((3-((4-(nDecyloxy)benzoyl)oxy)phenyl)imino) methyl)phenyl4- (-(4-(n-tetradecyloxy)phenyl)diazenyl)benzoate which is abbreviated as A14.

The molecular structure of the compound 4OC18 and the phase sequence is shown in Figure 3.

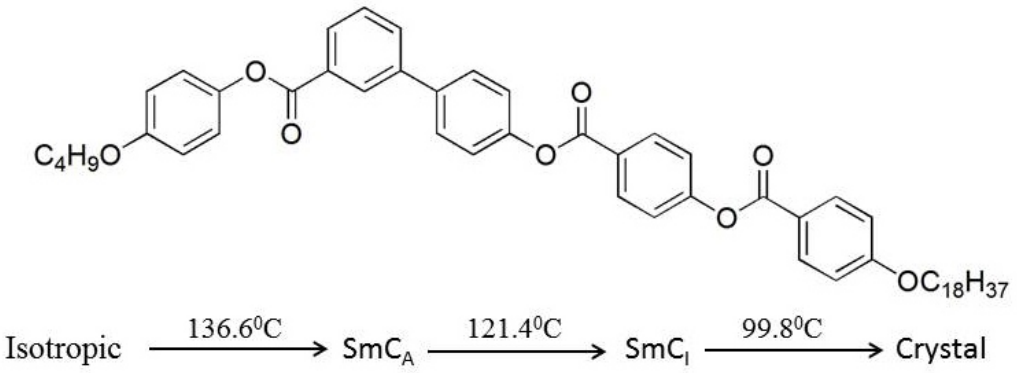

Figure 3: The molecular structure and the phase sequence of compound 4OC18 on cooling the sample from the isotropic phase.

This molecule consists of five benzene rings with terminal chains attached at both the ends of the molecule. This compound shows two new tilted smectic phases which are characterized to have an axial-vector order parameter in addition to the tilt order in the layers. We designated these higher and lower temperature phases as SmC_A and SmC_I, respectively. The subscript A denotes the anticlinic and anti-axial arrangement of molecules in successive layers. The subscript I for the lower-temperature phase indicates an intermediate arrangement of molecules in successive layers with the azimuthal angle difference in tilt directions between 0 and π. The POM studies on these phases were carried out for both planar and homeotropic alignments of the sample as shown in Figure 4.

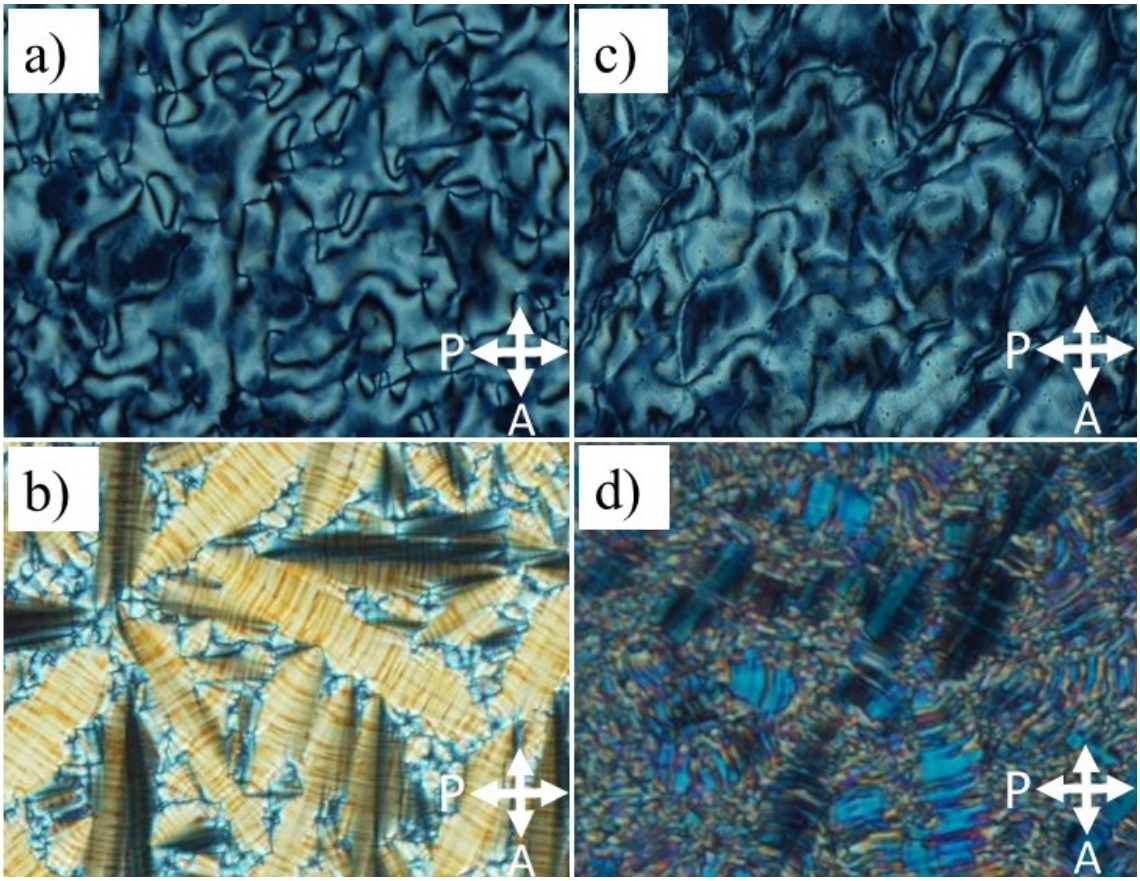

Figure 4: POM textures of compound 4OC18 on cooling it from isotropic phase in SmC_A phase at 125 ^{0}C for (a) homeotropic-alignment, (b) planar-alignment and in the SmC_I phase at 115 ^{0}C for (c) homeotropic-alignment (d) planar-alignment.

In the higher-temperature SmC_A phase, a schlieren texture (Figure 4a) with both unit and half strength defects was observed for the homeotropically-aligned sample. The existence of both half and unit strength defects confirm the anticlinic tilt of the molecules in the adjacent layers. For a planar-aligned sample, a focal-conic fan texture (Figure 4b) with optic axis parallel to the layer normal was observed. The optic axis parallel to the layer normal is consistent with the anticlinic tilt of the molecules in the successive layers. In the lower-temperature SmC_I phase, again, a schlieren texture in which the defect centers are less distinct was observed (Figure 4c) for a homeotropically-aligned sample. On the other hand, for a planar-aligned sample, a large number of irregular bands appeared parallel to the smectic layers making the focal-conic fans not clearly visible (Figure 4d). Both the textures in the SmC_I phase indicate the coexistence of different stable degenerate structures.

The XRD studies were carried out on an unoriented sample filled in Lindemann capillary tube while cooling the sample from the isotropic phase. XRD studies confirmed the tilted nature of molecules in the SmC_A and SmC_I phases with layer spacing as 42.6 Å and 43.1 Å, respectively. Both the phases do not possess any spontaneous electric polarization in the layers as no peaks were detected in the polarization reversal current measurements. Yet, an electro-optic response was observed under the application of an AC electric field.

In the second part, the experimental studies on another compound A14 consisting of azo-substituted BCHS molecules has been described. This compound also showed similar phases as that of compound 4OC18 confirming the generality of the observed phases. The molecular structure of the compound A14 and the phase sequence is shown in Figure 5.

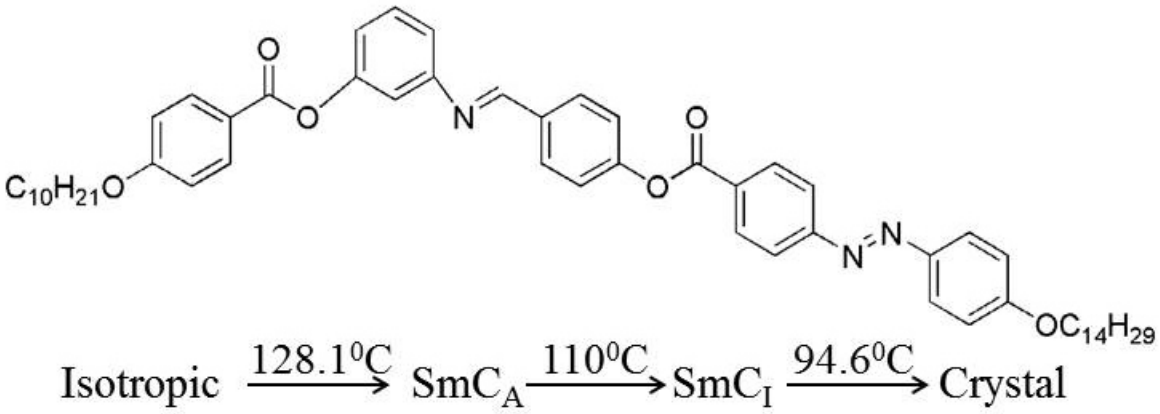

Figure 5: The molecular structure of compound A14 and phase sequence on cooling the sample from the isotropic phase observed by differential scanning calorimetry. The transition temperatures were measured by DSC.

The POM textures of the compound A14 between crossed polarizers are shown in Figure 6. As can be seen from Figure 6, the textures have similar characteristics as that of compound 4OC18. This sample has relatively higher birefringence giving rise to color textures in both the phases. The POM textures again confirmed the existence of the SmC_A and SmC_I phases for this compound.

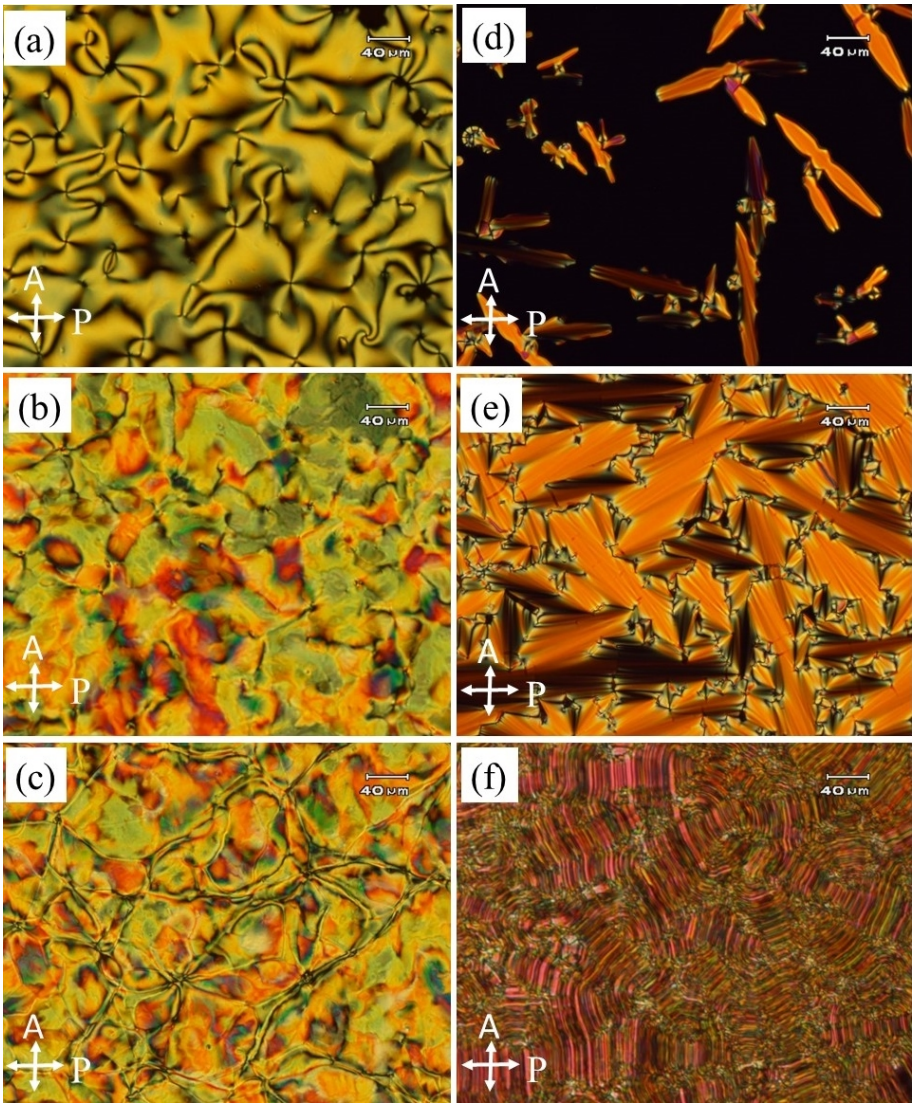

Figure 6: POM textures for a homeotropically-aligned sample (column one) in the SmC_A phase (a) schlieren texture with one and half defects just below the clearing temperature (b) in deep SmC_A phase, and (c) in the SmC_I phase. For a planar-aligned sample (column two) (d) batonnet growth of the SmC_A phase (e) completely grown focal-conic fan texture in the SmC_A phase, and (f) irregular band texture in the SmC_I phase.

The XRD studies for this compound also confirmed the tilted nature of the molecules in the smectic phases with layer spacing as 44.5 Å and 46.1 Å in the SmC_A and SmC_I phases, respectively. We also measured the layer spacing (tilt angle) variation as a function of temperature. The layer spacing (tilt angle) slightly increases (decreases) on cooling the sample from the SmC_A phase to SmC_I phase with a small jump at the SmC_A to SmC_I phase transition temperature as shown in Figure 7. This increment in the layer spacing is about 4% over the whole temperature range studied. This can be

attributed to a slight increase in the molecular length due to straightening of the end chains of the molecules with decreasing temperature. This behavior is contrary to the calamitic SmC phases consisting of rod-like molecules where the layer spacing usually decreases with decreasing the temperature.

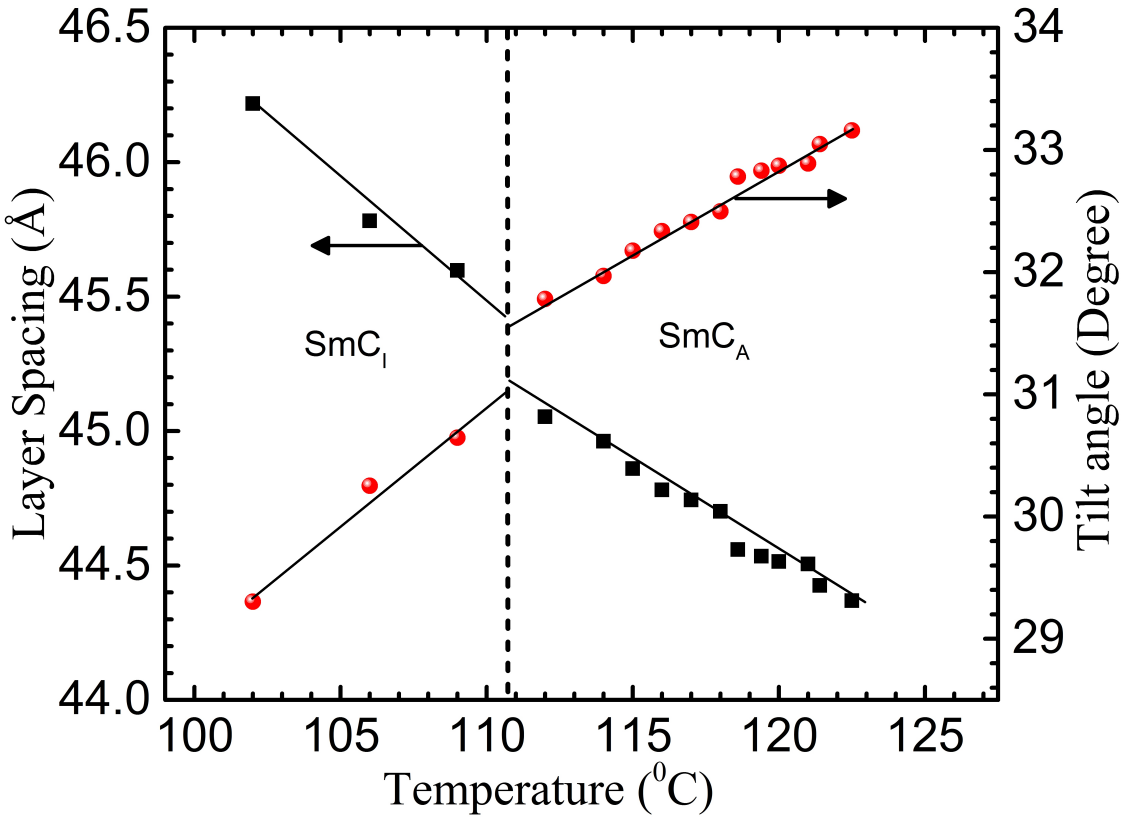

Figure 7: The variation of layer spacing and tilt angle with temperature from the SmC_A to SmC_I phase for compound A14. The data was recorded on cooling the sample from the isotropic phase.

Both the phases do not possess net electric polarization in the layers as no peaks were detected in the polarization reversal current measurements. However, in spite of the absence of layer polarization, some remarkable electro-optic effects were observed under the application of an AC electric field in both the smectic phases similar to that of the compound 4OC18.

We developed a theoretical model to account for the observed phases. We proposed that the molecules in these tilted phases adopt a zigzag shape for efficient packing in the smectic layers.

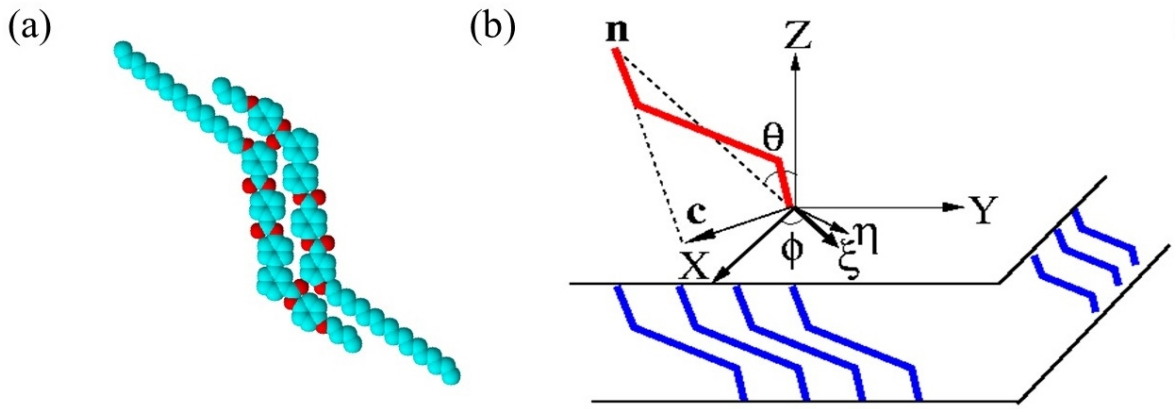

Figure 8: (a) The zigzag configuration of the BCHS molecules within the layer. (b) The pseudo-polar tilted organization of the BCHS molecules in the layer.

Figure 8a shows the zigzag packing of BCHS molecules in the smectic layers. This zigzag shape of the molecules induces an axial-vector order parameter in addition to the tilt order parameter in the layers. The schematic representation of the tilt and axial-vector order parameters used for the theoretical model are shown in Figure 8b. It should be noted that the zigzag packing of the molecules leads to the cancellation of the dipole moments of the molecules with no net electric polarization in the layers as found experimentally.

The theoretical model predicts five possible tilted smectic phases as shown in Figure 9:

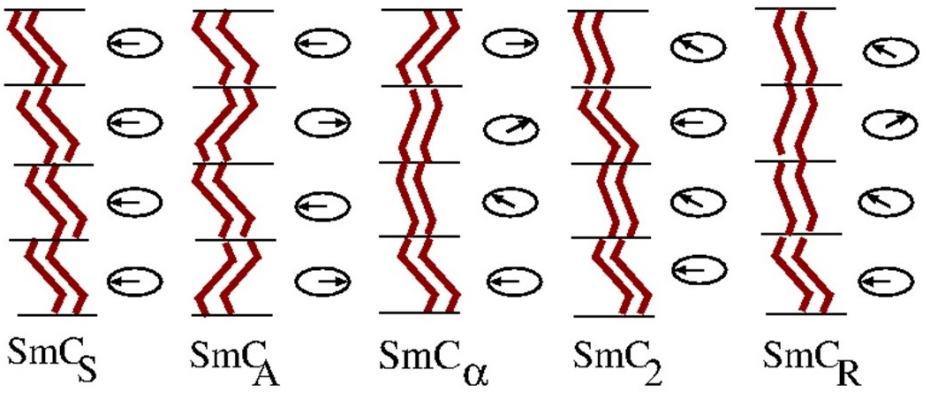

Figure 9: The schematic representation of the predicted structures in different smectic phases. The arrows show the tilt direction of the molecules in the adjacent layers.

(i) The **Sm**C_A phase with an anticlinic tilt and antiparallel axial-vector order in successive layers. This phase is observed experimentally at higher temperatures in the studied samples.

(ii) The **Sm**C_S phase with synclinic tilt and parallel axial-vector order in successive layers. This phase is not observed experimentally in these samples.

(iii) The **Sm**C_α phase with helically modulated tilt directions in successive layers. As the BCHS molecules are achiral, both left-handed and right-handed structures are equally possible.

(iv) A bilayer **Sm**C_2 phase, in which the sign of $\delta\phi$ between the neighboring pair of layers alternate.

(v) A random **Sm**C_R phase, in which the sign of $\delta\phi$ between the neighboring pair of layers vary randomly.

In our model, the **Sm**C_α, **Sm**C_2 and **Sm**C_R phases have same energy and are ,therefore, degenerate structures. The lower-temperature SmC_I phase observed in the studied samples is identified with the coexistence of these three degenerate SmC_α, SmC_2, and SmC_R structures.

In summary,

- We studied LC phases of compounds consisting of BCHS molecules. There are very few reports on the phase behavior of such compounds.
- We find two new pseudo-polar tilted smectic phases for two different compounds

consisting of BCHS molecules. This is the first report on the pseudo-polar tilted smectic phases exhibited by BCHS molecules.

- In these new types of tilted smectic phases, these BCHS molecules adopt a zigzag configuration which induces an axial-vector order parameter in addition to tilt order in the layers.
- Contrary to the $B2$ phase of bent-core banana-shaped molecules, the layers in these pseudo-polar tilted smectic phases are achiral in nature with no net electric polarization.
- A theoretical model is developed to account for the observed tilted smectic phase.
- In the higher-temperature SmC_A phase, an anticlinic tilt and antiparallel axial-vector order are observed.
- In the lower-temperature SmC_I phase, an intermediate structure with the coexistence of three different degenerate structures is observed.

Chapter 4

In this chapter, we have studied the field effects on the pseudo-polar tilted smectic phases exhibited by BCHS molecules. Both phases show the absence of spontaneous polarization in the layers as no peaks were detected in the polarization reversal current measurements. However, in spite of the lack of layer polarization, some remarkable electro-optic effects were observed under the application of an AC electric field in both the smectic phases. We divided this chapter into two parts. In the first part, we discussed the experimental results on the field effects for both compounds 4OC18 and A14. The changes in the average transmitted intensity were measured for both the phases of a planar-aligned samples under the application of an AC electric field. The effective birefringence of the planar-aligned sample in the higher-temperature SmC_A phase was estimated from the measured average transmitted intensity. The effective birefringence remains nearly constant up to a threshold field beyond which the birefringence starts to increase gradually. This clearly showed a field-induced transition beyond a threshold field.

A theoretical model to account for the field-induced changes in the effective birefringence for a planar-aligned sample in the SmC_A phase. The experimentally and theoretically calculated effective birefringence variation as a function of an applied field for compounds 4OC18 and A14 are shown in Figure 10.

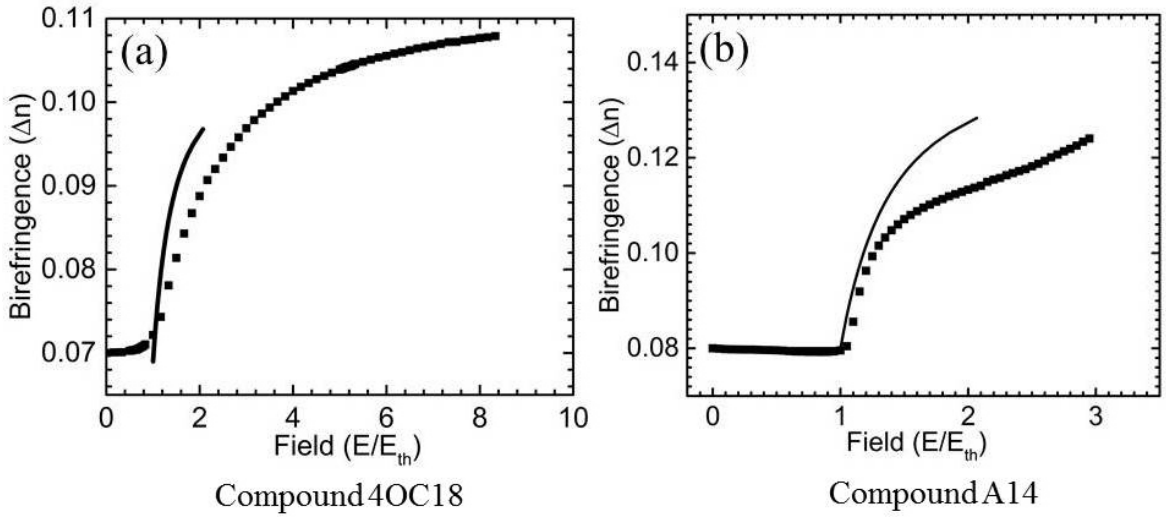

Figure 10: The effective birefringence of a planar-aligned sample in the SmC_A phase with increasing amplitude of applied electric field of frequency 1 kHz of compounds (a) 4OC18 (b) A14. The data points are experimental values whereas the solid lines show the theoretically calculated value of the effective birefringence using our model.

Our theoretical model predicts a Fréedericksz type transition of the tilt plane in the SmC_A phase beyond a threshold field.

In summary,

- The field effects on the observed pseudo-polar tilted smectic phases were studied for two compounds.
- The observed tilted smectic phases do not possess net electric polarization in the layers. Yet, some remarkable optical responses were observed with an applied AC electric field.
- The steady-state optical responses in both the mesophases indicated quadratic coupling of the electric field with the effective dielectric anisotropy of the sample.
- The average transmitted intensity measurements indicated a field-induced transition beyond a threshold field in the higher-temperature SmC_A phase.
- A theoretical model is developed to account for this field-induced transition in the higher-temperature SmC_A phase.
- The proposed model predicts a Frèedericksz type transition of the tilt plane in the SmC_A phase beyond a threshold field, which agrees well with the experimental results near the threshold field.

Chapter 5

In this chapter, we describe the experimental studies of a lower homologue of a compound consisting of an azo-substituted BCHS molecule (A9). The phase behavior of higher homologue (A14) is described in chapter 3 and chapter 4. Interestingly, this lower homologue shows a transition from the SmA to the deVries SmA phase which in turn undergoes a transition to the SmC phase at the lower temperatures. This is the first report on the observation of the deVries SmA phase exhibited by BCHS molecules. The phase sequence of the compound A9 is shown in Figure 11. Moreover, a compound showing the SmA-deVries SmA-SmC phase sequence is not reported in the literature.

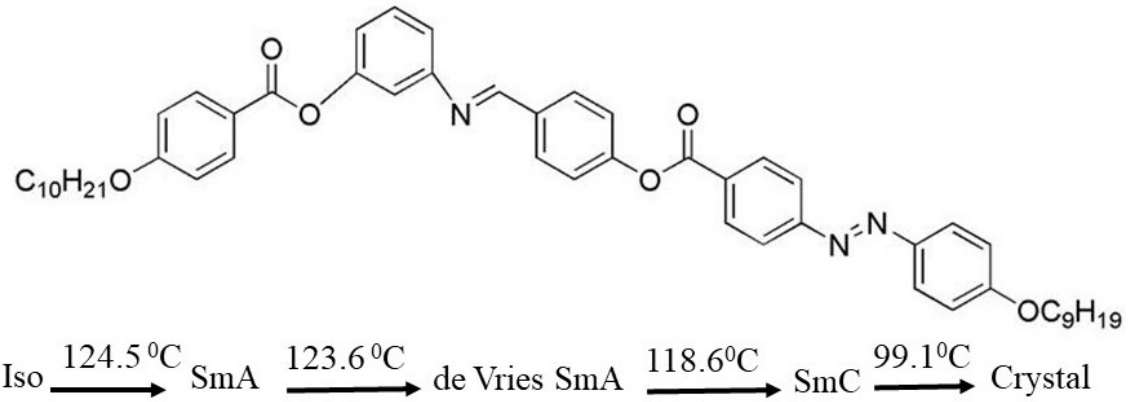

Figure 11: The molecular structure and the phase sequence observed on cooling the sample from the isotropic phase. The transition temperatures were detected by DSC thermogram except for the transition from the deVries SmA phase to SmC phase. The latter transition was detected by POM.

Three smectic phases (SmA, deVries SmA, and SmC) were observed between the isotropic liquid and crystal phases on cooling the sample from the isotropic phase. DSC thermogram showed a transition peak from the isotropic to the SmA phase. On further cooling, a transition peak was observed from the SmA to the deVries SmA phase. The transition from the SmA to deVries SmA phase was associated with a small enthalpy change (0.24 kJ/mole) indicating a very weak first-order transition. A first-order transition was expected as there is no symmetry change between these two phases. The transition from the deVries SmA to the SmC phase was not detected in DSC thermogram indicating a second-order phase transition as expected theoretically. However, the XRD and POM studies clearly detected the transition from the deVries

SmA to the SmC phase.

POM textures for a homeotropically-aligned sample are shown in Figure 12. A completely dark texture (Figure 12a) was observed in the SmA phase when the sample was cooled from the isotropic phase between crossed polarizers. No textural changes were detected on rotating the sample with respect to the polarizer indicating a uniaxial SmA phase. The texture remained dark as the sample goes from the SmA to the deVries SmA phase (Figure 12b). Again, no textural changes were observed as the sample was rotated with respect to the polarizer. Together with XRD results, these observations clearly indicated the existence of the deVries SmA phase. On further cooling of the sample, a schlieren texture with the presence of unit strength defect was observed in the SmC phase (Figure 12c) which indicates the synclinic tilted arrangement of the molecules in successive layers.

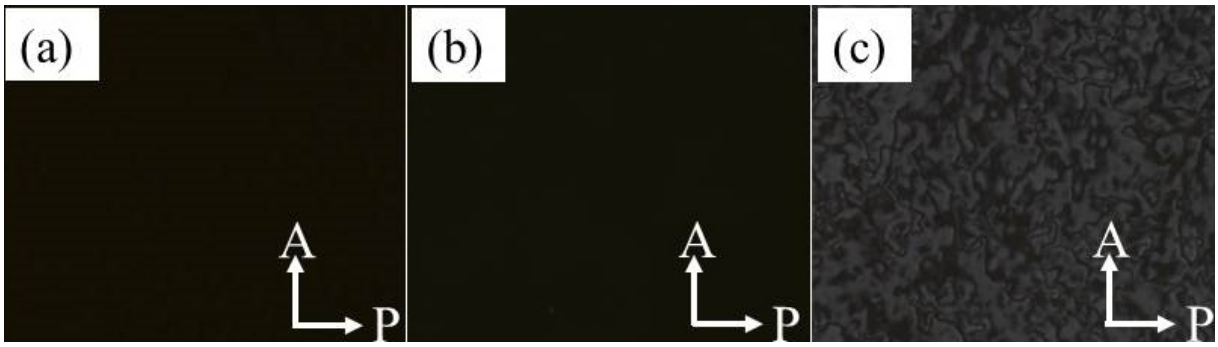

Figure 12: The homeotropically-aligned sample for compound A9 under cross polarizers on cooling the sample from the isotropic phase in (a) SmA phase (b) deVries SmA, and (c) SmC_S phase.

The presence of a sharp small-angle peak in addition to a diffusive peak in the wide-angle region in the XRD profile confirmed the layer structures in all these three phases. The observed layer spacing in the SmA phase (51.7 Å) is of the order of molecular length indicating non-tilted nature of the molecules in the layers. The layer spacing for the deVries SmA and SmC phases are smaller than the molecular length indicating that the molecules are tilted in the layers. The variation of layer spacing and tilt angle as a function of temperature is shown in Figure 13. The vertical dotted lines show the transition between different phases. The layer spacing remained constant in the SmA phase. On cooling the sample from the SmA to the deVries SmA phase,

the layer spacing decreased gradually. A very small change in the layer spacing was observed at the transition point from the deVries SmA to the SmC phase which was about 2%. This small change in the layer spacing at the transition from the deVries SmA to the SmC phase is the characteristic signature of the deVries SmA phase.

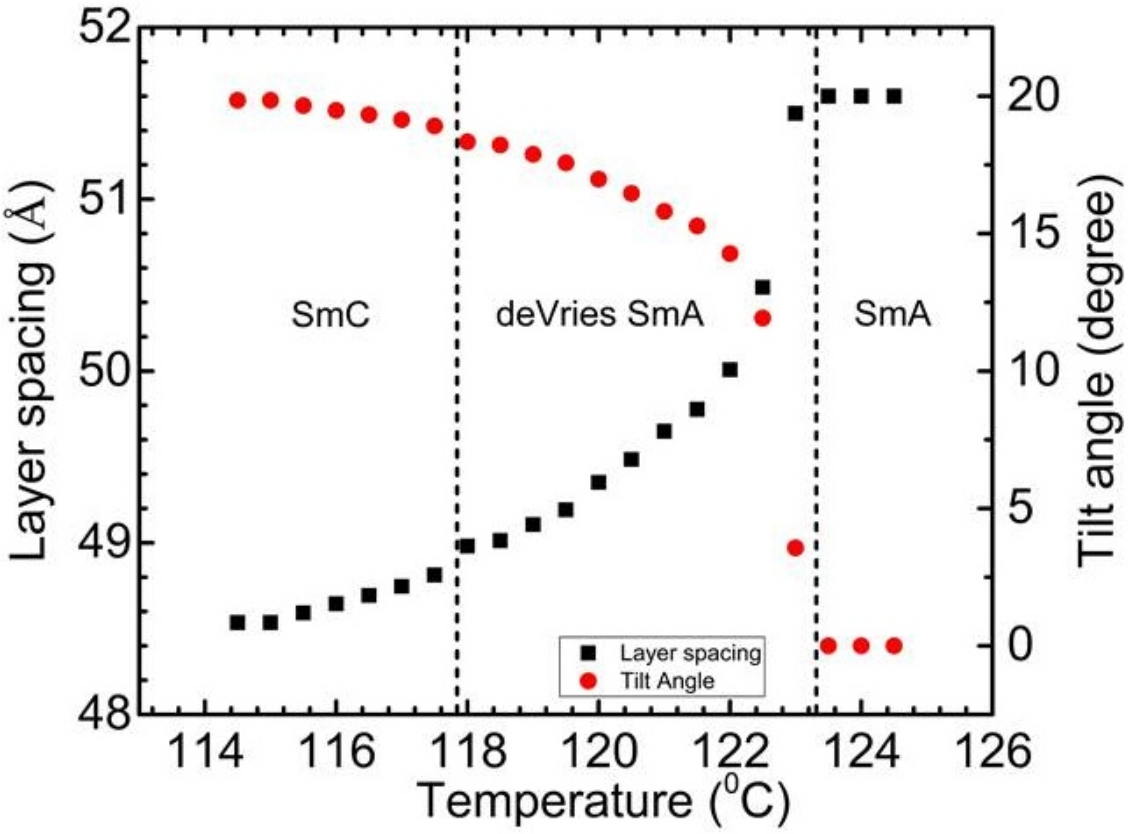

Figure 13: The variation of layer spacing and tilt angle with temperature for compound A9. The data was recorded on cooling the sample from the isotropic phase.

In summary,

- A compound consisting of azo-substituted BCHS molecules was studied which shows the SmA → deVries SmA→ SmC phase sequence on changing the temperature.
- This is the first report of a BCHS compound exhibiting the deVries SmA phase.
- Interestingly, this compound shows a first-order phase transition from the conventional orthogonal SmA phase to the deVries SmA phase which has not been reported in the literature earlier.
- Our experimental evidences indicate a diffusive cone model structure for the observed deVries SmA phase.

Chapter 6

In this chapter, we present experimental studies on the phase diagram of a binary mixtures of rod-like and BCHS molecules. The molecular structures and the phase sequences of pure compounds 4OC18 and 8OCB are shown in Figure 14.

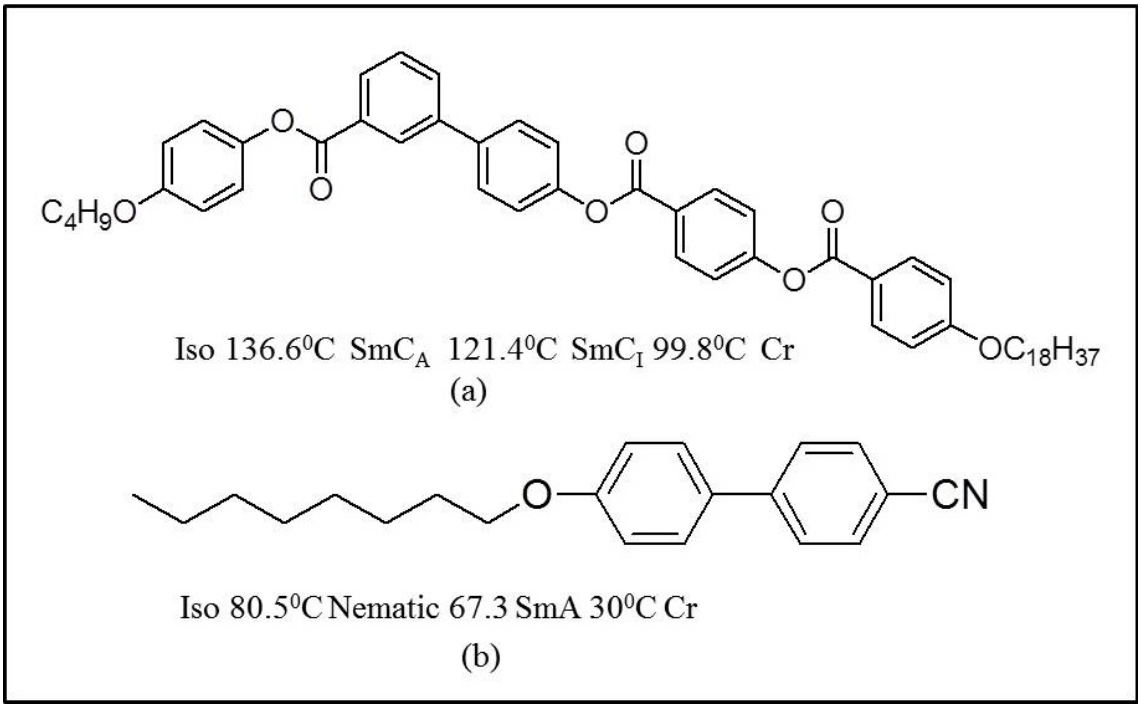

Figure 14: Molecular structures of (a) a pure compound 4OC18 consisting of BCHS molecules (b) compound 8OCB consisting rod-like molecules and phase sequence on cooling the sample from the isotropic phase.

The detailed physical properties of compound 4OC18 made of BCHS molecules are already discussed in chapter 3. The compound 8OCB consisting of rod-like molecules has been well studied in the liquid crystal literature. It is known that the presence of a strongly dipolar cyano end group in 8OCB rod-like molecules lead to an antiparallel orientational correlation between them. The overlapping of the aromatic cores of molecules gave rise to a partial bilayer SmA_d phase at lower temperatures in addition to the Nematic phase at higher temperatures. The temperature versus molar percentage phase diagram of the binary mixtures of these compounds is shown in Figure 15. It was found that two compounds mixed homogeneously at all concentrations at higher temperatures but phase segregation was observed at lower temperatures on increasing the molar concentration of BCHS molecules in the mixtures. For lower concentrations

of BCHS molecules in the mixtures, the calamitic Nematic and SmA_d phases were stable. The temperature ranges of stability of both the Nematic and SmA_d phases became narrow with increasing concentration of BCHS molecules in the mixtures.

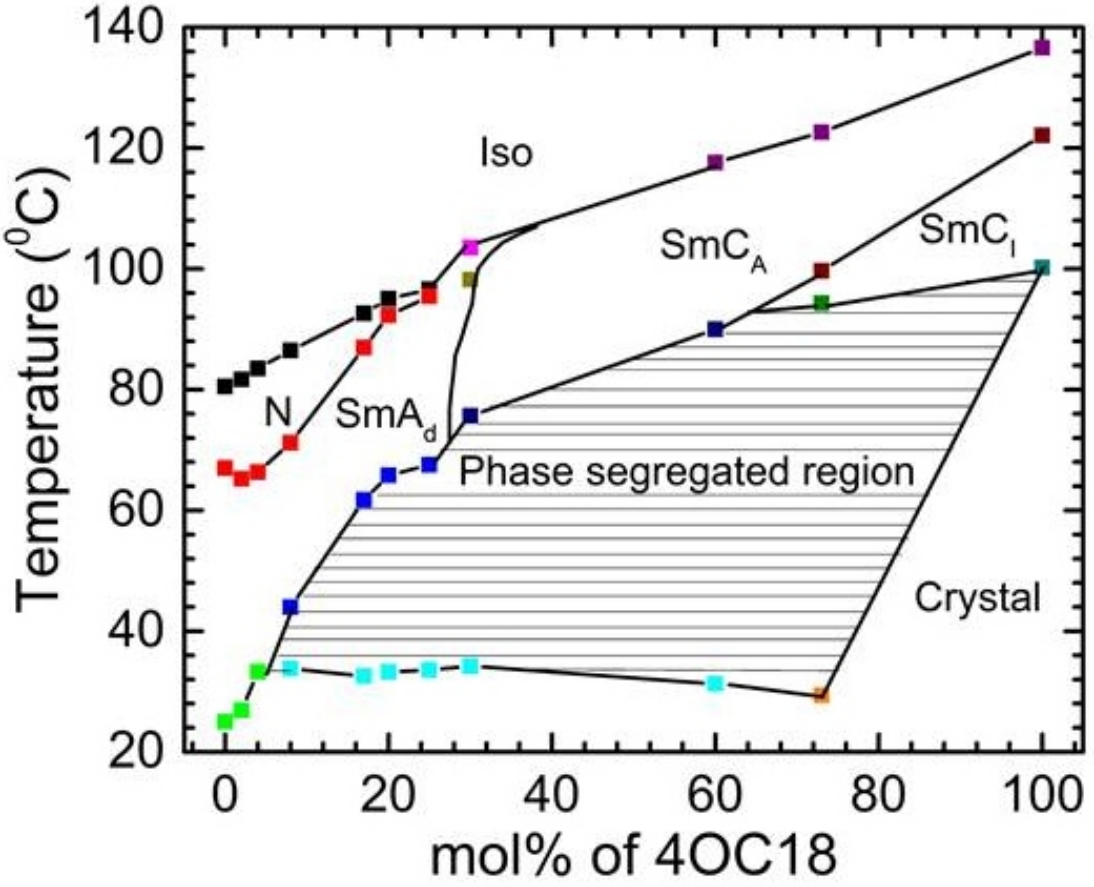

Figure 15: Temperature-concentration phase diagram for the binary mixture of BCHS and rod-like molecules.

Interestingly, it was found experimentally that the layer spacing in the SmA_d phase increased continuously upon increasing the molar concentration of BCHS molecules in the mixtures (Figure 16). The layer spacing in the SmA_d phase increased to a value which was about double the length of the rod-like molecules corresponding roughly to a bilayer configuration of rod-like molecules in the layers. Beyond a certain concentration of BCHS molecules, the calamitic liquid crystal phases became unstable and pseudo-polar smectic phases were stabilized due to BCHS molecules. These studies on the mixtures clearly demonstrated that the layer spacing in the SmA_d phase could be tuned continuously by controlling the concentration of BCHS molecules in the mixtures. The incorporation of the BCHS molecules in the uniaxial smectic layers of the rod-like

molecules introduced biaxiality in the layers due to hindered rotation of the BCHS molecules about their long axes and beyond a certain concentration, the pseudo-polar tilted smectic phases characterized by an axial-vector order parameter and a tilt order were stabilized.

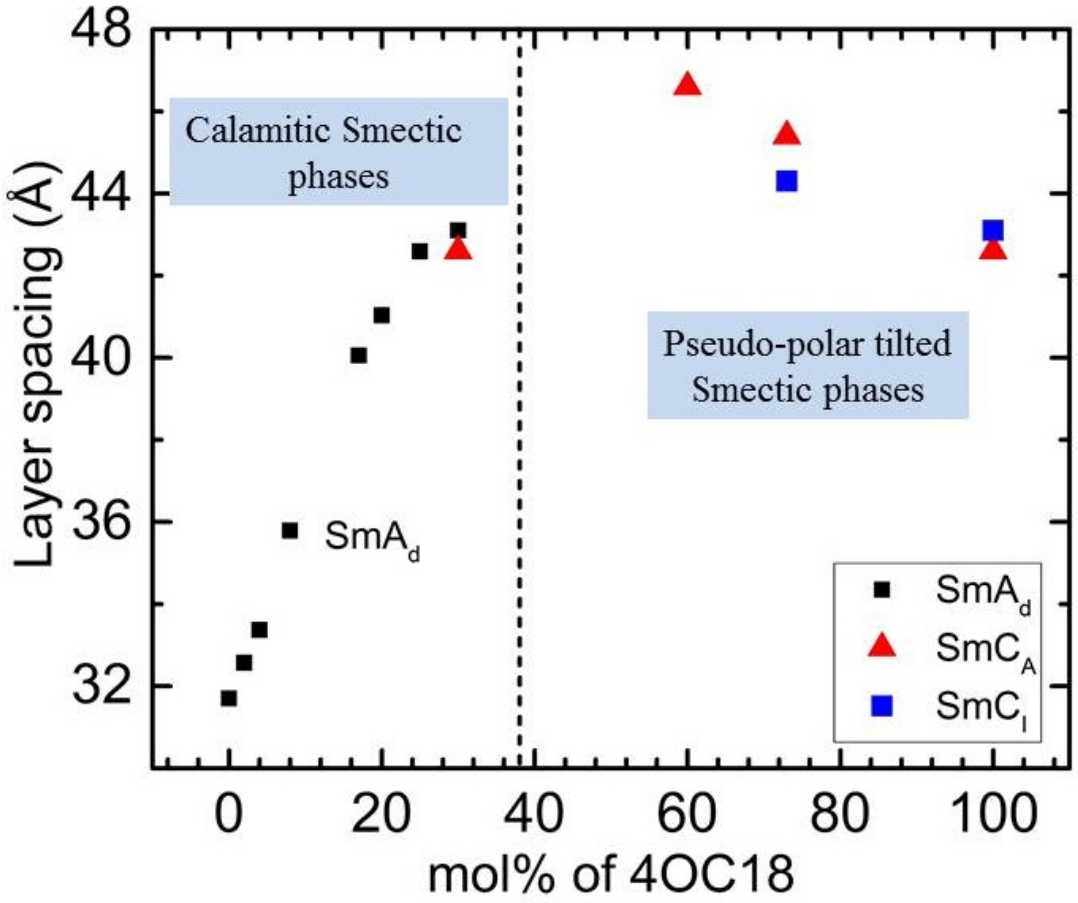

Figure 16: Layer spacing variation as a function of the molar percentage of compound 4OC18 in the binary mixtures. The dotted line roughly indicates the concentration above which the calamitic phases cease to exist and the pseudo-polar tilted smectic phases are stable.

In summary,

- The phase diagram of the binary mixture of compounds consisting of rod-like and BCHS molecules is constructed.
- The mixtures rich in rod-like component shows calamitic Nematic and SmA_d phases whereas rich in BCHS molecules mixtures exhibit pseudo-polar tilted smectic phases.
- The phase diagram of binary mixtures indicates that the pseudo-polar tilted smectic phases are the characteristic phases of BCHS molecules.

- The Iso-Nematic transition temperature (T_{NI}) increases with the increasing concentration of BCHS molecules. Thus, the guest BCHS molecules tend to increase the orientational order of the host rod-like molecules.
- The layer spacing in the SmA_d phase of the mixtures can be tuned by varying the concentration of BCHS molecules.

List of Publications

1. **Deepshika Malkar**, B.K. Sadashiva, and Arun Roy, "Pseudo-polar tilted smectic phases exhibited by bent-core hockey-stick shaped molecules", *Soft Matter,* **12**, 4960-4966 (2016).

2. G.Pratap, **Deepshika Malkar**, E.Varathan, Nitin.P.Lobo, Arun Roy, and T.Narasimhaswamy, "3-Cyano thiophene-based π-conjugated mesogens: XRD and ^{13}C NMR investigations", *Liq. Cryst.,* **12**, 1-14 (2019).

3. **Deepshika Malkar**, M.Monika, Veena Prasad, and Arun Roy, "Pseudo-polar smectic-C phases of azo-substituted achiral bent-core hockey-stick-shaped molecules", *Phys. Rev. E,* **101**, 12701 (2020).

4. **Deepshika Malkar**, Veena Prasad, and Arun Roy, "Evidence of Smectic-A to deVries SmA phase transition exhibited by bent-core hockey-stick shaped molecules", *Manuscript is under preparation.*

5. **Deepshika Malkar** and Arun Roy, "Tunable Smectic layer spacings in mixtures of rod-like and bent-core hocckey-stick shaped molecules", *Manuscript is under preparation.*

Contents

List of Tables

List of Figures

ABBREVIATIONS

LC	liquid crystal
DSC	differential scanning calorimetry
XRD	X-ray diffraction
POM	polarizing optical microscopy
BC	bent-core
BCHS	bent-core hockey-stick
MCHS	meta chain hockey-stick chain
8OCB	4'-(Octyloxy)-4-biphenylcarbonitrile
4OC18	4-n butyloxyphenyl 4-(4-n-octadecyloxybenzoyloxy-4-benzoyloxy) biphenyl-3-carboxylae
A9	4-(((3-((4-(Decyloxy)benzoyl)oxy)phenyl)imino)methyl)phenyl4-(-(4-(n-nonyloxy)phenyl)diazenyl)benzoate
A14	4-(((3-((4-(nDecyloxy)benzoyl)oxy)phenyl)imino)methyl)phenyl4-(-(4-(n-tetradecyloxy)phenyl)diazenyl)benzoate
PI	poly imide
ODSE	octadecyl triethoxy silane
N	Nematic
SmA	Smectic A
SmC	Smectic C
SmC_A	Anticlinic Smectic C
SmC_S	Synclinic Smectic C

NOTATION

d	layer spacing, Å
l	molecular length, Å
$\vec{n}$	director,
Δn	refractive index,
$\Delta\phi$	phase difference,
ϵ	dielectric constant,
$\epsilon_{\parallel}$	parallel dielectric constant,
$\epsilon_{\perp}$	perpendicular dielectric constant,
$\Delta\epsilon$	dielectric anisotropy,
n_e	refractive index of extraordinary ray,
n_o	refractive index of ordinary ray,
ϕ	azimuthal angle,
θ	tilt angle,
$\vec{\xi}$	tilt order parameter,
$\vec{\eta}$	axial-vector order parameter,
ϵ_0	permittivity of free space,
f	free energy density,
f_e	electric field free energy density,
F	total free energy,
$\hat{k}$	layer normal,
K	elastic constant,
λ	wavelength of incident light,
b	layer spacing,
ψ	angle between the optic axis of molecule and the polarizer,

Chapter 1

Introduction

In 1988, Austrian botanical physiologist Friedrich Reinitzer was working with cholesteryl benzoate (Figure 1.1) and found that it has two melting points [1, 2]. On heating it, he observed that at 145.5 ^{0}C it melts into a cloudy liquid, and on further heating around at 178.5 ^{0}C, it becomes optically clear.

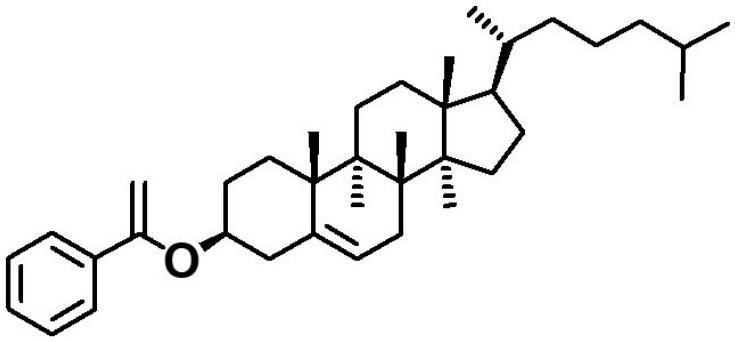

Figure 1.1: Molecular structure of cholesteryl benzoate.

Later on, Otto Lehmann, a German physicist, studied cholesteryl benzoate and the other compounds with more than one melting point under polarized microscope [3]. He found that the intermediate cloudy phase contains the property of both the isotropic liquid and the solid crystal. Therefore, he coined the name for the cloudy phases as "flüssiger Kristall," which means liquid crystal as it contains the property of the isotropic liquid and a solid crystal together. Daniel Vörlander, a German chemist, synthesized many liquid crystals in 20^{th} century [4] and the fascinating liquid crystal phases are established as intermediate phases of isotropic liquid and crystalline phases. Sometimes, liquid crystal phases are also called as mesophases or mesomorphic. The term mesophase originated from the Greek word meso, which means an intermediate or middle. When a liquid crystal compound is heated from it's crystal phase under the polarizing optical microscope, the solid changes into a cloudy liquid at the melting point. This phase was found to be strongly birefringent. Upon further heating, a second

transition appeared where this cloudy liquid becomes isotropic liquid and, therefore, optically transparent. The second transition point is known as the clearing point of the sample. The temperature range of stability of mesophase is defined by the melting point and the clearing point. Compounds that possess the LC phases are called as mesogenic. The fundamental requirement of the compounds to show the liquid crystal properties is that constitutent molecules should be anisotropic in shape [5, 6].

Broadly, liquid crystals can be classified (Figure 1.2) as thermotropic and lyotropic liquid crystals.

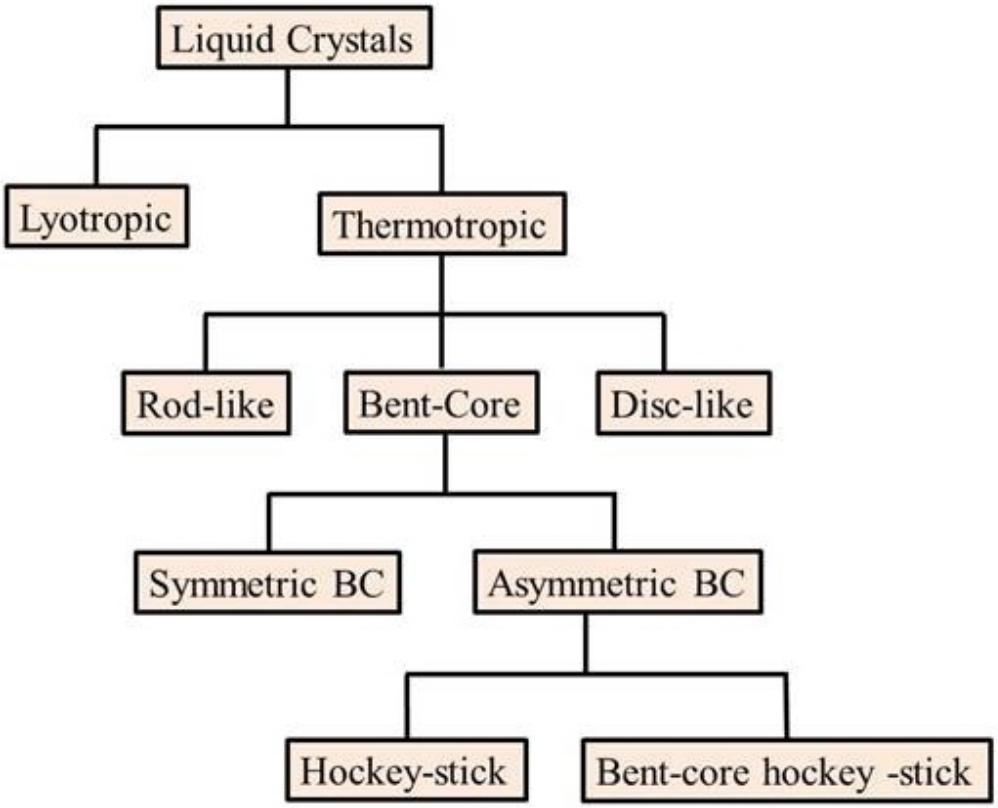

Figure 1.2: Classification of liquid crystals.

1.1 Thermotropic Liquid crystals

For thermotropic liquid crystals (thermo- means temperature and tropic means change), the mesophases appear on varying the temperature of the sample as shown in Fig-

ure 1.3. A mesophase is known as enantiotropic when it is stable on both the heating and cooling cycle of the sample. Whereas, a phase is said to be monotropic when it is stable only on cooling the sample.

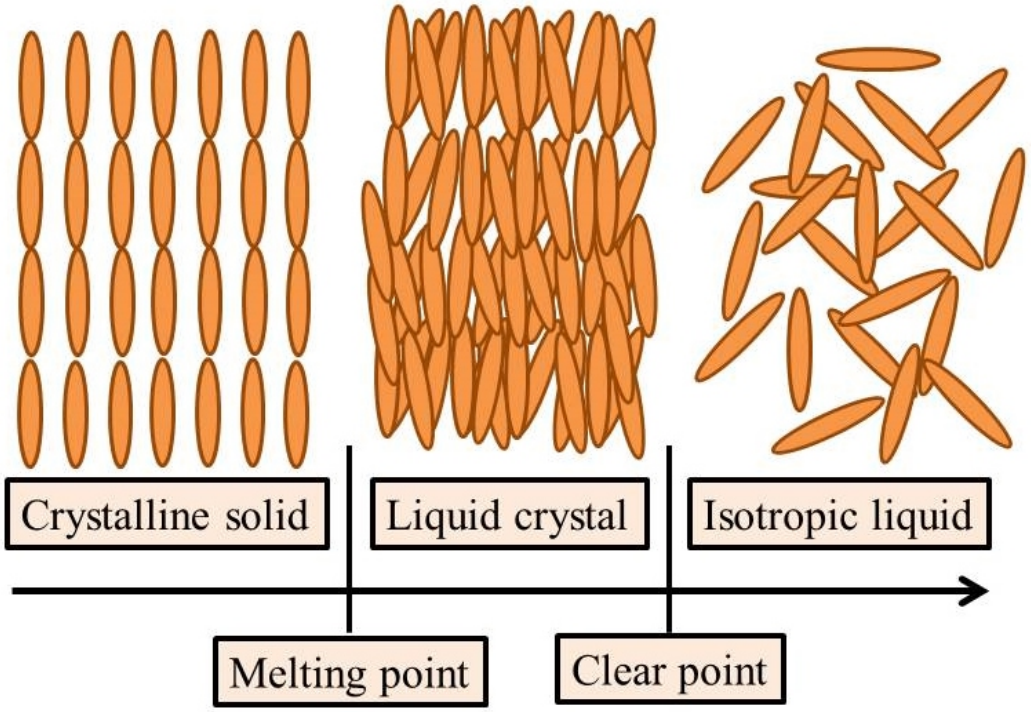

Figure 1.3: The stability range of thermotropic liquid crystals.

1.2 Lyotropic liquid crystals

Lyotropic liquid crystals (lyo- means dissolve and tropic means change) are formed when an amphiphilic molecule is dissolved in a suitable solvent under the appropriate physical conditions like concentration, temperature, and pressure [7]. The different lyotropic mesophases can be obtained by varying the concentration at a given temperature and pressure. The simplest example of a lyotropic liquid crystal is the mixture of soap and water.

A liquid crystal is known as amphotropic when it shows both thermotropic and lyotropic mesophases. We will restrict ourselves to the thermotropic liquid crystals as this thesis deals with various properties of thermotropic liquid crystals consisting

of rod-like and bent-core molecules. Based on the molecular shape, the thermotropic liquid crystals can be classified as:

1. Calamitic liquid crystals: constituent molecules are rod-like in shape.
2. Discotic liquid crystals: constituent molecules are disc-like in shape
3. Bent-core banana-shaped liquid crystals: constituent molecules have bent-core banana-like shape.

1.3 Common phases of rod-like liquid crystals

Liquid crystals consisting of rod-like molecules are known as calamitic liquid crystals. A rod-like molecule contains a rigid rod-like core and the terminal aliphatic chains are usually attached to either one or both end of the rigid part. Figure 1.4 shows the molecular structure of a rod-like molecule.

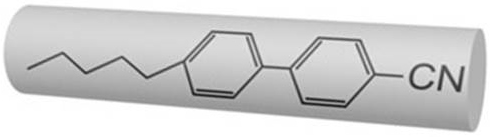

Rod- like

Figure 1.4: Schematic representation of a rod-like molecule.

The common mesophases formed by the calamitic liquid crystal are Nematic, Smectic phases.

1.3.1 Nematic phase

The simplest example of LC phases exhibited by rod-like molecules is the Nematic phase. The word Nematic originates form a Greek word which means thread and this phase is named as Nematic because of the thread-like structures often observed in the texture of the Nematic phase between crossed polarizers as shown in Figure 1.5.

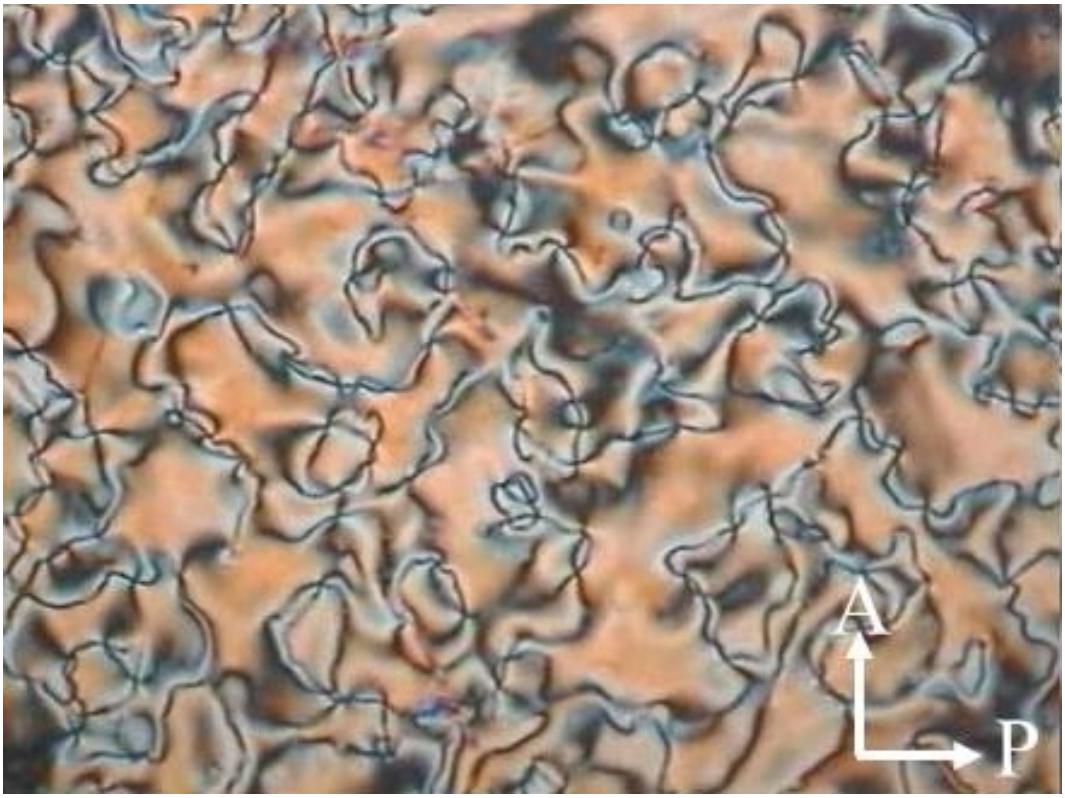

Figure 1.5: Schlieren texture in the Nematic phase for a planar-aligned sample between crossed polarizers [8].

In the Nematic phase, there is no long-range translational order between the center of mass of the molecules but the molecules are on average aligned with their long axes parallel to each other. The average orientation direction of the molecules is defined as director and is denoted by a unit vector $\hat{n}$. The director $\hat{n}$ in the sample gives the preferred direction of the long axes of the molecules at each point but $\hat{n}$ and -$\hat{n}$ are indistinguishable in the Nematic phase. The schematic representation of the organization of rod-like molecules in the Nematic phase is shown in Figure 1.6.

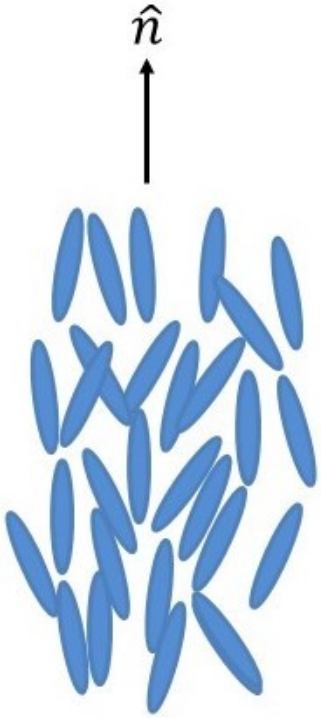

Figure 1.6: Schematic representation of the Nematic phase exhibited by rod-like molecules.

Figure 1.7 shows some example of Nematic liquid crystals.

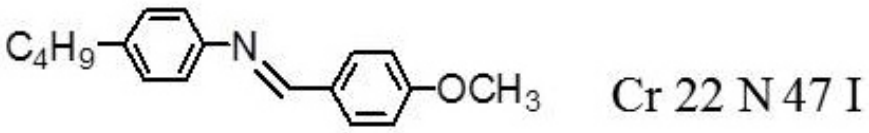

Cr 22 N 47 I

N-(pmethoxybenzylidene)-p'butylaniline,
MBBA

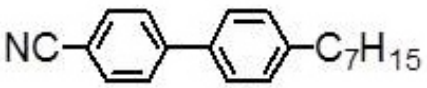

Cr 28.5 N 42 I

p-heptyl-p'-cynobiphenyl

Figure 1.7: Some examples of Nematic liquid crystals exhibited by rod-like molecules [9, 10].The temperatures are given in ^{0}C.

The molecules in the Nematic phase are free to rotate about their long axes and there are rotational symmetries, *i.e.*, cylindrical symmetry (D_{∞_h}) about the director $\hat{n}$ in this phase and it is uniaxial in nature. The director $\hat{n}$ can vary continuously in the bulk of the sample. The variation of the director $\hat{n}$ in space can give rise to various topological defects which are visible in a optical polarizing microscope. The XRD studies in the Nematic phase give only a diffusive peak (see Figure 1.8) in the wide-angle region indicating fluid-like structure. No sharp peaks are usually observed in the small-angle regions as there is no translational order in this phase. The inset of Figure 1.8 shows the magnified view of the diffusive peak in the wide-angle region.

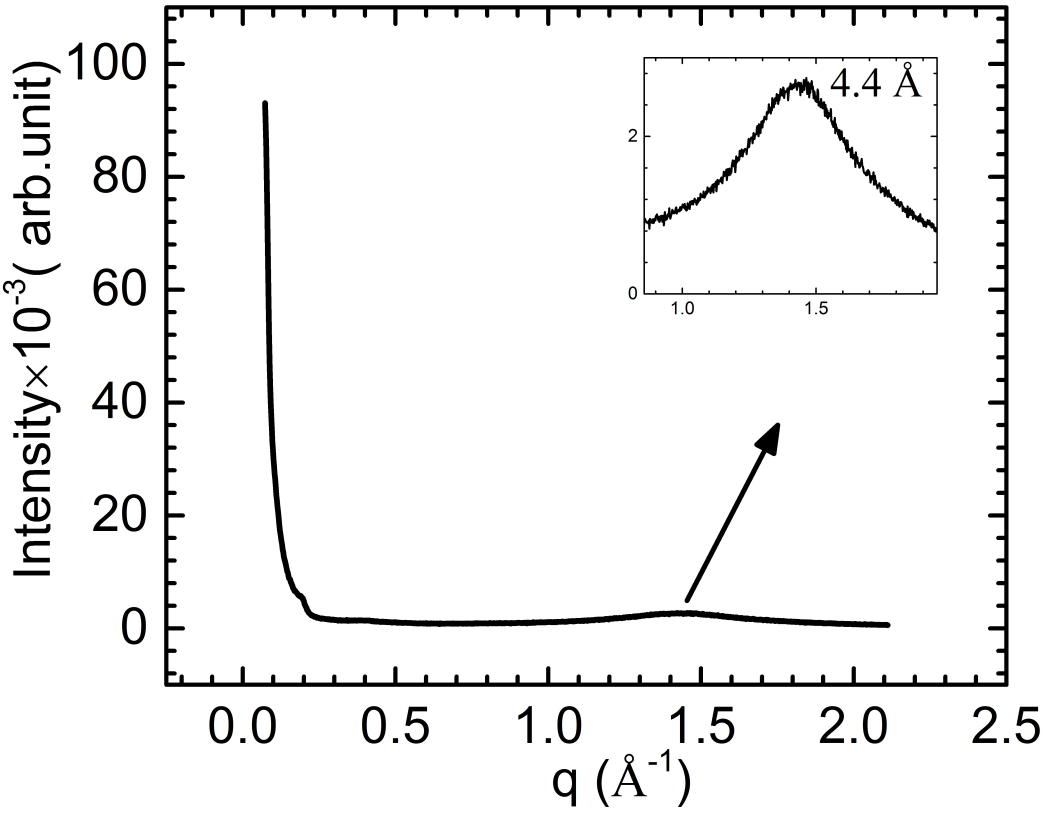

Figure 1.8: XRD intensity profile of compound 8OCB in the Nematic phase at 70 ^{0}C.

The orientational order of the rod-like molecules in the Nematic phase can be defined as follows. Let us consider the orientation of the long axis of a rod-like molecule is specified by the unit vector $\hat{a}$ and the molecule has cylindrical symmetry about $\hat{a}$. Without loss of generality, let us consider the average orientation direction of the molecules, *i.e.*, $\hat{n}$ as the Z-axis of a coordinate system at that point in the sample. The orientation of $\hat{a}$ can be specified by its polar angles θ and ϕ giving

$$a_x = \sin\theta\cos\phi$$
$$a_y = \cos\theta\cos\phi$$
$$a_z = \cos\theta$$

The distribution function $f(\theta,\phi)d\Omega$ gives the probability of finding a rod-like molecule oriented in a small solid angle $d\Omega$ at (θ,ϕ). As the uniaxial Nematic phase have completely cylindrical symmetry about the director $\hat{n}$. Therefore,

1. $f(\theta,\phi)$ is independent of ϕ.
2. $f(\theta)$=$f(\pi-\theta)$ as $\hat{n}$ and $-\hat{n}$ are indistinguishable.

The distribution function can be expanded in terms of the Legendre polynomials as

$$f(\theta)=\sum_{l=0}^{\infty} a_l P_l(\cos\theta) = a_0 + a_1 P_1(\cos\theta) + a_2 P_2(\cos\theta) + ...$$

where $l = 0, 1, 2, 3, 4.....$ are the orders of the polynomials. The first term in the expansion is independent of θ and gives an isotropic distribution of molecules. The coefficients of the terms with odd order $l = 1, 3, 5.....$ are zero due to the $f(\theta)$=$f(\pi-\theta)$ symmetry of the distribution function. Therefore, the first non-vanishing anisotropic term with $l = 2$ corresponding to the quadrupolar orientational order of the molecules can be taken as the order parameter. Thus, scalar orientational order parameter S can be defined as,

$$S = \tfrac{1}{2}\left\langle(3\cos^2\theta - 1)\right\rangle = \int f(\theta)\tfrac{1}{2}(3\cos^2\theta - 1)\sin\theta d\theta$$

where the angular brackets denotes the ensemble average with respect to the distribution function. Therefore, the probability of finding the molecules parallel or antiparallel to the director $\hat{n}$ is maximum at $\cos\theta = \pm 1$ giving S=1. For the random orientation, we would have

$$< \cos^2\theta >= \tfrac{1}{3} \text{ and } S = 0$$

Thus, the scalar order parameter S gives the measure of the degree of alignment of the long axes of the molecules along the director $\hat{n}$ in the Nematic phase. More generally, the combined orientational order parameter in the Nematic phase including the scalar order parameter S and the director $\hat{n}$ can be defined using a second rank tensor Q_{ij} which vanishes in the isotropic phase,

$$Q_{ij} = S(n_i n_j - \tfrac{1}{3}\delta_{ij})$$

where $i, j = x, y, z$. The tensor order parameter Q_{ij} is symmetric, trace-less and has five independent components. When the director is along the Z-axis, then

$$Q_{ij} = S \begin{bmatrix} -\frac{1}{3} & 0 & 0 \\ 0 & -\frac{1}{3} & 0 \\ 0 & 0 & \frac{2}{3} \end{bmatrix}$$

1.3.2 Smectic phases

The word smectic originates from the Greek word which means soap. In addition to the orientational order, the molecules in the smectic phase arrange themselves in a lamellar or layered structure and hence called smectic or soap-like. Thus, the molecules in this phase exhibit quasi long-range translational order along with the layer normal but within a layer, they are arranged liquid-like with no long-range transnational order. In addition, there is a long-range orientational order of the molecules. Thus, the smectic phase can be considered as crystal-like in one dimension and liquid-like in the other two dimensions. The X-ray diffraction studies give the direct evidence of the layered structure in the smectic phases. In the XRD intensity profile, a sharp-peak in the small-angle region corresponding to the translational order of the molecules is usually observed. In addition, a diffusive peak at the wide-angle region is observed, indicating the fluid-like short-range correlations of the molecules within the layers. The one-dimensional periodic modulation of the density along the layer normal (the Z-axis) can be expanded in term of Fourier series as

$$\rho(z) = \sum_{n=0}^{\infty} a_n \cos(2\pi n z/d)$$

where n is an integer and the coefficients a_n are determined as

$$a_n = \int \rho(z) \cos(2\pi n z/d) dz = \langle \cos(2\pi n z/d) \rangle$$

The coefficient a_1 of the first harmonic term can be taken as the order parameter for the smectic phase. The wave-vector $q = 2\pi/d$ is along with the layer normal denoted by the unit vector $\hat{k}$ and d is the layer thickness. Figure 1.9 shows the molecular structures of some compounds which exhibit smectic phases.

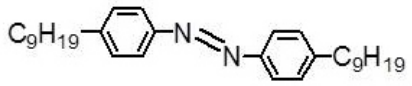

Cr 38 S_B 41 S_A 54 I

p,p'-dinonylazobenzene

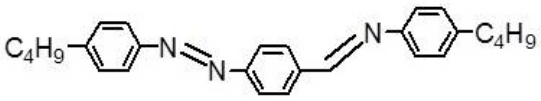

Cr 80 * S_S 89.5 *S_H 112.5 S_G 144 S_C 172.5 S_A 198.5* N 235.5* I

tetraphthal-bis-(p-butylaniline), TBBA

Figure 1.9: Some examples of the smectic liquid crystals exhibited by rod-like molecules. The temperatures are given in ^{0}C [11, 12]. * temperatures were observed on cooling cycle.

Based on the orientation of the molecules within the layers, smectic phases can be classified into different categories:

Smectic A phase

In the Smectic A phase (denoted as SmA), the long axes of the molecules are on average parallel to the layer normal as shown in Figure 1.10. The SmA phase also has D_{∞_h} point symmetry like the Nematic phase.

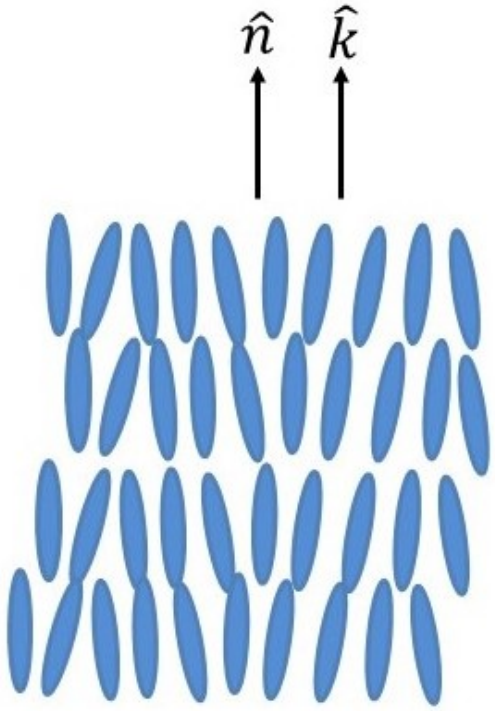

Figure 1.10: Schematic representation of the SmA phase exhibited by rod-like molecules.

Usually, the layer thickness (d) obtained from XRD studies is close to the molecular length (l) in this phase. Some of the compounds show a bilayer structure, where the layer thickness is about double of the molecular length ($d = 2l$) or an intercalated structure with the layer thickness between l and $2l$. The possible configuration of structures in the SmA phase is shown in Figure 1.11.

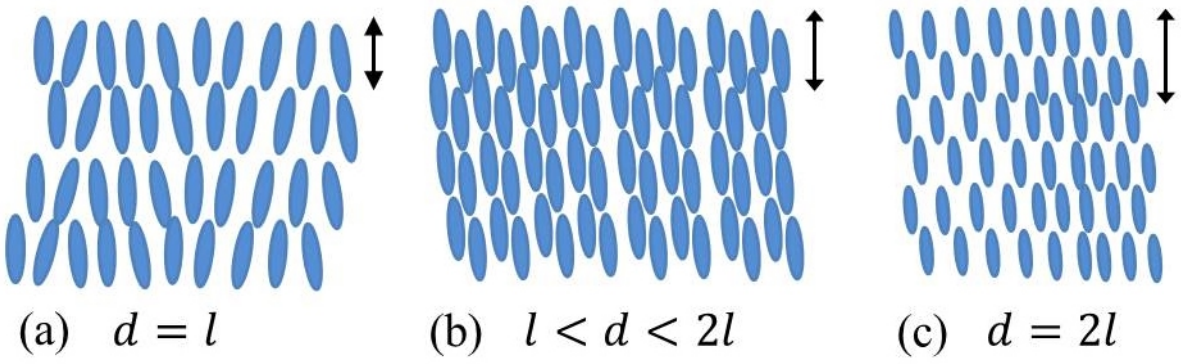

Figure 1.11: Schematic representation of possible molecular configuration in the SmA phase exhibited by rod-like molecules.

Smectic C phase

In the Smectic C (SmC) phase, the director $\hat{n}$ makes an angle θ, known as tilt angle with respect to the layer normal $\hat{k}$ as shown in Figure 1.12.

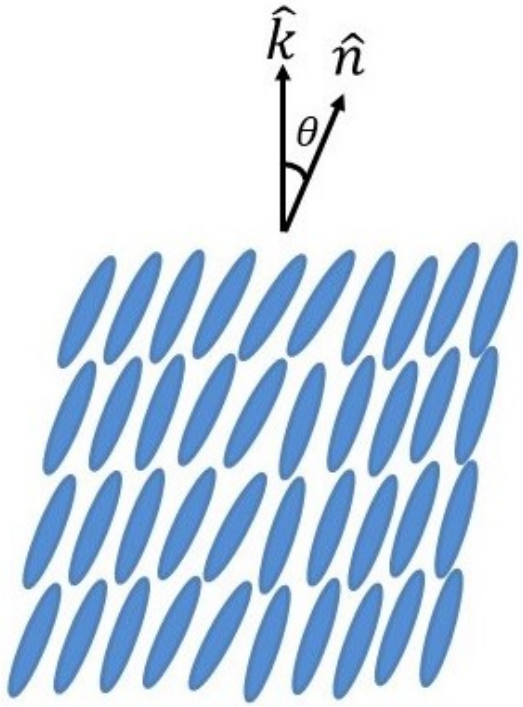

Figure 1.12: Schematic representation of the SmC phase exhibited by rod-like molecules.

The molecules are on average uniformly tilted with respect to the layer normal in successive layers. The tilt direction of the molecules are correlated from layer to layer. The tilt order in a layer can be described by a two dimensional vector, known as c-director $\vec{c}$ which is the projection of director $\hat{n}$ onto the layer plane as shown in Figure 1.13.

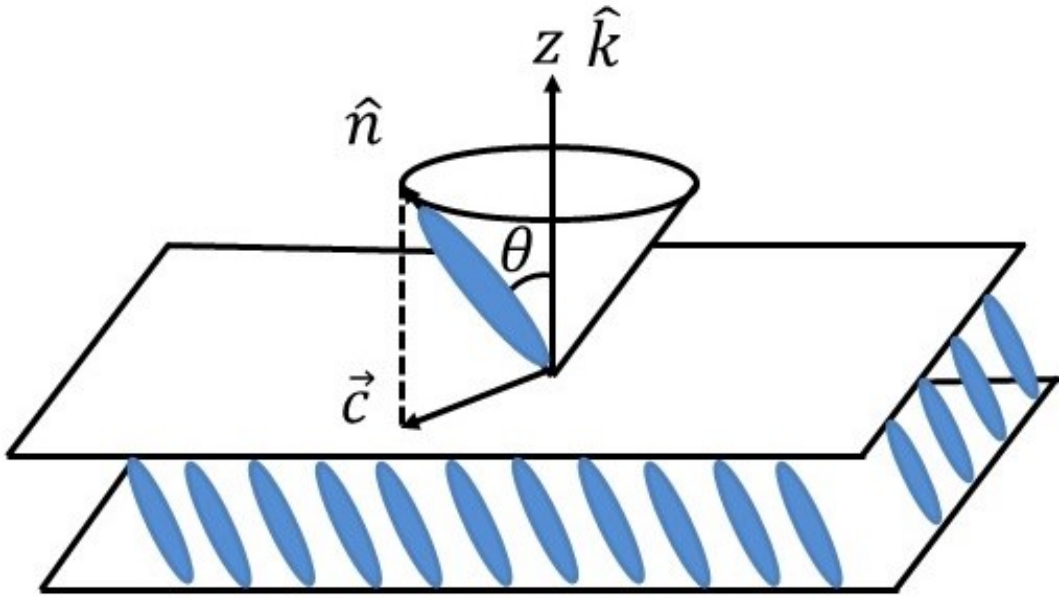

Figure 1.13: Schematic representation of c-director in the SmC phase.

The director $\hat{n}$ and -$\hat{n}$ still indistinguishable in the SmC phase. However, the c-director $\vec{c}$ and $-\vec{c}$ are distinguishable, therefore, $\vec{c}$ is a 2-d vector. The tilt of the molecules in the SmC phase introduces biaxiality in the layers. The SmC phase is optically biaxial with C_{2h} point symmetry. The layer spacing in this phase is reduced as $d = l\cos\theta$ where d is the layer thickness, l is molecular length and θ is the tilt angle of the molecules. The tilt order parameter in the SmC phase can also be defined by an axial-vector order parameter $\vec{\xi}$ which is defined as

$$\vec{\xi} = (\hat{n} \cdot \hat{k})(\hat{n} \times \hat{k})$$

where $\hat{k}$ and $\hat{n}$ are layer normal and the director, respectively.

1.3.3 Chiral Nematic or cholesteric phase

A molecule is said to be chiral when it lacks mirror symmetry. For example, the mirror images of hand can not be superimposed onto itself. A molecule can become chiral when all the four groups attached to the four bonds of a carbon atom forming tetrahedral structure are different as shown in Figure 1.14.

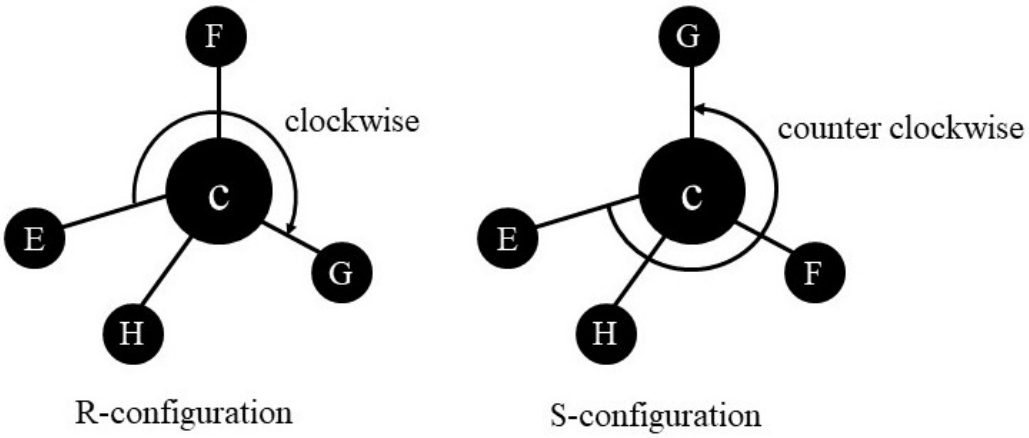

Figure 1.14: Schematic representation of two different spatial configuration.

Chirality is an inherent property of the system. A compound shows chiral Nematic phase if it is doped with chiral dopant or the molecules themselves are chiral. Chiral Nematic phase is also known as cholesteric phase as it was first observed for cholesterol derivatives. The chiral Nematic or cholesteric phase is denoted as N^*. Figure 1.15 shows some examples of chiral Nematic liquid crystals.

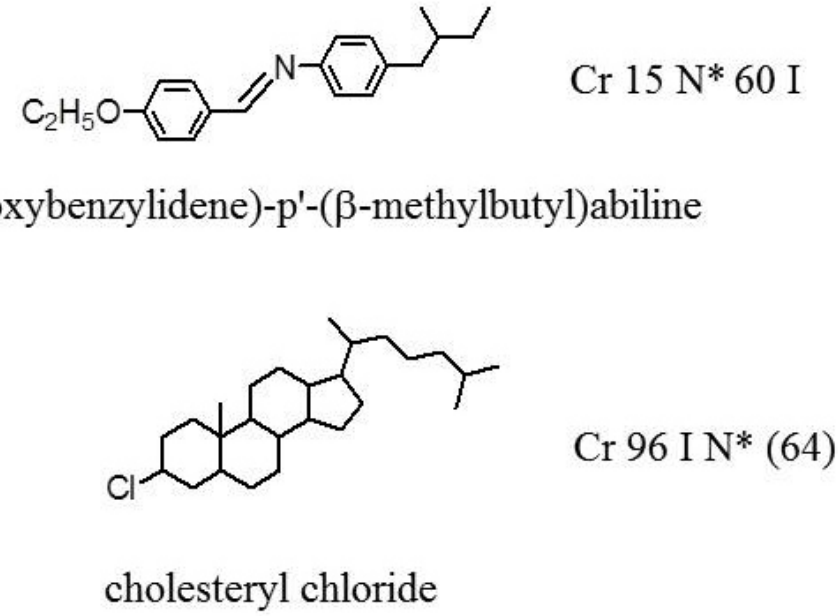

Figure 1.15: Some examples of chiral Nematic liquid crystals. The temperatures are given in ^{0}C. For the second compound the N^* phase was observed only on cooling [13, 14].

This phase is locally similar to the Nematic phase. However, because of the chirality

the director $\hat{n}$ varies in space and form a helical structure as shown in Figure 1.16.

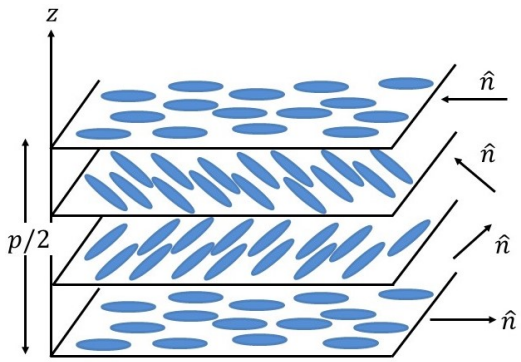

Figure 1.16: Schematic representation of chiral Nematic or cholesteric phase exhibited by rod-like molecules.

Taking the helix axis along the Z-axis, the helical structure of the director $\hat{n}$ in this phase can be written as

$$n_x = \cos(qz),\ n_y = \sin(qz),\ n_x = 0$$

where $q = 2\pi/p$ and p is the pitch of the helix. Here the pitch p is defined as the distance over which the director $\hat{n}$ has a full rotation of 2π. The sign of q distinguishes between left- and right-handed chiral Nematics. As the director $\hat{n}$ and -$\hat{n}$ are indistinguishable, the repetition period in the chiral Nematic phase is $p/2$.

1.4 Discotic Liquid Crystal

In 1977, Chandrasekhar at al. discovered discotic liquid crystals in which the constituent molecules are of disc shape [15]. Discotic liquid crystals are generally composed of an aromatic core surrounded by flexible terminal chains as shown in Figure 1.17. In these systems, the director $\hat{n}$ arises from the tendency of the disc-like molecules to align their short axes parallel to each other. The first synthesized discotic liquid crystal, benzene hexa-n-alkanoates, is shown in Figure 1.17b.

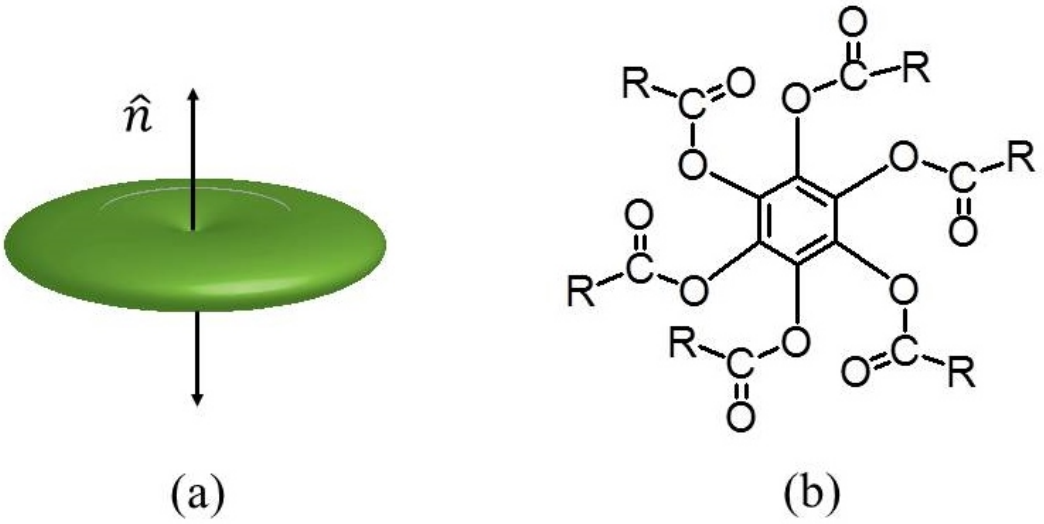

Figure 1.17: Schematic representation of (a) disc-like molecules and (b) an example of discotic liquid crystals.

In general, discotic liquid crystals form Nematic and columnar phase. The molecular arrangement in these phases are shown in Figure 1.18. The columnar phase is the simplest example of discotic liquid crystals, where the disc-like molecules stacked on the top of each other. The Nematic phase exhibited by disc-like molecules has only orientational order. The Nematic phase formed by disc-like molecules is often called as Discotic-Nematic (N_D) phase.

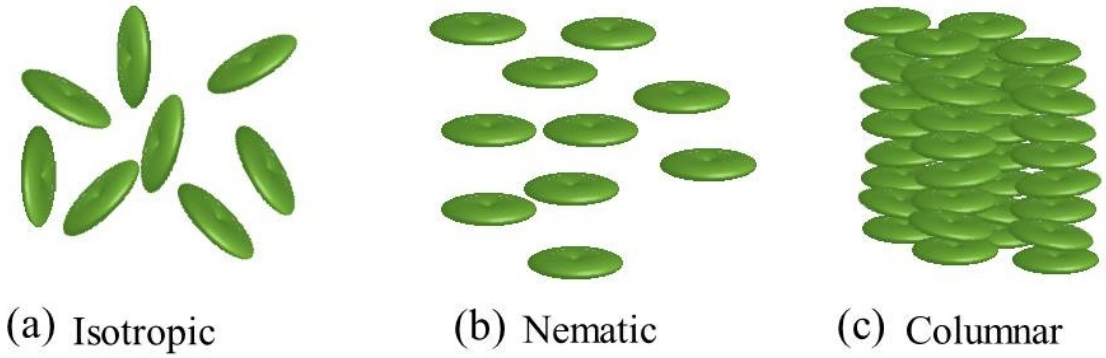

Figure 1.18: Some examples of mesophases exhibited by disc-like molecules.

1.5 Bent-core liquid crystals

In 1932, D. Vörlander synthesized several bent-core or banana-shaped molecules and reported their liquid crystal properties [16]. But in the beginning, scientists did not pay much attention towards bent-core (BC) molecules because of its kink shape as it hinders the free rotation of the molecules about their long axes. In 1975, Meyer et al. first reported [17] that chiral rod-like molecules in their tilted smectic phases can give rise to layer polarization and the coupling of polarization with an external electric field can produce a high-speed electro-optic response. Thus, in these systems

$$Tilt + chirality = polarity \tag{1.1}$$

However, the synthesis of the homochiral liquid crystal molecules increased the cost considerably. This created deviations of both theoreticians and experimentalists towards the alternate possibilities to find a ferroelectric liquid crystal phase consisting of achiral molecules. In 1990, R.H Tredgold reported theoretically that kinked shaped molecules could also possess spontaneous polarization and therefore, it could be ferroelectric liquid crystals [18]. In 1991, Y. Matsunaga et al. [19] synthesized liquid crystals consisting of achiral bent-core banana-shaped molecules and observed that they could form smectic phase. In 1996, H. Takezoe et al., for the first time reported experimentally that achiral bent-core banana-shaped liquid crystals possess spontaneous polarization in their smectic phases [20]. Figure 1.19 shows the typical molecular structure of a bent-core molecule [21].

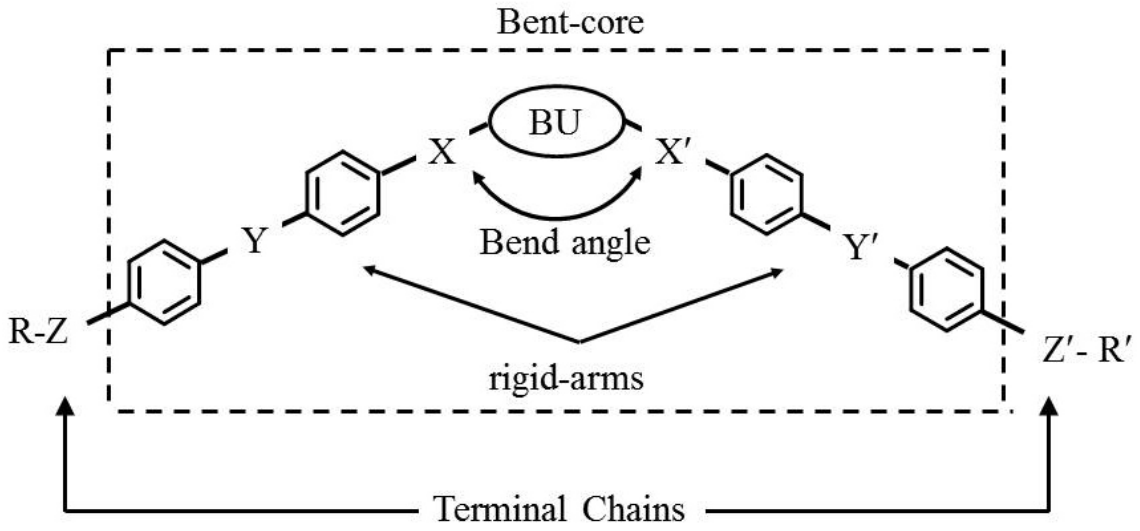

Figure 1.19: A typical molecular structure of a BC banana shaped molecule.

A bent-core banana-shaped molecule consists of a relatively rigid central bent-core moity which has two rod-like arms joined end to end making a bent angle which is typically 120 degrees between them. The flexible terminal chains (generally alkyl or alkoxy group) are attached at one or both ends of the rod-like arm of the molecules. The long axis of the bent-core banana-shaped molecule is defined by the line joining both ends of the molecule. The value of the bend angle for bent-core banana-shaped molecules ranges from 105 degrees shows strong bent to 140 degree. Figure 1.20 shows the front-, back- and side view of a BC molecule.

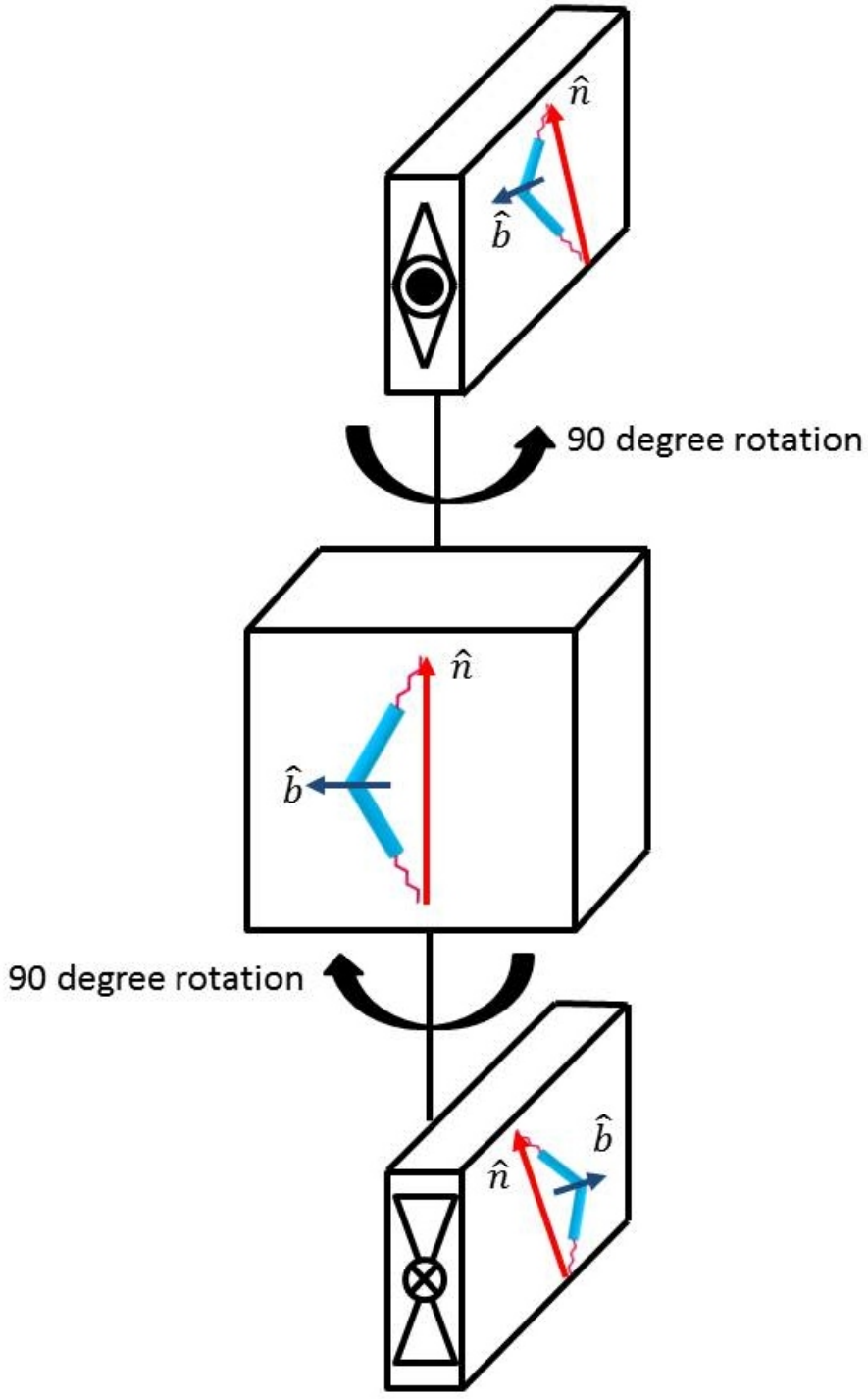

Figure 1.20: Schematic representation of a bent-core banana-shaped molecule showing front, side, and back view. The red and blue arrows show the long and arrow axes of the molecule.

In general, the packing of the bent-core banana-shaped molecules tends to form

a layered structure rather than a Nematic phase. The two rod-like arms at an angle in the bent-core banana-shaped molecules often give rise to net dipole moment along the arrow axis. The bent shape of the bent-core molecules hinders the free rotation of molecules about their long axes in the layered structure. Therefore, the permanent dipole moment of the molecules in the layer tends to align, resulting in a polarized layer. Bent-core banana-shaped molecules show layer polarization though the constituent molecules are achiral in nature.

The bent-core molecules grab the attention due to the polarity and chirality of their tilted smectic phases. The chirality of these B-phases occurs as a result of spontaneous symmetry breaking due to the close packing of the molecule in the layered structure. The strongly anisotropic shape of the molecules hinders the free rotation about their long axes [22]. Therefore, the orientation of a fixed banana-shaped molecule can be specified using three vectors (see Figure 1.21): long molecular axis defined as the line joining from one end to another end and defined as $\hat{a}$, bow direction $\hat{b}$, and vector $\hat{m}$, which is perpendicular to the molecular plane. The banana-shaped molecules have C_{2V} point symmetry and invariance of the director $\hat{n}$ *i.e.*, $\hat{n}$ to -$\hat{n}$ is still valid for this system.

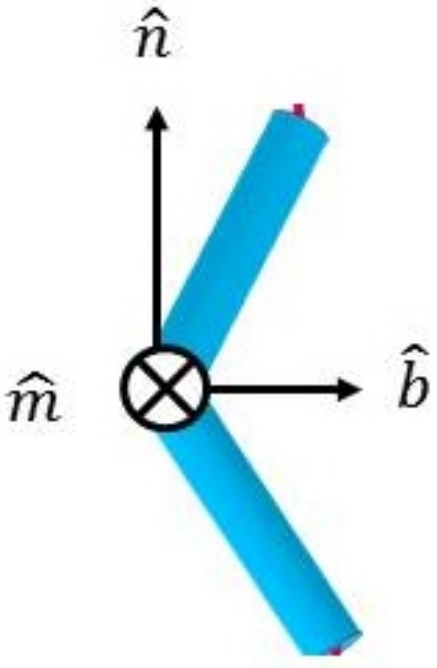

Figure 1.21: A Schematic representation of a bent-core banana-shaped molecules.

The investigation of the properties of variety of liquid crystal phases exhibited by bent-core banana-shaped molecules is an active field of research [23].

The bent-core molecules can be classified into three categories as shown in Figure 1.22:

1. bent-core banana-shaped molecules
2. bent-core dimers
3. hockey-stick shaped molecules

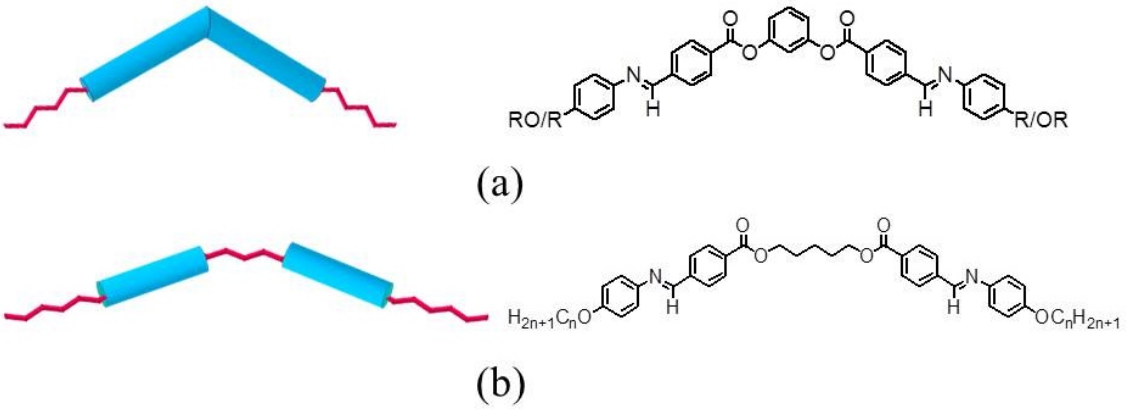

Figure 1.22: The pictorial representation of bent-core liquid crystals and the molecular structure of the representative compounds.

1.5.1 bent-core banana-shaped molecules

As discussed above, in a BC banana-shaped molecule, both the rigid-arms of the molecule are of similar length and the angle between them is about 120 (see Figure 1.22a). The BC banana-shaped molecule can be symmetric or asymmetric depending on the two arms of the molecule being the same or different but with similar length. The asymmetry can be introduced by using different chain lengths or different linkage groups in the two arms of the BC molecule, with the length of the arms being comparable.

1.5.2 bent-core dimers

In a bent-core dimer, two rigid arms are connected to each other with an odd-numbered non-cyclic spacer unit, which provides the flexibe angle between them. Figure 1.22b shows the schematic representation of the bent-core dimer molecule [24, 25, 26, 27, 28, 29]. The phase behavior of these type of molecules are not studied here and will not be discussed in this thesis.

1.5.3 hockey-sticks haped molecules

In a hockey-stick shaped molecule, the length of two arms of the molecule is different. These asymmetric molecules can further be divided into two categories:

1. meta chain hockey-stick shaped (MCHS) molecules
2. bent-core hockey-stick shaped (BCHS) molecules.

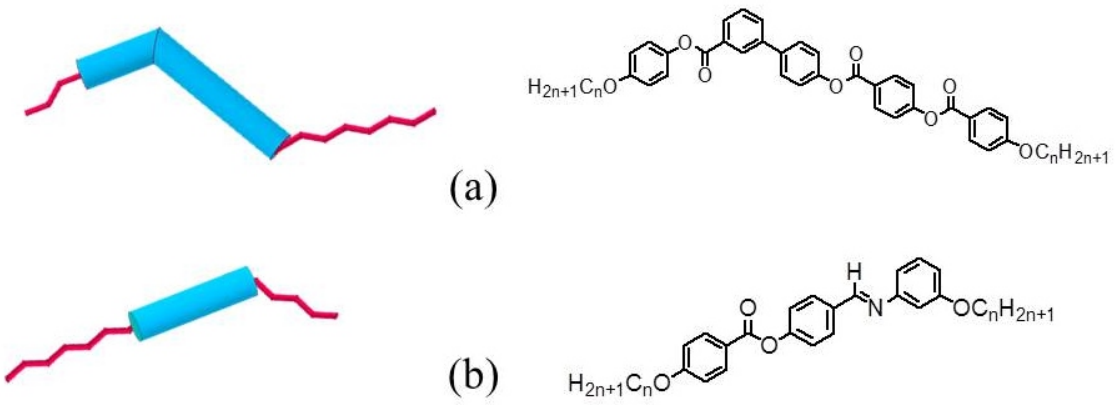

Figure 1.23: The pictorial representation of hockey-stick shaped molecules and the molecular structure.

A meta chain hockey-stick (MCHS) shaped molecule is consists of a rigid core and one of the terminal chains is attached at an angle to the long axis of the rigid core. This can be accomplished by attaching the terminal chain at the meta position of the corresponding benzene ring of the rigid core. The meta position of the terminal chains introduces the bent structure in the molecule [30, 31, 32, 33] as shown in Figure. 1.23b.

In the other category of asymmetric bent-core molecules, one rigid arm of BC molecule is relatively shorter than the other arm of the molecules as shown in Figure 1.23a. We denoted these kind of BC molecules as bent-core hockey-stick shaped (BCHS) molecules. There are only a few reports on phase behavior of BCHS molecules including syntheses of these kinds of molecules [34, 35, 36, 37, 38, 39, 40, 41, 42]. In this thesis, we will describe our experimental and theoretical studies on the phases exhibited by BCHS molecules. For the first time, we report two new type of tilted smectic phases. We also developed a theoretical model to explain the molecular organization of BCHS molecules in their smectic phases in chapter 3. The smectic phases exhibits by BCHS molecules show some interesting electro-optic effects under the application of an electric field, which is described in chapter 4. The homologue with shorter chain length shows different kinds of phase behavior than the higher homologue, which is described in chapter 5 in detail. We also studied the phase diagram of the binary mixture of BCHS and rod-like molecules in chapter 6.

We now briefly describe the different phases exhibited by bent-core banana-shaped molecules. Initially, seven mesophases exhibited by BC banana-shaped molecules were identified. These mesophases were designated as Bi, where i ranges from 1-7 and B stand for the banana, bent, bow, or boomerang [43]. Later on, another phase, $B8$ was observed. We briefly describe the molecular organization in different Bi mesophases exhibited by BC banana-shaped molecules.

1.5.4 $B1$ phase

Sekine et al. observed the $B1$ phase in a compound as shown in Figure 1.24 and designated it as SmA_b phase based on XRD studies [20]. Later on, Watanabe proposed a 2D rectangular columnar structure (see Figure 1.26) for the $B1$ phase [44]. The mosaic textures (see Figure 1.25a) are generally observed in this phase.

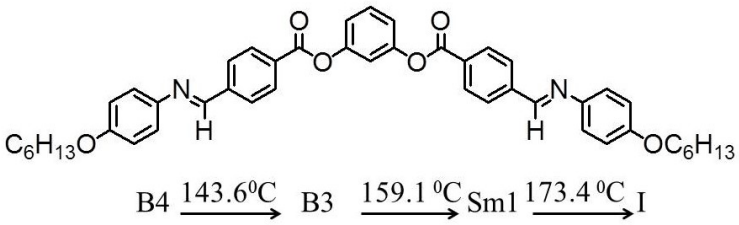

Figure 1.24: Molecular structure of a compound showing $B1$ mesophase [20].

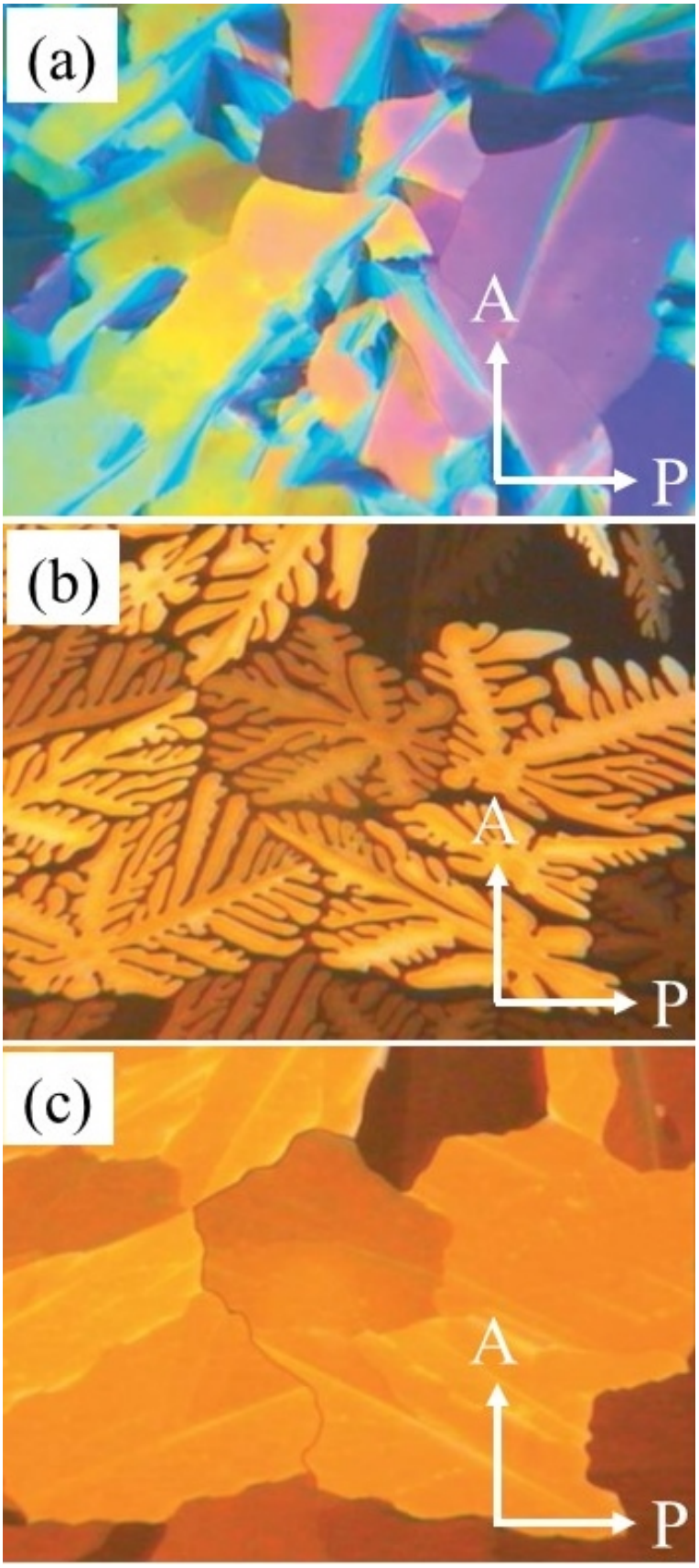

Figure 1.25: (a) Mosaic texture of the banana $B1$ phase (b) Dendritic growth of the banana $B1$ phase separating from the isotropic melt, and (c) On further cooling the dendritic aggregates transform into a mosaic B texture [8].

In the XRD intensity profile, several sharp peaks were observed in the small-angle region in addition to a diffusive broad scattering peak at the wide-angle region. The XRD studies suggest a 2D center rectangular columnar structure in the $B1$ mesophase as shown in Figure 1.26.

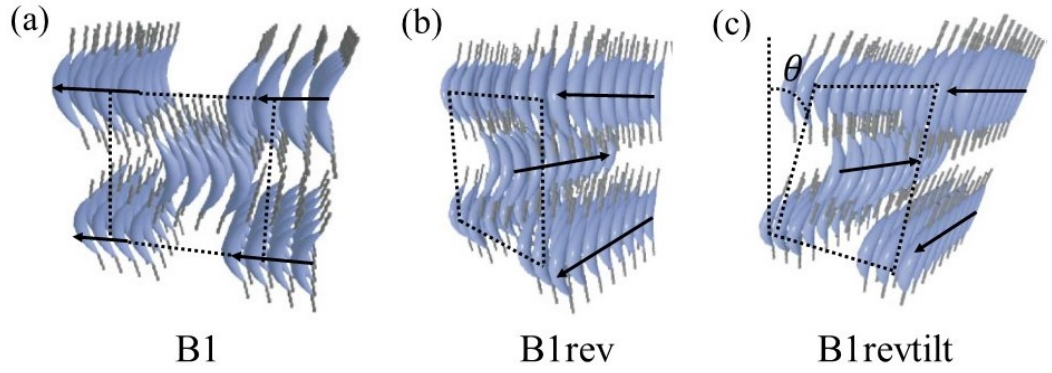

Figure 1.26: The proposed 2D rectangular columnar structure in the $B1$ mesophase.

1.5.5 $B2$ Mesophases

The $B2$ mesophase is the most common mesophase among all the observed banana mesophases. In 1996, Niori et al. first observed $B2$ phase in compound as shown in Figure 1.27a [45].

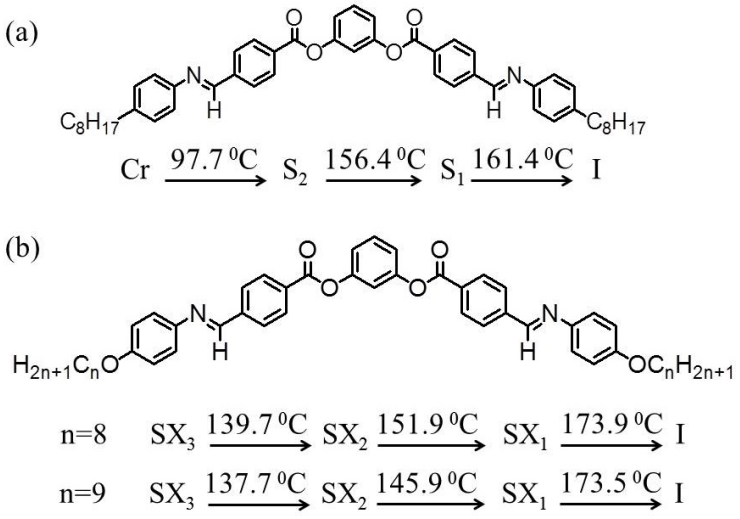

Figure 1.27: Molecular structure of a compound showing $B2$ mesophase.

In general, BC banana shaped molecules with relatively long terminal chains show the $B2$ phase. A variety of POM textures such as fingerprint or finger pattern, focal-conic fan texture, schlieren texture, etc are observed in the $B2$ phase. The chiral domain of opposite handedness were also observed on slow cooling from the isotropic phase. Figure 1.28 shows some examples of POM textures in the $B2$ phase. This mesophase grabs more attention due to the spontaneous breaking of chiral symmetry and the electro-optic response observed in this phase

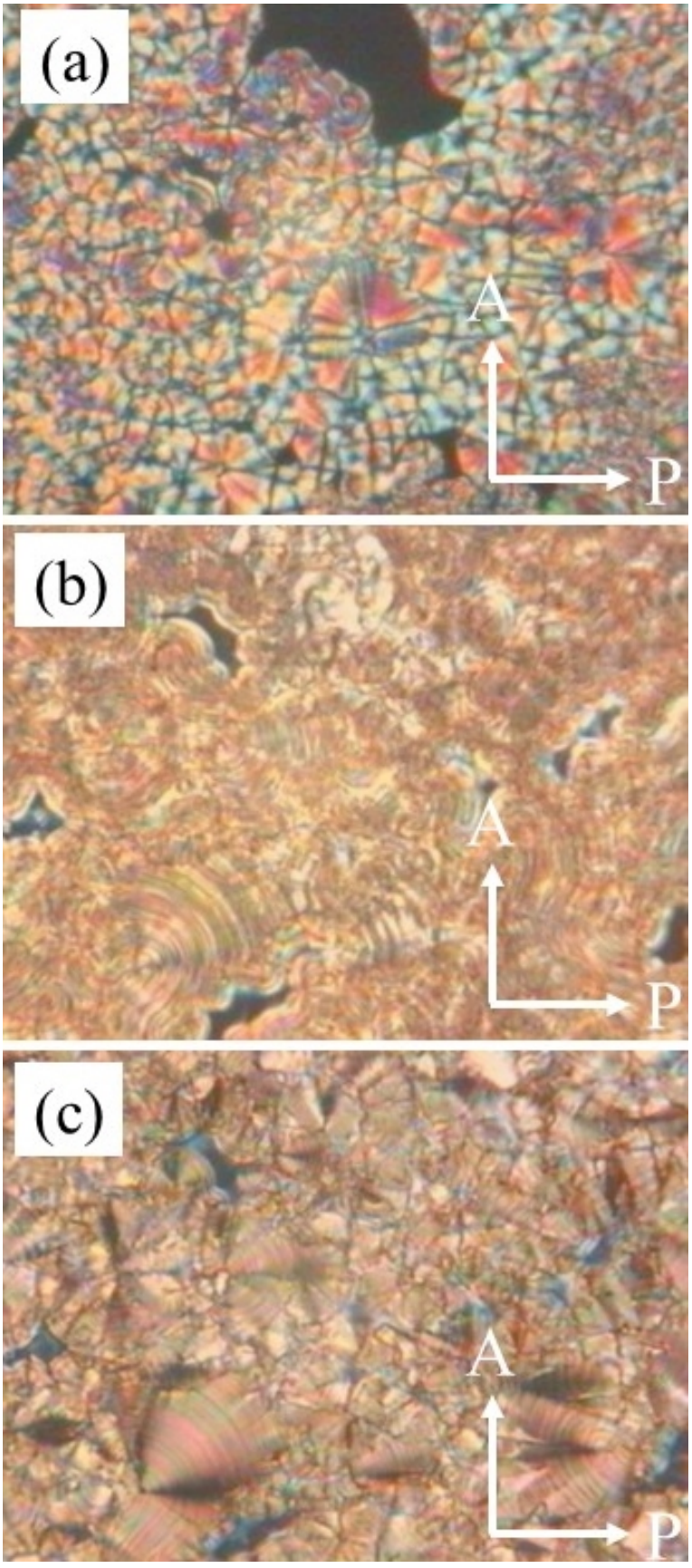

Figure 1.28: (a) A focal-conic fan like texture in the $B2$ phase. (b) Poorly developed fan-like texture of the banana $B2$ phase, with striation across individual fans (see bottom left), and (c) Same sample region after cooling into the $B3$ phase. [8].

By careful electro-optic studies on compounds, shown in Figure 1.27, Link et al. [46] first proposed that the molecules in the $B2$ phase are tilted with respect to the layer normal with an in-plane layer polarization due to the close packing of BC molecules. They also showed that tilt and polarization in the layer also lead to spontaneous breaking of chiral symmetry in this phase. The layers in the B_2 phase become chiral though the constituent molecules are achiral. The handedness of a layer is determined by the relative orientations of the polarization and tilt direction with respect to the layer normal as shown in Fig. 1.29.

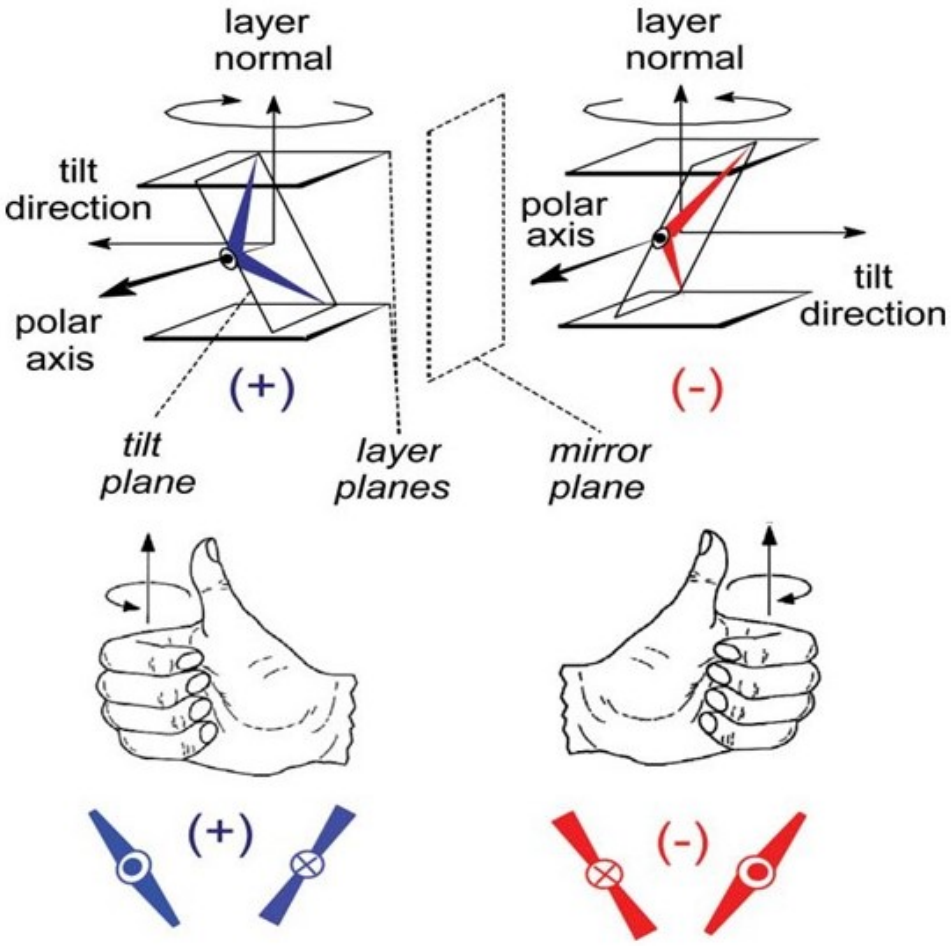

Figure 1.29: Chirality in the symmetric BC banana shped molecules.

Therefore, in these Smectic phases

$$Tilt + polarity = Chirality. \tag{1.2}$$

In modern notation, these polar tilted smectic phases are denoted as SmCP phases, where C and P indicate the tilt and polarization, respectively. These SmCP phases can be homochiral or racimic depending on the sign of the handedness of the adjacent layers in the staking of smectic layers [46, 47]. Based on the relative orientations of the interlayer polarizations and the tilt directions, four possible configurations $\mathrm{SmC}_{S,A}P_{F,A}$ are possible, as shown in Fig. 1.30.

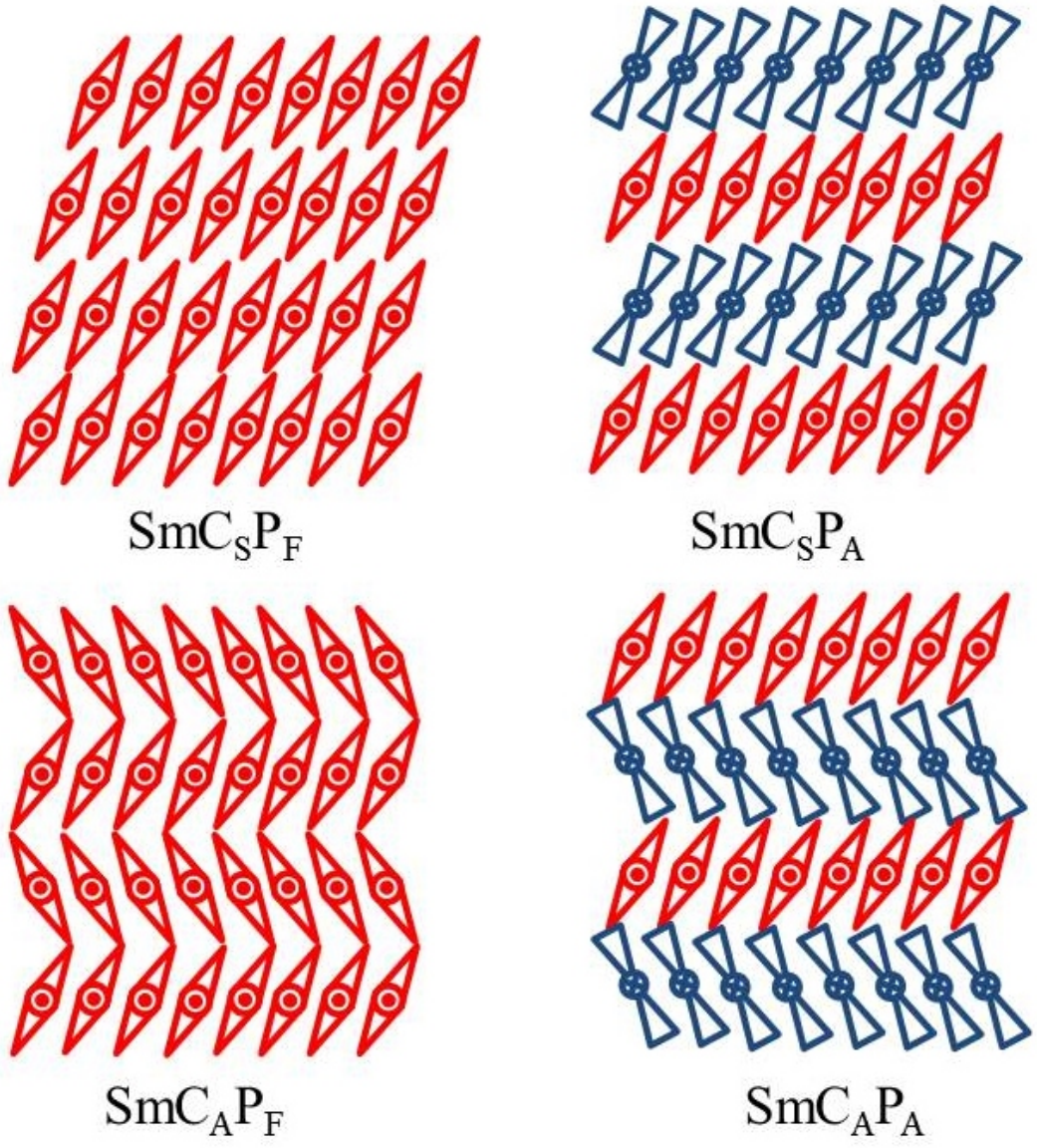

Figure 1.30: Four possible configuration of BC banana shped molecules based on interlayer polarization and the tilt direction of the molecules.

Here, the subscripts S and A stand for the synclinic and anticlinic tilted arrange-

ment of the molecules in the adjacent layers repectively. The subscript F and A denote the ferroelectric and antiferroelectric configuration of polarization in the adjacent layers respectively. A phase is said to be synclinic when the tilt of molecules in successive layers is in the same direction and anticlinic if the tilt in the successive layer is in the opposite direction. A system is said to be homochiral or racemic if the layer chirality remains uniform or alter between the successive layers respectively. Therefore, SmC_SP$_F$ and SmC_AP$_A$ are Homochiral, and SmC_SP$_A$ and SmC_AP$_F$ are racemic. In most of the compounds, the SmC_SP$_A$ (synclinic antiferroelectric) and SmC_AP$_A$ (anticlinic antiferroelectric) are observed as the ground state. Under the application of an applied electric field, the antiferroelectric phase switches to the ferroelectric phase, as shown in Figure 1.31.

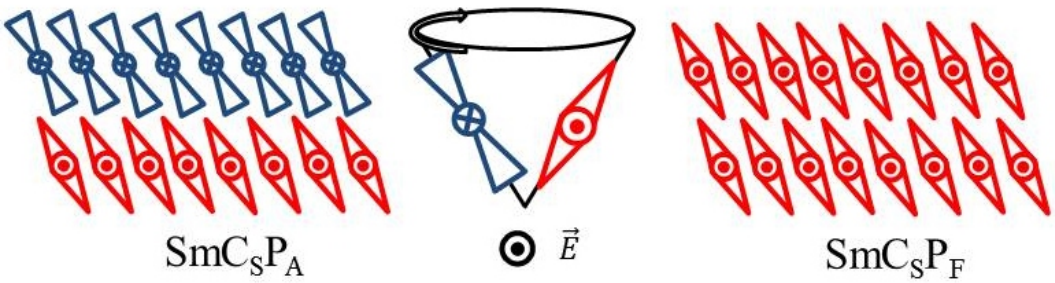

Figure 1.31: Transition from the antiferroelectric phase to ferroelectric phase under the application of an electric field.

The switching process from the antiferroelectric to ferroelectric state results from the collective rotation of the molecules around the cone as shown in Figure 1.31 [21, 48, 49]. The X-ray diffraction patterns of the $B2$ phase are similar to that of smectic phases, *i.e.*, small-angle sharp peak in addition to a the wide-angle diffusive peak [20].

1.5.6 $B3$ Phase

Very less information is known about the structures and properties of this phase compared to the other Bi phases. This phase frequently appears between $B2$ and $B4$ phases [50]. Figure 1.32 shows the POM texture of the $B3$ phase on rapid cooling from the $B2$ phase.

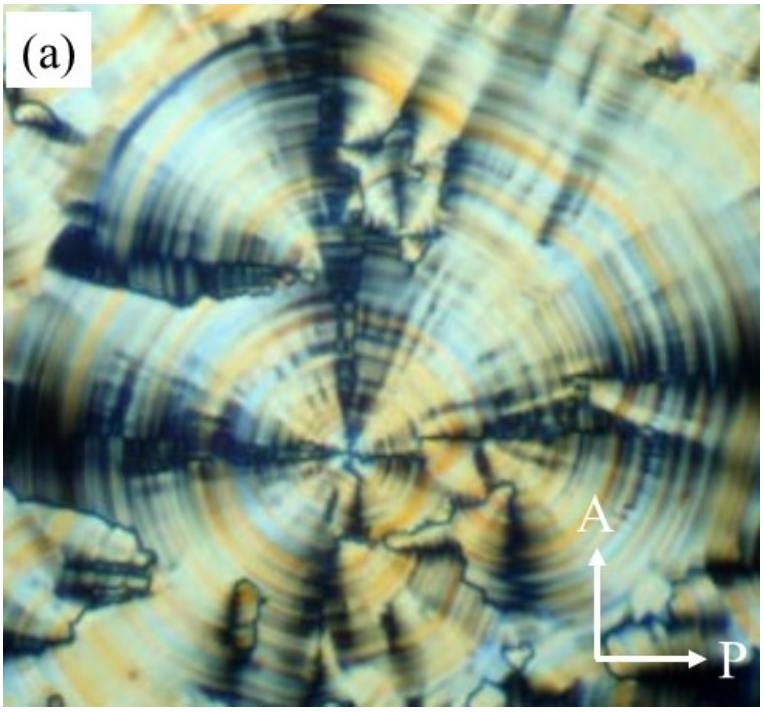

Figure 1.32: POM texture in $B3$ phases between crossed polarizers.

But the slow cooling from the higher phase gives rise to a broken domain texture in the B3 phase. Therefore, the formation of textures depends on the cooling rate as well. For the $B3$ phase, the XRD studies show several sharp peaks in the small-angle region in addition to multiple sharp peaks in the wide-angle region, indicating to have crystal structure rather than high order smectic phase [20, 44, 46, 51]. However, the dielectric [52] and terahertz spectroscopics [53] studies suggested that the $B3$ phase is a higher-order smectic phase rather than the crystal phase. In this thesis, we will only deal with the fluid lamellar smectic phases. The detail structure and properties of $B3$ phase will not be relevant to the discussions of this thesis.

1.5.7 $B4$ Phase

The $B4$ mesophase appears in the lowest temperature, *i.e.*, below a $B2$ or $B3$ phase in the bent-core molecular system [54, 55]. POM texture between the crossed polarizers in $B4$ phase appears as transparent dark-blue as shown in Figure 1.33.

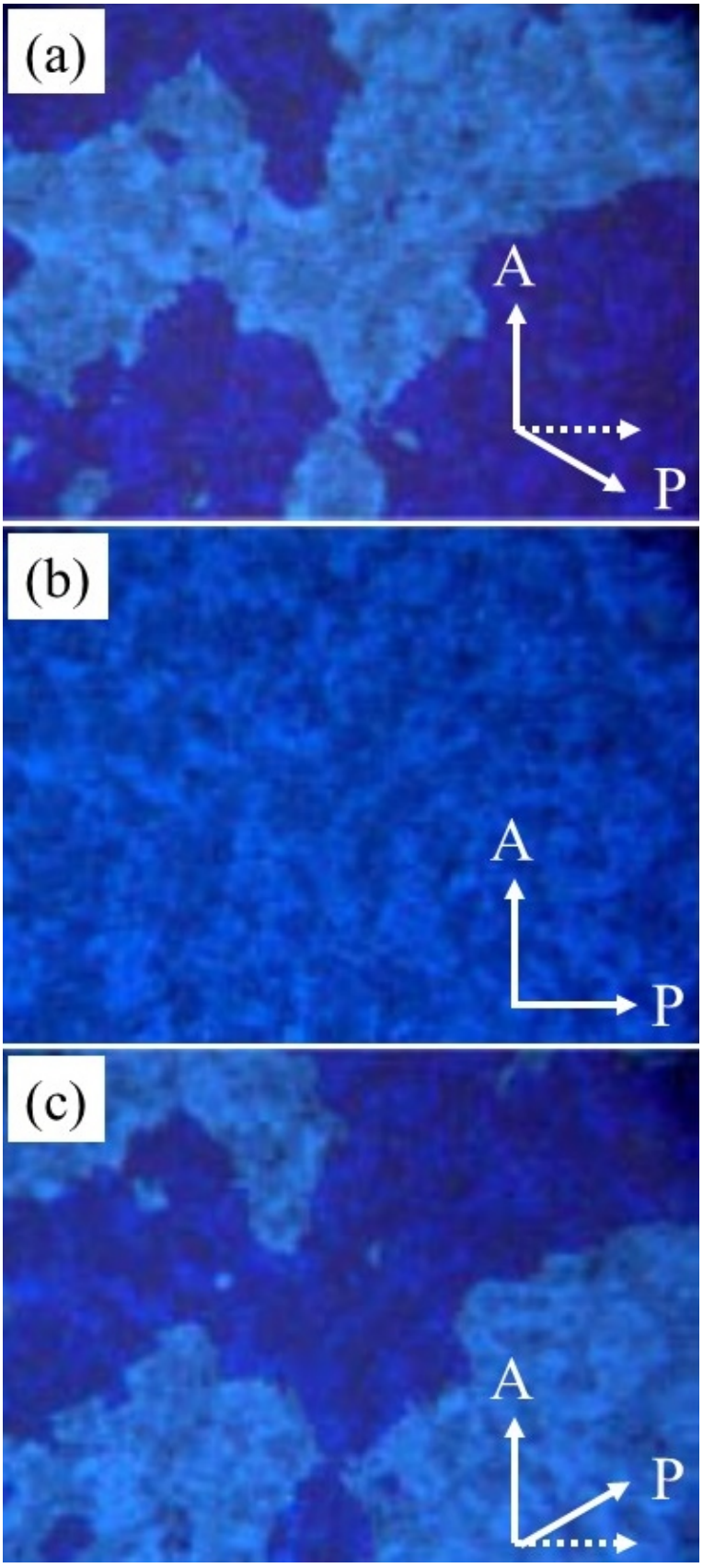

Figure 1.33: POM texture of compound P-8-OPIMB in the $B4$ phase (b) between the crossed polarizers, by rotating one of the polarizers (a) clockwise and, (c) anticlockwise [8].

Two different domains with different brightness are observed between slightly uncrossed polarizers [56]. The brightness of each domain interchanged by rotating the polarizer clockwise or anticlockwise as shown in Figure 1.33. The circular dichroism (CD) spectrum also clearly shows the presence of different domains with opposite handedness, and this indicates that the observed domains are chiral [57].

In the XRD intensity pattern of the $B4$ mesophase, higher-order reflections of up to third-order were observed in the small-angle regions. The presence of several peaks in the small-angle region indicates the crystalline order in the $B4$ mesophase. However, the dielectric studies for a low-frequency relaxation also suggest that the $B4$ phase has a lamellar structure rather than a crystalline phase [52, 55]. This mesophase exhibits a second harmonic generation (SHG) even in the absence of an electric field indicating the presence of spontaneous non-centrosymmetric order in the system. The $B4$ mesophase does not switch with an applied field and usually possess a low value of dielectric constant. A TGB-like structure is observed in this phase which is consistent with X-ray micro-beam experiments [20].

1.5.8 $B5$ Phase

This mesophase was first observed in 1998 in a derivative of 2-methylresorcinol as shown in Figure 1.34 [58, 59]. Later, this phase was also observed in the derivatives of 2-methyl- [60] and of 5-fluororesorcinol (see Figure 1.35) [61]. In general, the $B5$ mesophase appears below B2 phase, and the transition from the $B2$ to $B5$ phase is first-order with small enthalpy change across the transition [50, 61, 62, 63]. The POM texture and the electro-optical effects observed in the $B5$ phase are similar to those in the $B2$ phase.

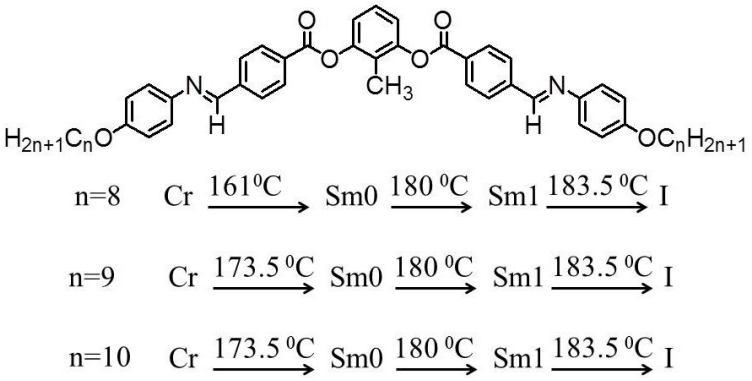

Figure 1.34: Molecular structure of a compound with different chain lengths showing $B5$ mesophase [60].

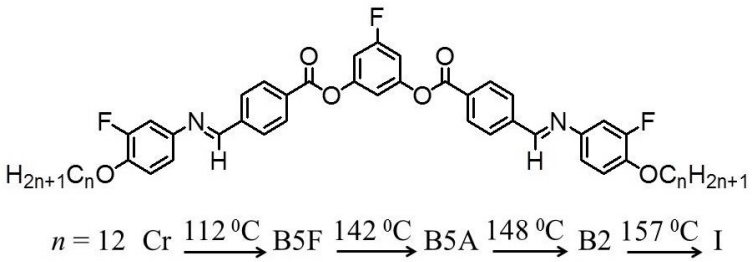

Figure 1.35: Molecular structure of a compound showing $B5$ mesophase [61].

Though, the XRD profiles in this phase are distinguishable from the $B2$ phase. The XRD intensity pattern in this phase shows higher-order reflections of up to sixth order in the small-angle region indicating a periodic lamellar structure. However, inconsistency is there about the tilted and non-tilted nature of the molecules in the lamellar structure [61, 62]. In the 2D XRD pattern of the surface orientated sample, the scattering in the wide-angle appears perpendicular to the small-angle layer reflections, suggesting a 2D rectangular cell in a layer. The proposed structure in the $B5$ phase for in-plane molecular packing [50, 62] is shown in Figure 1.36.

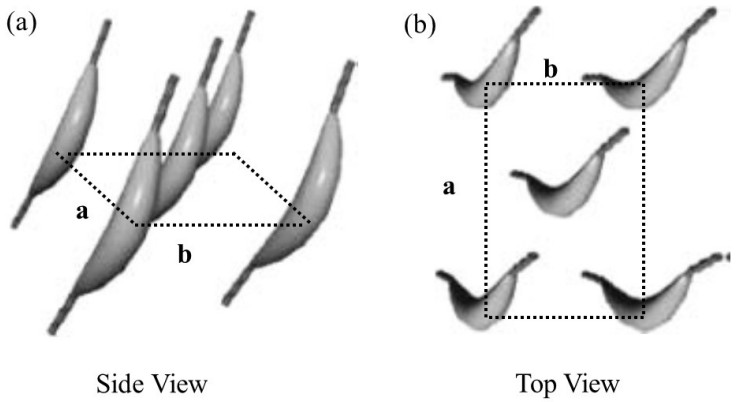

Figure 1.36: Molecular representation in $B5$ mesophase.

1.5.9 $B6$ Phase

The $B6$ mesophase was first observed in the compound shown in Figure 1.37 [64].

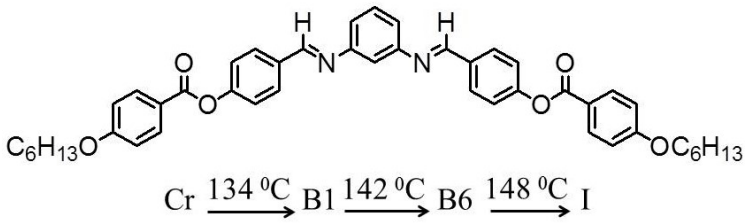

Figure 1.37: Molecular structure of a compound showing $B6$ mesophase [64].

The BC banana-shaped molecules with relatively shorter terminal chains exhibit this phase. Upon cooling the sample from the isotropic phase, a long fan-shaped texture was observed similar to the SmA phase exhibited by rod-like molecules as shown in Figure 1.38 [65].

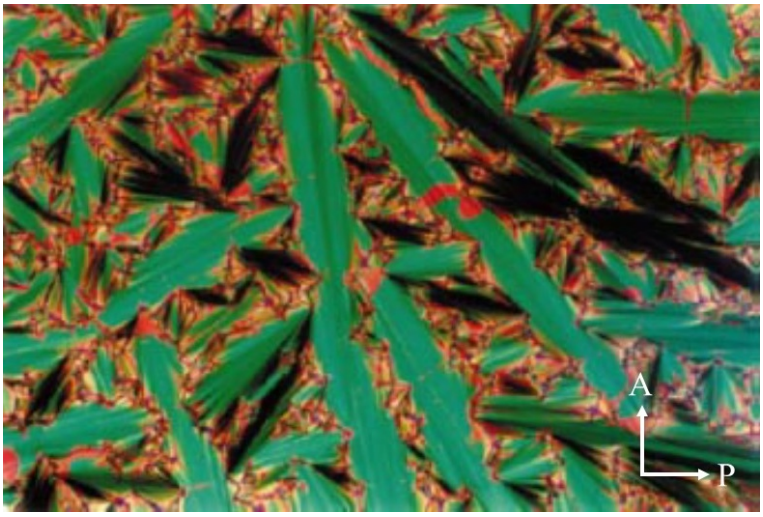

Figure 1.38: POM texture in the $B6$ mesophase on cooling from the isotropic phase [70].

The homeotropic-alignment of the sample could not be achieved in this phase. Some compounds show the B6 to B1 to $B2$ phase sequence on increasing the terminal chain length of the molecules [50, 66, 67, 69].

The XRD studies for an orientated sample show higher-oreder reflections in the small-angle region in addition to the diffusive wide-angle reflection. The observed layer spacing in this mesophase is equal to half of the molecular length [50, 66], indicating the intercalated structure as shown in Figure 1.39.

Figure 1.39: Molecular organization in the $B6$ mesophase.

In addition, the molecules are tilted with respect to the layer normal and the observed tilt angle is of the order of about 10-30 degrees [50, 67]. The phase transition from $B6$ to $B1$ and $B1$ to $B2$ can occur on increasing the terminal chain length of the homologues [66, 67, 69, 70]. Though, the phase sequence $B1$ to $B2$ for a compound is rarely found [58, 67, 71]. This change was explained based on a frustrated packing model of the molecules [68, 67, 69].

1.5.10 $B7$ Phase

The $B7$ phase was first observed [50] in a compound derived from 2-nitroresorcinol. Figure 1.40 show the example of compounds showing the $B7$ phase.

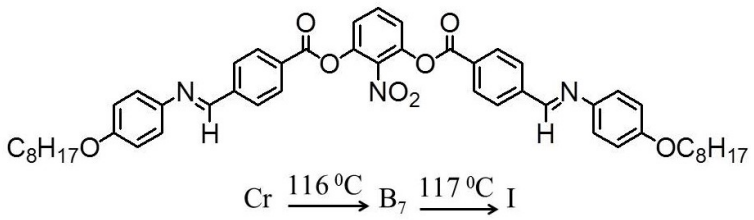

Figure 1.40: Molecular structure of compound showing $B7$ mesophase [50].

The $B7$ phase grabs considerable attention due to its characteristic textures as shown in Figure 1.41 [50, 72, 73, 74, 75, 76, 77]. The spiral filament is a typical texture observed in the $B7$ phase. Jakli et al. reported that the left-handed and right-handed spiral exists with equal probability. The spiral texture consists of smectic filaments that form single, double, or triple coils [77]. The $B7$ phase also shows the chiral micromosaic domains with different optical rotation as observed in the $B2$ phase. The different types of textures, for example, circular domains with equidistant concentric rings, myelinic-like, checker-board-like, and banana-leaf-like textures, accordion-like domains have been observed in this phase [77].

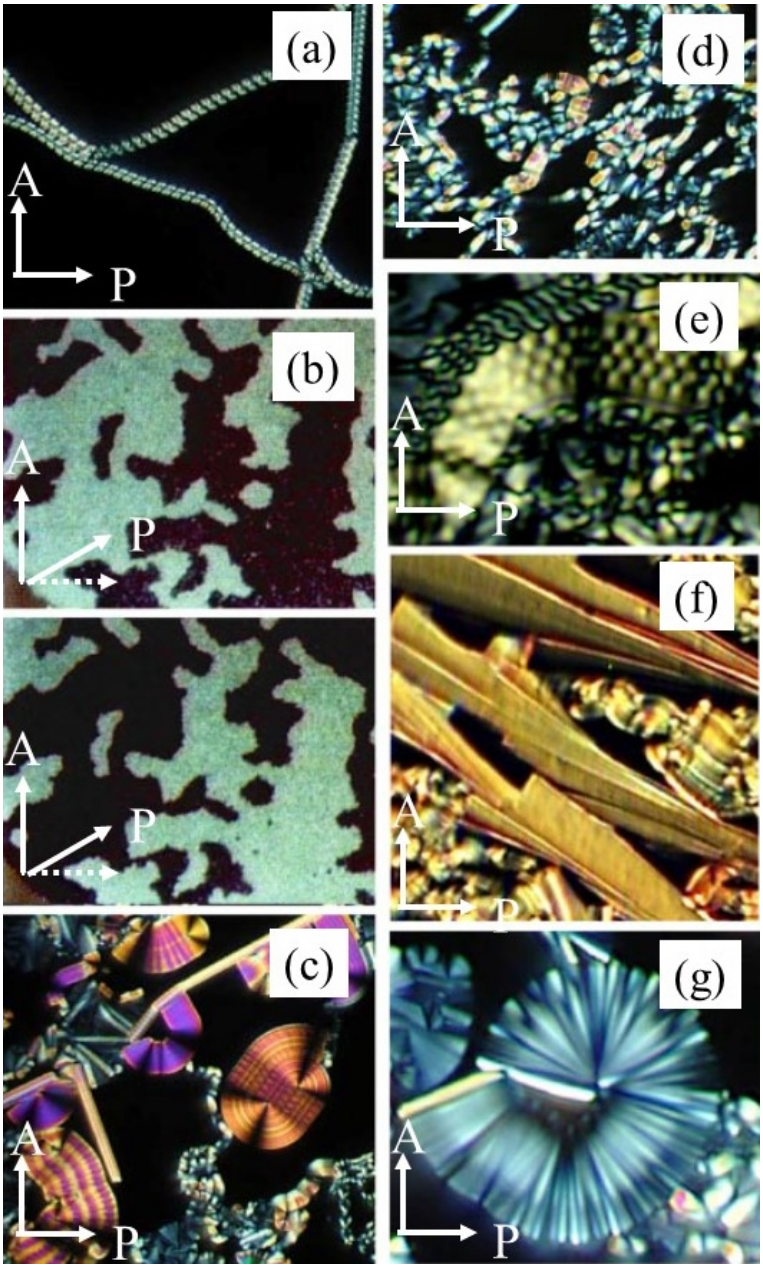

Figure 1.41: Different POM textures observed in the $B7$ mesophase [54].

The XRD studies in the $B7$ mesophases indicate the presence of the several peaks in the small-angle region in addition to the diffusive peak in the wide-angle region [50, 75, 78, 79]. Coleman et al. suggested a 2D modulated layer structures in this phase based on high-resolution synchrotron XRD results [79] for a compound PBCOB (see Figure 1.42). The modulated observed structure in this phase is different than that in the $B1$ mesophase.

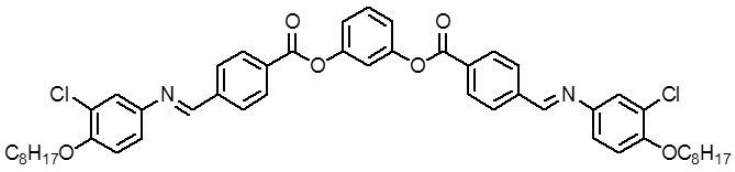

Figure 1.42: POM texture for the $B7$ mesophase [50].

A ferroelectric-like polarization switching was observed under the application of an electric field in the $B7$ mesophase just below the transition temperature from the isotropic phase. The switching behavior changes to tri-stable switching on decreasing the temperature. Fluorine-containing compound also shows similar ferroelectric bi-stable switching [72, 80]. Two kinds of surface stabilized molecular orientational states, low and high birefringence, are observed in these compounds in the absence of an applied electric field. These two different states are explained by the differences in the orientation of the molecular bending plane which depends on the layer tilt [81, 82].

1.5.11 $B8$ Phase

In 2001, Bedel et al. reported some compounds 21_n [83] consisting of symmetric BC molecules with decyl chains exhibiting a $B8$ mesophase as shown in Figure 1.43. However, the homologue of this compound with shorter terminal chains does not show this phase. Figure 1.44 shows POM texture in the $B8$ phase between the crossed polarizers.

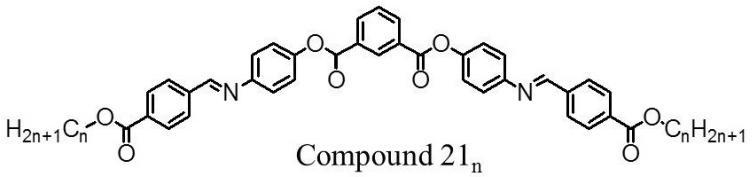

Compound 21_n

n=7 Cr $\xrightarrow{183.9\,^0C}$ Sm0 $\xrightarrow{190.6\,^0C}$ I

n=8 Cr $\xrightarrow{178.6\,^0C}$ Sm0 $\xrightarrow{187.8\,^0C}$ I

n=9 Cr $\xrightarrow{174\,^0C}$ Sm0 $\xrightarrow{184\,^0C}$ I

n=10 Cr $\xrightarrow{173.5\,^0C}$ Sm0 $\xrightarrow{180\,^0C}$ Sm1 $\xrightarrow{183.5\,^0C}$ I

Figure 1.43: Molecular structure of compound with differnet chain length showing $B8$ mesophase [83].

In this phase, a spiral domain growth is observed upon gradual cooling from the isotropic phase as shown in Figure 1.44a. A fan-shaped texture (Figure 1.44b.) was observed on further cooling, where the extinction brushes are parallel to the layer normal. This phase shows antiferroelectric type switching under the application of an electric field. For a homologue n=10, the XRD studies for an oriented sample in the lower temperature range in the $B8$ mesophase designated as Sm0, show sharp diffraction peaks and its higher-order as observed in the $B2$ mesophase. This phase is a tilted smectic phase with a tilt angle about 25 degrees. On the other hand, an additional sharp peak was observed in the small-angle region in the higher temperature range of the B8 phase designated as Sm1. The layer spacing corresponding to this additional peak suggests the bilayer structure in this phase. Later, these phases Sm0 and Sm1 were identified as SmC_SP$_A$ and SmC_SG$_2$P$_A$, respectively [84]. Where SmCP denotes the polar tilted smectic phases, the subscript S indicates the synclinic arrangement of the molecules in the layers, and A denotes the antiferroelectric behavior. The subscript G and 2 denote the general and bilayer structure in the latter.

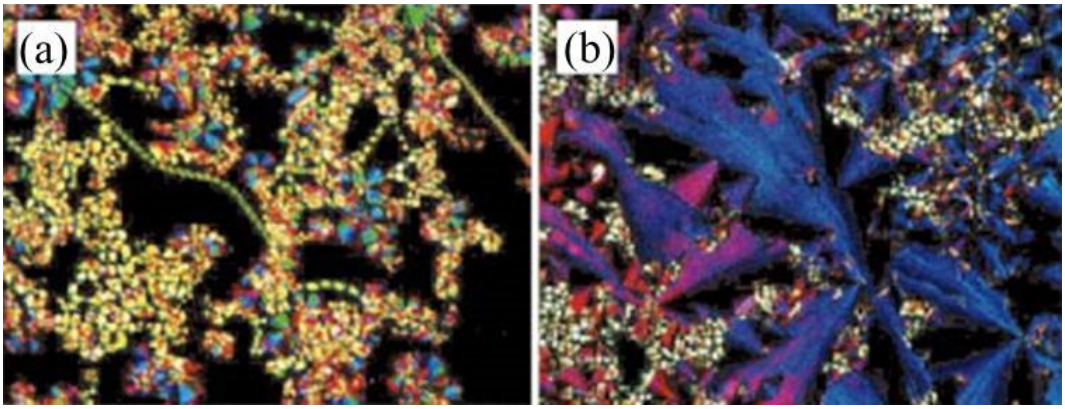

Figure 1.44: POM texture for $B8$ mesophase on cooling from the isotropic phase [83].

1.5.12 Orthogonal smectic phases exhibited by bent-core molecules

In the orthogonal smectic phases, The BC molecules are not tilted with respect to the layer normal but the layers are transversely polarized. Depending on the stacking of these polarized layers, two possible configurations denoted as SmAP_F and SmAP_A are

shown in Figure 1.45.

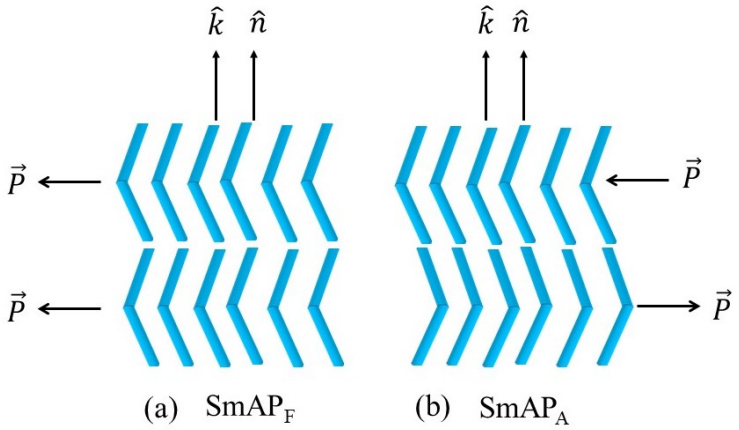

Figure 1.45: Two possible configurations in orthogonal smectic phase.

Here, SmA and P indicate the orthogonal smectic phase and the polarization in the layers, respectively. The Subscripts A and F indicate the ferroelectric and antiferroelectric arrangement of polarization direction in successive layers.

Figure 1.46 shows the typical POM textures of homeotropically and planar aligned samples in the SmAP_A.

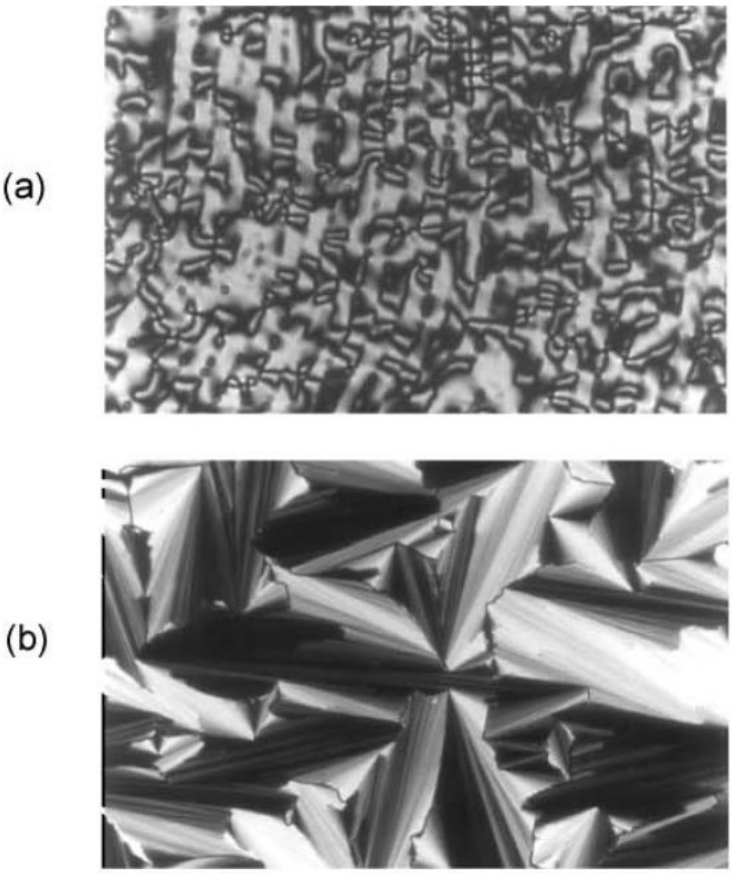

Figure 1.46: POM texture in the SmAP_F phase for (a) homeotropically and (b) planar-aligned sample [85].

The SmAP_A phase is observed as a stable ground state in most of the orthogonal smectic phases exhibited by bent-core molecules [86]. The ferroelectric state can be induced from the antiferroelectric state with an applied electric field. The SmAP_F phase relaxes back to the SmAP_A phase upon removing the applied field. Figure 1.47 shows the field-induced transition from the SmAP_A phase to the SmAP_F phase under the application of an AC electric field.

Figure 1.48 shows the typical current response for an antiferroelectric phase of BCLCs under the application of a triangular wave voltage.

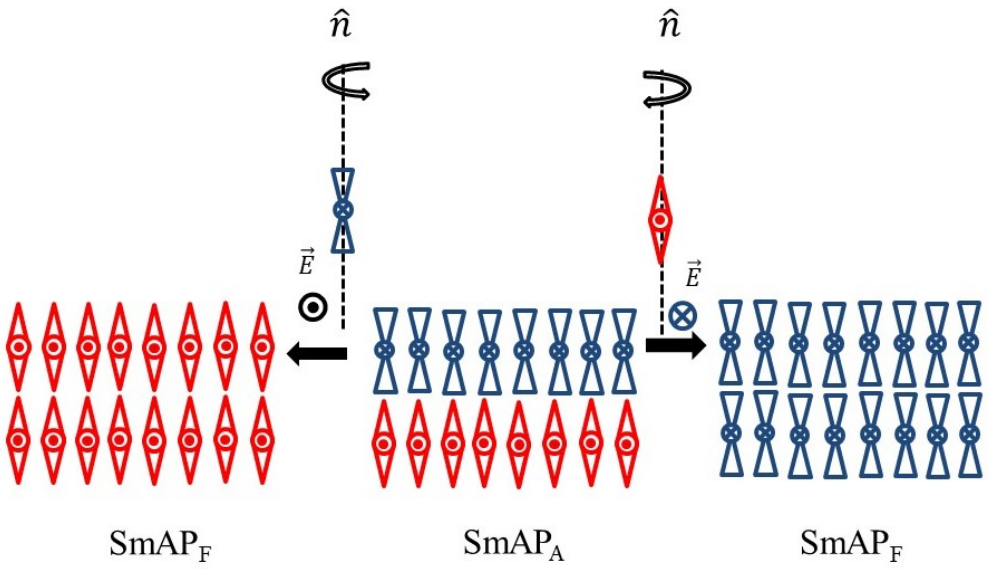

Figure 1.47: Schematic representation of the field-induced transition from the SmAP_A phase to the SmAP_F phase with an AC electric field.

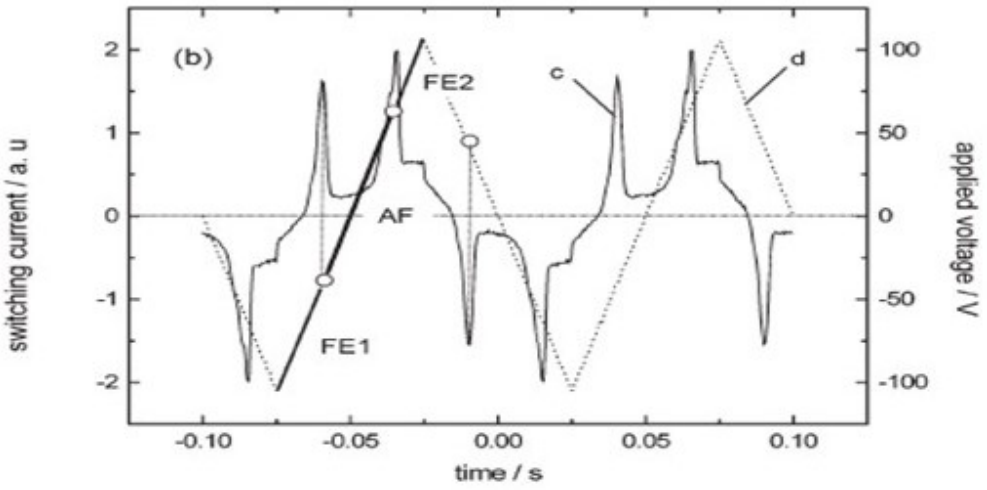

Figure 1.48: Current response of the antiferroelectric phase of BC molecules.

The presence of two polarization reversal current peaks in each half cycle of an applied voltage is the characteristic of the antiferroelectric phase. The observed values of the spontaneous polarization (P_s) are typically in the range between 500–800 nC cm^{-2}. The value of P_s is significantly larger than those of ferroelectric and antiferroelectric smectic phases exhibited by chiral rod-like molecules (P_s 5–200 nC cm^{-2}).

Bibliography

[1] R. Friedrich, Contributions to the Knowledge of Cholesterol, *Liq. Cryst.*, **5**, (1989).

[2] R. Friedrich, Beiträge Zur Kenntniss Des Cholesterins, Monatshefte für Chemie, **9**, 421-441 (1888).

[3] O. Lehmann, On Flowing Crystals, Zeitschrift für Physikalische Chemie, **4**, 462 (1889).

[4] D. Vörlander, Kristallinisch-Flüssige Substanzen, (1908).

[5] W. H. de Jeu, Physical Properties of liquid crystal Materials, Gordon and Breach, Science Publishers Ltd., (1980).

[6] S. Chandrasekhar, Liquid Crystals, Cambridge University Press, Cambridge, (1992).

[7] D. Chandler, Interfaces and the Driving Force of Hydrophobic Assembly, *Nature*, **437**, 640-647 (2005).

[8] I. Dierking, *Textures of Liquid Crystals.*, WILEY-VCH Verlag GmbH and Co. KGaA, Weinheim Ltd. (2003).

[9] H. Keller, B. Scheurle, R. Hatz, and W. Bartsch, *Angew. Chem.,* **82**, 984 (1970).

[10] G. W. Gray, *J. Phys. Colloque*, **36**, C1-337 (1975).

[11] W. H. de Jeu and W. A. P.Classen, *J. Chem. Phys.*, **67**, 3705 (1977).

[12] J. Doucet, A. M. Levelut, and M. Lambert, *Phys. Rev. Lett.*, **32**, 301 (1974).

[13] D. Dolphin, Z. Muljiani, J. Cheng, and R. B. Meyer, *J. Chem. Phys.*, **58**, 413 (1973).

[14] L. B. Ledder, *J. Chem. Phys.*, **55**, 2649 (1971).

[15] S. Chandrasekhar, B. K. Sadashiva, K. A. Suresh, Liquid Crystals of Disc-Like Molecules, *Pramana*, **9**, 471-480 (1977).

[16] D. Vörlander, A. Apel, *Ber. Dtsch. Chem. Ges*, 1101 (1932).

[17] R. B. Meyer, l. Liebert, L. Strzelecki, and P. Keller, *J. Phys. (Paris) Lett.*, **36**, L-69 (1975).

[18] R. H. Tredgold, *Ferroelectrics*, **119**, 119-121 (1990).

[19] Y. Matsunaga, and S. Miyata, *Mol. Cryst. Liq. Cryst.*, **237**, 311-317 (1993).

[20] T. Sekine, T. Niori, M. Sone, J. Watanabe, S. W. Choi, Y. Takanishi, and H. Takezoe, *Jpn. J. Appl. Phys.*, **36**, 6455 (1997).

[21] R. A. Reddy, and C. Tschierske, *J. Mater. Chem.*, **16**, 907-961 (2006).

[22] F. Kentischer, R. MacDonald, P. Warnick, and G. Heppke, *Liq. Cryst.*, **25**, 341-347 (1998).

[23] J. W. Goodby, P. J. Collings, T. Kato, C. Tschierske, H. F. Gleeson, and P. Raynes, Handook of Liquid Crystals, ed., Willey, VCH, Germany, 2nd edn, vol. 4, pp. 603–767 (2014).

[24] Y. Takanishi, T. Izumi, J. Watanabe, K. Ishikawa, H. Takezoe, and A. Iida, *J. Mater. Chem.*, **9**, 2771 (1999).

[25] J. P. F. Lagerwall, F. Giesselmann, M. D. Wand, and D. M. Walba, *Chem. Mater.*, **16**, 3606 (2004).

[26] V. Prasad, D. S. S. Rao, and S. K. Prasad, *Liq. Cryst.*, **27**, 585 (2000).

[27] C. V. Yelamaggad, S. A. Nagamani, U. S. Hiremath, D. S. S. Rao, and S. K. Prasad, *Liq. Cryst.*, **29**, 1401 (2002).

[28] W. Weissflog, C. Lischka, S. Diele, I. Wirth, and G. Pelzl, *Liq. Cryst.*, **27**, 43 (2000).

[29] K. Pelz, W. Weissflog, U. Baumeister, and S. Diele, *Liq. Cryst.*, **30**, 1151 (2003).

[30] F. C. Yu, and L. J. Yu, *Liq. Cryst.*, **35**, 799-813 (2008).

[31] B. Das, S. Grande, W. Weissog, A. Eremin, M. W. Schroder, G. Pelzl, S. Diele, and H. Kresse, *Liq. Cryst.*, **30**, 529-539 (2003).

[32] A. Chakraborty, M. K. Das, B. Das, U. Baumeister, and W. Weissog, *J. Mater. Chem. C*, **1**, 7418 (2013).

[33] R. Stannarius, J. Li, and W. Weissog, *Phys. Rev. Lett.*, **90**, 025502 (2003).

[34] P. Sathyanarayana, S. Radhika, B. K. Sadashiva, and S. Dhara, *Soft Matter*, **8**, 2322 (2012).

[35] M. Alaasar, *Liq. Cryst.*, **43**, 2208-2243 (2016).

[36] S. Radhika, H. T. Srinivasa, and B. K. Sadashiva, *Liq. Cryst.*, **38**, 785 (2011).

[37] M. Alaasar, S. Poppe, C. Kerzig, C. Klopp, A. Eremin, and C. Tschierske, *J. Mater. Chem.*, **5**, 8454-8468 (2017).

[38] D. D. Sarkar, R. Deb, N. Chakraborty, and V.S. R. Nandiraju, *Liq. Cryst.*, **39**, 1003-1010 (2012).

[39] E. R. Cioanca, E. L. Epure, I. C., G. Lisa, D. Wilson, N. Hurduc, and D. Scutaru, *Mol. Cryst. Liq. Cryst.*, **537**, 51-63 (2011).

[40] D. Malkar, B.K. Sadashiva, and A. Roy, *Soft Matter*, **12**, 4960 (2016).

[41] M. Monika, Veena Prasad, and N.G. Nagaveni, *Liq. Cryst.*, **42**, 1490-1505 (2015).

[42] D. Malkar, M. Monika, Veena Prasad, and A. Roy, *Phys. Rev. E*, **101**, 012701 (2020).

[43] H. Takezoe and Y. Takanishi, *Jpn. J. Appl. Phys.*, **45**, 2A, 597–625 (2006).

[44] J. Watanabe, T. Niori, T. Sekine, and H. Takezoe, *Jpn. J. Appl. Phys.*, **37**, L139-L142 (1998).

[45] T. Niori, T. Sekine, J. Watanabe, T. Furukawa, and H. Takezoe, *J. Mater. Chem.*, **6**, 1231 (1996).

[46] D. R. Link, G. Natale, R. Shao, J. E. Maclennan, N. A. Clark, E. Korblova, and D. M. Walba, *Science*, **278**, 1924-1927 (1997).

[47] J. Xu, Selinger et.al., *J. Chem. phy.*, **115**, 4333 (2001).

[48] C. Keith, R. A. Reddy, U. Baumeister, and C. Tschierske, *J. Am. Chem. Soc.*, **126**, 14312-14313 (2004).

[49] M. W. Schröder, S. Diele, G. Pelzl, and W. Weissflog, *Chem. Phys. Chem*, **5**, 99-103 (2004).

[50] G. Pelzl, S. Diele, and W. Weissflog, *Adv. Mater.*, **11**, 707-724 (1999).

[51] H. Chan, and I. Dierking, *Phys. Rev. E*, **70**, 021703 (2004).

[52] J. Saletnikova, H. Schmalfuss, H. Nadasi, W. Weissflog, and H. Kresse, *Liq. Cryst.*, **27**, 1663-1667 (2000).

[53] Y. Takanishi, K. Ishikawa, J. Watanabe, H. Takezoe, M. Yamashita, and K. Kawase, *Phys. Rev. E*, **71**, 061701 (2005).

[54] G. Heppke, D. Kruerke, C. Lohning, D. Lotzsch, S. Rauch, and N. K. Sharma, Frieburger Arbeitstagung Flussige Kristalle, Freiburg, Germany, P 70 (1997).

[55] H. Nadasi, Ch. Lischka, W. Weissflog, I. Wirth, S. Diele, G. Pelzl, and H. Kresse, *Mol. Cryst. Liq. Cryst.*, **399**, 69-84 (2003).

[56] P. Collings et al., Abtr. Workshop on Banana-Shaped Liquid Crystals: Chirality by Achiral Molecules, p. 15, Berlin, Germany (1997).

[57] J. Thisayukta, Y. Nakayama, S. Kawauchi, H. Takezoe, and J.Watanabe, *J. Am. Chem. Soc.*, **122**, 7441-7448 (2000).

[58] G. Dantlgraber, D. Shen, S. Diele, and C. Tschierske, *C. Chem. Mater.*, **14**, 1149-1158 (2002).

[59] Y. Takanishi, H. Takezoe, J. Watanabe, Y. Takahashi, and A. Iida, *J. Mater. Chem.*, **16**, 816-818 (2006).

[60] A. Eremin, I. Wirth, S. Diele, G. Pelzl, H. Schmalfuss, H. Kresse, H. Nadasi, K.F. Csorba, E.G. Baitz, and W. Weissflog, *Liq. Cryst.,* **29**, 775-782 (2002).

[61] H. Nadasi, W. Weissflog, A. Eremin, G. Pelzl, S. Diele, B. Das, and S. Grande, *J. Mater. Chem.*, **12**, 1316-1324 (2002).

[62] S. Diele, S. Grande, H. Kruth, C. Lischka, G. Pelzl, W. Weissflog, and I. Wirth, *Ferroelectrics*, **212**, 169-177 (1998).

[63] J. Svoboda, V. Novotna, V. Kozmik, M. Glogarova, W. Weissflog, S. Diele, and G. Pelzl *J. Mater. Chem.*, **13**, 2104 (2003).

[64] W. Weissflog, C. Lischka, I. Benne, T. Scharf, G. Pelzl, and S. Diele, Kruth, H. Proc. SPIE: Int. Soc. Opt. Eng., **3319**, 14-19 (1998).

[65] R. A. Reddy, V. A. Raghunathan, and B. K. Sadashiva, textitChem. Mater., **17** 274 (2005).

[66] W. Weissflog, I. Wirth, S. Diele, G. Pelzl, H. Schmalfuss, T. Schoss, and A. Wurflinger *Liq. Cryst.*, **28** 1603 (2001).

[67] J. C. Rouillon, J. P. Marcerou, M. Laguerre, H.T. Nguyen, and M. Achard, F. *J. Mater. Chem.*, **11**, 2946-2950 (2001).

[68] Arun Roy *Eur. Phys. J. E.*, **18**, 253 (2005).

[69] H. N. S. Murthy, and B. K. Sadashiva, *Liq. Cryst.*, **29**, 1223-1234 (2002).

[70] D. Shen, S. Diele, G. Pelzl, I. Wirth, and C. Tschierske, *J. Mater. Chem.*, **9** 661 (1999).

[71] H. N. S. Murthy, and B. K. Sadashiva, *J. Mater. Chem.,* **14**, 2813 (2004).

[72] J. P. Bedel, J. C. Rouillon, J. P. Marcerou, M. Laguerre, H. T. Nguyen, and M. F. Achard, *J. Mater. Chem.,* **12**, 2214 (2002) .

[73] C. K. Lee, A. Primak, A. Jakli, E. J. Choi, W. C. Zin, and L. C. Chien, *Liq. Cryst.*, **28**, 1293 (2001).

[74] R. A. Reddy, and B. K. Sadashiva, *Liq. Cryst.*, **30**, 273 (2003).

[75] H. N. S. Murthy, and B. K. Sadashiva, *Liq. Cryst.*, **30**, 1051 (2003).

[76] G. Heppke, D. D. Parghi, and H. Sawade, *Liq. Cryst.*, **27**, 313 (2000).

[77] A. Jakli, Ch. Lischka, W. Weissflog, G. Pelzl, and A. Saupe, *Liq. Cryst.*, **27**, 1405 (2000).

[78] G. Pelzl, M. W. Schröder, U. Dunemann, S. Diele, W. Weissflog, C. Jones, D. Coleman, N. A. Clark, R. Stannarius, J. Li, B. Das, and S. Grande *J. Mater. Chem.*, **14**, 2492 (2004).

[79] K. F.-Csorba, A. Vajda, A. Jakli, C. Slugovc, G. Trimmel, D. Demus, E. Gacs-Baitz, S. Holly, and G. Galli, *J. Mater. Chem.*, **14**, 2499 (2004).

[80] J. P. Bedel, J. C Rouillon, J. P. Marcerou, M. Laguerre, M. F. Achard, and H. T. Nguyen, *Liq. Cryst.* **27**, 103 (2000).

[81] D. M. Walba, E. Körblova, R. Shao, J. E. Maclennan, D. R. Link, M. A. Glaser, and N. A. Clark, *Science*, **288**, 2181 (2000).

[82] D. Walba, E. Körblova, R. Shao, and N. A. Clark, *J. Mater. Chem.*, **11**, 2743 (2001).

[83] J. P. Bedel, J. C. Rouillon, J. P. Marcerou, M. Laguerre, H. T. Nguyen, and M. F. Achard, *Liq. Cryst.*, **28**, 1285 (2001).

[84] J. P. Bedel, J. C. Rouillon, J. P. Marcerou, H. T. Nguyen, and M. F. Achard, *Phys. Rev. E*, **69**, 061702 (2004).

[85] R. A. Reddy and B. K. Sadashiva, *J. Mater. Chem.*, **14**, 310 (2004); S. T. Wang, X. F. Han, A. Cady, Z. Q. Liu, A. Kamenev, L. Glazman, B. K. Sadashiva, R. A. Reddy and C. C. Huang, *Phys. Rev. E*, **70**, 061705 (2004).

[86] A. Eremin, S. Diele, G. Pelzl, H. Nadasi, W. Weissflog, J. Salfetnikova, and H. Kresse, *Phys. Rev. E*, **64**, 051707 (2001).

Chapter 2

Experimental Techniques

In this chapter, we will discuss some of the experimental techniques used in this thesis. To characterize the liquid crystals, we have used a variety of exerimental techniques such as polarizing optical microscopy (POM), differential scanning calorimetry (DSC), X-ray diffraction (XRD), electro-optic measurements, polarization switching current measurements.

2.1 Alignment of Liquid crystals

To measure the physical properties of the LC sample, the average orientational direction of the molecules, *i.e.*, the director $\hat{n}$ should be aligned in a preferred direction. In general, the director $\hat{n}$ can be aligned either parallel or perpendicular to the plane of the glass plates of the liquid crystal cell [1, 2, 3].

2.1.1 Planar-alignment

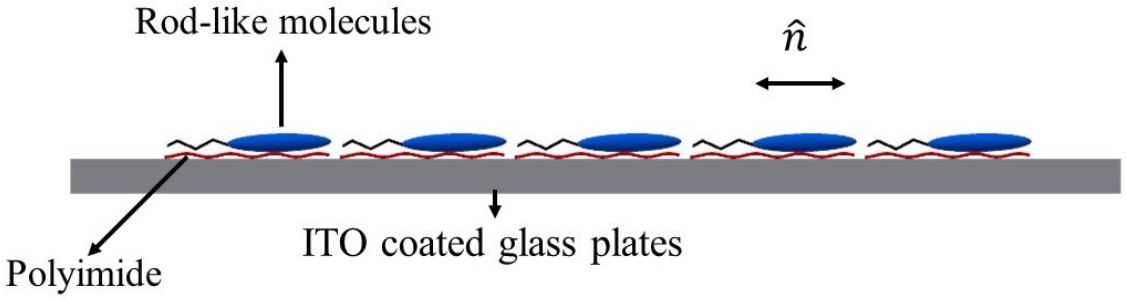

Figure 2.1: Pictorial representation of the planar-alignment of rod-like molecules on glass-substrate.

The alignment is said to be planar if the molecules are parallel to the glass plates of the liquid crystal cell. The planar-alignment of the molecules can be obtained by the coating of polyimide (PI) on the glass plates. The rubbing in a specific direction on PI coated cells create micro-groves on the glass plates. These micro-groves help align the long axis of the molecules parallel to the glass plate along the rubbing direction giving rise to the homogeneous planar-alignment, as shown in Figure 2.1.

2.1.2 Homeotropic-alignment

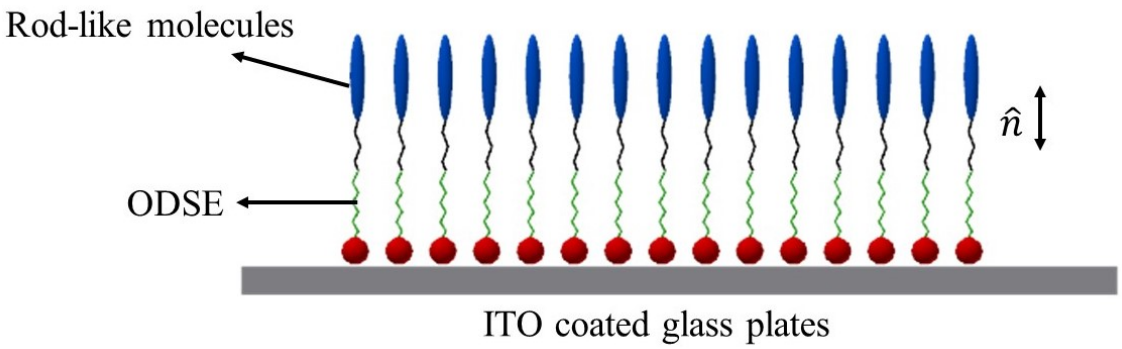

Figure 2.2: Pictorial representation of the homeotropic-alignment of rod-like molecules on glass-substrate.

When the molecules align perpendicular to the glass substrate, the alignment is said to be homeotropic. To get the homeotropic alignment, a glass plate is coated with a surfactant that has long-chain, as for example, octadecyl triethoxy silane (ODSE). These molecules are amphiphilic in nature, which contain two-parts: a polar head group and aliphatic chains. The polar head group of these molecules absorb on the glass plate of the liquid crystal cell, whereas the long aliphatic chains interact with the terminal chains of the LC compound. This gives rise to the perpendicular arrangement of the LC molecules with respect to the glass plate of the liquid crystal cell as shown in the Figure 2.2.

2.2 Construction of liquid crystal Cells

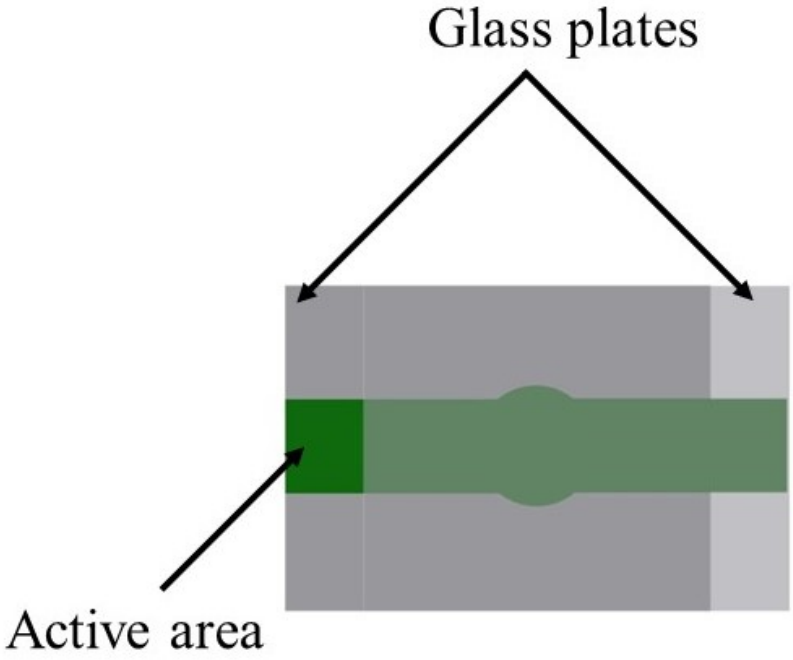

Figure 2.3: Top view of a homemade liquid crystal cell.

To study the various physical properties of the liquid crystals, we used homemade liquid crystal cells of different thicknesses. We have constructed two types of liquid crystal cells depending on the requirements:

1. ODSE coated cells for the homeotropic alignment of the molecules.
2. Polyimide (PI) coated cells for the planar alignment of the molecules.

To construct the liquid crystal cells, we used Indium-tin-oxide (ITO) coated glass plates of thickness 0.5 mm. The molecular structure of ODSE is shown in Figure 2.4a. To prepare the homeotropic cell, commercially available ITO glass plates were coated with ODSE (0.1 % ODSE in 99.9 % toluene). The coated cell was cured in a oven at 150 ^{0}C for an hour. The glass plates were cut in the appropriate size and assembled on top of each other in such a way that the active area of the cells overlaps. The separation between the two glass plates was maintained by either mylar spacer of a

given thickness or using glass beads in the form of powder mixed with epoxy glue by putting at the edges of the cells. The cell was cured at 150 ^{0}C for 45-60 minutes in a oven after applying the epoxy glue.

To get the homogeneous planar-alignment of the molecules with respect to the glass plates, we used polyimide (PI) coating. The chemical structure of polyimide is given in Figure 2.4b. Polyimide is a polymer of imide monomers. Polyimide is highly viscous, which was diluted with N-Methyl-2-pyrrolidone or methyl carbitol (2-(2-Methoxyethoxy)ethanol) solvent (0.1 *ml* of polyimide in 10 *ml* of the solvent). A clean glass cylindrical rod was used for uniform coating of PI on the ITO coated glass plates. For the polymerization, the glass plates were baked at 258-280 ^{0}C for an hour. After baking the glass plates, the coated glass surface was rubbed in a particular direction using premier tissue paper. This creates the grooves on the coated glass plates, which favor the uniform alignment of the molecules along the rubbing direction.

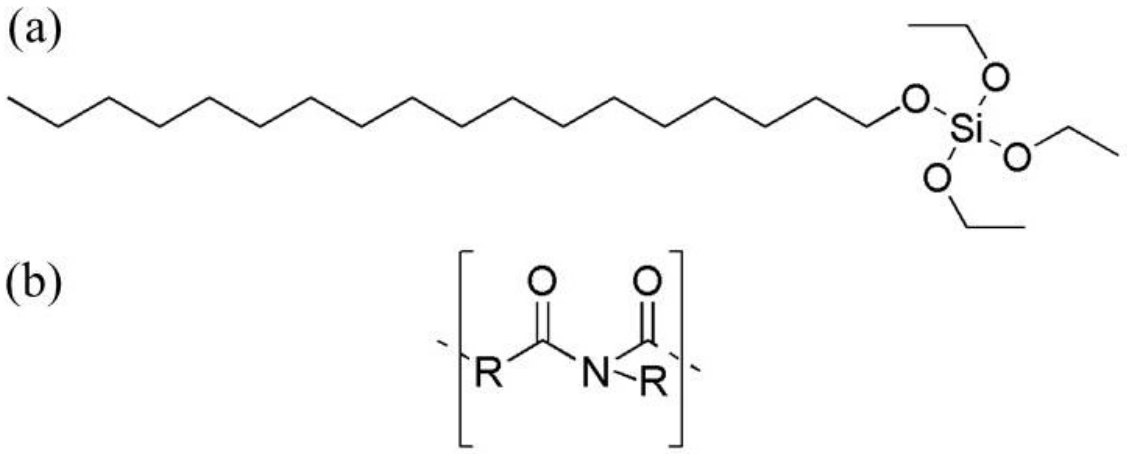

Figure 2.4: Chemical structure of (a) Octadecyl triethoxy silane (ODSE) and (b) Polyimide (PI).

The thickness of liquid crystal cells was measured using Ocean Optics Spectrometer (S-2000). The capacitance of the empty cell was measured before filling the LC sample. The liquid crystal sample was filled into cells by capillary action in the isotropic phase using a hot stage.

2.3 Differential Scanning Calorimetry

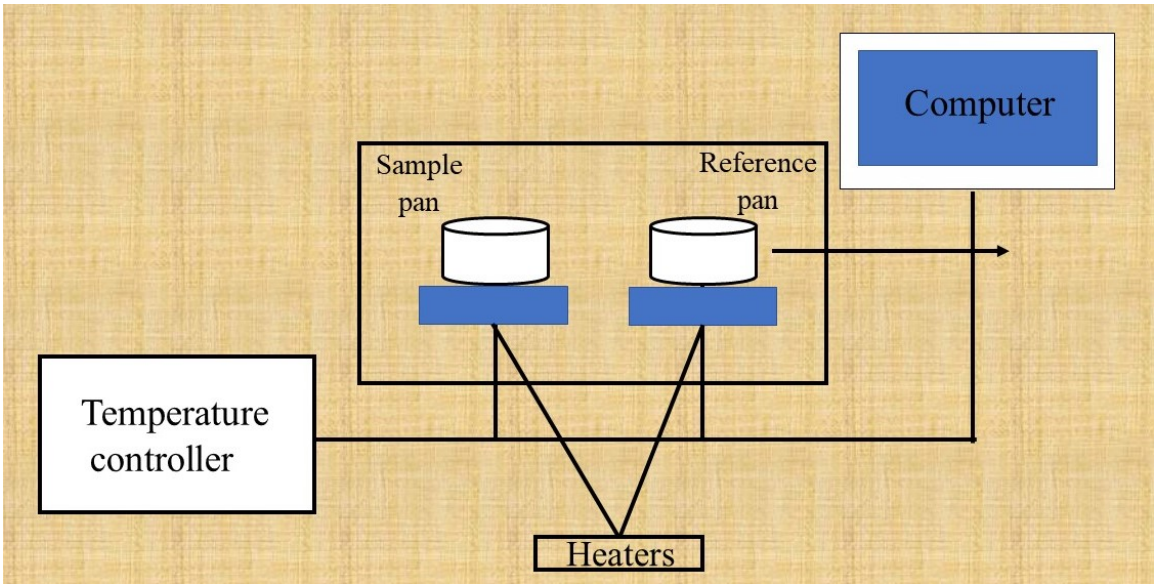

Figure 2.5: Schematic representation of a DSC set-up.

Differential scanning Calorimetry (DSC) is a powerful and versatile thermo analytic technique to measure the transition temperatures. A schematic representation of the DSC set-up is shown in Figure 2.5. The DSC thermogram measures the temperatures and corresponding enthalpy changes associated with the sample as a function of temperature and time. DSC thermogram gives an accurate method to provide heat capacities and enthalpy changes. It measures the heat capacity changes at constant pressure as a function of temperature.

$$C_P = \left(\frac{dQ}{dT}\right)_P = \left(\frac{\partial H}{\partial T}\right)_P$$

where C_P is the heat capacity, H is the enthalpy, T is the temperature, and Q is the total heat.

The area under the observed curve between any two given temperatures (T_1, T_2) gives a change in the enthalpy,

$$\Delta H = \int_{T_1}^{T_2} \left(\frac{\partial H}{\partial T}\right)_T dT$$

$$\Delta H = \int_{T_1}^{T_2} C_P dT \tag{2.1}$$

In DSC thermograms, we observed the transition peaks as the sample goes from one state to the other state. The change in the enthalpy is equal to the area of obtained peak associated with the transition. For the minimum error in the measurements, the area under the curve should be maximized which gives the enthalpy change corresponding to the phase transition. The area under the curve can be maximized by controlling the various parameters during the experiments. The scan rate also plays an essential role while taking measurements as it defines the speed at which the temperature is increased/decreased. A lower temperature rate gives a taller and sharp peak in the DSC thermogram. The temperature range describes the sensitivity range, a small change in heat capacity can get amplified on decreasing the range. In the DSC thermogram, the transition temperatures are often taken the point at which the curve start rising from the baseline. On the other hand, the transition points are taken at the maxima if sharp peaks are observed in the DSC thermogram. When a solid melts, the molecules lose orientational as well as translational order and the entropy of the system increases.

In the case of LC samples, there is more than one phase between the isotropic liquid and the crystal phase depending on the orientational and translational order of the molecules as described in chapter 1. Therefore, we get more than one peak in the DSC thermograms in the case of liquid crystals. Sometimes, we can not detect the phase transition using DSC if it is a second-order phase transition. For example, compound 8OCB shows two mesophases between the isotropic liquid and crystal phase: Nematic (only orientational order no translational order) and SmA_d phase (translational order in one dimension and orientational order in 2D). There is a very small peak at the transition from the Nematic to the SmA_d phase indicating a weak first-order phase transition. The DSC thermogram of a the compound 8OCB consists of rod-like molecules is shown in Figure 2.6.

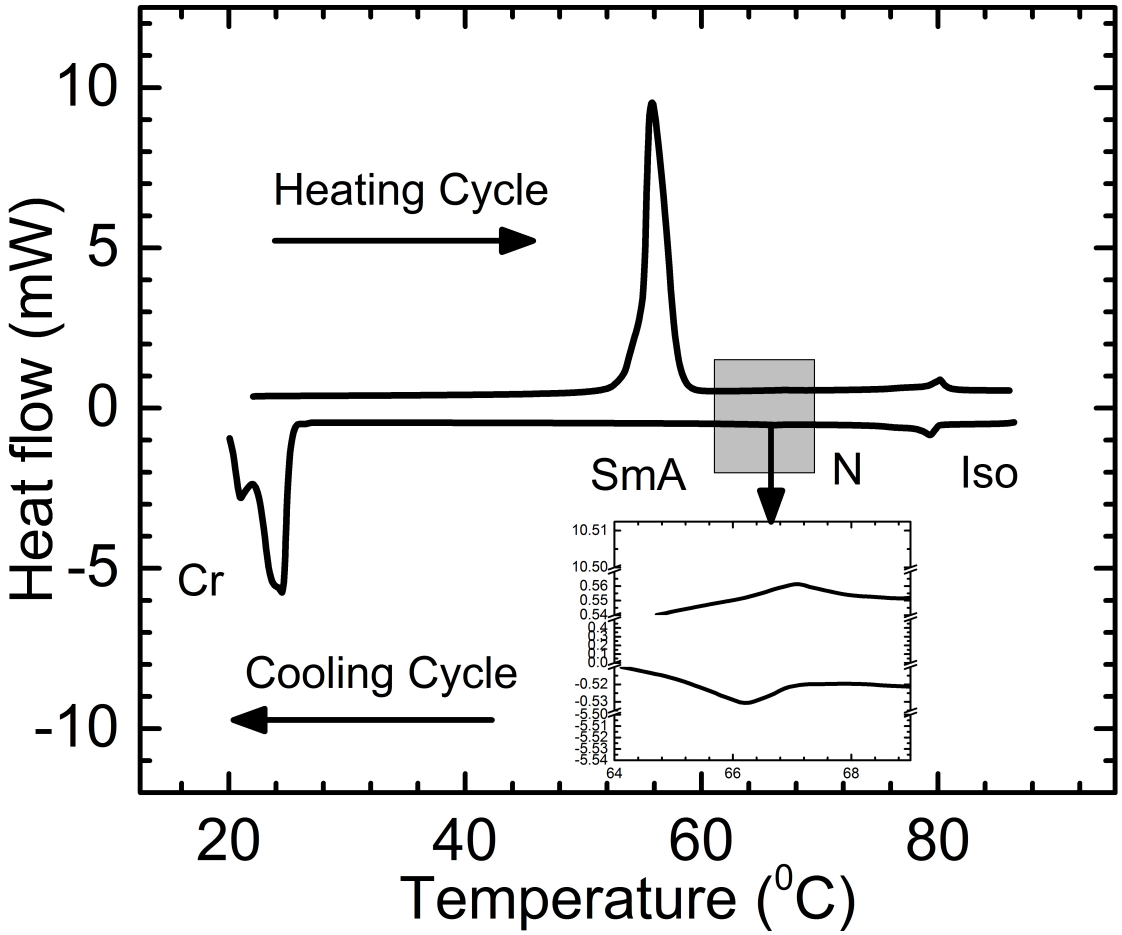

Figure 2.6: DSC thermogram of the compound 8OCB on cooling and heating at a fixed rate of 3 ^{0}C/min. The inset shows the clear transition between the Nematic and SmA_d phase on heating and cooling.

2.4 X-ray diffraction

The X-ray diffraction (XRD) technique is a common and powerful tool to investigate the molecular organization in the liquid crystal phases. The characteristic length scale of the positional order in the LC sample is determined using Bragg's law. According to Bragg's law, the refracted X-ray from the adjacent planes of crystals will undergo constructive interference only if the path difference between the adjacent crystal planes is an integral multiple of the wavelength of X-ray.

$$2d \sin\theta = n\lambda \tag{2.2}$$

where d is the layer spacing between the adjacent crystal planes, θ is the angle between the incident beam and scattering plane, known as Bragg's angle, n is an integer, and λ is the wavelength of the incident X-ray beam.

In the case of the Nematic phase, we observed only a diffusive peak in the XRD profile corresponding to the orientational order of the molecule as shown in Figure 2.7a. Which indicates the fluid-like order of the molecules in the Nematic phase. Whereas, for the SmA phase, we observed a sharp peak in the small-angle region corresponding to the translational order in addition to a diffusive peak in wide-angle range corresponding to the fluid-like organization of the molecules within the layer. If layer spacing obatined from the XRD data is approximately equal to the molecular length then it indicates that the long axis of the molecules is parallel to layer normal in the lamellar structure, which is the characteristic of the non-tilted SmA phase. The XRD studies indicate the tilted Smectic phase if the observed layer spacing by XRD data is smaller than the molecular length (d<l). The shorter layer spacing than the molecular length indicates that the molecules are tilted with respect to the layer normal as expected in the tilted smectic phase. Figure 2.7b shows the XRD intensity profile in the SmA phase of the compound 8OCB. The layer spacing in the SmA phase of compound 8OCB is 31.7 Å which is intermediate between l and $2l$ where l is the molecular length of 8OCB molecules (21.7 Å). Therefore, the observed layer spacing in the SmA phase indicates the intercalated structure of the molecules within the layers.

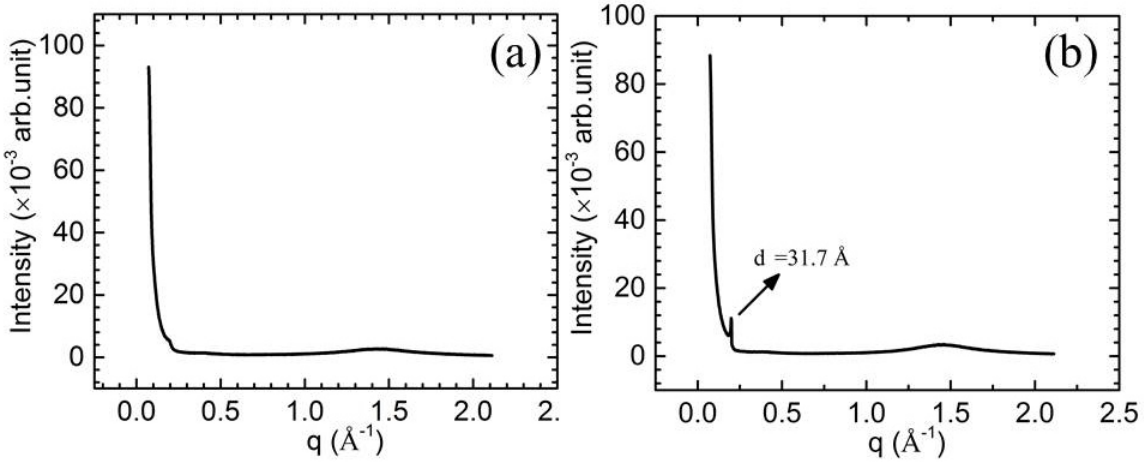

Figure 2.7: The XRD intensity profile of compound 8OCB on cooling from the isotropic phase in (a) Nematic phase at 75 ^{0}C (b) SmA phase at 60 ^{0}C.

In this thesis, all the XRD data was taken on cooling the sample from the isotropic phase. The LC samples were filled in the Lindemann capillary of outer diameter about 1 mm in the isotropic phase.

2.5 Parallel plate capacitor

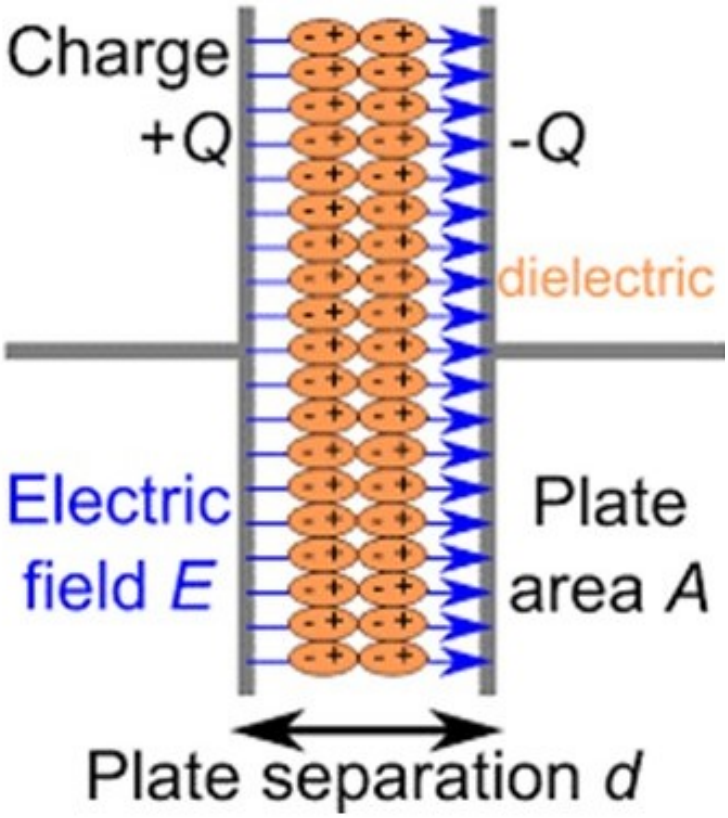

Figure 2.8: A schematic representation of a parallel plate capacitor.

The capacitance of a capacitor is given by,

$$C = \frac{Q}{V}$$

where Q is the total charge, and V is the potential difference between two plates (see Figure 2.8). The capacitance is a physical quantity to measure the capacity of storing the electric charge in a given potential difference V. This is a geometrical quantity which depends on the size, shape, and separation between two plates [4].

Let us consider a parallel plate capacitor separated by a distance d. Therefore, the total charge enclosed is given by, E_1+E_2=σ/ϵ_0 where σ=Q/A is the surface charge density and ϵ_0 is the permittivity of free space. The potential difference between the plates is given by,

$$\begin{aligned} V &= \int_0^d E dZ \\ &= \int_0^d \frac{\sigma}{\epsilon_0} dZ \\ V &= \frac{\sigma d}{\epsilon_0} \end{aligned}$$

Therefore, the capacitance of a parallel plate can be written as,

$$C = Q/V$$

$$\boxed{C = \frac{\epsilon_0 A}{d}} \tag{2.3}$$

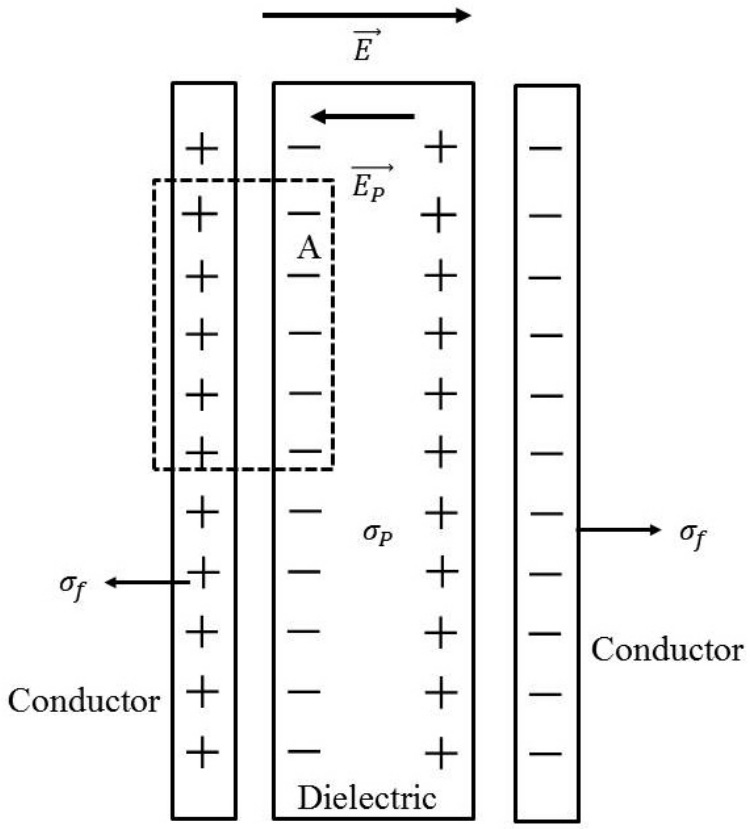

Figure 2.9: Parallel plate capacitor in the presence of a dielectric material.

when a dielectric material is placed between two parallel plates. Then, by applying the Gauss' law to the Gaussian surface in the Figure 2.9.

$$E = \frac{\sigma_f - \sigma_P}{\epsilon_0}$$
$$E = \frac{\sigma_f - P}{\epsilon_0}$$

where $\sigma_p = P$ and $P = \xi_e \epsilon_0 \vec{E}$, ξ_e is the electric susceptibility of the dielectric material.

$$E(1 + \xi_e)\epsilon_0 = \sigma_f$$

The total charge on the capacitor is,

$$Q = \sigma A = \epsilon_0 E A(1 + \xi_e) = \epsilon_0 V A(1 + \xi_e)/d$$

The capacitance of the capacitor is defined as

$$C = Q/V = \epsilon_0 A(1 + \xi_e)/d$$

$$\boxed{C/C_0 = (1 + \xi_e) = \epsilon}$$

ϵ is known as the relative permittivity or dielectric constant of the material. $C_0 = A\epsilon_0/d$ is the capacitance between parallel plates in the absence of a dielectric material. Therefore, when a dielectric material is placed between two parallel-plate capacitors, the capacitance is increased by a factor $\epsilon = 1+\xi_e$ Therefore, the dielectric constant ϵ is the property of the material which tells us how effective an electric field is in polarizing the material.

2.6 Impedance analysis of LC sample

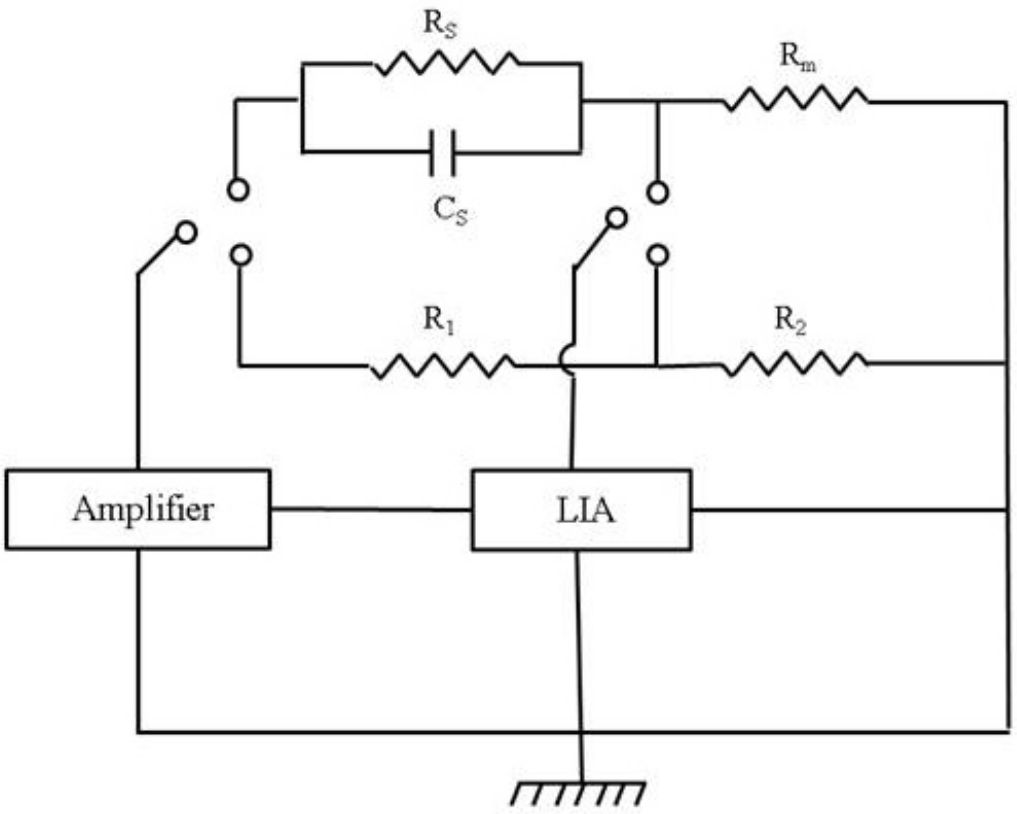

Figure 2.10: The schematic representation of RC equivalent circuit.

The liquid crystal samples are not free from the ionic impurities and possess a finite resistance. Therefore, a liquid crystal cell can be considered as a parallel-plate capacitor with a resistance R_S and capacitance C_S in parallel as shown in Figure 2.10. A fixed known resistor, R_m $(= 1k\Omega)$ is connected in series with liquid crystal cell. An AC voltage of frequency 5641 Hz from the lock-in amplifier (Standford Research System model no. SR830) is fed into a voltage amplifier. The output of the amplifier is connected to either a potential divider or the liquid crystal cell in series with R_m. Using a manual double pole double throw (DPDT) switch. The potential divider is made of two resistors $R_1 = 1M\Omega$ and $R_2 = 100k\Omega$ connected in series. This circuit was used to measure the output amplitude and the phase of the amplified signal. The amplitude and the phase of the voltage drop across R_m are measured by the lock-In amplifier. The capacitance C_S and the resistance R_S are measured by using impedance analysis [5]. The impedance of a capacitor is given by

$$Z = \frac{1}{\omega C} e^{-j\frac{\pi}{2}}$$

where $\omega = 2\pi f$ is the angular frequency and f is the frequency of the applied signal, and $j = \sqrt{-1}$.

The impedance of the liquid crystal cell is given by,

$$\frac{1}{Z_C} = \frac{1}{R_S} + \frac{1}{X_C}$$

where $X_C = \frac{1}{j\omega C_S}$

$$\frac{1}{Z_C} = \frac{1}{R_S} + j\omega C_S$$

$$Z_C = \frac{R_s(1 - j\omega C_S R_S)}{(1 + \omega^2 {C_S}^2 {R_S}^2)}$$

The total impedance of the circuit is given by,

$$Z_T = Z_C + Z_m$$

$$Z_T = \frac{R_S(1 - j\omega C_S R_S)}{(1 + \omega^2 {C_S}^2 {R_S}^2)} + R_m$$

$$Z_T = \frac{[R_S + R_m(1 + \omega^2 {C_S}^2 {R_S}^2) - j\omega C_S {R_S}^2]}{1 + \omega^2 {C_S}^2 {R_S}^2}$$

An AC input voltage $V = V_0 e^{j(\omega t + \phi_0)}$ is applied to the LC sample, where ϕ_0 is the phase. The total current is given by,

$$I_T = \frac{V_0 e^{j(\omega t + \phi_0)}}{Z_T}$$

$$I_T = \frac{V_0 e^{j(\omega t + \phi_0)}(1 + \omega^2 {C_S}^2 {R_S}^2)}{[R_S + R_m(1 + \omega^2 {C_S}^2 {R_S}^2) - j\omega C_S {R_S}^2]} \tag{2.4}$$

The voltage drop across R_m which was measured by lock-in amplifier is given by,

$$V_m e^{j(\omega t + \phi_m)} = I_T R_m$$

$$V_m e^{j(\omega t + \phi_m)} = \frac{V_0 e^{j(\omega t + \phi_0)}(1 + \omega^2 {C_S}^2 {R_S}^2) R_m}{R_S + Rm(1 + \omega^2 {C_S}^2 {R_S}^2) - j\omega C_S {R_S}^2}$$

where V_m and ϕ_m are the amplitude and the phase of the measured voltage. On comparing real and imaginary parts,

$$V_m \cos(\omega t + \phi_m) = V_0 \frac{A\cos(\omega t + \phi_0)[R_S + AR_m] - B\sin(\omega t + \phi_0)}{[R_S + AR_m]^2 + B^2}$$

$$V_m \sin(\omega t + \phi_m) = V_0 \frac{A\sin(\omega t + \phi_0)[R_S + AR_m] + B\cos(\omega t + \phi_0)}{[R_S + AR_m]^2 + B^2}$$

where $A = 1 + \omega^2 {C_S}^2 {R_S}^2$, $B = \omega C_S {R_S}^2$. Solving the above two equations,

$$\boxed{C_S = \frac{V_0 V_m \sin(\phi_m - \phi_0)}{R_m \omega ({V_0}^2 + {V_m}^2 - 2V_0 V_m \cos(\phi_m - \phi_0))}} \tag{2.5}$$

and

$$\boxed{R_S = R_m(\frac{{V_m}^2 - {V_o}^2}{V_m(V_m - V_0 \cos(\phi_m - \phi_o))} - 2)} \tag{2.6}$$

The dielectric constant of the LC sample is the ratio of measured capacitance with LC sample (C_S) and the empty cell capacitance (C_0), *i.e.*, $\frac{C_S}{C_0}$.

We can also calculate the conductivity of LC sample using Equation 2.6as,

$$\boxed{\sigma = \frac{d}{R_S A}} \tag{2.7}$$

where A is the effective or active area of the liquid crystal cell and d is the thickness of the sample.

2.7 Refractive index

When light passes through an anisotropic material, the ray splits into ordinary and extraordinary rays with refractive indices n_o and n_e, respectively [3, 6]. In case of uniaxial liquid crystal, $n_e = n_\parallel$ and $n_o = n_\perp$. Therefore, the birefringence of an anisotropic material is given by

$$\Delta n = n_e - n_o = n_\parallel - n_\perp \tag{2.8}$$

After passing through the sample, the optical path difference between these two rays is given by

$$\Delta\phi = \frac{2\pi}{\lambda}\int_0^d (n(z) - n_o)dz \tag{2.9}$$

Therefore, the transmitted intensity shows a series of minima and maxima depending on the path difference whether $\Delta\phi$ equals an integer n or $n + 1/2$, respectively.

2.8 Electro-optic setup

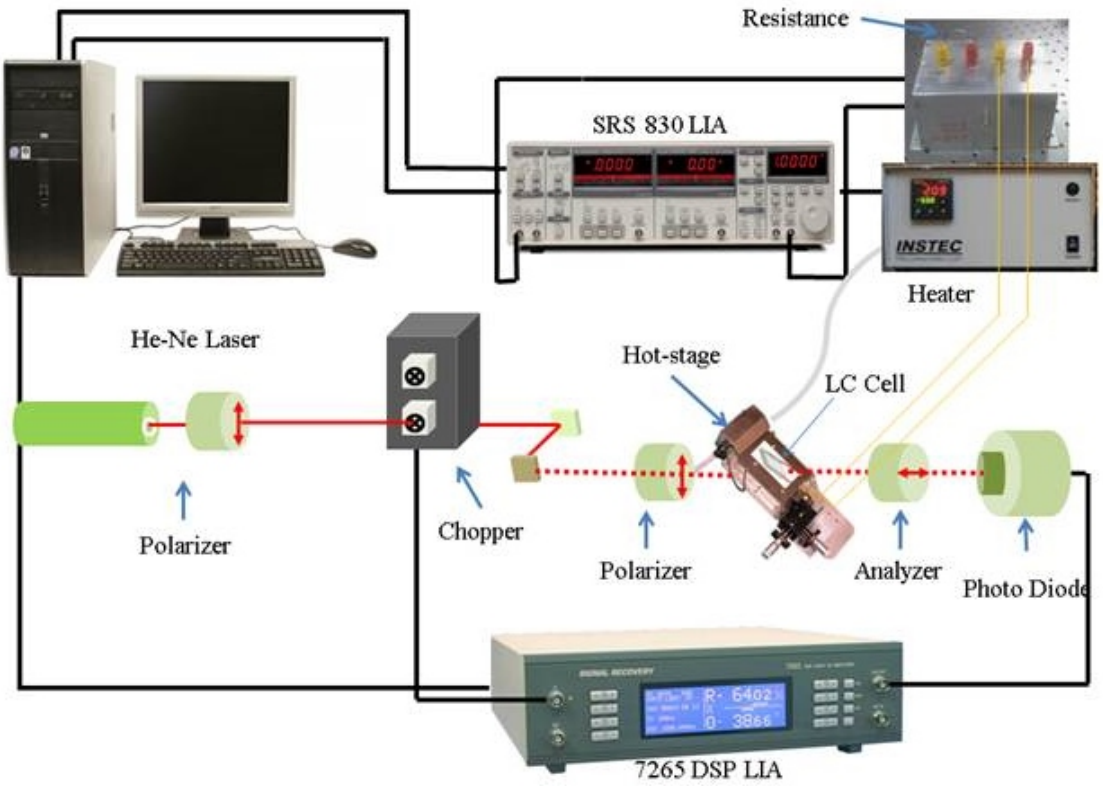

Figure 2.11: Schematic representation of the electro-optic experimental set-up to measure the dielectric constant and the transmitted optical intensity simultaneously as a function of temperature.

For simultaneous measurements of dielectric constant and the transmitted optical intensity passing through the planar-aligned sample as a function of the temperature,

we used a home-built experimental set-up as shown in Figure 2.11. The dielectric constant and transmitted optical intensity data was collected simultaneously using a LabVIEW program. First, we measure the capacitance of an empty liquid crystal cell. Then the LC sample was filled into the liquid crystal cell. The filled liquid crystal cell was kept under polarizing optical microscope (ORTHOLUX II POL-BK) between crossed polarizers using a hot stage (INSTEC HS400). The hot stage was connected to a temperature controller (INSTEC STC200) with temperature stability of $\pm 0.1^0$C with the temperature resolution of 0.1^0C. During the experiments, the temperature of the sample was controlled by the temperature controller using the PID algorithm which was interfaced with the computer. The data was recorded on cooling the sample from the isotropic phase for given temperature steps. The impedance analysis had been done under the application of a sinusoidal AC voltage of frequency 5641 Hz and amplitude 0.5 volts as a function of temperature. The amplitudes and phases of the voltage drop across a known resistor of 1 $k\Omega$, which was connected in series with the sample, were measured using a lock-in amplifier (model no. SR830). The lock-in amplifier was interfaced to the computer. Using Equation 2.5, we measured the capacitance of the LC sample as a function of temperature. The dielectric constant data was extracted by taking the ratio with the empty cell capacitance measured prior to filling the sample into the liquid crystal cell.

To measure the transmitted optical intensity passing through the planar-aligned sample between crossed polarizers, the sample was kept under microscope with the director $\hat{n}$ at 45 degrees with respect to the polarizer to get the maximum intensity. A He-Ne laser beam (wavelength λ= 632.8 nm) is passed through a linear polarizer followed by a chopper (Perkin Elmer model no. 198A). The light path of the laser beam is shown in Figure 2.11. The transmitted intensity passing through the planar-aligned sample under crossed polarizers was collected with a photo-diode which was mounted on the microscope. The output of the photo-diode was connected to a dual channel DSP lock-in amplifier (Perkin Elmer Model 7260). DSP lock-in amplifier provides a high-resolution measurement of relatively clean signals over several orders of magnitude and frequency. The transmitted optical intensity passing through the planar-aligned sample is given by,

$$I_t = \frac{I_0}{2}\sin^2 2\psi(1-\cos\Delta\phi) + I_d \tag{2.10}$$

where I_0 is the incident intensity of a linearly polarized light, ψ is the angle between the polarizer and the optic axis of the molecule, I_d= dark current (measured in the absence of incident light). The path difference between ordinary and extraordinary ray is given by $\Delta\phi=\frac{2\pi\Delta nd}{\lambda}$, where $\Delta n = n_e - n_o = n_\parallel - n_\perp$ where n_e and n_o are refractive indices corresponding to the extraordinary and ordinary rays of lights, respectively and d is the sample thickness.

The angle ψ was kept fixed at 45 degrees with respect to the polarizer to get the maximum intensity,

$$I = \frac{I_0}{2}(1-\cos\Delta\phi) + I_d \tag{2.11}$$

Then the intensity will be maximum and minimum at $\Delta\phi = \pi$ and $\Delta\phi = 0$, respectively. Therefore,

$$I_{max} = I_0 + I_d \tag{2.12}$$

$$I_{min} = I_d \tag{2.13}$$

Using above two equations,

$$I_{max} - I_{min} = I_0 \tag{2.14}$$

Putting the value of I_0 in the main equation

$$I - I_d = \frac{1}{2}(I_{max} - I_{min})(1-\cos\Delta\phi) \tag{2.15}$$

$$\Delta\phi = \cos^{-1}[1 - 2(\frac{I - I_{min}}{I_{max} - I_{min}})] \tag{2.16}$$

$$\Delta n = \frac{\Delta\phi\lambda}{2\pi d} \tag{2.17}$$

For a given thickness of the planar-aligned sample and the wavelength of light, the birefringence of the sample can be calculated using the above equation. To calibrate our experimental set-up, we used a compound 8OCB. Most of the physical properties of the compound 8OCB are already reported [7, 8, 9]. In the first experiment, we measured the dielectric constant of a planar-aligned sample of thickness 5 μm as a function of temperature. The measurements were taken on cooling the sample from the isotropic phase in small temperature steps. The transmitted optical intensity passing through a planar–aligned sample was also measured. The data was collected simultaneously using a LabVIEW program. The measured dielectric constant and transmitted optical intensity of the sample are shown in Figure 2.12 .

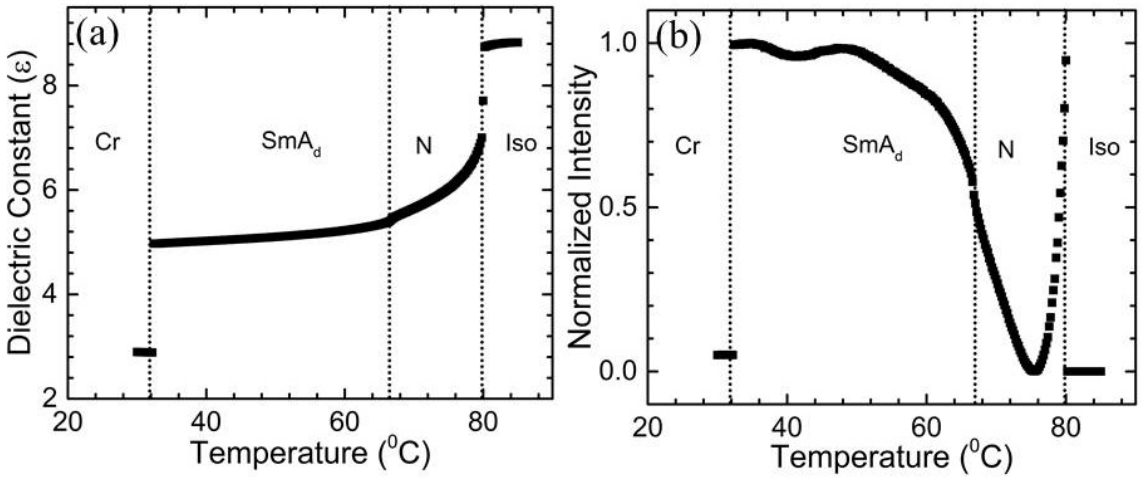

Figure 2.12: The variation of the (a) real part of dielectric constant and (b) optical intensity as a function of temperature.

In the second experiment, the sample was heated above the clearing temperature of the sample. Then the sample was cooled down from the isotropic phase to a fixed temperature of in the Nematic phase. The amplitude of the applied voltage of frequency 5641 Hz was increased in small steps from a low value to 5 volts in our experiments. The dielectric constant and the transmitted optical intensity data was collected si-

multaneously as a function of applied voltage at a given temperature as shown in Figure 2.13.

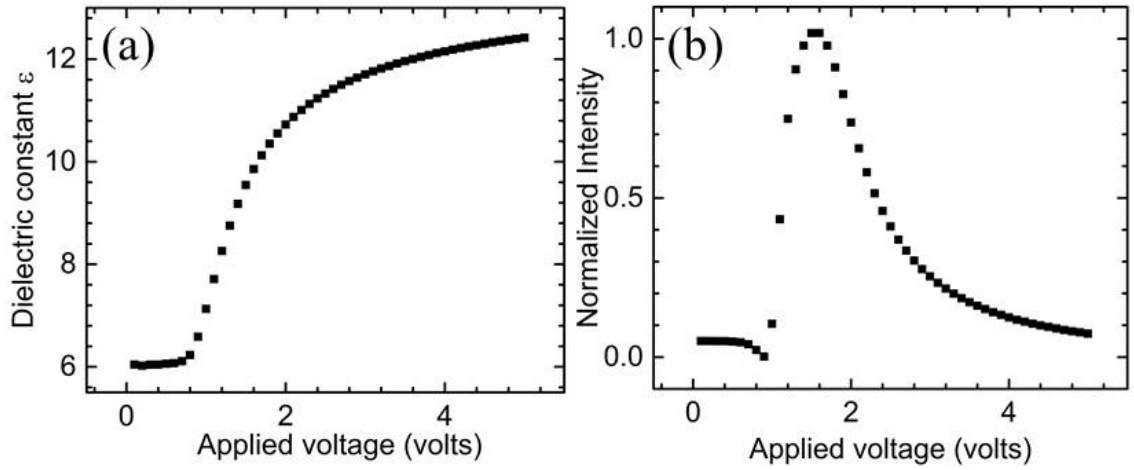

Figure 2.13: The variation of (a) the dielectric constant and (b) the optical intensity as a function of applied voltage at a constant temperature 74 ^{0}C in the Nematic phase. The data was collected on cooling the sample from the isotropic phase.

2.9 Textural Intensity Measurements

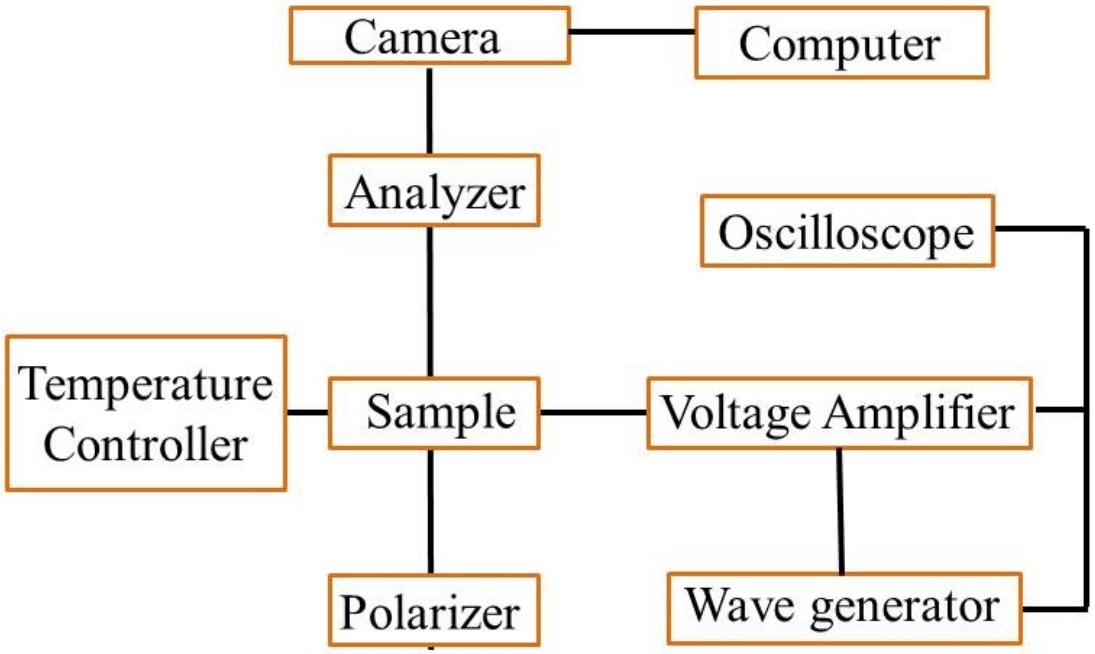

Figure 2.14: A flow chart of an experimental set-up to measure the textural intensity of the LC sample between crossed polarizers as a function of an applied field.

Some of the liquid crystal samples show the electro-optic response under the application of an AC electric field. To measure the electro-optic response of the sample, we measured the textural intensity or the effective birefringence changes under the application of an electric field. The experiments were performed on a home-built experimental setup as shown in Figure 2.14. To measure the textural intensity, the sample was mounted on a polarizing optical microscope (OLYMPUS BX50) between crossed polarizers. The microscope was equiped with a hot stage. The temperature of the hot stage was controlled by a temperature controller LINKAM(T95HS). A wave function generator (Agilent 33220A) was used to apply the voltage. The output of the function generator was connected to a voltage amplifier (TREK model no. 601B-3) with amplification gain about 100. The output of the voltage amplifier was connected to the LC sample. To measure the textural intensity, a planar-aligned sample of a given thickness was slowly cooled from the isotropic phase to the LC phase of interest. A

red filter was used to record the intensity while taking POM images. After stabilizing the temperature, a voltage of varying amplitudes and constant frequency was applied to the LC sample. At constant intervals of applied voltage, the POM images were captured using an Olympus DPS12 camera, which was connected to the microscope. The average transmitted intensity passing through a planar-aligned sample was extracted from POM images using a MATLAB program. We also calculated the effective birefringence of a planar-aligned sample using average transmitted intensity passing through the sample.

2.10 Steady-state optical responses

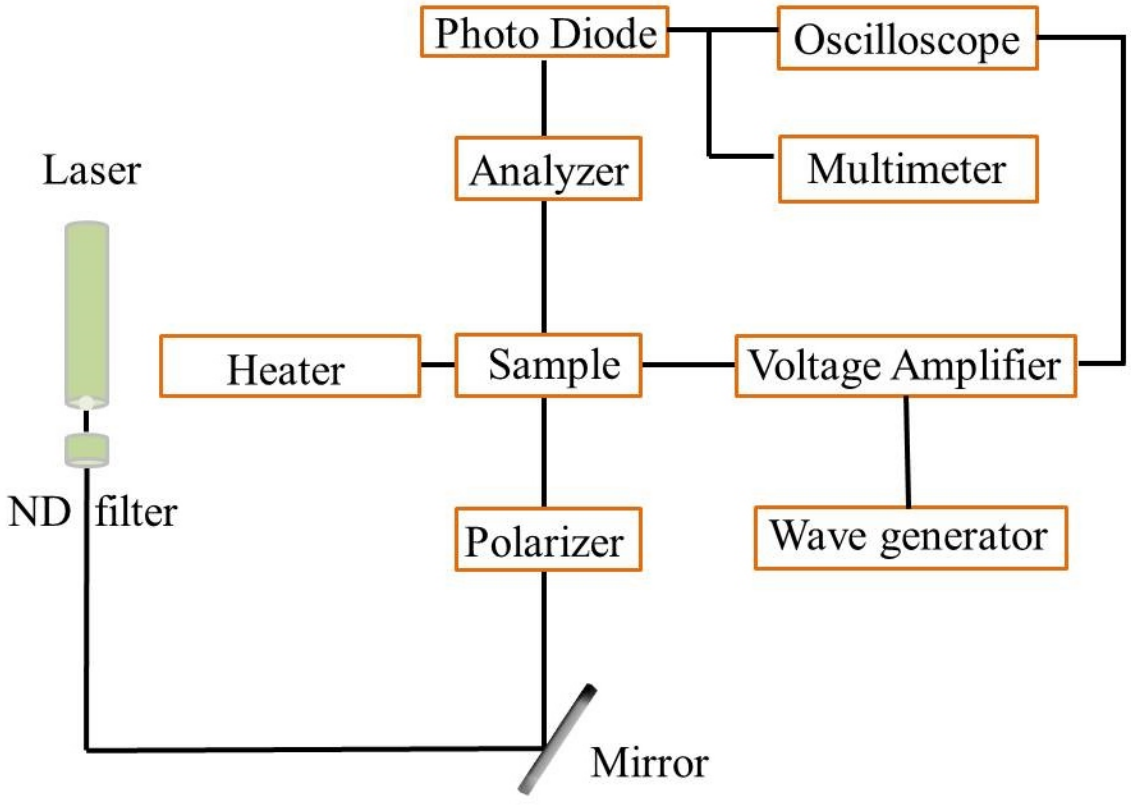

Figure 2.15: A flow chart diagram to represent the optical set up to measure the optical responses of LC samples as a function of an applied field.

To measure the steady-state optical response of a planar-aligned sample, the experimental set-up is shown in Figure 2.15. The steady-state optical response of a planar-

aligned sample was measured between the crossed polarizers on cooling the sample from the isotropic phase. The sample was loaded into a hot stage. During the experiments, the temperature of the sample was controlled by a homemade temperature controller using the PID algorithm. A wave function generator (Agilent 33220A) was used to apply the voltage of varying amplitude at a constant frequency. The output of the function generator was amplified using a voltage amplifier (TREK Model 60B1) with the amplification gain about 100. The output voltage of the amplifier was applied to the LC sample. The optical response of the sample was measured on cooling from the isotropic phase to the temperature of interest in the mesophases. After getting a stabilized temperature in the mesophases, a voltage of constant frequency was applied to the LC sample with increasing amplitude at a fixed voltage steps and corresponding optical data was recorded.

To measure the optical intensity as a function of an applied field, a He-Ne laser of wavelength 632.8 nm was passed through the planar-aligned sample. The output optical signal passing through the sample with a varying amplitude of the applied voltage at a constant temperature was collected using a high gain low noise photodiode. An oscilloscope (Agilent Technologies MSO6012A) was used to monitor the response of the sample with applied voltage.

2.11 Polarization Switching Current Measurements

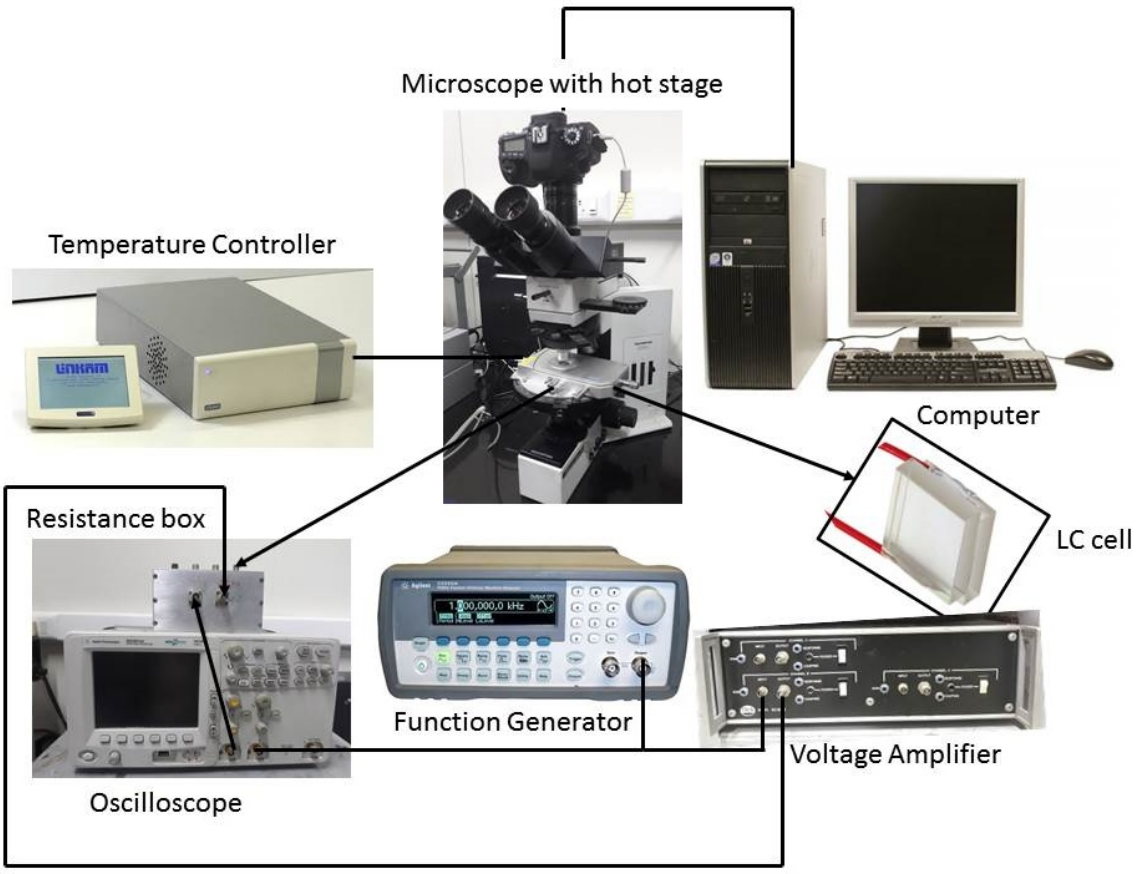

Figure 2.16: A pictorial representation of the experimental setup for the polarization switching current measurements.

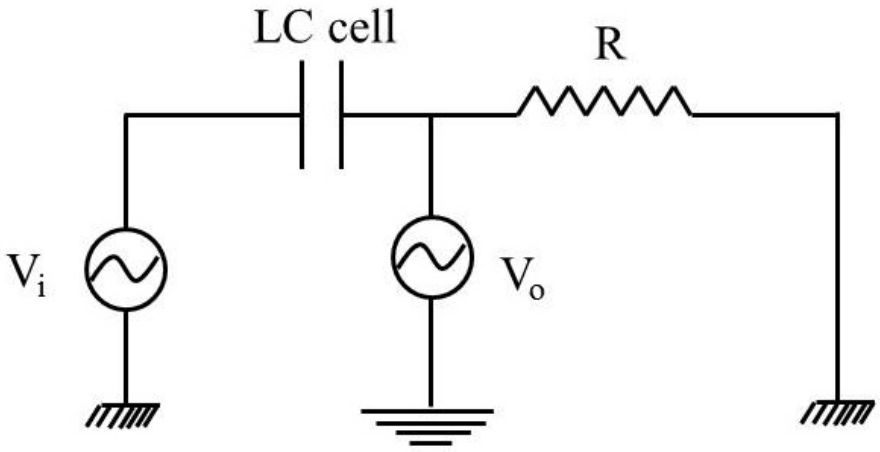

Figure 2.17: A RC equivalent circuit to measure the voltage drop across the resistor R.

Figure 2.16 shows the schematic representation of the experimental setup to measure the polarization switching current measurements. The equivalent circuit corresponding to the experimental setup is shown in Figure 2.17. The sample was studied under polarizing optical microscope between crossed polarizers (OLYMPUS BX50). The temperature of the sample was controlled by a temperature controller LINKAM (T95HS) which was connected to a hot stage (LTS420E). The sample was mounted in the sample holder inside the hot stage. To measure the layer polarization of the sample, we used a triangular wave voltage technique [10]. A triangular wave voltage at a constant frequency was applied to the LC sample using a function generator (Agilent 33220A). The output of the function generator was connected to the amplifier (TREK Model 601B with amplification gain about 100). The amplified voltage was applied to the sample. The voltage drop across a known resistance (1 KΩ), which was connected in series to LC sample, was monitored by an oscilloscope. The polarization reversal current measurement is a powerful tool to know the ferroelectric or antiferroelectric behavior of liquid crystal samples. The appearance of one peak in the half-cycle in the current response indicates the ferroelectric behavior of the LC samples. Whereas, the presence of two peaks in the half-cycle of the current response shows the antiferroelectric behavior of the LC samples. The observations of polarization reversal current peaks in the current response can easily detect the polar behavior of the liquid crystal samples. In the present thesis, we use triangular wave voltage technique to measure the spontaneous polarization [10]. The particular reason to use the triangular wave was to determine accurately the spontaneous polarization by the easy subtraction of the background contributed due to the conductive and the capacitive current. The induced current I (t) in the sample cells under the application of an applied voltage V(t) can be written as:

$$I = I_C + I_P + I_i \tag{2.18}$$

$$I = C\frac{dV}{dt} + \frac{dP}{dt} + \frac{V}{R} \tag{2.19}$$

where I_C= Capacitive current due to the charge accumulation in the capacitor

I_i= conductive current due to the ion flow

I_P= polarization reversal current due to polarization realignment

P= spontaneous polarization

The extraction of I_p from the other parts of current is shown in Figure 2.18.

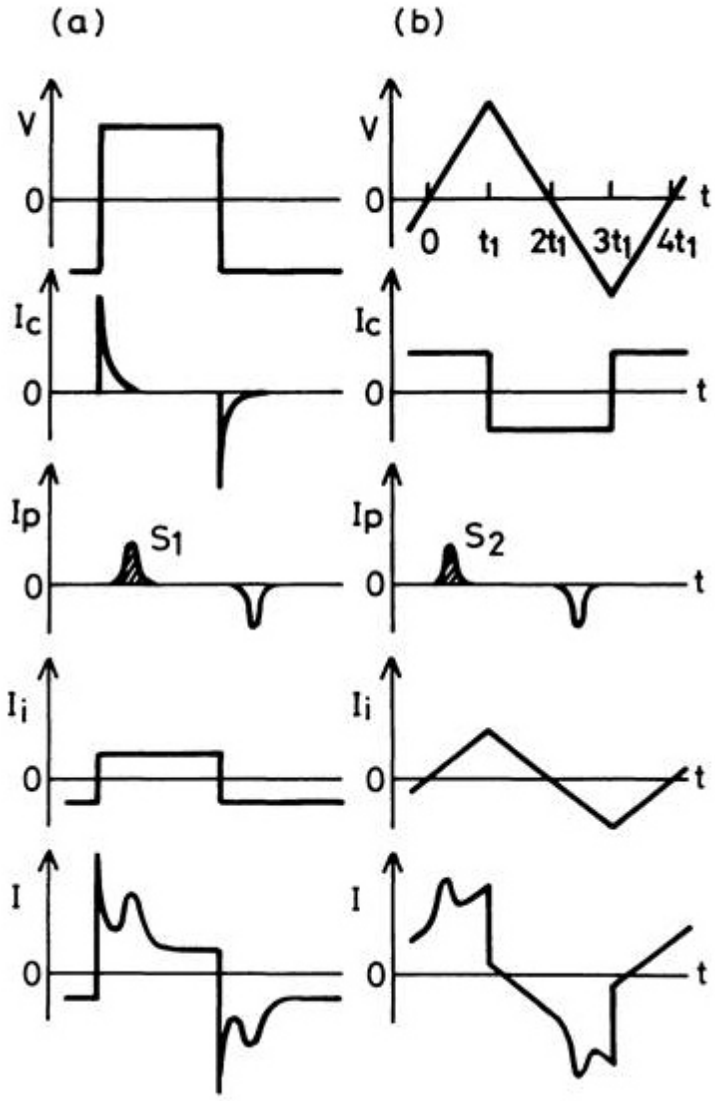

Figure 2.18: The schematic representation of the current by rapidly reversing a field (a) or by applying a triangular wave voltage (b) three contributions, I_c, I_p and I_i to overall current I, are due to the charge accumulation, the polarization realignment, and the ion flow respectively [10].

Bibliography

[1] P. G. de Gennes, and J. Prost, *The Physics of Liquid Crystals*, (Clarendon, Oxford, 1994).

[2] S. Chandrasekhar, *Liquid Crystals*, (Cambridge University Press, Cambridge, 1992).

[3] W. H. de Jeu, *Physical Properties of liquid crystal Materials*, Gordon and Breach, Science Publishers Ltd. (1980).

[4] David J. Griffiths *INTRODUCTION TO ELECTRODYNAMICS*, WILEY-VCH Verlag GmbH and Co. KGaA, Weinheim Ltd. (2003).

[5] B. Kundu *Experimental Investigation on physical propertoes of some novel liquid cystals with banana-shaped and rod-like molecules*, Dept. of soft condensed matter physics, Raman Research Institute, Bangalore, India (2008).

[6] I. Dierking, *Textures of Liquid Crystals.*, WILEY-VCH Verlag GmbH and Co. KGaA, Weinheim Ltd. (2003).

[7] A.J.Leadbetter, R.Richardon, and C.N. Colling, *J. Phy. Colloq.*, **36**, C1 (1975).

[8] K. C. Lim and J. T. Ho *Phys. Rev. Lett.*, **40**, 944-946 (1978).

[9] M. J. Bradshaw, E. P.Raynes, J. D. Bunning, and T. E. Faber, *J. Physique*, **46**, 1513 (1985).

[10] K. Miyasato, S. Abe, H. Takezoe, A. Fukuda, and E. Kuze, *Jpn. J. App. Phys.*, **22**, L661- L663 (1983).

Chapter 3

Pseudo-Polar Tilted Smectic Phases Exhibited by bchs Molecules

3.1 Introduction

The understanding of the properties of the variety of liquid crystal (LC) phases exhibited by bent-core (BC) banana-shaped molecules is an active field of research in soft matter physics [1, 2, 3, 4]. A typical bent-core molecule contains two rigid rod-like arms joined end to end with an angle of about 120 degrees between them. The flexible aliphatic chains are usually attached to one or both ends of the rigid core of the molecule. The bent configuration of the rigid arms gives rise to a shape polarity to the molecule which accounts for many unusual properties of bent-core liquid crystals (BCLCs) [5, 6]. The manifestation of polar order and spontaneous breaking of chiral symmetry of achiral bent-core (BC) banana-shaped molecules in their tilted smectic phases led to considerable efforts to explore various phases of BCLCs [7, 8]. Since the first report [7] on symmetric BC molecules showing an in-plane polar order in their smectic phases, the phase behavior of such molecules has been explored in great detail. The existence of sufficiently large transverse shape polarity of the symmetric BC molecules often leads to chirality in their tilted smectic phases even though the constituent molecules are achiral [6]. Many liquid crystal phases with properties very different from those exhibited by rod-like or disc-like molecules have been observed [9, 10, 11, 12]. Even the existence of the lowest symmetry fluid lamellar phase with a triclinic C_1 point symmetry of the layers has been reported [13, 14]. The BC molecules can be classified into two categories as symmetric and asymmetric BC molecules. In a symmetric BC banana-shaped molecule, both the arms and the terminal chains are the same, giving rise to the C_{2V} point symmetry of the molecule. In a asymmetric BC

molecule, the two arms are different reducing the symmetry of the molecule considerably. The asymmetry in the BC molecule can be introduced in two ways:

(a) using different terminal chain lengths or linkage groups in the two arms of the BC molecule, while the length of the two arms of the BC molecule being comparable. These types of asymmetric BC molecules can still be considered to have a BC banana-like shape. Some of these types of asymmetric BC banana-shaped molecules exhibit new LC phases such as the orthogonal smectic phases with transverse electric polarization [15, 16, 17].

(b) The other type of asymmetric BC molecule has one arm relatively longer than the other arm giving rise to a hockey-stick like shape. In this thesis, we refer to these types of asymmetric BC molecule as bent-core hockey-stick shaped (BCHS) molecules as shown in Figure 3.1a.

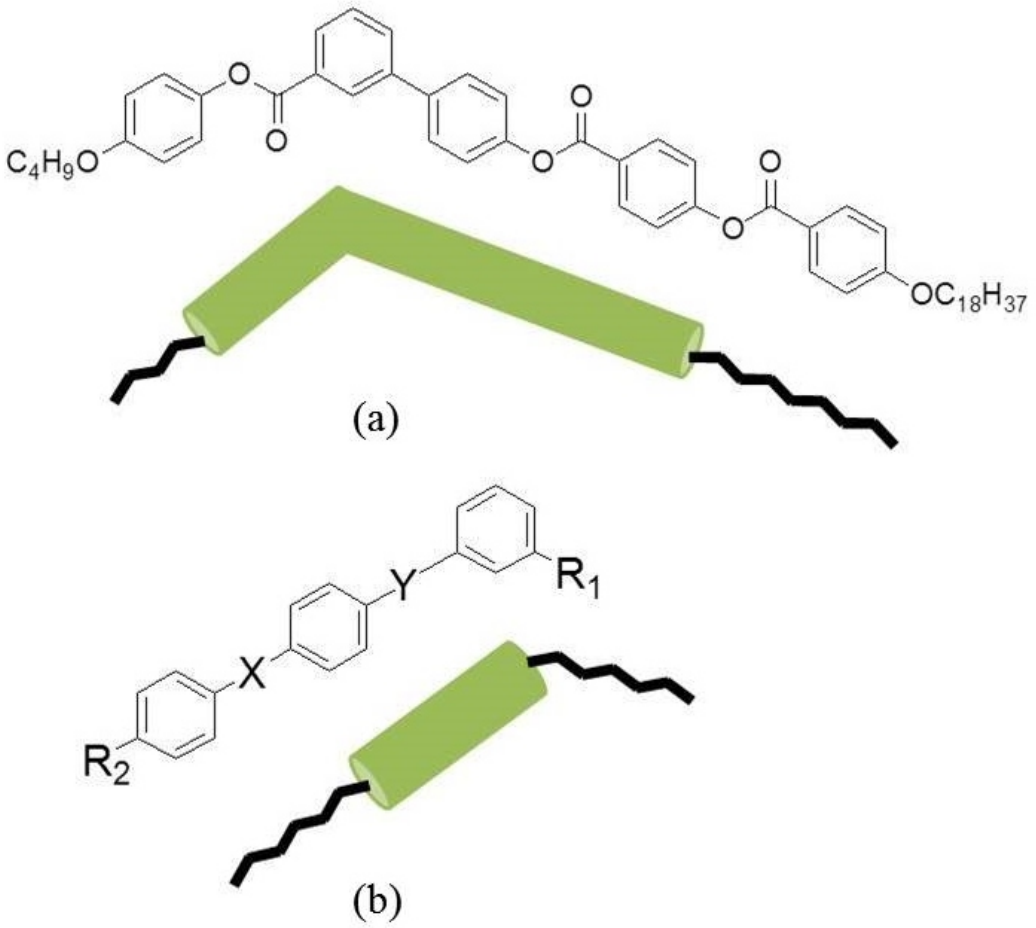

Figure 3.1: The molecular structure of a (a) bent-core hockey-stick (b) a meta hockey-stick shaped molecules.

There are some reports [18, 19, 20] on the phase behavior of another type of molecules which are also termed as hockey-stick shaped molecules. These molecules have a rigid rod-like core and one of the terminal chains are attached at an angle to the long axis of the rod-like core. This can be accomplished by attaching the terminal chain at the meta-position of the terminal benzene ring of the linear core. The meta-position of the terminal chain introduces the bent structure in the molecule as shown in Figure 3.1b. These types of hockey-stick shaped molecules can be termed as meta chain hockey-stick shaped (MCHS) molecules in contrast to the BCHS molecules as discussed above. These two different kinds of asymmetric BCHS molecules are shown in the Figure 3.1. In the present thesis, we will restrict our discussion to only BCHS molecules.

Most of the studies on BC molecules are performed on samples consisting of BC banana-shaped molecules. The BCHS molecules can be considered to have an intermediate shape between the BC banana-shaped and the rod-like molecules as shown in Figure 3.2 [21, 22, 23, 24].

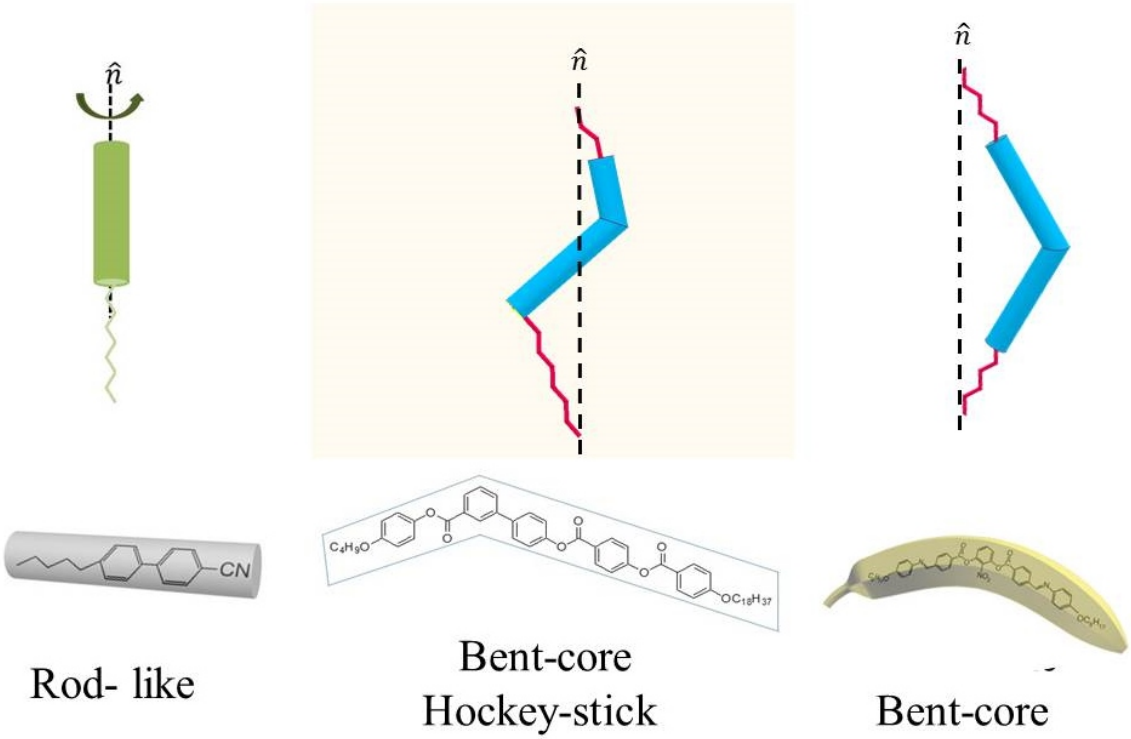

Figure 3.2: Molecular shape of a bent-core hockey-stick shaped molecule lies between a rod-like and a symmetric bent-core banana-shaped molecules.

For rod-like molecules in their smectic C (SmC) phases, the molecules arrange themselves in fluid layers in which the long axes of the molecules are on average aligned at an angle with respect to the layer normal. This tilted organization of the molecules produces a layer spacing smaller than the molecular length. But the molecules within the layers rotate almost freely about their long axes due to their rod-like shape which gives rise to an almost uniaxial local symmetry about the director [25]. On the other hand, for the BC banana-shaped molecules in their tilted smectic phases, the free rotation of the molecules about their long axes are highly hindered due to the strong shape polarity of the molecules. This effect gives rise to the polar order and consequent chiral symmetry breaking in the layers [6]. These BCHS molecules have an intermediate shape between rod-like and symmetric BC banana-shaped molecules. It is interesting to investigate the molecular organization of these BCHS molecules in their tilted smectic phase. There are very few reports on the synthesis of BCHS molecules and their phase behavior. Only a few studies have been carried out on the tilted smectic phases of BCHS molecules [26, 27, 28, 29, 30, 31, 32].

In this cahpter, we will describe our experimental studies on the tilted smectic phase of such compounds. This chapter is divided into two parts: In the first part, we will describe the experimental studies on two LC compounds consisting of BCHS molecules. Whereas, the second part deals with the theoretical model that accounts for the observed mesophases of both compounds. The observed mesophases were characterized using different experimental techniques such as: differential scanning calorimetric (DSC), polarizing optical microscopy (POM), X-ray diffraction (XRD) studies, dielectric constant, and polarization reversal current measurements.

First, we studied the LC compound, which showed two unusual smectic phases between the isotropic liquid and crystal phases. Based on experimental studies, we characterized these phases as pseudo-polar SmC phases because the molecules are tilted at an angle to layer normal and the layers possess an in-plane axial-vector order parameter in addition to the tilt order. In analogy with polar order of BC banana-shaped molecules in the layers of $B2$ phase, here the layers have a pseudo-polar orde even though there is no net electric polarization. We characterized these SmC phases

as pseudo-polar tilted smectic phases with an in-plane axial-vector order parameter in addition to the tilt order. In these phases, the BCHS molecules adopt a zigzag configuration for close packing in the layers. As in a BCHS molecule one rigid arm is relatively shorter than the other arm of the BC molecule, these molecules have head-tail asymmetry. The average orientation direction of the long axes of the BCHS molecules, *i.e.*, the director $\hat{n}$ in a given layer is at an angle with respect to the layer normal $\vec{k}$. As there is no net polarization in the layers, therefore the BCHS molecules in a given smectic layer have equal probability of pointing up and down, *i.e.*, the molecules in the layers align with a head-tail symmetry giving a apolar director $\hat{n}$.

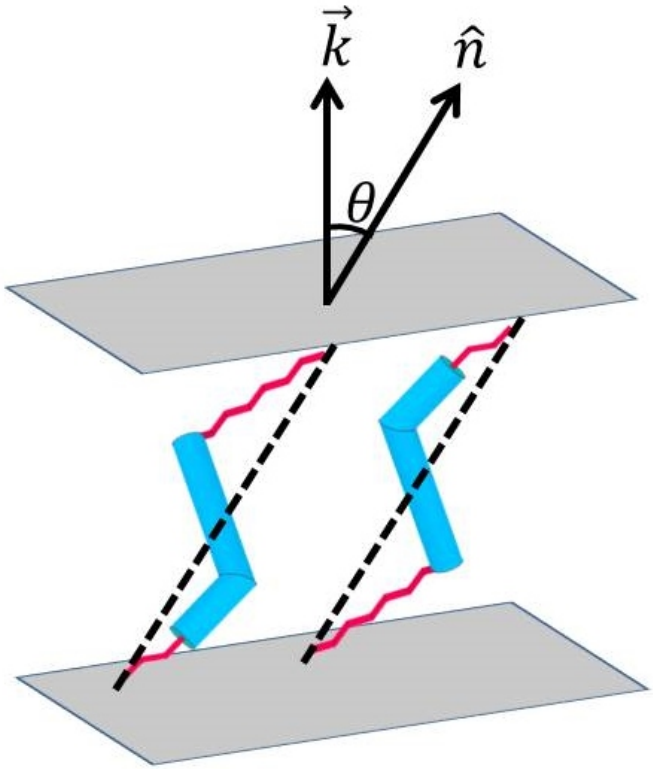

Figure 3.3: The schematic representation of the BCHS molecules having an equal probability of pointing up and down *i.e.*,head-tail asymmetry in a given tilted smectic layer. The dotted line represents the long axis joining both the ends of the molecules.

In addition, the zigzag plane of the molecules in a layer aligns on average parallel to the tilt plane which induce an in-plane axial-vector order parameter ($\vec{\eta}$) in the layers. The layers in these smectic phases have an achiral C_{2h} point symmetry without any spontaneous electric polarization, hence, the name pseudo-polar.

Sample preparation

For the experimental studies, we used both the planar and the homeotropically-aligned samples. Commercially available (Instec Inc.) liquid crystal cells of thickness 5 μm were used for planar-alignment. For the homeotropic-alignment, the LC sample was sandwiched between a clean glass plate and a glass cover-slip. The ODSE coated cells did not give hometropic-alignment for most of these samples.

3.2 Compound 4OC18

In this section, we will discuss about a compound 4-n butyloxyphenyl-4-(4-n-octadecyloxy benzoyloxy-4-benzoyloxy) biphenyl-3-carboxylate. This compound is abbreviated as 4OC18 in this thesis. The synthesis and the preliminary investigations on the compound 4OC18 had been studied earlier [28]. The molecular structure of compound 4OC18 and the phase sequence on cooling the sample from the isotropic phase is shown in Figure 3.4.

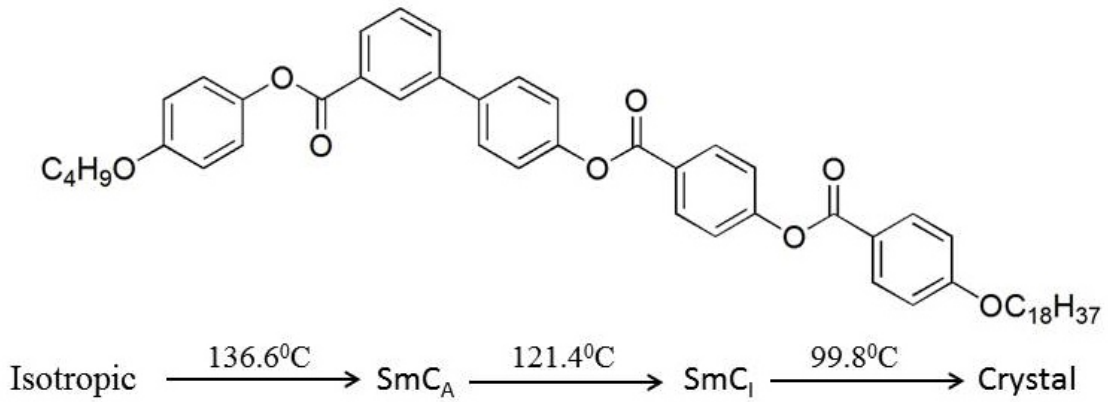

Figure 3.4: Molecular structure of the compound 4OC18 and phase sequence of the sample on cooling from the isotropic phase. The transition temperatures were detected in DSC thermogram.

The minimized energy configuration of 4OC18 molecule is shown in Figure 3.5. The molecular length was measured end to end in minimized energy configuration

using Chem Draw software. The end to end estimated molecular length of compound 4OC18 is about 53 Å.

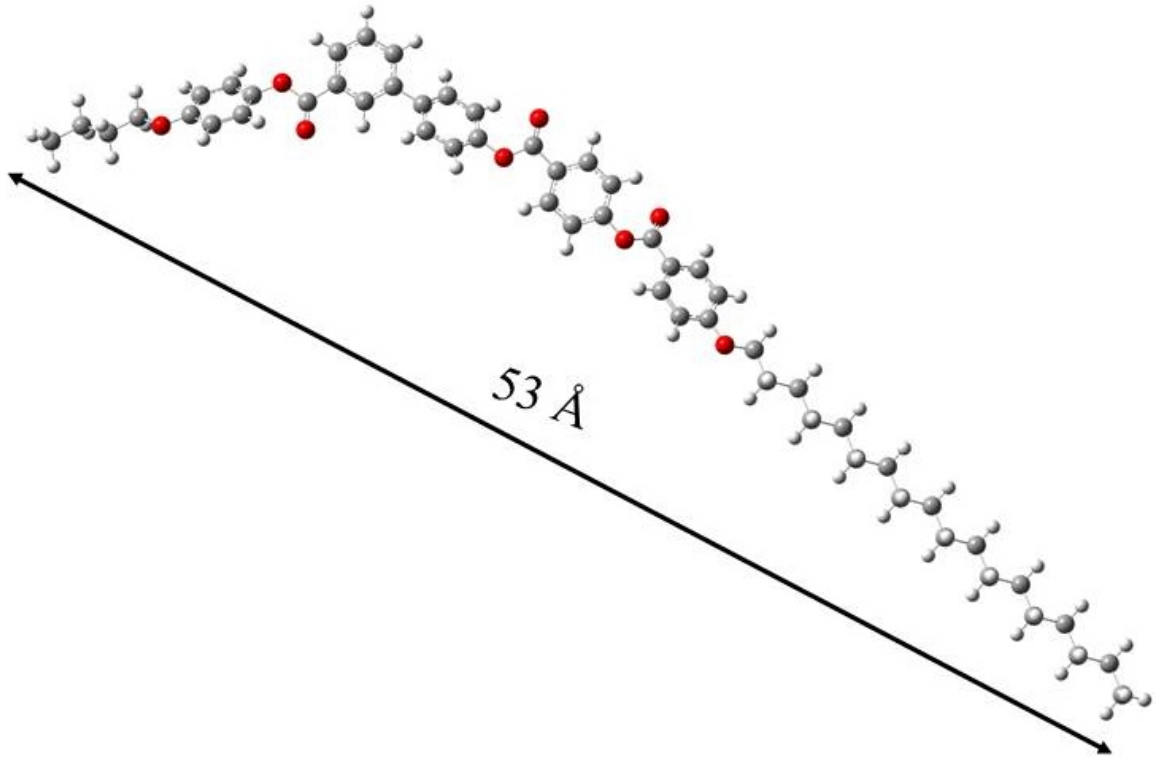

Figure 3.5: The molecular structure of the compound 4OC18 in the minimized energy.

3.2.1 Differential Scanning Calorimetry Investigations

The differential scanning calorimetry (DSC) studies were performed on METLLER Toledo DSC with a fixed heating and cooling rate. The DSC thermogram for compound 4OC18 was taken at a cooling and heating rate of 3 ^{0}C/min as shown in Figure 3.6. The DSC thermogram clearly shows the existence of two mesophases between the isotropic liquid and crystal phases. We designate the high and low-temperature mesophases as SmC_A and SmC_I phases, respectively. The SmC phase stands for the tilted smectic phase and the subscript A denotes the anticlinic arrangement of molecules in successive layers. The subscript I stands for the lower-temperature phase denotes an intermediate arrangement of molecules in successive layers with the azimuthal angle difference in tilt directions between 0 and π. This phase is analogous to the ferrielectric phases exhibited by rod-like chiral molecules. A similar intermediate azimuthal angle differ-

ence in the tilt direction was also observed for some rod-like chiral molecules in their ferrielectric phases [33, 34, 35, 36]. However, it should be noted here that for the studied compounds in this chapter, the layers in the observed mesophases do not possess any net electric polarization and the molecules are achiral in nature. A small enthalpy change was observed across the transition from the higher-temperature SmC_A to the lower-temperature SmC_I phase. The small enthalpy change (0.07 kJ/mole) indicates a very weak first-order phase transition between these phases. The inset of Figure 3.6 shows a clear phase transition from the SmC_A to the SmC_I phase on cooling and heating of the sample.

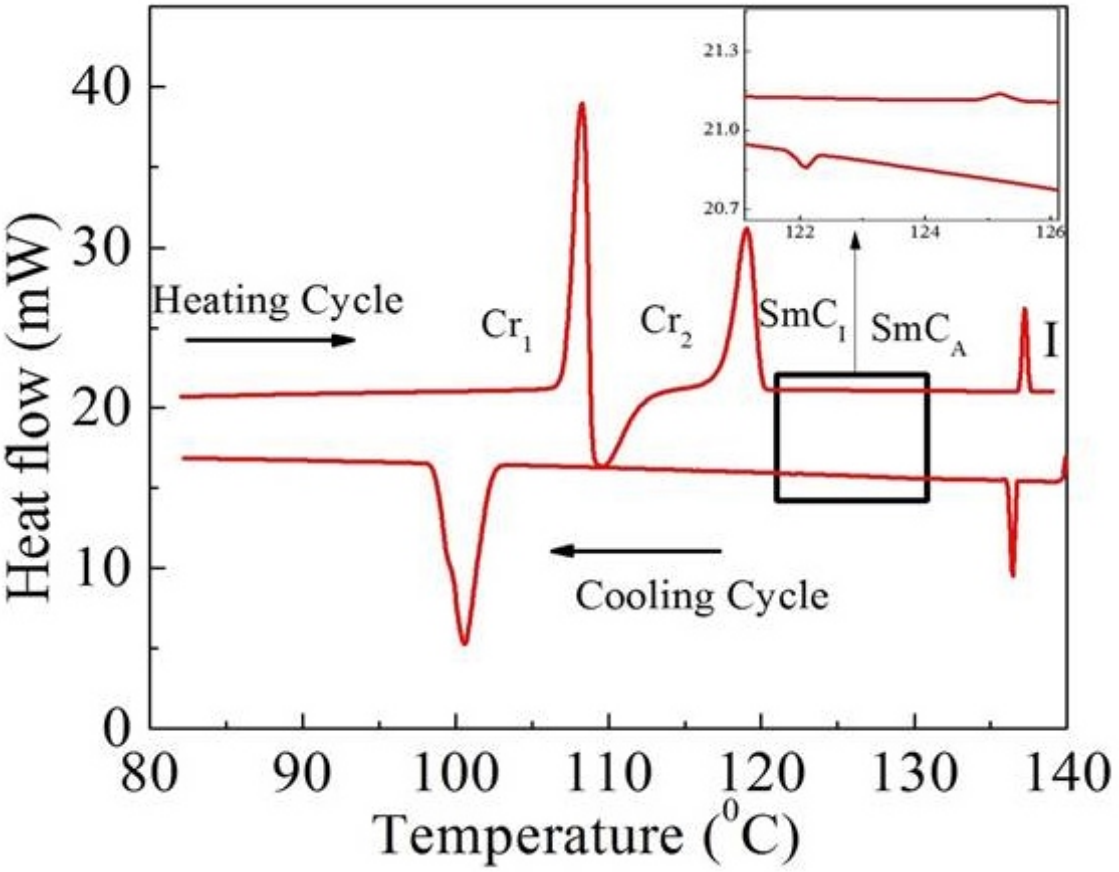

Figure 3.6: DSC thermogram of the compound 4OC18 on heating and cooling at a rate of 3 ^{0}C/min. The inset shows a clear transition between the SmC_A and SmC_I phases on heating and cooling cycles.

3.2.2 X-ray Diffraction Investigations

The X-ray diffraction (XRD) studies were carried out on an unoriented sample filled in the Lindemann capillary tubes (outer diameter about 1 mm) while cooling the sample from the isotropic phase. The layer spacing for the observed mesophases were calculated from the XRD data using Bragg's diffraction law:

$$2d \sin\theta = n\lambda,$$

where d is the layer spacing, λ (1.54 Å) is the wavelength of the incident X-ray beam, and θ is the Bragg's angle and n is an integer.

The XRD intensity profile as a function of wave-vector for compound 4OC18 is shown in Figure 3.7. For the compound 4OC18, we observed three sharp small-angle peaks with the ratio of wave vectors as 1:2:3 in addition to a diffusive peak in the wide-angle region. The presence of the sharp small-angle peaks with the wave-vector ratio as 1:2:3 indicates lamellar order in both the observed mesophases. The effective layer spacing for the higher-temperature SmC_A and lower-temperature SmC_I phases are 42.6 Å and 43.1 Å, respectively. The presence of the diffusive peak in the wide-angle region in addition to the sharp peak in the small-angle region provide the evidence of the fluid lamellar structure. The diffusive peak in a wide-angle region has d-spacing as 4.6 Å in both the smectic phases. The d-spacing corresponding to the wide-angle peak typically gives average lateral separation between the molecules in the layer.

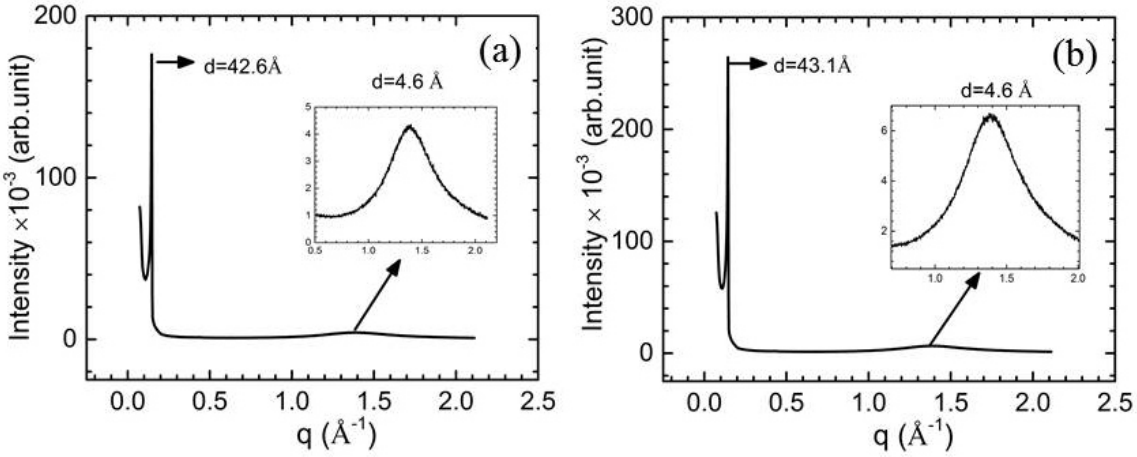

Figure 3.7: The XRD intensity profile for the sample in (a) the SmC_A phase at 124 ^{0}C and (b) the SmC_I phase at 116 ^{0}C on cooling from the isotropic phase. The insets show the magnified view of the diffusive peak in the wide-angle region.

For the investigated compound, the layer spacing in both the observed mesophases are smaller than the molecular length (53 Å estimated by the molecular formula) indicating that the molecules are tilted with respect to the layer normal. We also studied layer spacing variation as a function of temperature as shown in the Figure 3.8.

Peak Fitting

To calculate the layer spacing variation as a function of the temperature, we have fitted the sharp peaks in the small-angle region obtained in the XRD data using origin Pro 2016. We used a peak analyzer for the peak fitting. We followed a few steps to fit the peaks using peak analyzer as given below:

1. Created the baseline using the manual option.
2. Then chose line mode as adjacent-averaging smoothing by adjusting some parameters.
3. Created baseline using a line interpolation method.
4. Then subtracted the baseline.
5. We found the peaks by using a quick peak option in origin.

The layer spacing gradually increased with decreasing the temperature from the

higher-temperature SmC_A to the lower-temperature SmC_I phase. The slight increase in the layer spacing can be attributed due to an increase in the chain length of the molecules on decreasing temperature, as the molecular chains get straightened on lowering the temperature.

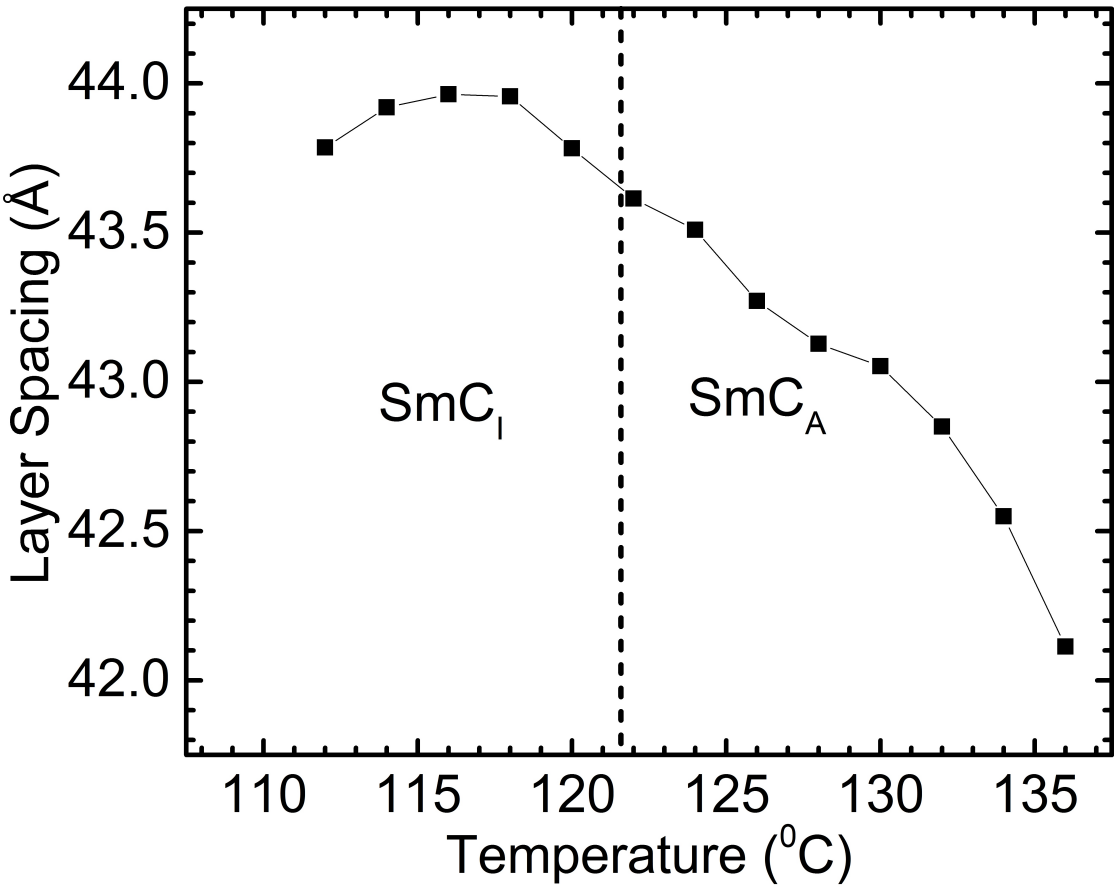

Figure 3.8: The variation of layer spacing with temperature from the SmC_A phase to the SmC_I phase. The vertical dotted line shows the transition between the observed smectic mesophases.

To investigate the morphology of the lower-temperature SmC_I phase of the compound 4OC18, we performed cryo-SEM imaging as shown in Figure 3.9. These studies also revealed the layer structure in the SmC_I phase as observed in XRD studies. However, cryo-SEM studies were not able to resolve the molecular organization in the layers of the SmC_I phase.

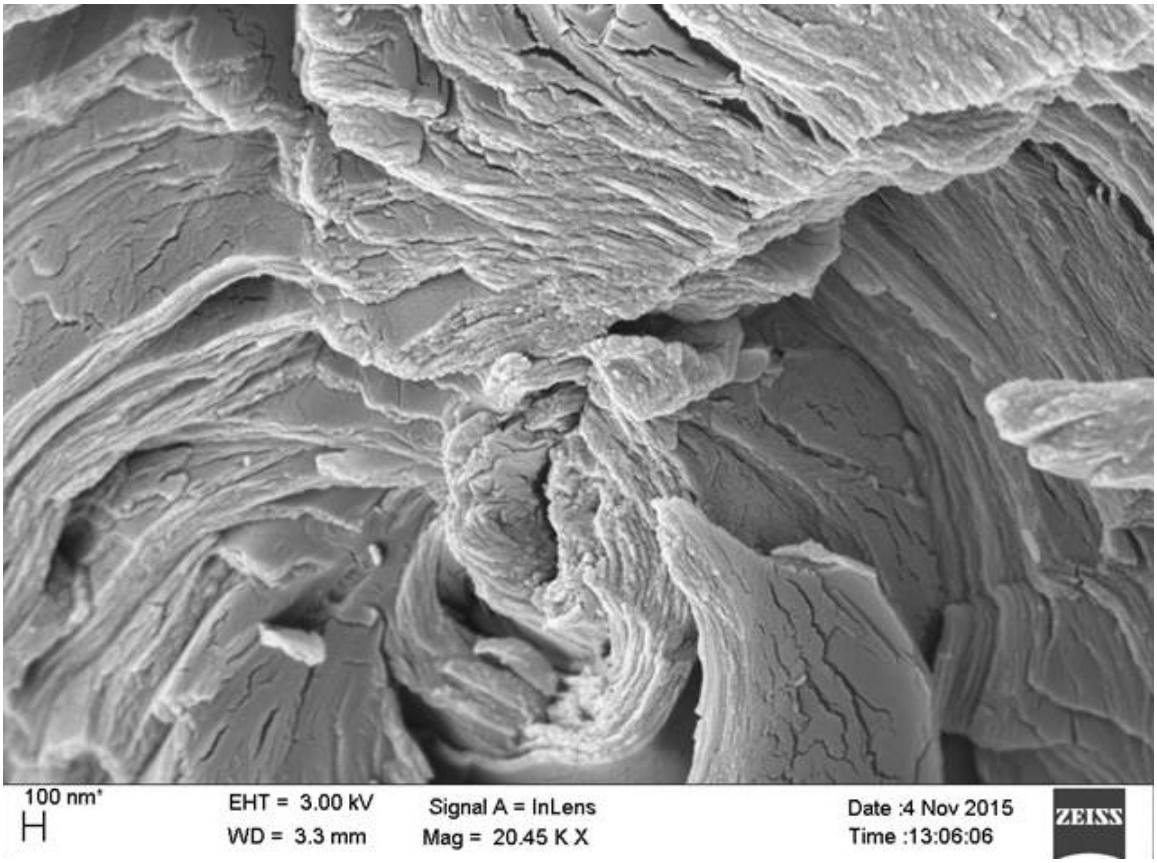

Figure 3.9: The cryo-SEM morphology of the lower-temperature SmC_I.

3.2.3 Polarizing Optical Microscopy Investigations

The polarizing optical microscopy (POM) observations between crossed polarizers were carried out for both planar as well as the homeotropic alignment of the samples. The POM textures of the samples were investigated using OLYMPUS BX50 microscope. The POM textures of the samples were captured using OLYMPUS camera DP12 at 20X magnification. The sample was loaded onto the hot stage LINKAM (LTS420E) which was connected to a temperature controller (LINKAM T95HS) with a resolution of 0.1 ^{0}C. The sample was slowly cooled from the isotropic phase to the higher-temperature SmC_A phase for POM studies.

For a homeotropically-aligned sample, a schlieren texture (see Figure 3.10a) with half-and unit-strength defects was observed in the higher-temperature SmC_A phase. The existence of the schlieren texture represents the tilt organization of the molecules in

the layers. The tilted nature of the molecules was also confirmed in the XRD studies. The presence of half-and-unit strength defects in the schlieren texture revealed the tilt organization of the molecules in the successive layers are opposite. The opposite molecular tilt in the successive layers showed an anticlinic arrangement of the molecules in the successive layers in the higher-temperature SmC_A phase [37, 38]. On further cooling, the sample undergoes a phase transition to the lower-temperature SmC_I phase, again a schlieren texture was observed with hazy defects. It can be clearly seen from Figure 3.10c that the defect centers were less distinct in the lower-temperature SmC_I phase.

For the planar-alignment of the sample, commercially available PI coated liquid crystal cells of thickness 5 μm were investigated between crossed polarizers. For the planar-aligned sample, a focal-conic fan texture was observed in the SmC_A phase as shown in Figure 3.10b. The fan texture showed typical lamellar order in the SmC_A phase. The extinction brushes in the focal-conic fan texture appeared parallel to the layer normal when it is parallel/perpendicular to the polarizer, indicating one of the optic axes is parallel to the layer normal as expected in the anticlinic SmC_A phase. On further cooling of the sample, a transition takes place from the SmC_A phase to the SmC_I phase around 122 ^{0}C. In the SmC_I phase, a large number of irregular bands appeared parallel to the smectic layers (see Figure 3.10d). The presence of irregular bands parallel to the smectic layers made focal-conic fans less visible. The irregular bands in the fans indicate the coexistence of different degenrate structures in the lower-temperature SmC_I phase.

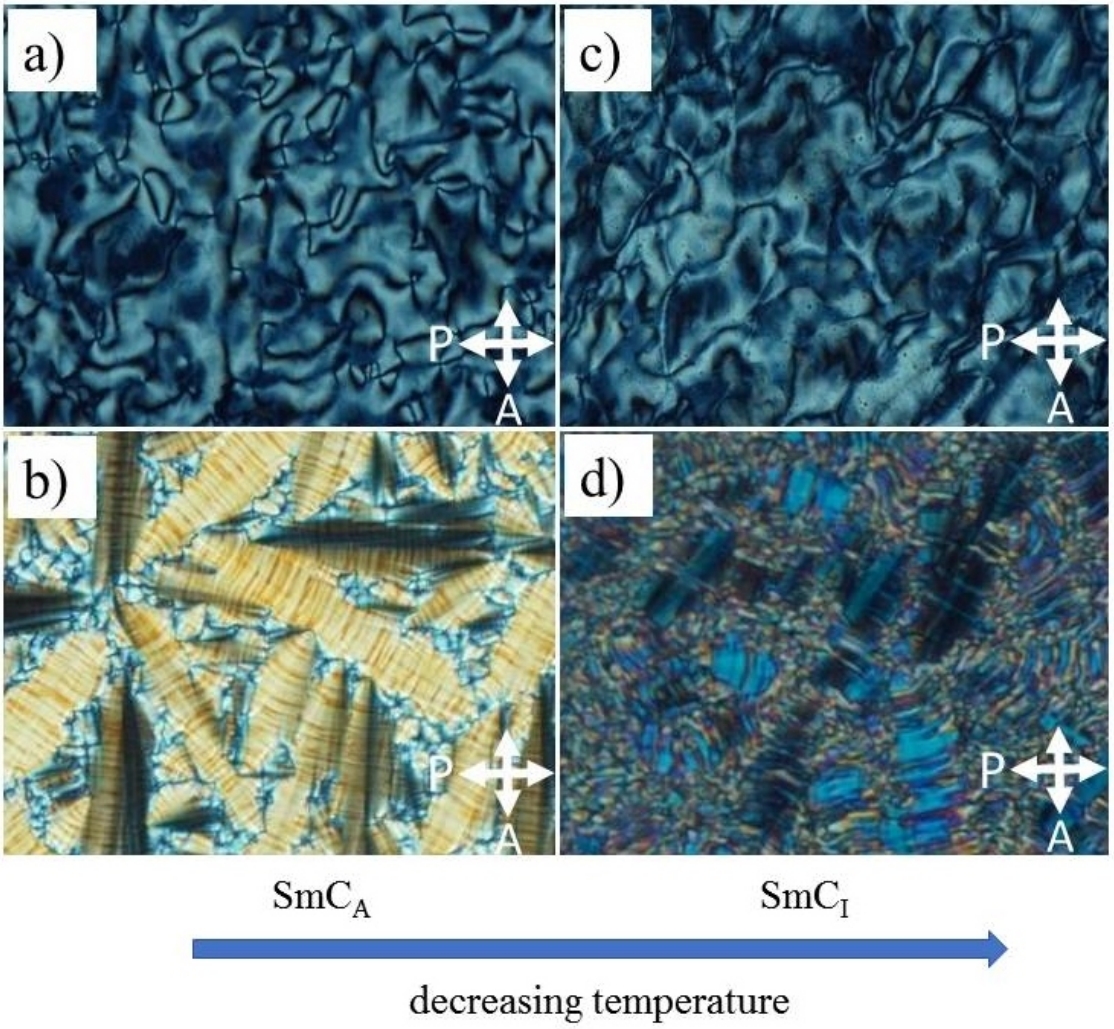

Figure 3.10: The POM textures of the compound 4OC18 in (a) the SmC_A phase at 125 ^{0}C for a homeotropically, (b) a planar-aligned sample and in the SmC_I phase at 115 ^{0}C for (c) a homeotropically (d) planar-aligned sample.

3.2.4 Polarization Switching Current Measurements

To investigate the existence of layer polarization, a planar-aligned sample of thickness 5 μm was used for the polarization switching current measurements under the application of an applied AC electric field. The polarization switching current measurements were carried out on a home-built experimental setup which is explained in section 2.11. We used a triangular wave voltage technique to study the electric polarization state of the smectic layers of the planar-aligned sample [39]. During the experiments, the temperature of the sample was controlled by a temperature controller METLLER

(FP80) with a temperature resolution of 0.1 ^{0}C. The sample was slowly cooled from the isotropic phase between the crossed polarizers to the higher-temperature SmC_A phase in the presence of a low-frequency electric field in order to get a better alignment. The measurements were taken after achieving the stabilized temperature. The current response of a planar-aligned sample was recorded by measuring the voltage drop across a known resistor (1 $k\Omega$) under the application of a triangular wave voltage of a given amplitude and a frequency. The resistor was connected in series with the liquid crystal sample.

The current response of the LC sample in the SmC_A phase is shown in Figure 3.11a. No polarization reversal current peaks were observed in the current response indicating the absence of net electric polarization in the layers in the SmC_A phase. Upon further cooling, the sample from the higher-temperature SmC_A to the lower-temperature SmC_I phase between the crossed polarizers, a large number of the irregular bands were observed under POM as shown in Figure 3.10d. The similar experimental studies were carried out in the lower-temperature SmC_I phase to detect the current response of the sample. The absence of polarization reversal current peaks (Figure 3.11b) revealed the lack of net electric polarization in the layers in the SmC_I phase. Thus, the layers appeared to be non-polar in both of these smectic phases.

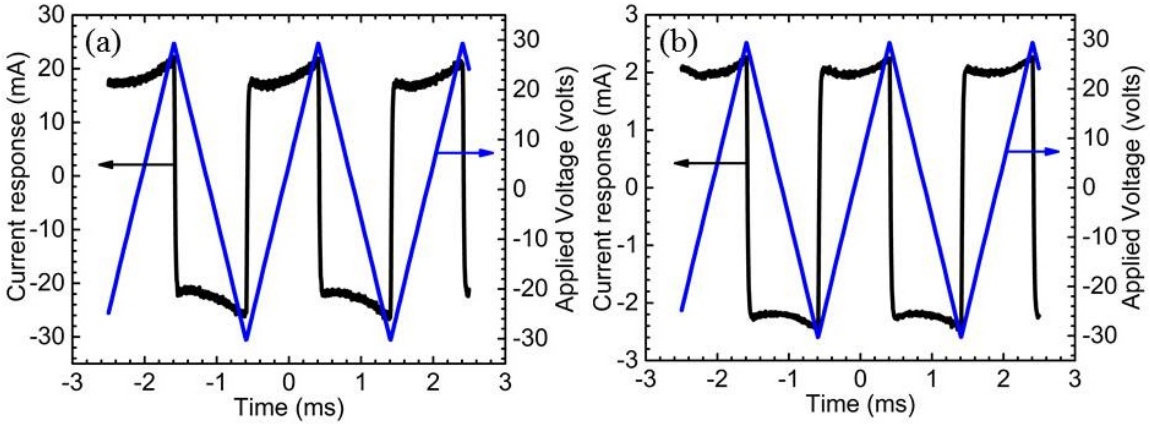

Figure 3.11: The current response of the sample under the application of a triangular wave voltage (30 V, 500 Hz) in (a) the SmC_A phase at 130 ^{0}C and (b) the SmC_I phase at 116 ^{0}C .

3.3 Compound A14

In this section, we studied another azo substitutred compound 4-(((3-((4-(n-Decyloxy) benzoyl)oxy)phenyl)imino)methyl)phenyl4-(-(4-(n-tetradecyloxy)phenyl)diazenyl) benzoate. This compound also consisting of BCHS molecules. This compound is denoted as A14 for further discussion in the present thesis. This azo-substituted compound is the 14^{th} homologue of a series which showed similar phase behavior as of that compound 4OC18 discussed in subsection 3.2.1. We also studied the other homologue of the same series and found that compounds with chain length n >10 showed the same phase behavior as that of compounds 4OC18. Whereas, for n <10 compounds showed different phase behavior. The phase behavior of 9^{th} homologue of the same series will be discussed in chapter 5. The molecular structure of compound A14 and the phase sequence on cooling the sample from the isotropic phase are shown in Figure 3.12.

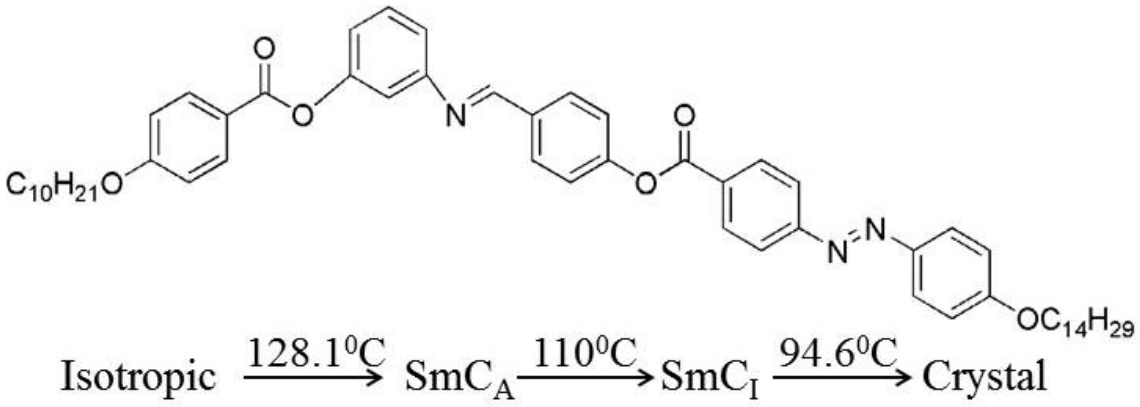

Figure 3.12: The molecular structure of the compound A14 and phase sequence on cooling the sample from the isotropic phase.

Here, again one arm of the molecule is relatively shorter than the other arm of the BC molecule. The estimated end to end molecular length of compound A14 from the minimized energy configuration is about 53 Å. The molecular structure of compound A14 in the minimized energy configuration is shown in Figure 3.13.

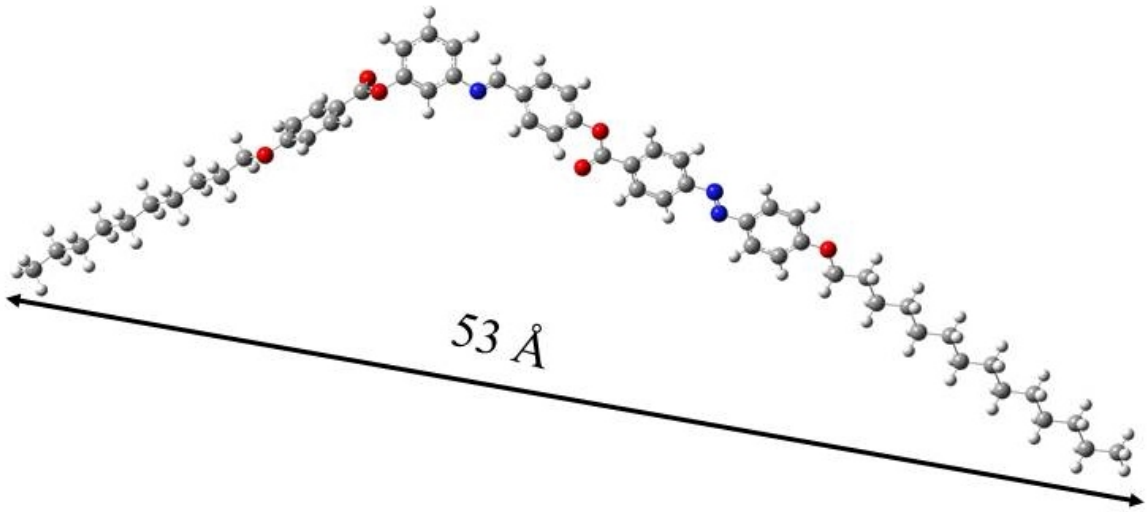

Figure 3.13: The molecular structure of compound A14 in the minimized energy configuration.

3.3.1 Differential Scanning Calorimetry Investigations

The DSC thermogram of the compound A14 on cooling and heating at a fixed rate of 3 ^{0}C/min is shown in Figure 3.14. Two mesophases were observed between the isotropic liquid and crystal phases in the DSC thermogram. Again, a samll enthalpy change (0.11 kJ/mol) was observed on the transition from the higher-temperature SmC_A phase to the lower-temperature SmC_I phase. The inset of Figure 3.14 shows the weak transition peaks between the observed mesophases on heating and cooling the sample. This compound also showed the same phase behavior as of that the compound 4OC18, and the observed mesophases for compound A14 were also denoted as SmC_A and SmC_I phases for the higher-temperature and the lower-temperature, respectively.

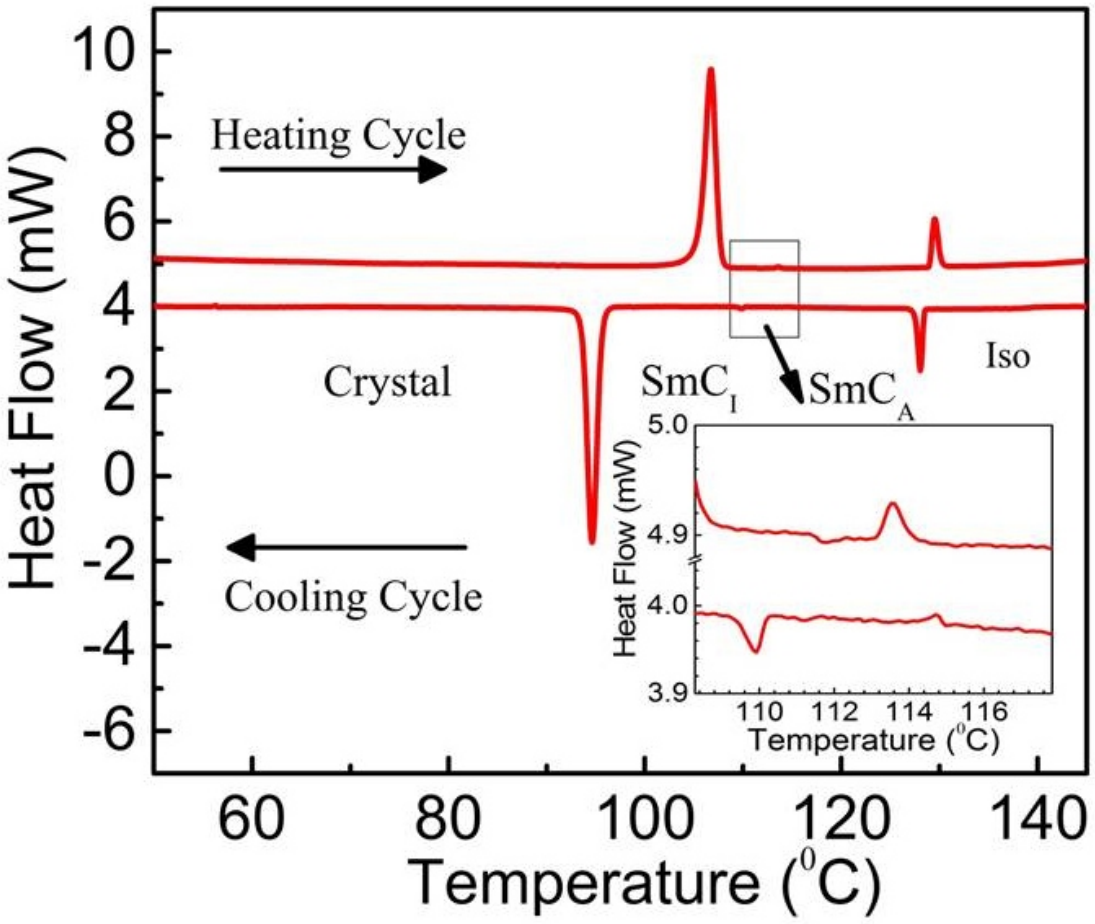

Figure 3.14: The DSC thermogram on heating and cooling the sample at a rate of 3 ^{0}C/min showing the transition peaks. The inset shows the weak first-order transition peak between the observed SmC phases.

3.3.2 X-ray Diffraction Investigations

The XRD studies were carried out for compound A14 on cooling the sample from the isotropic phase to the respective phases with an exposure time of about 30 minutes in each phase as shown in Figure 3.15. In the small-angle region, sharp peaks were observed in both the mesophases in addition to the diffusive peak in the wide-angle region. The sharp peaks in the small-angle region give the layer spacing of the SmC_A phase and the SmC_I phase as 44.3 Å and 46.1 Å, respectively. The presence of a diffusive peak in the wide-angle region is the characteristic of the fluid lamellar smectic phases. In the wide-angle region, the diffusive peaks were observed with d-spacing 4.4 Å and 4.5 Å in both the smectic phases, respectively.

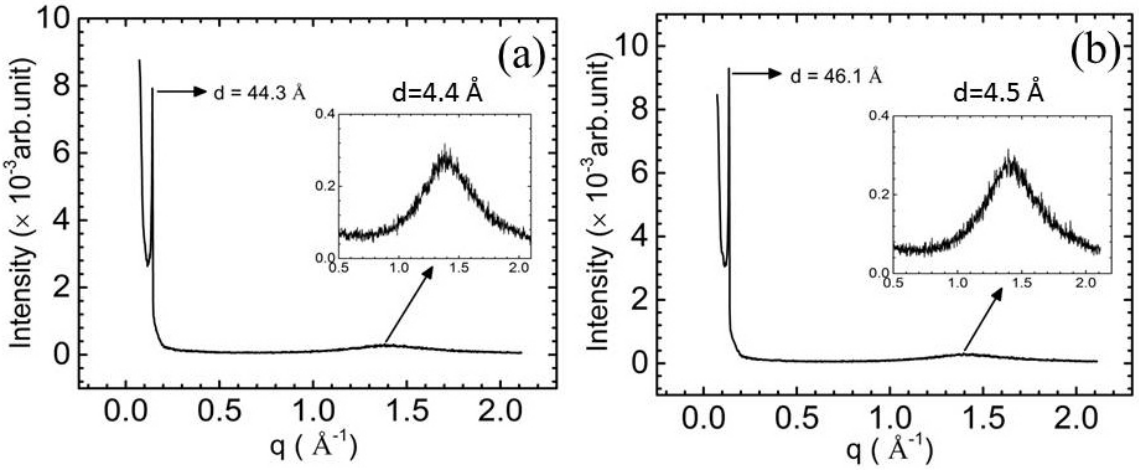

Figure 3.15: The X-ray diffraction intensity profile in (a) the SmC_A phase with a layer spacing 44.3 Å at 125 ^{0}C and (b) the SmC_I phase with layer spacing 46.1 Å at 106 ^{0}C.

We also studied the variation of the layer spacing (tilt angle) as a function of temperature as shown in Figure 3.16. A gradual increase (decrease) in the layer spacing (tilt angle) was observed on decreasing the temperature. A small jump in the layer spacing (tilt angle) was observed at the transition from the higher-temperature SmC_A phase to the lower-temperature SmC_I phase. The slight increase in the layer spacing in the SmC_I phase can be accounted for by the straightening of the terminal chain with decreasing the temperature. The layer spacing for compound A14 varied similarly to the compound 4OC18 as a function of temperature as discussed in subsection 3.2.2.

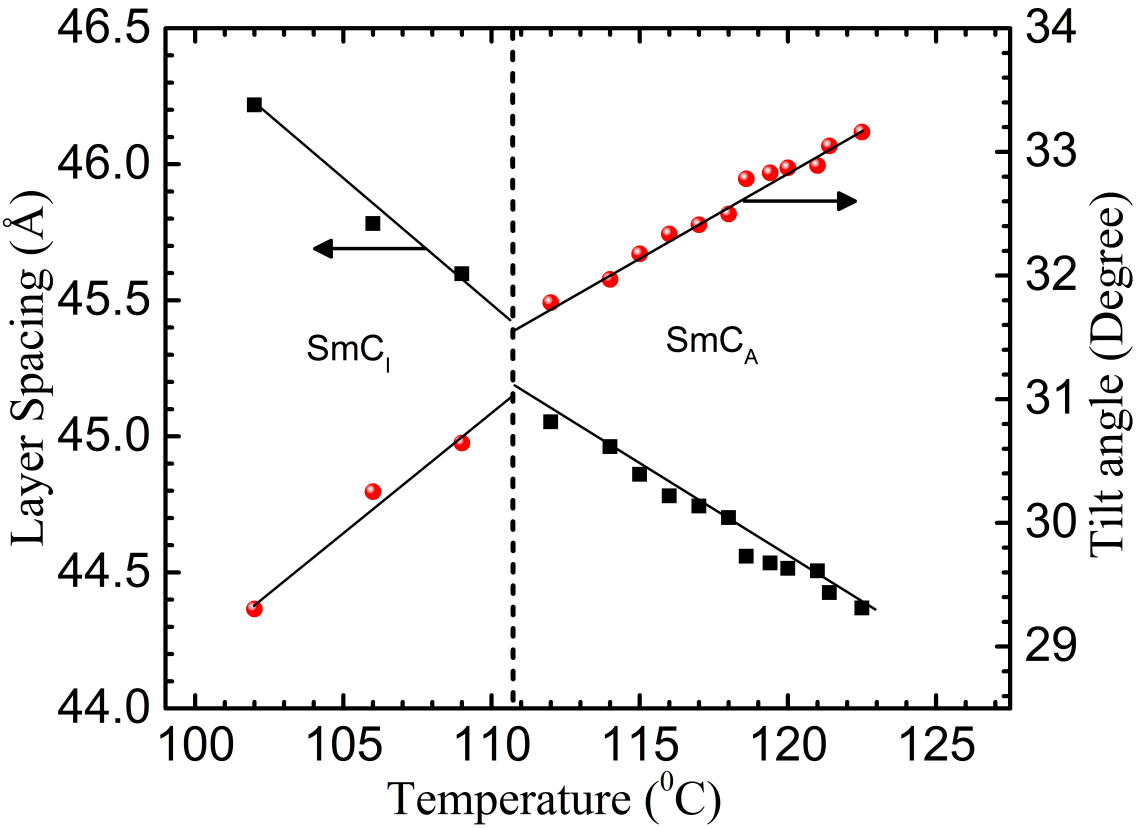

Figure 3.16: The variation of the layer spacing and the calculated tilt angle as a function of temperature. The dashed line indicates the transition temperature between the observed SmC phases and the solid lines through the data points are a guide to the eye. The black squares and red circles data points represent layer spacing and tilt angle respectively.

3.3.3 Polarizing Optical Microscopy Investigations

A birefringent schlieren texture with the existence of half-and unit-strength defects was observed for a homeotropically-aligned sample just below the transition temperature on cooling from the isotropic phase to the SmC_A phase as shown in Figure 3.17a. The appearance of schlieren texture confirmed the tilted nature of the molecules in the smectic layers which corroborated with XRD studies. The presence of half-strength defects in the schlieren texture indicate the anticlinic arrangement of molecules in the successive layers in the higher-temperature SmC_A phase as the half-strength defects in the schlieren texture appear due to the existence of dispiration defects in the anticlinic SmC phase. At lower-temperatures in the SmC_A phase, the schlieren texture acquired

a birefringence color and defect network become less visible (Figure 3.17b) due to an increase in the birefringence of the sample. On further cooling, the sample goes to the lower-temperature SmC_I phase. Here again, a birefringent schlieren texture (Figure 3.17c) was observed for a homeotropically-aligned sample with the existence of some domain structures separated by walls. The presence of different domains indicated the coexistence of different degenerate structures in this phase.

For a planar-aligned sample, a batonnet growth of the SmC_A phase was observed on cooling the sample from the isotropic phase at a rate of 1 ^{0}C/min between crossed polarizers as shown in Figure 3.17d. On further cooling of the sample, the batonnet growth gives rise to a clear focal-conic fan texture (Figure 3.17e), typically observed for anticlinic SmC_A phase at around 120 ^{0}C. A transition from the SmC_A to the SmC_I phase takes place around 110 ^{0}C. In the SmC_I phase, a large number of irregular bands appeared parallel to the layers (see Figure 3.17f) for the planar-aligned sample. The presence of irregular bands made the focal-conic fans less visible in the SmC_I phase. The presence of a large number of irregular bands again indicates the existence of different stable degenerate states in the SmC_I phase.

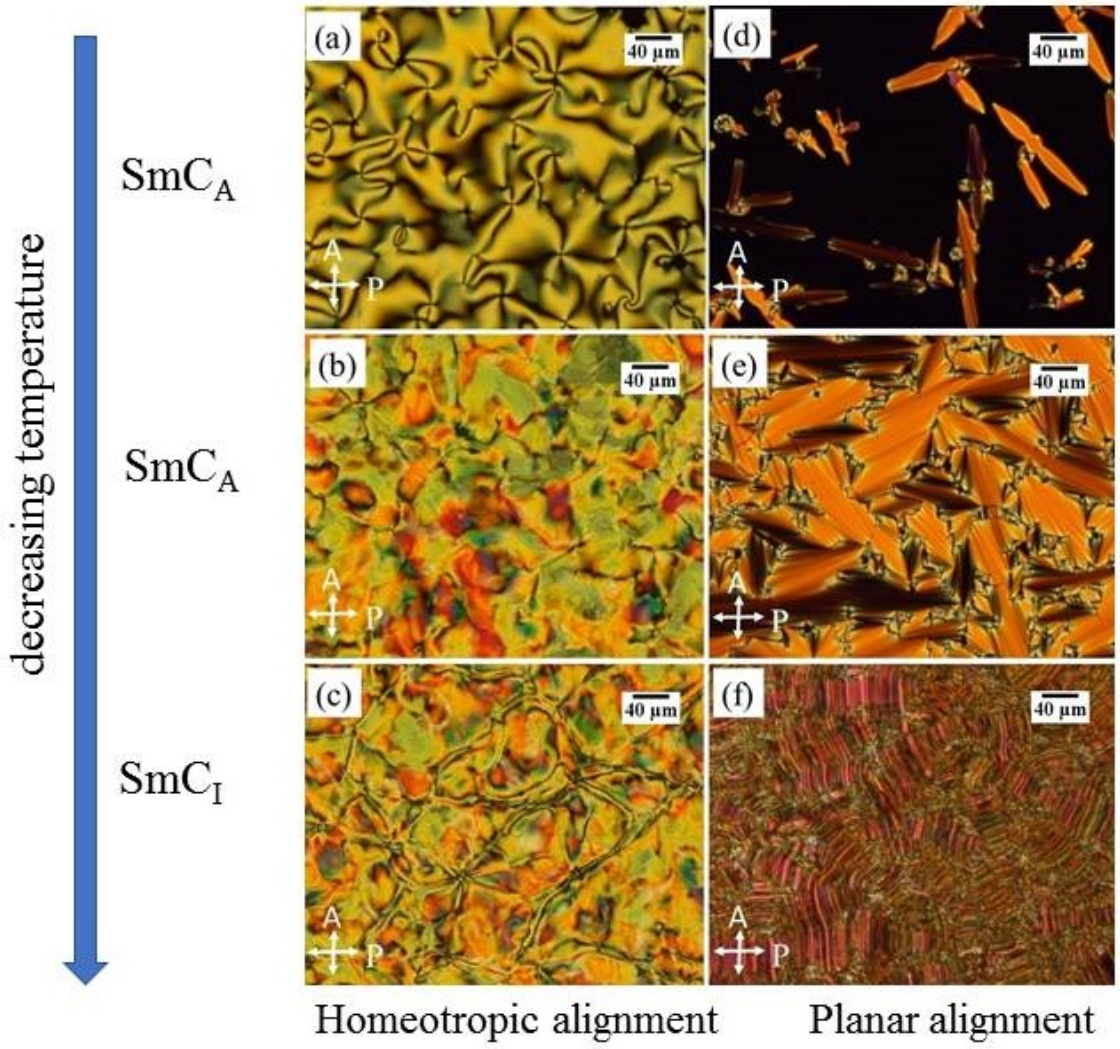

v

Figure 3.17: Polarizing optical microscopy textures (left column) for a homeotropically-aligned sample (a) a schlieren texture with unit- and half-strength defects just below the clearing temperature in the SmC_A phase (b) at lower-temperature in the SmC_A phase and (c) in the SmC_I phase. Right column, for a planar-aligned sample (d) a smectic batonnet growth just below the clearing temperature in the SmC_A phase (e) a completely grown focal-conic fans texture in the SmC_A phase (f) irregular band texture in the SmC_I phase.

For the compound A14, we also measured the change in the average transmitted intensity of the planar-aligned sample between crossed polarizers as a function of temperature. The variation of the average transmitted intensity as a function of temperature on cooling the sample from the isotropic phase is shown in Figure 3.18. The POM images were captured after stabilizing the temperature of the studied sample.

To calculate the average transmitted intensity, the POM images were captured at a constant interval of temperature. We used a red filter of wavelength 650 nm to avoid the color effects of the observed texture in both the mesophases. The average transmitted intensity was extracted from the POM images by averaging over the pixels using a MATLAB program. While capturing the POM images, the temperature of the sample was controlled by a temperature controller METLLER FP80 with a resolution of 0.1 ^{0}C.

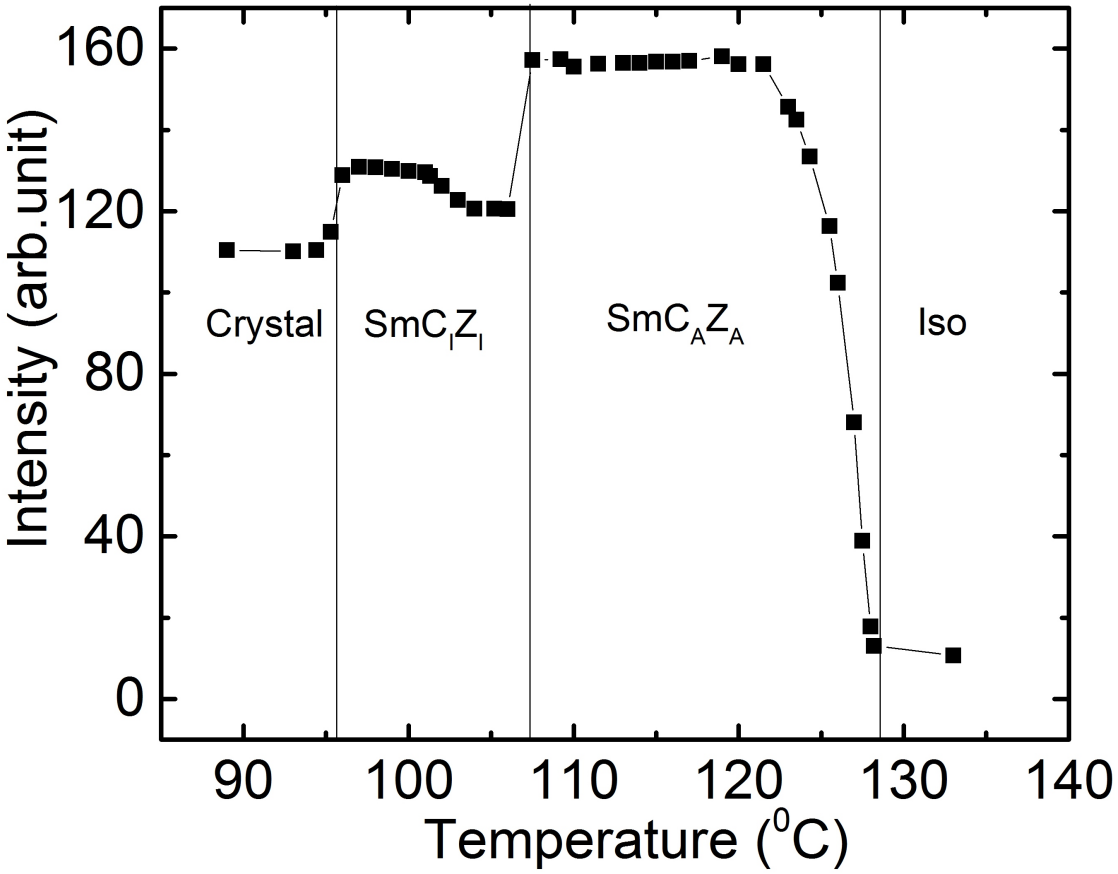

Figure 3.18: The variation of average transmitted intensity with the temperature of a planar-aligned sample of thickness $5\mu m$ between crossed polarizers.

The transition between different mesophases could be clearly detected from the variation of the average transmitted intensity with decreasing temperature. At the transition from the isotropic to the SmC_A phase, the intensity increased sharply due to the increase in the birefringence of the sample below the transition temperature and saturated at lower-temperatures in the SmC_A phase. At the transition point from the SmC_A to the SmC_I phase, a sharp decrease in the intensity was observed due to the

growth of irregular bands in the SmC_I phase. As some amount of light was scattered from the irregular band structure, the intensity decreases in the lower-temperature SmC_I phase.

3.3.4 Polarization Switching Current Measurements

The polarization switching current measurements were carried out for compound A14 to study the polarization state of the smectic layers in both the observed mesophases. The sample was cooled from the isotropic phase to the higher-temperature SmC_A phase at a rate of 3 ^{0}C/min in the presence of a low-frequency electric field. Figure 3.19a shows the current response in the higher-temperature SmC_A phase. The absence of polarization reversal current peaks indicated the absence of net electric polarization in the smectic layers in the SmC_A phase. Similar experiments were carried out in the lower-temperature SmC_I phase (see Figure 3.19b). Similar to compound 4OC18, no polarization peaks were observed in the current response of the sample in the lower-temperature SmC_I phase. The absence of the current reversal peaks in the response indicated the absence of net electric polarization in the layers. Therefore, in both the tilted smectic phases of compound A14, we found an absence of net electric polarization in the layers.

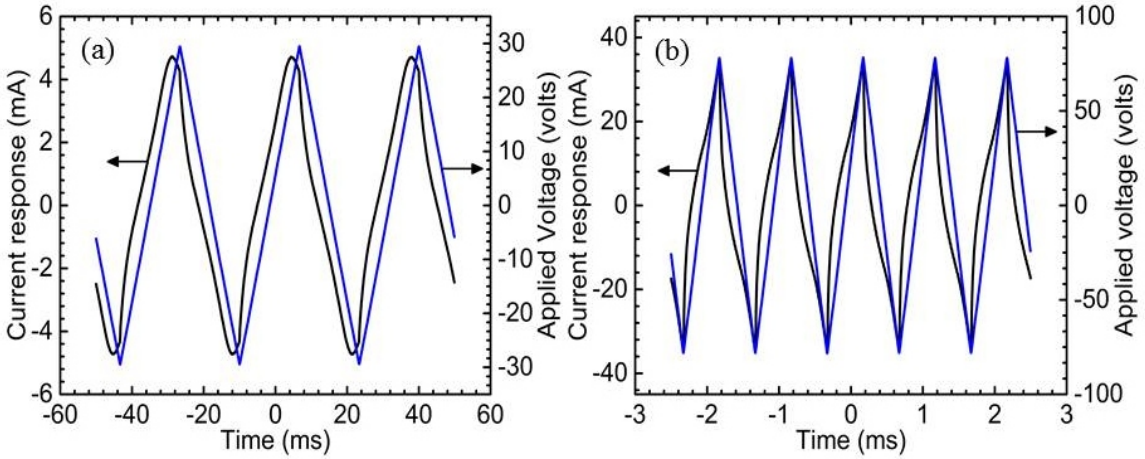

Figure 3.19: The current response of the compound A14 under the application of triangular wave voltage in (a) the SmC_A phase (29 V, 50 Hz) at 120 ^{0}C and (b) the SmC_I phase (78 V, 200 Hz) at 102 ^{0}C on cooling from the isotropic phase.

Thus, the polarization switching current measurements showed that the layers in both the observed mesophases d not possess any net electric polarization. However, in spite of the absence of layer polarization, some remarkable electro-optic effects were observed for both compounds under the application of an AC electric field in both of these smectic phases. We will explain the field effects on the observed mesophases in chapter 4 Based on our experimental results, we present a theoretical model in the next section to account for the tilted smectic phases.

3.4 Theoretical Model

Both the studied compounds showed a similar phase behavior indicating that the observed mesophases are more generic phases exhibited by BCHS molecules. In this section, we will discuss the theoretical model to explain the molecular organization in the observed tilted smectic phases. First, we defined the order parameters in the observed tilted smectic phase.

3.4.1 Order parameters

We defined the long axis as the line joining both the ends of the BCHS molecules. In the tilted smectic phases, the BCHS molecules aligned with head-tail symmetry, *i.e.*, asymmetric BCHS molecules in a tilted smectic layer point in the opposite direction with equal probability as discussed in section 3.1. The average orientation direction of the long axes of the BCHS molecules, *i.e.*, the director $\hat{n}$ in a given layer is at an angle with respect to the layer normal $\vec{k}$. The molecular organization of BCHS molecules in the tilted smectic phases can defined by two order parameters: tilt order parameter $\vec{\xi}$ and orientational order parameter $\vec{\eta}$ as shown in Figure 3.20.

The tilt order of director $\hat{n}_i$ in a given layer can be described by an axial-vector $\vec{\xi}$ which is given by

$$\vec{\xi} = (\hat{k} \cdot \hat{n})(\hat{k} \times \hat{n})$$

where the unit vectors $\hat{k}$ and $\hat{n}$ denote the layer normal and average orientation direction of the long axes of the molecules, respectively [40]. It should be noted here that the c-vector $\vec{c}$ is perpendicular to the tilt orderparameter $\vec{\xi}$ in a given layer. Here, we assume the layer normal along the Z-axis. Therefore, the tilt order parameter is given by

$$\vec{\xi_i} = n_{iz}(-n_{iy}, n_{ix})$$
$$\vec{\xi_i} = \cos\theta_i(-\sin\theta_i \sin\phi_i, \cos\phi_i \sin\theta_i)$$

$$\vec{\xi_i} = \frac{1}{2}\sin 2\theta_i(-\sin\phi_i, \cos\phi_i) \tag{3.1}$$

where n_{ix}, n_{iy} and n_{iz} are the cartesian coordinates of director $\hat{n}$ in the i^{th} layer.

Because of the asymmetric structure of the molecules, the rigid bent ends of the molecules strongly hinder the free rotation of the molecules about their long axis in the tilted smectic layers. Therefore, the packing and the entropy consideration favored a zigzag configuration [41] of the BCHS molecules in the tilted smectic phases. The zigzag configuration of the BCHS molecules in the layered structure is shown in Figure 3.20a. The zigzag structure of the molecules in the layered structure induced a strong biaxiality. Therefore, we needed an additional order parameter to define the orientation of the short axis of the molecules in the layered structure. The average orientation of the short axes of the BCHS molecules can be described by another axial-vector order parameter $\vec{\eta}$. This additional axial-vector order $\vec{\eta}$ align parallel to $\vec{\xi}$ as the tilt order tends to align the bend-plane of BCHS molecules Figure 3.20b.

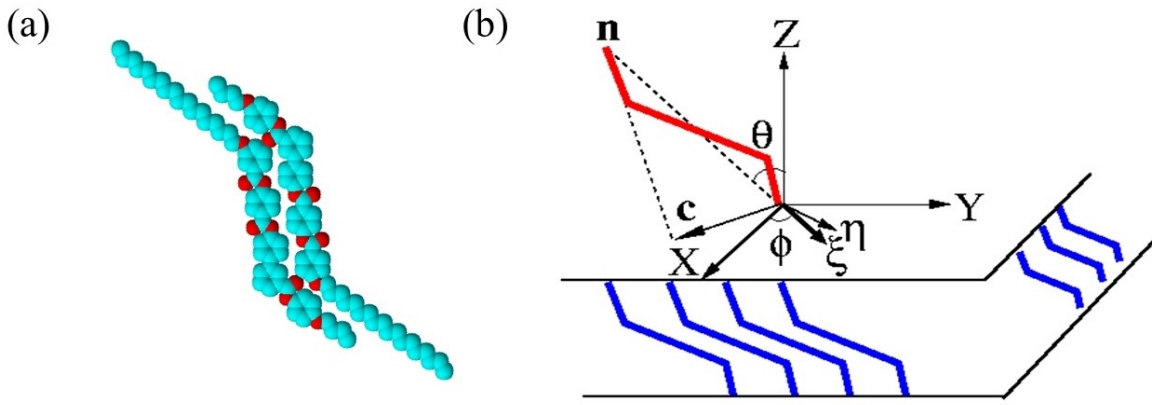

Figure 3.20: (a) The zigzag configuration of BCHS molecules within the layer. (b) The pseudo-polar tilted organization of the BCHS molecules in the layer.

To understand the axial-vector orderparameter $\vec{\eta}$, let us take an example of a symmetric BC molecule with a vector $\vec{P}$ along the arrow axis. This $\vec{P}$ changed the sign under mirror reflection when we put a mirror plane perpendicular to $\vec{P}$. On the other hand, this $\vec{P}$ did not change the sign under mirror reflection if a mirror was placed parallel to $\vec{P}$ as shown in Figure 3.21a. Therefore, $\vec{P}$ showed the property of a true vector. Whereas, in the case of zigzag molecule, we consider a vector $\vec{\eta}$ perpendicular to the bend planes. In this case, $\vec{\eta}$ did not change sign under mirror reflection when a mirror was placed perpendicular to $\vec{\eta}$. But, $\vec{\eta}$ changed sign under mirror reflection when a mirror was placed parallel to this $\vec{\eta}$. Therefore, $\vec{\eta}$ shows the property of an axial-vector as shown in Figure 3.21b. Hence, we considered an additional axial-vector order parameter $\vec{\eta}$ to describe the orientation of the short axis of BCHS molecules in the layer.

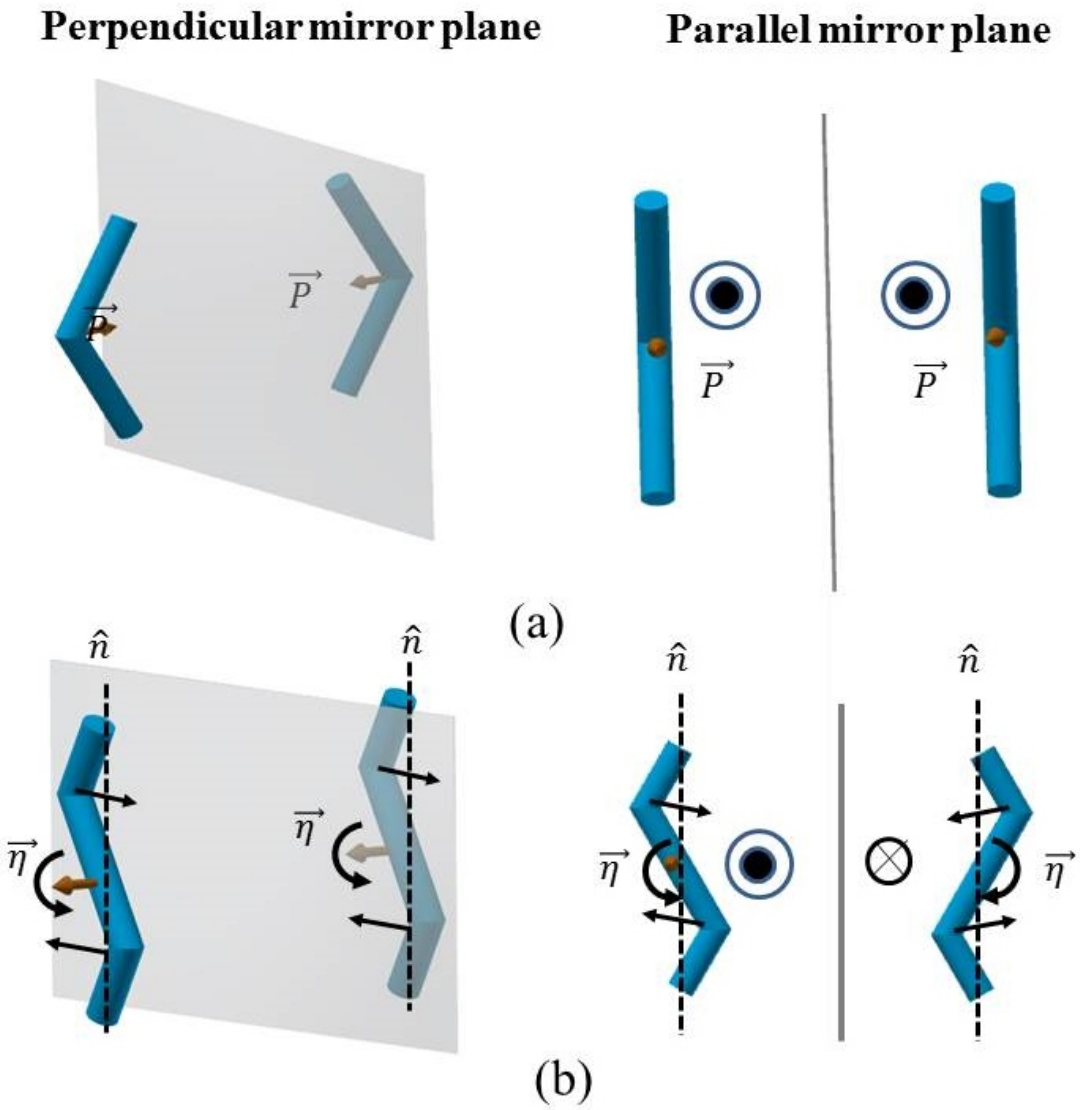

Figure 3.21: Perpendicular and parallel mirror reflections to vectors $\vec{P}$ and $\vec{\eta}$ of (a) symmetric BC banana shaped (b) bent-core hockey-stick shaped molecules.

3.4.2 Free energy expansion

Using these two order parameters, the free energy of an N layer system can be written as

$$F = \sum(f_h + f_{inh})$$

where f_h denotes the homogeneous free energy density of a given layer arising from the intralayer interaction between the molecules, whereas f_{inh} denotes interaction energy

density between the layers. The summation is over the N number of layers. Consistent with the achiral symmetry of the system, f_h can be written as,

$$f_h = \frac{A}{2}(\xi - \xi_o)^2 - \lambda_1 \xi \eta cos\psi + \frac{1}{2\chi}\eta^2 \tag{3.2}$$

where ξ and η denote the magnitudes of the tilt and axial-vector order respectively and ξ_o is the magnitude of the bare tilt order of the molecules in the absence of axial-vector order $\vec{\eta}$. ψ is the angle between tilt order ($\vec{\xi}$) and axial-vector order $\vec{\eta}$. We have considered terms up to quadratic order in both order parameters in equation EEquation 3.2. The two order parameters $\vec{\xi}$ and $\vec{\eta}$ have the same symmetries which gave rise to bilinear coupling (second term of free energy density in Equation 3.2) between them consistent with the achiral symmetry of the system analogous to the coupling of the tilt and polarization in the chiral system [42]. Minimization of Equation 3.2 gives

$$\psi = 0, \eta = \lambda\chi\xi, \xi = A\xi_o/(A - \lambda^2\chi)$$

The minimization of the Equation 3.2 clearly indicates an induced axial-vector order $\vec{\eta}$ along with the tilt order $\vec{\xi}$ in the layers. We found that with this type of packing, the layers have an achiral C_{2h} point symmetry and the electric dipole moments of the molecules in the layer expected to cancel each other with no net polarization in the layers as found experimentally.

To describe the possible stacking of the layers, the interaction between the layers needed to be taken into account. Assuming nearest neighbor interactions, the effective interaction energy density between the layers can be written as

$$f_{inh} = J_1(\vec{\xi_i} \cdot \vec{\xi}_{i+1}) + J_2(\vec{\xi_i} \cdot \vec{\xi}_{i+1})^2, \tag{3.3}$$

where $\vec{\xi_i}$ and $\vec{\xi_{i+1}}$ denote the tilt order of the i^{th} and $i+1^{th}$ layer, respectively. The coefficients J_1 and J_2 denote the coupling constants for the bilinear and biquadratic interactions between the successive layers, respectively. In our system, we considered that the molecules are already tilted uniformly in each layer due to intralayer interactions. The stacking of these tilted layers was determined by minimizing the free

energy given in Equation 3.3 due to the interlayer interactions between the molecules. The bilinear and the biquadratic coefficients could have contributions from the entropy as well as the dispersion interaction between the molecules in the neighboring layers. Therefore, the coefficient J_1 and J_2 were expected to be temperature-dependent in our model. For $J_1 > 0$, the bilinear interaction between the layers favored an anticlinic organization whereas, for $J_1 < 0$, the synclinic organization is stabilized. The biquadratic interaction between the layers with $J_2 > 0$ accounts for the favorable non-coplanar orientation of the molecular director in the successive layers due to the asymmetric bent structure of the molecules. We assumed that the intralayer interaction between the molecules is much stronger than the interlayer interactions. The magnitudes of $\vec{\xi}$ and $\vec{\eta}$ determined by minimizing Equation 3.2, are homogeneous across different layers.

In this constant amplitude approximation, the inter-layer interaction part of the free energy can be written as [33, 16]

$$f_{inh} = J_1\xi^2\cos(\phi_{i+1} - \phi_i) + J_2\xi^4\cos^2(\phi_{i+1} - \phi_i), \tag{3.4}$$

where ξ is the magnitute of tilt $\vec{\xi_i}$ and ϕ_i denotes the azimuthal orientation of the tilt order parameter $\vec{\xi_i}$ in the i^{th} layer.

$$\vec{\xi_i} \cdot \vec{\xi_{i+1}} = \xi_i(-\sin\phi_i, \cos\phi_i) \cdot \xi_{i+1}(-\sin\phi_{i+1}, \cos\phi_{i+1})$$

In constant amplitude approximation, $\xi_i = \xi_{i+1} = \xi$.
Therefore,

$$\vec{\xi_i} \cdot \vec{\xi_{i+1}} = \xi^2(\cos\phi_i\cos\phi_{i+1} + \sin\phi_i\sin\phi_{i+1})$$

$$\vec{\xi_i} \cdot \vec{\xi_{i+1}} = \xi^2\cos(\phi_{i+1} - \phi_i)$$

3.5 Theoretical results

The minimization of Equation 3.4 with respect to ϕ_i's give five possible configuration of tilted smectic phases as shown in Figure 3.22:

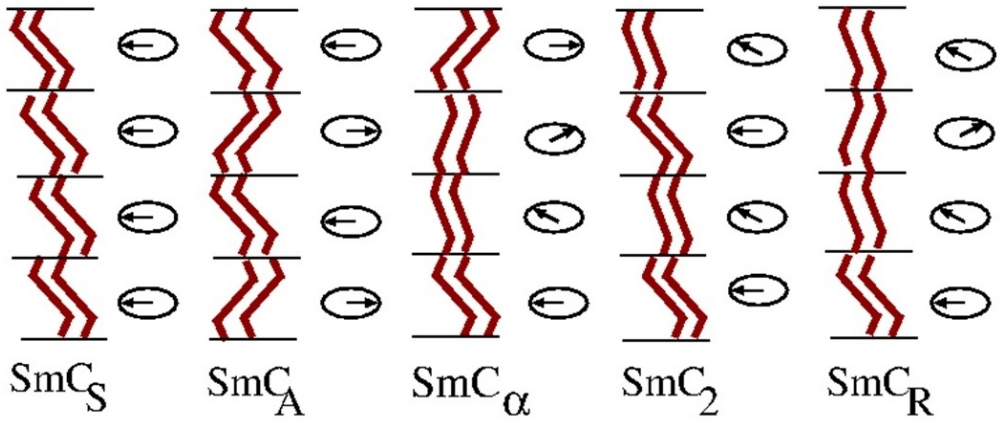

Figure 3.22: The schematic representation of the predicted structures in the different phases. The arrows show the tilt direction of the molecules in the successive layers.

(I) The $\mathbf{SmC_A}$ phase with an anticlinic tilt and antiparallel axial-vector order between successive layers was stabilized when $J_1 > 0$ and $|J_1| > J_2\xi^2$. This phase was identified with the higher-temperature SmC_A phase as observed experimentally in these samples.

(II) The $\mathbf{SmC_S}$ phase with synclinic tilt and parallel axial-vector order between successive layers was stabilized when $J_1 < 0$ and $|J_1| > J_2\xi^2$. This phase was not observed in the studied samples.

For $|J1| < J_2\xi^2$, minimization of Eq. 3.4 leads to $\cos(\phi_{i+1} - \phi_i) = -(J_1/J_2\xi^2)$ and three degenerate structures can be stabilized.

(III) The $\mathbf{SmC}_\alpha$ phase was stabilized with a helically modulated tilt directions in the successive layers. As the BCHS molecules are achiral, both left-handed and right-handed structures are equally possible.

(IV) A bilayer $\mathbf{SmC_2}$ phase in which the sign of $\delta\phi$ between neighboring pair of layers

alternate.
(V) A random $\mathbf{SmC_R}$ phase, in which the sign of $\delta\phi$ between the neighboring pair of layers vary randomly.

The lower-temperature $\mathbf{SmC_I}$ phase observed in our system perhaps represents the coexistence of $\mathbf{SmC}_\alpha$, $\mathbf{SmC_2}$, and $\mathbf{SmC_R}$ structures as discussed above. Figure 3.23 shows the phase diagram and stability regions of the different phases in the $J_1 - J_2$ parameter plane.

As discussed earlier, the parameters J_1 and J_2 are temperature-dependent in our model. For the studied sample, we assumed that $J_2 > 0$ and J_1 is large and positive at high temperatures. On decreasing the temperature, J_1 decreases and a transition to the SmC_I phase occurs as shown in Figure 3.23. The possible configurations of the tilt order of the molecules in the layers are also indicated for the different phases in Figure 3.23. For the studied compounds, the crystallization transitions preceded the transition from the SmC_I phase to the SmC_S phase on further cooling of the sample and the SmC_S phase was not observed for the studied samples.

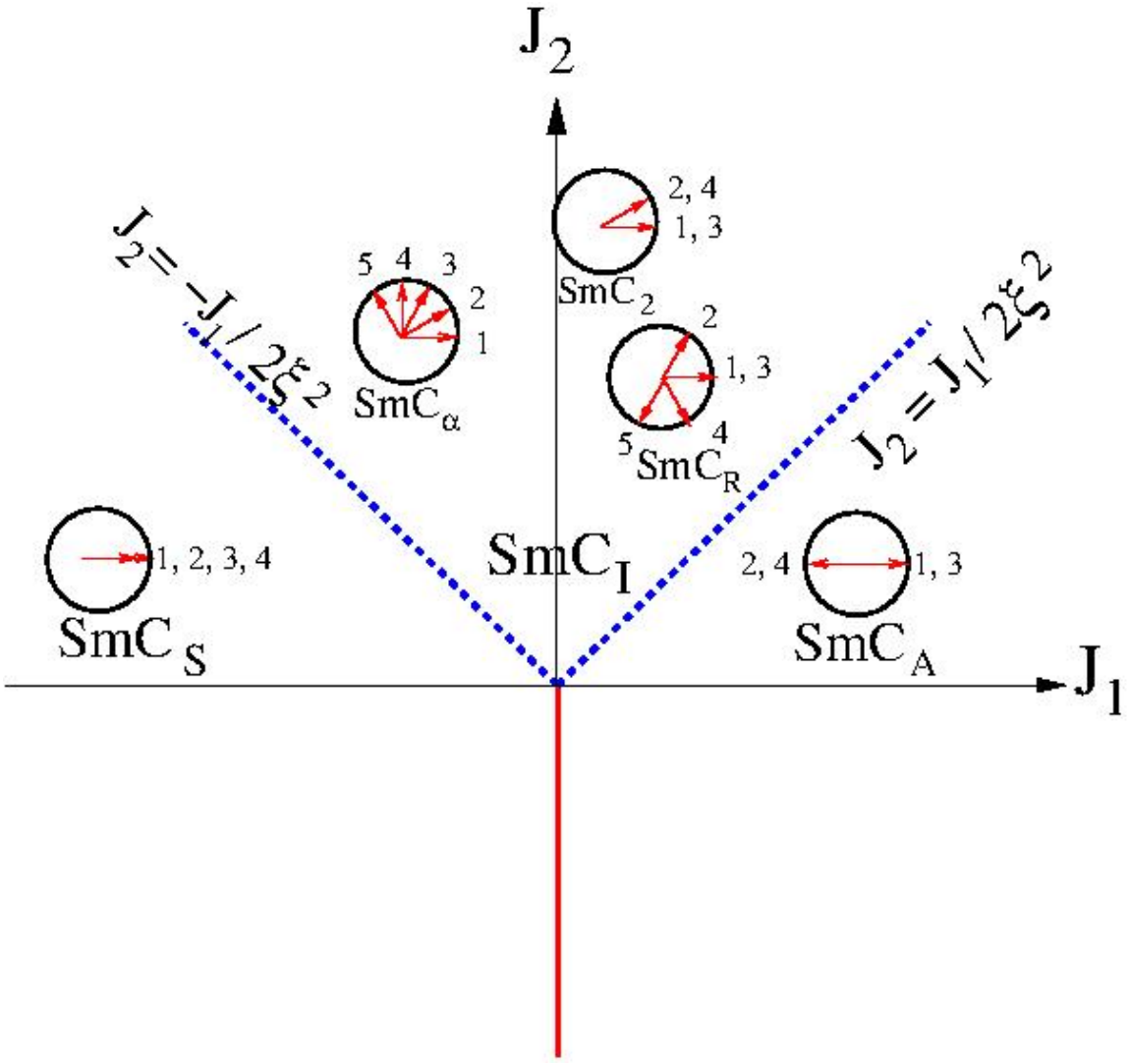

Figure 3.23: The phase diagram showing the stability regions of different phases and the transitions between them in the J_1-J_2 parameter plane. The thick solid and the dotted lines indicate first-order and second-order transitions respectively. The possible configurations of the tilt order in layers for different phases were also indicated. Note that SmC_2, SmC_R, and SmC_A phases are degenerate configurations in our model denoted collectively as the SmC_I phase.

3.6 Conclusions

In conclusion, we have investigated two compounds consisting of bent-core hockey-stick shaped molecules. The studied compounds showed two pseudo-polar tilted smectic phases which are characterized by an in-plane axial-vector order parameter in addition

to tilt order in the smectic layers. At the higher-temperatures, an anticlinic SmC_A phase with an antiparallel axial-vector order was observed. Whereas, at the lower-temperatures, an intermediate tilted SmC_I phase with coexisting degenerate structures of SmC_α, SmC_2, and SmC_R was observed. Two different compounds consisting of BCHS molecules showed very similar phase behavior which indicate that the observed phases are generic phases exhibited by BCHS molecules. A theoretical model to account for the observed mesophases was developed to describe the organization of the BCHS molecules in the tilted smectic phases. In the next chapter, we will describe the experimental results on the effects of an applied electric field in these mesophases and use this model to account for the observed field effects.

Bibliography

[1] S. Chandrasekhar, *Liquid Crystals*, (Cambridge University Press, Cambridge, 1992).

[2] J. W. Goodby, P. J. Collings, T. Kato, C. Tschierske, H. F. Gleeson, and P. Raynes, *Handbook of Liquid Crystals*, (Germany, **4**, 2014).

[3] H. Takezoe and E. Alexey, *Bent-shaped liquid crystals: structures and physical properties*, CRC Press (2017).

[4] A. Jakli and A. Saupe, *One- and two-dimensional fluids: physical properties of smectic, lamellar, and columnar liquid crystals*, CRC Press (2006).

[5] F. C. Yu and L. J. Yu, *Chem. Mater.*, **18**, 5410-5420 (2006).

[6] D. R. Link, G. Natale, R. Shao, J. E. Maclennan, N. A. Clark, E. Korblova, and D. M. Walba, *Science*, **278**, 1924–1927 (1997).

[7] T. Niori, T. Sekine, and J.Watanabe et al., *J. Mater. Chem.,* **6**, 1231–1233 (1996).

[8] R. A. Reddy and Carsten Tschierske, *J. Mater. Chem.*, **16**, 907-961 (2006).

[9] A. Roy, N. V. Madhusudana, P. Toledano, and A. M. Figueiredo-Neto, *Phys. Rev. Lett.*, **82**, 1466–1469 (1999).

[10] R. A. Reddy, C. Zhu, R. Shao, E. Korblova, T. Gong, Y. Shen, E. Garcia, M. A. Glaser, J. E. Maclennan, D. M. Walba and N. A. Clark, *Science*, **322**, 72-77 (2011).

[11] L. E. Hough, H. T. Jung, D. Kruerke, M. S. Heberling, M. Nakata, C. D. Jones, D. Chen, D. R. Link, J. Zasadzinski, G. Heppke, J. P. Rabe, W. Stocker, E. Korblova, D. M. Walba, M. A. Glaser, and N. A. Clark, *Science*, **325**, 456-460 (2009).

[12] M. Nagaraj, V. Gortz, J. W. Goodby, and H. F. Gleeson, *Appl. Phys. Lett.*, **104**, 021903 (2014).

[13] A. Jakli, D. Kruerke, H. Sawade, and G. Heppke, *Phys. Rev. Lett.*, **86**, 5715 (2001).

[14] N. Chattham, E. Korblova, R. Shao, D. M. Walba, J. E.Maclennan, and N. A. Clark,*Phys. Rev. Lett.*, **104**, 067801 (2010).

[15] A. Eremin, S. Diele, G. Pelzl, H. Nadasi, W. Weissflog, J. Salfetnikova, and H. Kresse, *Phys. Rev. Lett.*, **64**, 051707 (2001).

[16] D. Pociecha, M. Cepic, E. Gorecka, and J. Mieczkowski, *Phys. Rev. Lett.*, **91**, 185501 (2003).

[17] M. Gupta, S. Datta, S. Radhika, B. K. Sadashiva, and A. Roy, *Soft Matter*, **7**, 4735-4741 (2011).

[18] F. C. Yu, and L. J. Yu, *Liq. Cryst.*, **35**, 799–813 (2008).

[19] B. Das, S. Grande, W. Weissflog, A. Eremin, M. W. Schröder, G. Pelzl, S. Diele, and H. Kresse, *Liq. Cryst.*, **30**, 529-539 (2003).

[20] A. Chakraborty, M. K. Das, B. Das, U. Baumeister, and W. Weissflog, *J. Mater. Chem. C*, **1**, 7418 (2013).

[21] R. Stannarius, J. Li, and W. Weissflog, *Phys. Rev. Lett.*, **90**, 025502 (2009).

[22] T. J. Dingemans, N. S. Murthy, and E. T. Samulski, *J. Phys. Chem. B*, **105**, 8845–8860 (2001).

[23] M. Horcic, Vaclav Kozmik, Jiri Svoboda, and Vladimira Novotna, *J. Mater. Chem. C*, **1**, 7560-7567 (2013).

[24] E. Enz, S. Findeisen-Tandel, R. Dabrowski, F. Giesselmann, W. Weissflog, U. Baumeister, and J. Lagerwall, *J. Mater. Chem.*, **19**, 2950 (2009).

[25] Z. Luz, and S. Meiboom, *J. Chem. Phys.*, **59(1)**, 275-295 (1973).

[26] P. Sathyanarayana, S. Radhika, B. K. Sadashiva, and S. Dhara, *Soft Matter*, **8**, 2322 (2012).

[27] M. Alaasar, *Liq. Cryst.*, **43**, 2208-2243 (2016).

[28] S. Radhika, H. T. Srinivasa, and B. K. Sadashiva, *Liq. Cryst.*, **38**, 785 (2011).

[29] M. Alaasar, S. Poppe, C. Kerzig, C. Klopp, A. Eremin, and C. Tschierske, *J. Mater. Chem. C*, **5**, 8454-8468 (2017).

[30] D. D. Sarkar, R. Deb, N. Chakraborty, and V.S. R. Nandiraju, *Liq. Cryst.*, **39**, 1003-1010 (2012).

[31] E.R. Cioanca, E. L. Epure, I. C., G. Lisa, D. Wilson, N. Hurduc, and Dan Scutaru, *Mol. Cryst. Liq. Cryst.*, **537**, 51-63 (2011).

[32] M. Monika, V. Prasad, and N. G. Nagaveni, *Liq. Cryst.*, **42**, 1490–1505 (2015).

[33] A. Roy and N. V. Madhusudana, *Euro. Phys. Lett.*, **36**, 221-226 (1996).

[34] P. M. Johnson, D. A. Olson, S. Pankratz, T. Nguyen, J. Goodby, M. Hird, and C. C. Huang, *Phys. Rev. Lett.*, **84**, 4870 (2000).

[35] L. S. Matkin et al., *Phys. Rev. E,* **64**, 021705 (2001).

[36] I. Musevic and M. Skarabot, *Phys. Rev. E*, **64**, 051706 (2001).

[37] Y. Takanishi, H. Takezoe, A. Fukuda, H. Komura, and J. Watanabe, *J. Mater. Chem.*, **2**, 71 (1992).

[38] Y. Takanishi, H. Takezoe, A. Fukuda, and J. Watanabe, *Phys. Rev. B*, **45**, 7684 (1992).

[39] K. Miyasato, S. Abe, H. Takezoe, A. Fukuda, and E. Kuze, *Jpn. J. App. Phys.*, **22**, L661-L663 (1983).

[40] V. L. Lorman, A. A. Bulbitch, and P. Toledano, *Phys. Rev. E*, **49**, 1367-1374 (1994).

[41] E. N. Keller, E. Nachaliel, D. Davidov, and C. Böffel, *Phys. Rev. A*, **34**, 4363-4369 (1986).

[42] S. Garoff and R. B. Meyer, *Phys. Rev. Lett.*, **38**, 848-851 (1977).

Chapter 4

Field Effects on Pseudo-Polar Tilted Smectic Phases

4.1 Introduction

In the previous chapter, we studied two compounds consisting of bent-core hockey-stick shaped (BCHS) molecules [1, 2, 3, 4, 5, 6]. These compounds showed two pseudo-polar tilted smectic phases between the isotropic liquid and crystal phases [7, 8]. Based on the experimental results, we proposed a theoretical model for the molecular organization of BCHS molecules in the observed tilted smectic phases. As described in section 3.4, the BCHS molecules adopt a zigzag configuration for close packing in the layers of these smectic phases [9]. The molecules aligned with a head-tail symmetry within a layer and the average orientation direction of the long axes of the BCHS molecules, *i.e.*, the director $\hat{n}$ in a given layer is at an angle to the layer normal. In addition, the bend planes of the zigzag molecules in a layer align on average parallel to the tilt plane, which induced an in-plane axial-vector order parameter ($\vec{\eta}$) in the layers. The layers in these smectic phases have an achiral C_{2h} point symmetry without any spontaneous electric polarization. The polarization reversal switching current measurements indicated the absence of net electric polarization in the layers of the observed mesophases of both compounds. However, a field-induced change in the birefringence of the samples was observed under the application of an AC electric field in both the observed mesophases.

In this chapter, we will discuss the effects of an applied electric field on the observed pseudo-polar tilted smectic phases. This chapter is divided into two parts. In the first part, we will present the experimental results and discuss the electric field effects on the observed mesophases for two compounds 4OC18 and A14. In the second part, we will also describe the theoretical model to account for the observed field-induced

changes in the effective birefringence of the sample in the higher-temperature SmC_A phase.

4.2 Experimental Studies

The field effects on the observed mesophases were investigated using electro-optical (EO) measurements and polarized optical microscopy (POM) studies. The experimental setups used for these studies were discussed in chapter 2. For the measurements, we used commercially available liquid crystal cells of thickness 5 μm. The ITO coated glass plates of the cell were pretreated for a planar-alignment of the sample with electrode area 5x5 mm^2.

4.3 Compound 4OC18

4.3.1 Dielectric and Optical Transmittance Measurements

The dielectric constant measurements were performed on a customized experimental setup which was described in detail in section 2.8. The sample was placed between crossed polarizers and studied using a POM (ORTHOLUX II POL-BK) at 10 X magnification equipped with a hot stage. The real part of the effective dielectric constant of a planar-aligned sample of thickness 5 μm was measured on cooling from the isotropic phase. The dielectric constant was measured as a function of temperature under the application of a sinusoidal AC voltage of frequency 5641 Hz and an amplitude of 0.5 volts. The dielectric constant data was taken at a constant temperature interval of 0.2 ^{0}C using a temperature controller (INSTEC Inc.) with a temperature resolution of $\pm 0.1^0$C. The amplitudes and phases of the voltage drop across a known resistor of 1 kΩ connected in series with the sample were measured using a lock-in amplifier (LIA). Using impedance analysis (see section 2.6), we measured the capacitance of the sample from which the effective dielectric constant was calculated by taking the ratio with the

empty cell capacitance. The empty capacitance was measured before filling the sample into the liquid crystal cell.

Figure 4.1a shows the temperature variation of the real part of the effective dielectric constant of the compound 4OC18 on cooling the sample from the isotropic phase. The measured dielectric constant does not vary appreciably in the isotropic phase on cooling the sample. A sharp decrease in the dielectric constant is observed around 136 ^{0}C indicating the phase transition from the isotropic phase to the higher-temperature SmC_A phase. The dielectric constant in the SmC_A phase remained constant with a value of about ∼4.3. Again a sharp decrease in the dielectric constant was observed at about 120 ^{0}C which clearly indicates the transition from the SmC_A to the SmC_I phase. The low value of the dielectric constant in both the tilted smectic phases indicates the absence of electric polarization in the layers as found from the polarization switching current reversal measurements. On further cooling, a sharp decrease in the dielectric constant was observed at the transition from SmC_I to the crystal phase.

In addition to the dielectric constant measurements of a planer-aligned sample, several attempts were made to measure the dielectric constant of a homeotropically-aligned sample. But over several trials with different alignment techniques, we were not able to get homeotropic-alignment of the sample in both commercially available and custom made liquid crystal cells using ITO coated glass plates. Therefore, the dielectric constant measurements for homeotropically-aligned samples could not be achieved and the direct measurement of the dielectric anisotropy of the sample was not possible. However, the sign of the dielectric anisotropy in the higher-temperature SmC_A phase could be inferred by assuming that the component of the dielectric tensor perpendicular to the director mostly contributed to the measured dielectric constant for a planar-aligned sample and the average dielectric constant $\bar{\epsilon} = (\epsilon_{\parallel} + 2\epsilon_{\perp})/3$ in the SmC_A phase was same as the extrapolated values from the isotropic phase [10]. Then, the measured dielectric constant of the planar-aligned sample smaller than $\bar{\epsilon}$ implied $\Delta\epsilon > 0$ in both the observed mesophases. Therefore, the dielectric constant measurements indicate a positive dielectric anisotropy in the SmC_A and SmC_I phases of compound 4OC18.

We also simultaneously measured the transmitted optical intensity passing through a planar-aligned sample of thickness 5 μm as a function of temperature as shown in Figure 4.1b. The transmitted intensity increased sharply at about 136 ^{0}C as the sample was cooled from the isotropic phase. The abrupt increase in the optical intensity indicate the transition from the isotropic phase to the higher-temperature SmC_A phase. The optical intensity remained almost constant in the SmC_A phase. On further cooling, a decrease in the intensity was observed around 120 ^{0}C indicating the transition from the higher-temperature SmC_A phase to the lower-temperature SmC_I phase. The decrease in the transmitted intensity in the lower-temperature phase could be attributed to the presence of a large number of irregular bands in the texture as observed in the POM studies which scattered the incident light. On further cooling, the sample goes to the crystal phase at about 96 ^{0}C. Therefore, the simultaneous measurements of the dielectric constant and the transmitted optical intensity as a function of temperature clearly detected the phase transitions between the observed mesophases.

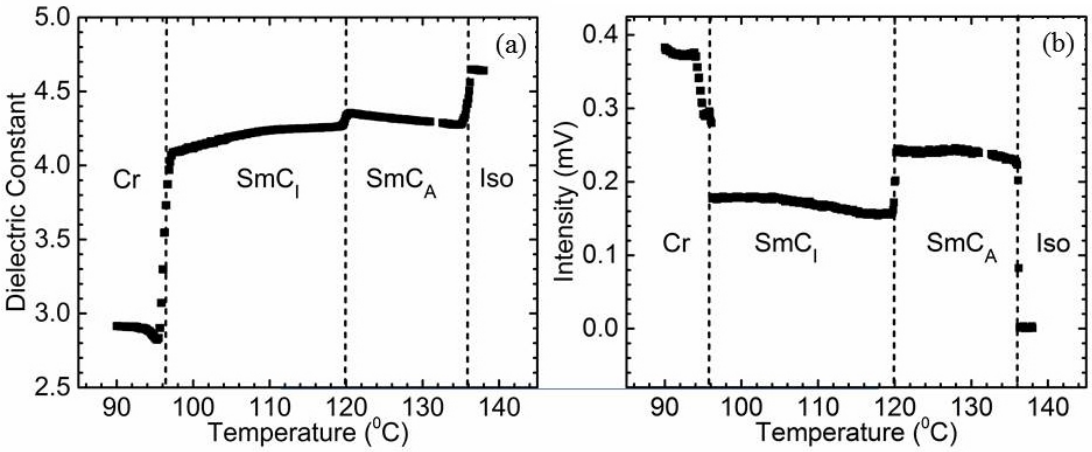

Figure 4.1: (a) The variation of the real part of effective dielectric constant and (b) transmitted optical intensity as a function of the temperature of the compound 4OC18 for a planar-aligned sample of thickness 5 μm on cooling from the isotropic phase between crossed polarizers. The vertical line shows the phase transition among the different phases.

4.3.2 Steady-state electro-optic responses

As discussed earlier in subsection 3.2.4, both the observed mesophases SmC_A and SmC_I did not exhibit any polarization reversal current peaks in the current response

under the application of a triangular wave voltage [11]. Further, the measured value of the effective dielectric constant in these phases was also relatively small. Hence, it could be concluded that the layers in these smectic phases did not possess any net electric polarization for both compounds. Yet, for both the mesophases, a field-induced change in the optical transmittance through a planar-aligned sample of thickness 5 μm was observed under the application of an AC electric field. The time-dependent electro-optic transmittance of the sample at a given temperature was measured using a He-Ne Laser passing through a planar-aligned sample of thickness 5 μm between the crossed polarizers. The transmitted intensity was monitored using a high gain low noise photo-diode. The output signal of the photo-diode was measured by an oscilloscope (Agilent Tec. MSO6012A). During the experiments, the temperature of the sample was controlled by a home-built temperature controller using a PID algorithm.

The steady-state electro-optic response of the compound 4OC18 in both the SmC_A and SmC_I phases on the application of a triangular wave voltage of frequency 30 Hz is shown in Figure 4.2. The observed electro-optic response is symmetric with respect to the positive and negative values of the applied voltage, indicating a quadratic coupling of the electric field with the effective dielectric anisotropy of the sample. The electro-optic response clearly originated from the effective change in the birefringence of the sample due to the reorientation of the molecules in the smectic layers with applied fields. It can be seen from Figure 4.2a that the transmitted intensity decreased with increasing the magnitude of the applied field in the higher-temperature SmC_A phase. Thus, the optical intensity was minimum at zero volts and it attained the maximum values for both positive and negative maximum of the applied voltage. This behavior tends to give about 90 degrees phase shift between the applied field and the optical response. However, it should be noted that there was a negligible phase difference between the optical response and the applied voltage for the frequency used in the experiments. This effect arose because of the zero-field optical phase difference introduced by the sample between the ordinary and extraordinary rays. For a planar-aligned sample of thickness 5 μm in the SmC_A phase, the zero-field phase difference $\Delta\Phi_0$ lied between π and 2π. This phase difference increased with increasing the magnitude of the applied field and gave rise to a decrease in the transmitted intensity with increasing magnitude

of the field.

In the lower-temperature SmC_I phase, the optical intensity increased with increasing magnitude of the applied electric field (see Figure 4.2b). The maxima of the transmitted intensity coincided with the corresponding maxima and minima of the applied voltage. The zero-field phase difference in the SmC_I phase of the sample possibly lies between zero and π due to the presence of many degenerate structures in the texture. Then, the field-induced increase in the phase difference beyond the zero-field value in the SmC_I phase gives an increasing intensity with increasing magnitude of the field. The measured optical contrast in the lower-temperature SmC_I phase is lower compared to that in the SmC_A phase due to the coexistence of different degenerate structures in the lower-temperature SmC_I phase [12].

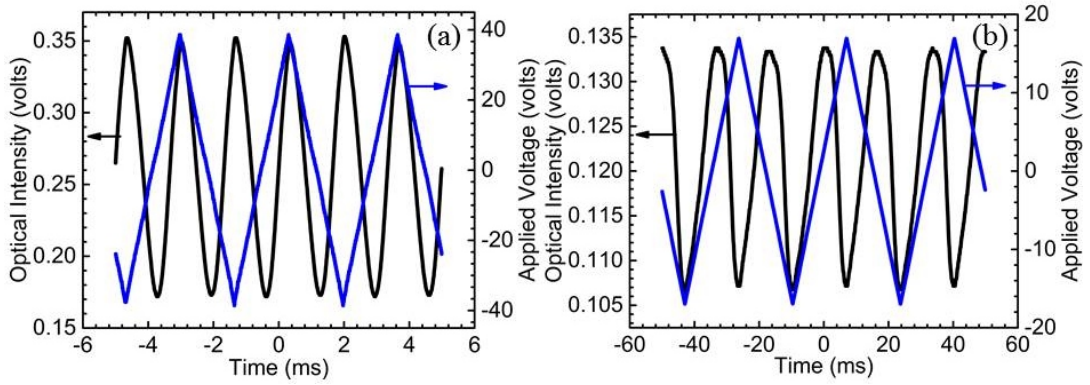

Figure 4.2: The optical response of the compound 4OC18 between crossed polarizers for a planar-aligned sample of thickness 5 μm under the application of triangular wave voltage of frequency 30 Hz in (a) the SmC_A phase and (b) the SmC_I phase.

4.3.3 Field effects on POM textures

To further investigate the structures of observed mesophases of compound 4OC18, we measured field-induced changes in the birefringence of a planar-aligned sample of thickness 5 μm. The POM textures [13] were studied for a planar-aligned sample under the application of an AC electric field of frequency 1 kHz. The sample was slowly cooled from the isotropic phase to the high-temperature SmC_A phase and observed between the crossed polarizers in a polarizing optical microscope (Olympus BX-50). During

the experiment, the temperature of the sample was controlled using a LINKAM hot stage (LTS420E) and temperature controller LINKAM (HST95) with a temperature resolution 0.1 ^{0}C. The POM textures were captured by OLYMPUS camera (DP12) at 20X magnification at a constant temperature with a varying amplitude of the applied electric field.

The POM texture in the SmC_A phase between the crossed polarizers in the absence of an AC electric field of frequency 1 kHz is shown in Figure 4.3a. It was observed that upon increasing the amplitude of the applied field, beyond a threshold value, few orange color bands parallel to the layers began to grow at the cost of the otherwise smooth yellow color fan regions of the texture in the SmC_A phase. Upon further increasing the amplitude of the applied field, the orange color bands started to increase in number, and the fans in the texture became uniform orange in color at higher fields (see Figure 4.3b). Even at higher values of the applied electric field, the fans remained uniform in color, but the birefringence color of the fans changed gradually to purple (Figure 4.3c). Using the Michel-Levy interference color chart, we found that the birefringence color of the focal-conic fan regions increased upon the increasing amplitude of the applied electric field. It was also found that the optic axis parallel to the layer normal remained the same without any rotation of the brush pattern under the application of the field. Interestingly, a few orange color bands parallel to the layers were found to be stable in the high-temperature SmC_A phase even in the zero field. The stability of these orange color bands parallel to the layers in the absence of an electric field possibly arises due to the surface field effects.

The sample was cooled from the higher-temperature SmC_A phase to the lower-temperature SmC_I phase between the crossed polarizers. The POM texture in the SmC_I phase at zero fields is shown in the Figure 4.3d. The fan regions of the texture in the SmC_A phase became obscure due to the appearance of a large number of irregular bands parallel to the smectic layers across the transition from the SmC_A to the SmC_I phase. It was found that upon increasing the amplitude of the applied electric field in the SmC_I phase, the bands parallel to the layers gradually decreased in number (see Figure 4.3e) and even at higher fields, fan texture tends to get restored as shown

in Figure 4.3f. As discussed in subsection 3.2.3, these large numbers of bands in the SmC_I phase appeared due to the coexistence of different degenerate structures. These degenerate domains with random tilt directions in the layers gradually aligned due to the applied electric field for a planar-aligned sample which tend to restore the fan texture as observed experimentally at high fields. Therefore, the applied field tend to remove the degeneracy of different stable structures in the SmC_I phase at the zero fields giving rise to a uniform fan texture.

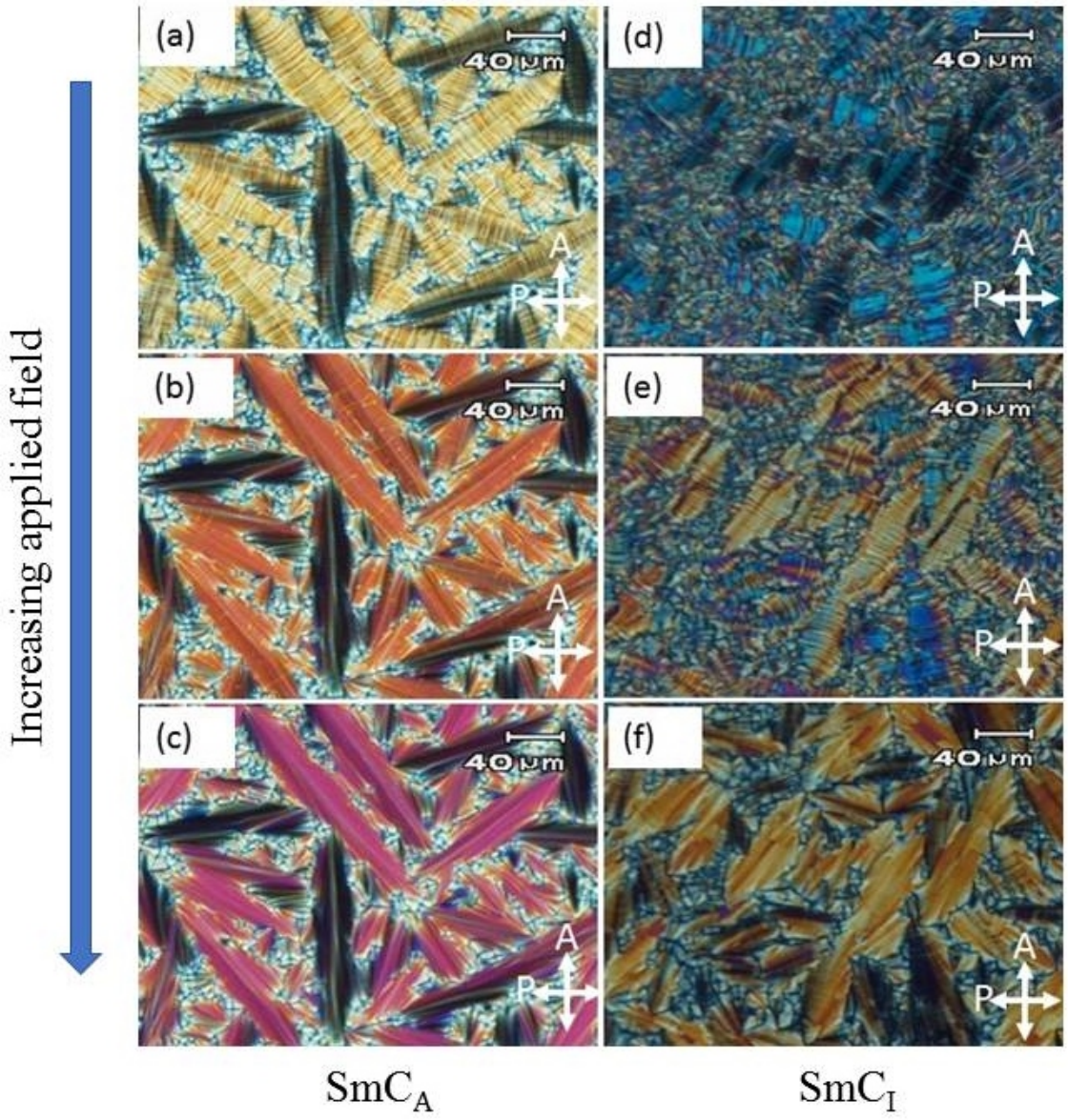

Figure 4.3: The field-induced effects on the POM textures with a planar-aligned sample at a constant temperature 125^0C with a varying electric field of amplitudes (left column) in the SmC_A phase at (a) 0 V/μm (b) 2.5 V/μm (c) 20 V/μm and at 115^0C (left column) in the SmC_I phase at (d) 0 V/μm (e) 2 V/μm (f) 20 V/μm.

To quantitatively determine the field-induced changes in the effective birefringence of a planar-aligned sample in the SmC_A phase, the average transmitted intensity passing through a planar-aligned sample was measured with increasing the amplitude of applied AC electric field of frequency 1 kHz. The sample was cooled from the isotropic phase to a given temperature in the SmC_A phase allowing sufficient time to stabilize temperature. The POM images of a planar-aligned sample of thickness 5 μm placed be-

tween the crossed polarizers were captured for different amplitude of the applied field. A red filter of wavelength 650 nm was used for the measurement of average transmitted intensity and to avoid the effects of birefringence colors appearing in white light. The average transmitted intensity of the POM images was then extracted using a MATLAB program [12].

The variation of optical average transmitted intensity in the SmC_A phase as a function of the applied field is shown in Figure 4.4a. The optical average transmitted intensity remained nearly constant up to a threshold field (1 V/μm) beyond this value the average transmitted intensity decreased gradually and tend to saturate beyond 10 V/μm in the higher-temperature SmC_A phase. The decrease in the average transmitted intensity beyond the threshold field indicates an increase in the effective birefringence of the sample as observed in POM investigations. Similarly, we also measured the average transmitted intensity in the lower-temperature SmC_I phase. The variation of average transmitted intensity in the lower-temperature SmC_I phase as a function of an applied field is shown in Figure 4.4b. Initially, the intensity increased sharply with the increasing field up to a field of about 3.2 V/μm and then got saturated to a nearly constant value beyond this field. The increase in the intensity in the SmC_I phase indicates an increase in the effective birefringence of the sample. The applied field aligned the different degenerate structures in the SmC_I phase, leading to a rapid increase in the intensity. The average transmitted intensity get saturated when a majority of the degenerate structure aligned, giving rise to a field-induced fan texture in the SmC_I phase, as observed in POM investigations.

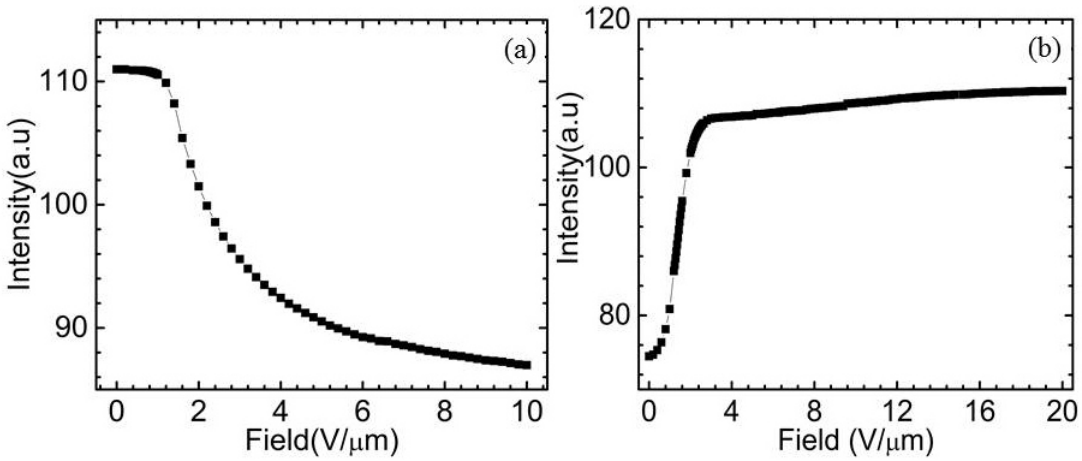

Figure 4.4: The variation of average transmitted intensity passing through a planar-aligned sample of thickness 5 μm between crossed polarizers under the application of an AC electric field of frequency 1 kHz in (a) the SmC_A at 124 ^{0}C and (b) the SmC_I at 115 ^{0}C phases, respectively.

4.4 Compound A14

We also studied the field effects on the smectic phases exhibited by another compound A14 consisting of BCHS molecules. As we discussed in section 3.3, this compound also shows similar phase behavior as that of the compound 4OC18. In this section, we will present the field effects on the observed mesophases of compound A14 which further corroborated the experimental observations for the compound 4OC18. Again, a planar-aligned sample of the thickness of 5 μm was used to study the field effects in the smectic phases.

4.4.1 Dielectric Constant Measurements

Similar to compound 4OC18, we measured the real part of the effective dielectric constant of compound A14 as a function of temperature. Figure 4.5 shows the temperature variation of the real part of the effective dielectric constant of compound A14 on cooling the sample from the isotropic phase. The measured dielectric constant sharply increases at the transition from the isotropic phase to the SmC_A phase. On further decreasing the temperature, dielectric constant saturated to a value of about 5.25 deep

in the SmC_A phase. The dielectric constant varied continuously across the transition from the SmC_A to the SmC_I phase. This compound also shows relatively low values of the effective dielectric constant in both the smectic phases as that of compound 4OC18.

The low value of the dielectric constant in the observed mesophases confirmed the absence of electric polarization in the layers. For this compound also, we could not achieve homeotropic-alignment of the sample in their smectic phases using ITO coated liquid crystal cells. The sign of dielectric anisotropy in the higher-temperature SmC_A phase of compound A14 was estimated by adopting the same assumption as that of compound 4OC18. The average value of the dielectric constant $\bar{\epsilon}$ in the SmC_A phase was greater than the value of $\epsilon_\perp$ in the observed tilted smectic phases indicating negative dielectric anisotropy ($\Delta\epsilon < 0$) in the observed smectic phases of compound A14 [10].

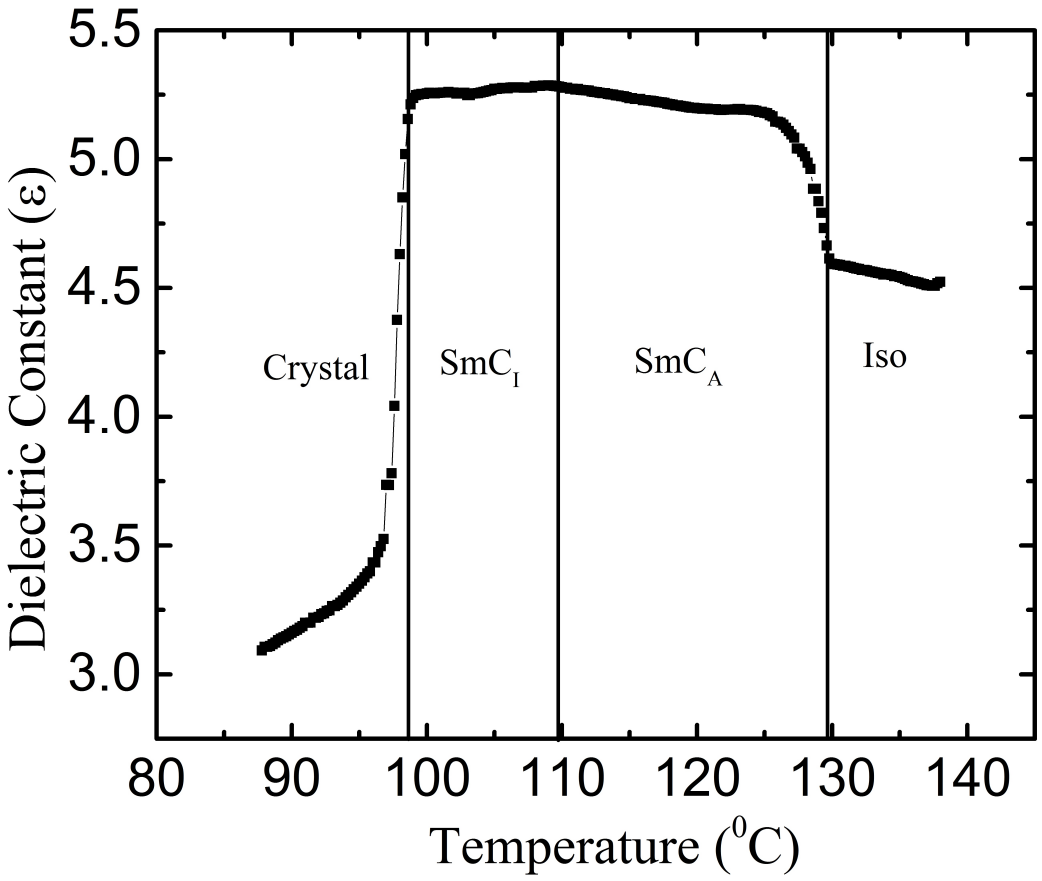

Figure 4.5: The variation of the real part of the effective dielectric constant of the compound A14 as a function of temperature for a planar-aligned sample of thickness, 5 μm.

4.4.2 Steady-state electro-optic responses

As discussed earlier in section 3.3, the polarizing switching current and dielectric constant measurements clearly indicated that the layers in the observed mesophases of compound A14 also did not possess any net electric polarization. But a field-induced change in the optical transmittance through the sample between the crossed polarizers was observed in both the mesophases similar to that for compound 4OC18. The experiments were performed under the same conditions as that of compound 4OC18. Briefly, the optical transmittance passing through the sample of thickness 5 μm between the crossed polarizers was measured under the application of an AC triangular voltage wave. Figure 4.6 shows the electro-optic response in both the mesophases under the application of an AC electric field of frequency 30 Hz. The change in the optical transmittance through the sample originated from the effective change in the birefringence with the field. The changes in the effective birefringence of the sample arise due to the reorientation of the molecules in the smectic layers with the applied fields which could also be inferred from the observed field effects on POM textures. Thus, the observed smectic phases of compound A14 could be identified with the SmC_A and SmC_I phases of compound 4OC18.

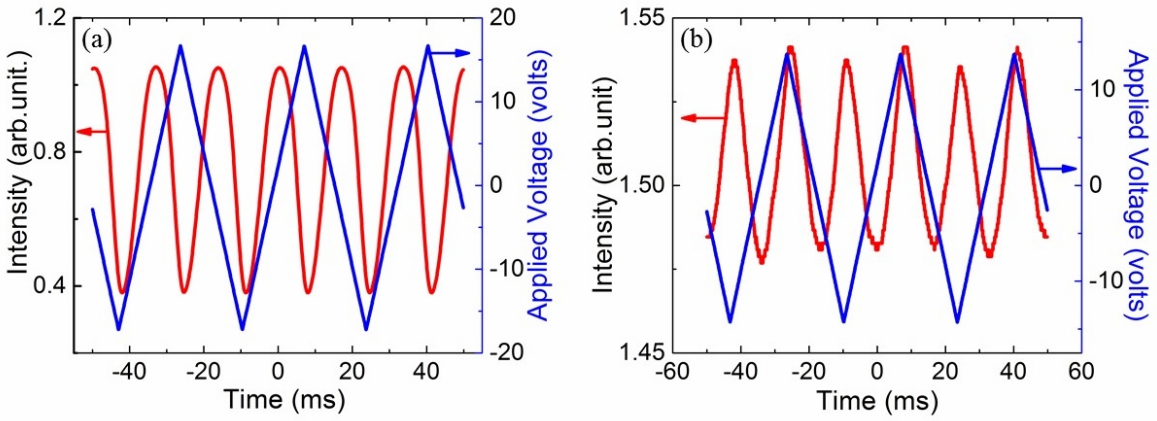

Figure 4.6: The optical response of compound A14 between crossed polarizers for a planar-aligned sample of thickness 5 μm under the application of triangular wave voltage of frequency 30 Hz in the (a) SmC_A and (b) SmC_I phases.

4.4.3 Field effects on POM Textures

The POM textures in the SmC_A and SmC_I phases of compound A14 were studied with an applied AC electric field of frequency 1 kHz. A planar-aligned sample of thickness 5 μm was cooled from the isotropic phase to the higher-temperature SmC_A phase. A focal-conic fan texture [13] (Figure 4.7e) was observed in the SmC_A phase between the crossed polarizers in the absence of an applied electric field. Interestingly, it was found that upon increasing the amplitude of the electric field, the birefringence color of the focal-conic fan texture started to change beyond a threshold field (4 V/μm). The birefringence color changed gradually from purple to blue and then to green (Figure 4.7b-d) on increasing the amplitude of applied field beyond the threshold field. The birefringence color changes with field were observed without any rotation of the extinction brushes in the SmC_A phase. This implied that the birefringence of the sample increases with field without any change in the local optic axis.

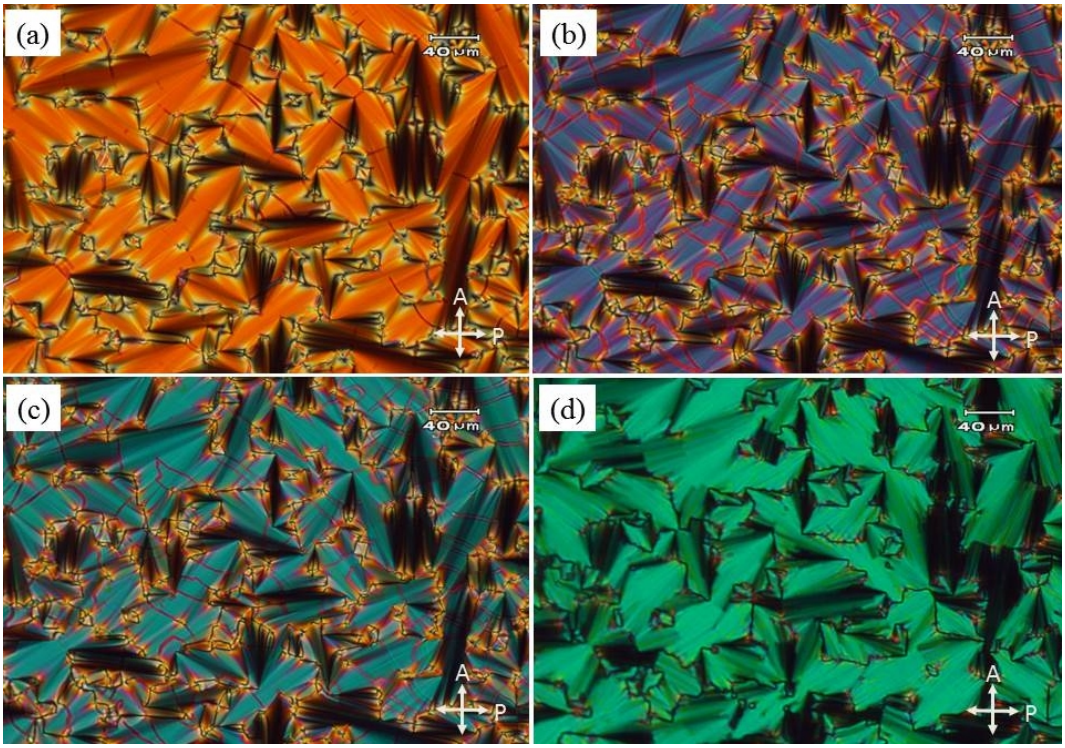

Figure 4.7: The changes in the birefringence color of POM textures of a planar-aligned sample of thickness 5 μm at 115 ^{0}C in the SmC_A phase under the application of an AC electric field of frequency 1 kHz with increasing amplitudes (a) 0 V/μm (b) 4.4 V/μm (c) 8.6 V/μm, and (d) 16 V/μm. The scale bar used in all the images is 40 μm.

The changes of the POM textures in the SmC_I phase with increasing field are shown in Figure 4.8. The number of irregular bands decreased with an increasing field in the SmC_I phase as found in the case of compound 4OC18. The decrease in the number of irregular bands indicates that the coexisting degenerate structure aligned due to the field. The tilt directions of the molecules in the layers gradually aligned due to the applied in-plane electric field of a planar-aligned sample tending to restore the uniform fan texture. The field-effect on the POM textures of compound A14 was similar to that of compound 4OC18. Though, the field-induced transition from the irregular band texture to the clear focal-conic fan texture was not observed in the SmC_I phase up-to an electric field strength of 20 V/μm used in our experiments.

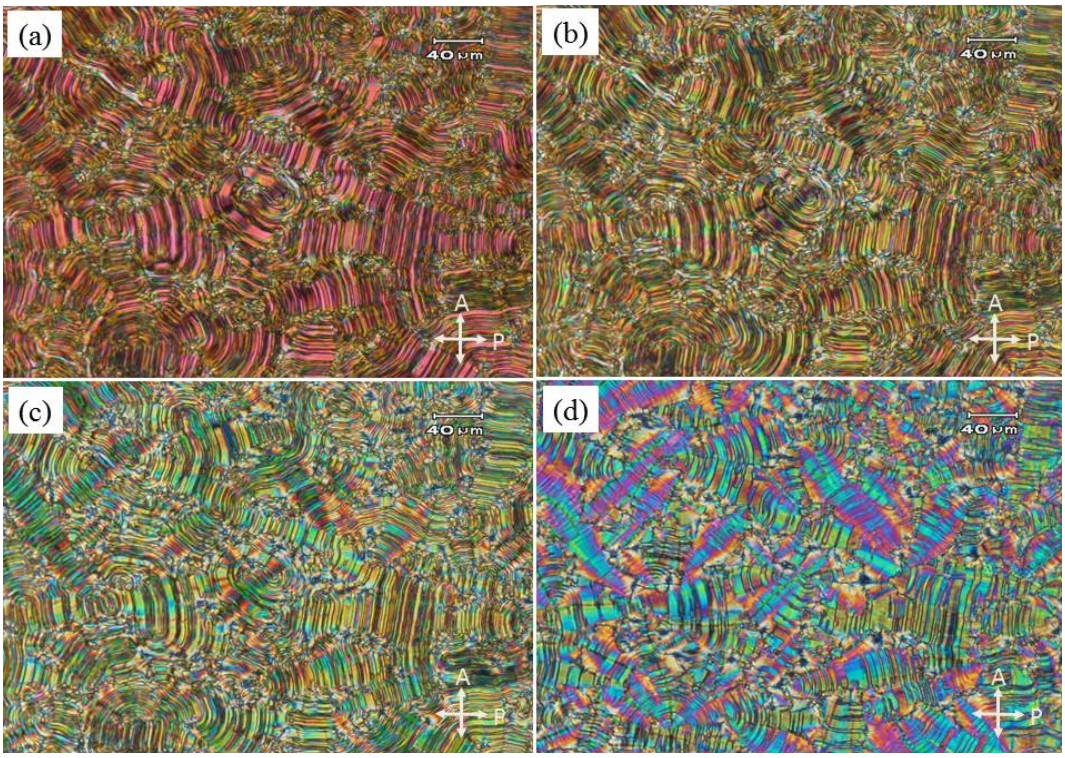

Figure 4.8: The changes in the birefringence color of POM textures of a planar-aligned sample of thickness 5 μm in the SmC_I phase under the application of an AC electric field of frequency 1 kHz with increasing amplitudes (a) 0 V/μm (b) 4.4 V/μm (c) 8.6 V/μm, and (d) 16 V/μm at 104 ^{0}C. The scale bar used in all the images is 40 μm.

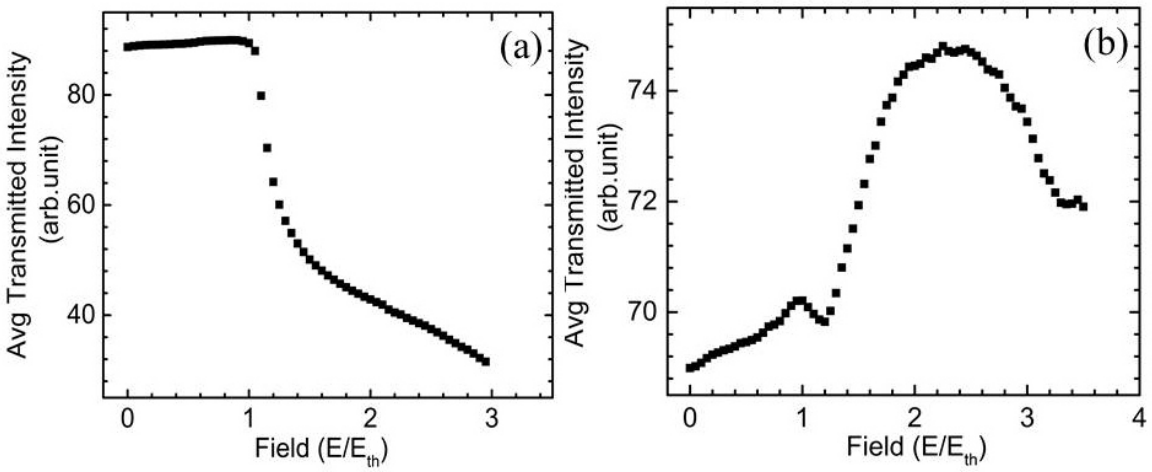

Figure 4.9: The variation of average transmitted intensity passing through a planar-aligned sample of thickness 5 μm between crossed polarizers under the application of an AC electric field in (a) SmC_A at 124 ^{0}C and (b) SmC_I at 115 ^{0}C phases respectively.

4.5 Average Transmitted Intensity

We measured the transmitted intensity through a planar-aligned sample of thickness 5 μm in the observed mesophases with an applied AC electric field of frequency 1 kHz. The variation of the average transmitted intensity in both the SmC_A and SmC_I phases is shown in Figure 4.9. As observed in POM investigations, the textural intensity remained nearly constant up to a threshold field (4 V/μm) beyond which the intensity started to decrease gradually with an increasing field (see Figure 4.9a). The gradual decrease in the intensity beyond the threshold field implies an increase in the effective birefringence of the sample in the higher-temperature SmC_A phase.

For the lower temperature SmC_I phase of compound A14, the average transmitted intensity did not increase smoothly with the applied field because of the presence of irregular band structure, as shown in Figure 4.9b. With the applied electric field, the number of irregular bands decreased in number resulting in an increase in the average transmitted intensity. At a threshold voltage, the birefringence color of the texture changed with an applied field gives rise to an increase in the intensity. The number of irregular bands in the lower-temperature SmC_I phase decreased in number

but these bands did not disappear even at the high electric field ($20V/\mu m$) used in our experiments. Due to the presence of the irregular band in the lower-temperature SmC_I phase, we could not estimate the change in the effective birefringence of the sample with the applied field.

The effective birefringence changes of a planar-aligned sample of thickness 5 μm were measured quantitatively by monitoring the variation of average transmitted intensity with the field. The variation of intensity with an applied field could be easily correlated with the change in the birefringence of the sample in the SmC_A phase due to the uniform texture. But in the SmC_I phases, the texture was not uniform due to the coexistence of different degenerate structures and the determination of the changes in the birefringence of the sample was not possible. Therefore, we had only estimated the effective birefringence of a planar-aligned sample of thickness 5 μm in the higher-temperature SmC_A phase. In this section, we now described the method which was used to estimate the effective birefringence of the sample using photomicrography under the application of the electric field. Both the compounds, 4OC18 and A14, showed similar behavior with an applied field. Using the average transmitted intensity passing through the sample, we estimated the change in the effective birefringence of a planar-aligned sample of thickness 5 μm in the SmC_A phase with an applied field as follows [14, 15, 16]:

The transmitted intensity at a given pixel of the POM image of a planar-aligned sample in the absence of an applied electric field can be written as:

$$I_0 = \frac{I_i}{2}\sin^2(2\psi_0)(1-\cos\Delta\phi_0) \tag{4.1}$$

where I_0 is the transmitted intensity at zero-field, I_i is the incident intensity of light, ψ_0 is the angle between the local optic axis and the polarizer, and $\Delta\phi_0$ is the local phase difference: $\Delta\phi_0 = \frac{2\pi\Delta n_0 d}{\lambda}$. Δn_0 is the effective birefringence of the sample at zero-field. Here, d is the sample thickness, λ is the wavelength of the incident light. The subscript $(_0)$ denotes the value of the corresponding quantity at zero electric fields. For the higher-temperature SmC_A phase, the phase difference ($\Delta\phi_0$) in the absence of a field is about 3.8665.

Similarly, the transmitted intensity at a given pixel of the POM image of the planar-aligned sample under an applied field can be written as:

$$I = \frac{I_i}{2}\sin^2(2\psi)(1-\cos\Delta\phi) \tag{4.2}$$

where I is the transmitted intensity at non-zero field, I_i is the incident intensity of light, ψ is the angle between the local optic axis and the polarizer, and $\Delta\phi$ is the local phase difference at non-zero field : $\Delta\phi = \frac{2\pi\Delta nd}{\lambda}$, Δn is the effective birefringence of the sample at that pixel under an applied electric field.

In our experiments, we used a wavelength of $\lambda = 650$ nm of a red filter. The angle between the optic axis and the polarizer does not change under the application of field at a given pixel , *i.e.*, ψ_0=ψ. Therefore, dividing Equation 4.2 by Equation 4.1 gives,

$$\frac{I}{I_0} = \frac{1-\cos(\Delta\phi)}{1-\cos(\Delta\phi_0)} \tag{4.3}$$

where $\Delta\phi$ is the total phase difference, $\Delta\phi = \Delta\phi_0 + \delta\phi$, and $\delta\phi$ is the small change in the phase difference in the presence of an applied electric field. Therefore, Equation 4.3 can be written as

$$\frac{I}{I_0} = \frac{1-\cos(\Delta\phi_0+\delta\phi)}{1-\cos(\Delta\phi_0)}$$

$$\frac{I}{I_0} = \frac{\sin^2(\frac{\Delta\phi_0+\delta\phi}{2})}{\sin^2(\frac{\Delta\phi_0}{2})}$$

$$\sqrt{\frac{I}{I_0}} = \frac{\sin(\frac{\Delta\phi_0+\delta\phi}{2})}{\sin(\frac{\Delta\phi_0}{2})} \tag{4.4}$$

Assuming the field-induced change in the path difference $\delta\phi$ is small, we can write $\delta\phi \to 0, \sin\frac{\delta\phi}{2} \to \frac{\delta\phi}{2}, \cos\frac{\delta\phi}{2} \to 1$

$$\sin(\frac{\Delta\phi_0}{2}+\frac{\delta\phi}{2}) = \sin\frac{\Delta\phi_0}{2}\cos\frac{\delta\phi}{2} + \cos\frac{\Delta\phi_0}{2}\sin\frac{\delta\phi}{2} = \sin\frac{\Delta\phi_0}{2} + \cos\frac{\Delta\phi_0}{2}\frac{\delta\phi}{2} \tag{4.5}$$

Using Equation 4.4 and Equation 4.5,

$$\sqrt{\frac{I}{I_0}} = 1 + \frac{\delta\phi}{2}\cot\frac{\Delta\phi_0}{2}$$

Therefore, the small field-induced change in the phase difference is given by,

$$\boxed{\delta\phi = 2\tan\frac{\Delta\phi_0}{2}(\sqrt{\frac{I}{I_0}} - 1)} \tag{4.6}$$

The small change in the phase difference of the sample was estimated by using eq Equation 4.6 in the higher-temperature SmC_A phase by averaging over the pixels of the POM images. The small change in the effective birefringence of the sample under the application of electric field can be calculated as $\delta n = \frac{\delta\phi\lambda}{2\pi d}$. Therefore, the effective birefringence of a planar-aligned sample can be calculated as, $\Delta n = \Delta n_0 + \delta n$. The zero-field effective birefringence of the sample was estimated using the Michel-Levy interference color chart (see Figure 4.10) for a given thickness.

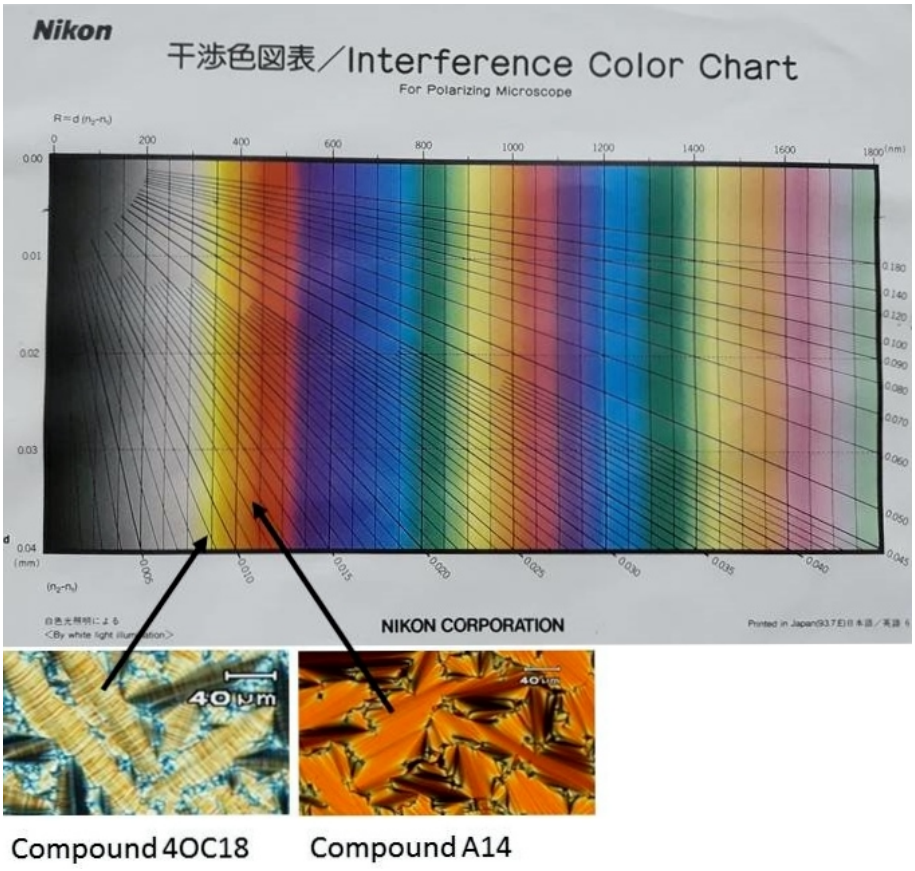

Figure 4.10: The Michel-Levy interference color chart to estimate the effective birefringence at zero-field using POM textures.

For compound 4OC18, we have estimated the effective birefringence at zero-field, Δn_0 =0.08, for a planar-aligned sample of thickness 5 μm in the focal-conic fan texture in the SmC_A phase. The field-induced changes in the effective birefringence for compound 4OC18 in the higher-temperature SmC_A phase are shown in Figure 4.11. The effective birefringence of the sample remains constant at low field and increases gradually above a threshold value with the applied field.

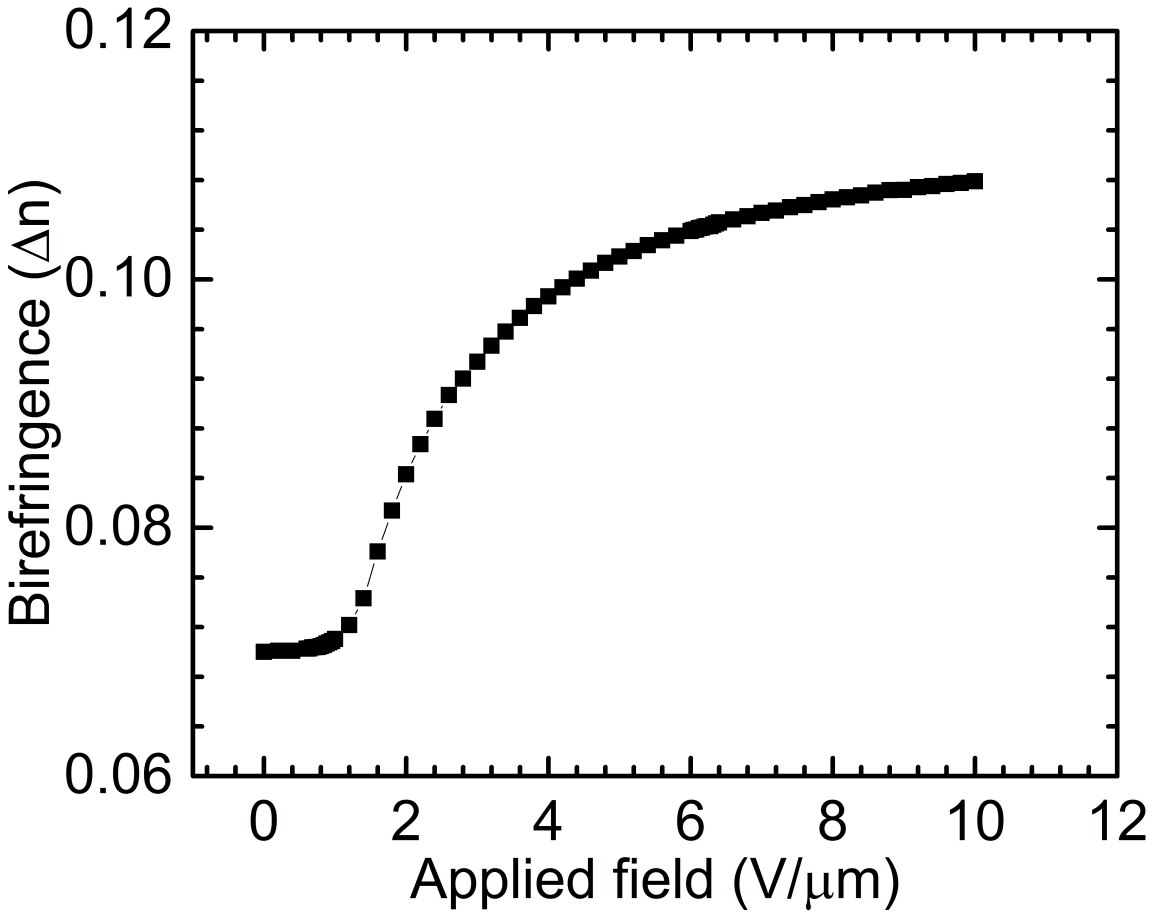

Figure 4.11: The experimentally measured effective birefringence for compound 4OC18 of a planar-aligned sample of thickness 5 μm in the higher-temperature SmC_A phase at a constant temperature with increasing amplitude of the applied electric field of frequency 1 kHz.

Similarly, for the compound A14, the estimated zero-field effective birefringence for orange color focal-conic fan texture of a planar-aligned sample of thickness 5 μm in the SmC_A phase is about Δn_0=0.07. Figure 4.12 shows the field-induced change in the effective birefringence of compound A14 in the SmC_A phase. The effective birefringence of compound A14 in the SmC_A phase also changed in the same manner

as that of compound 4OC18.

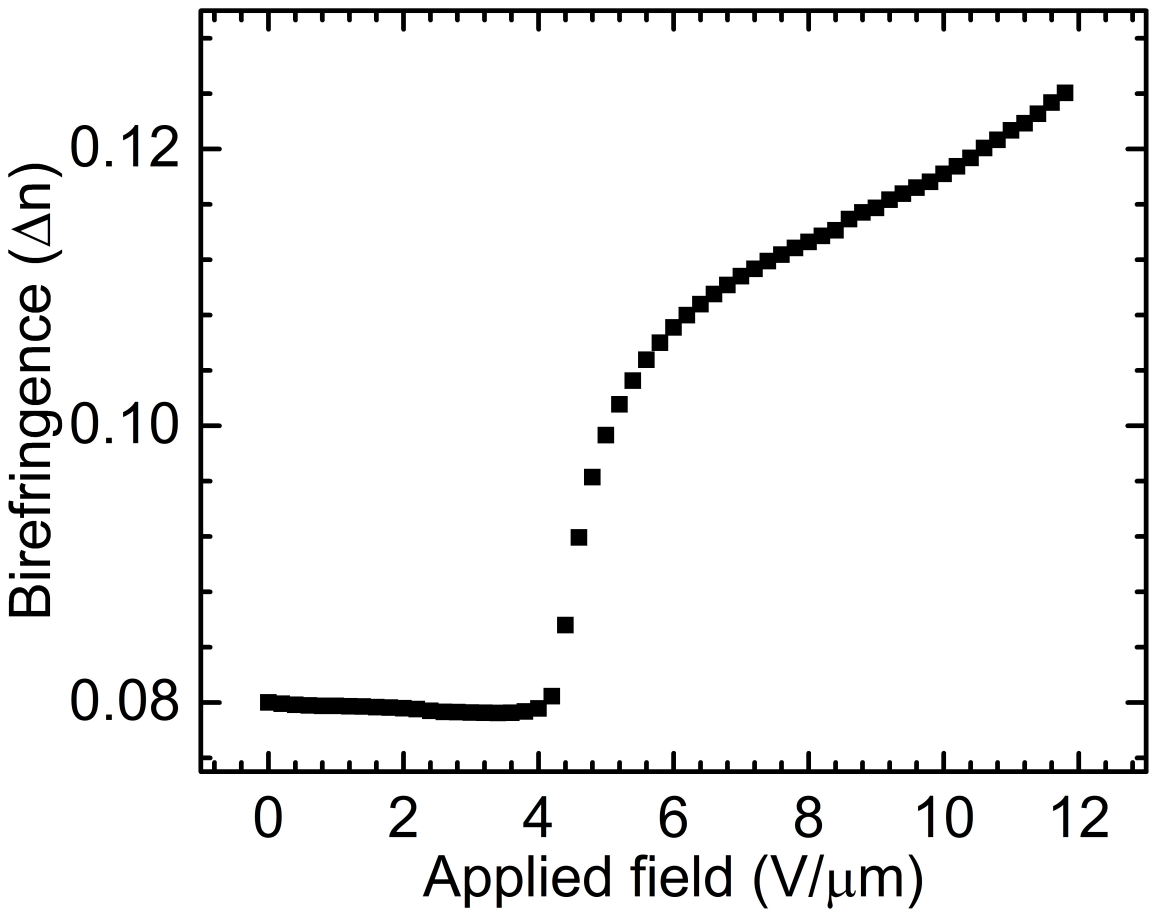

Figure 4.12: The experimentally measured effective birefringence for compound A14 of a planar-aligned sample of thickness 5 μm in the higher-temperature SmC_A phase at fixed temperature with increasing amplitude of the applied electric field of frequency 1 kHz.

The field-induced variation in the transmitted intensity (effective birefringence) passing through the sample showed a clear threshold phenomenon in the observed tilted smectic phases for both the studied compounds.

4.6 Theory of field-induced transition

Experimentally, we found that the birefringence of the samples changes with an applied electric field. In this section, we will discuss the theoretical model to account for the field-induced change in the effective birefringence of a planar-aligned sample in

the higher-temperature SmC_A phase. In particular, the threshold field-effect observed experimentally in our system. To explain the field-induced effects on the structure of observed mesophases, we need two order parameters: tilt order parameter $\vec{\xi}$ and orientational order parameter $\vec{\eta}$. These order parameters were explained in subsection 3.4.1. In the SmC_A phase, the tilt order of the BCHS molecules in a layer can be described by an axial-vector $\vec{\xi}$ which is given by,

$$\vec{\xi} = (\hat{k} \cdot \hat{n})(\hat{k} \times \hat{n})$$

where the unit vectors $\hat{k}$ and $\hat{n}$ denote the layer normal and average orientation direction of the long axes of the molecules, respectively [17, 18]. The c-director, $\vec{c}$, is defined as the projector of director $\hat{n}$ onto the layer plane, which is perpendicular to the tilt order $\vec{\xi}$.

The rigid bend ends of BCHS molecules strongly hindered the free rotation of the molecules about their long axess in the tilted smectic layers. Therefore, the packing and entropy considerations favored a zigzag configuration of the BCHS molecules in the tilted smectic layers as described in section 3.5 [9]. When the long axes of these zigzag molecules are on average tilted, the tilt plane favored the bend plane of the zigzag molecules align parallel to itself (see Figure 4.13). The orientational order of the short axis of the BCHS molecules can be described by an axial-vector order parameter $\vec{\eta}$. The order parameters $\vec{\xi}$ and $\vec{\eta}$ have the same symmetry, and the lowest order bilinear coupling favored them to be parallel to each other [7].

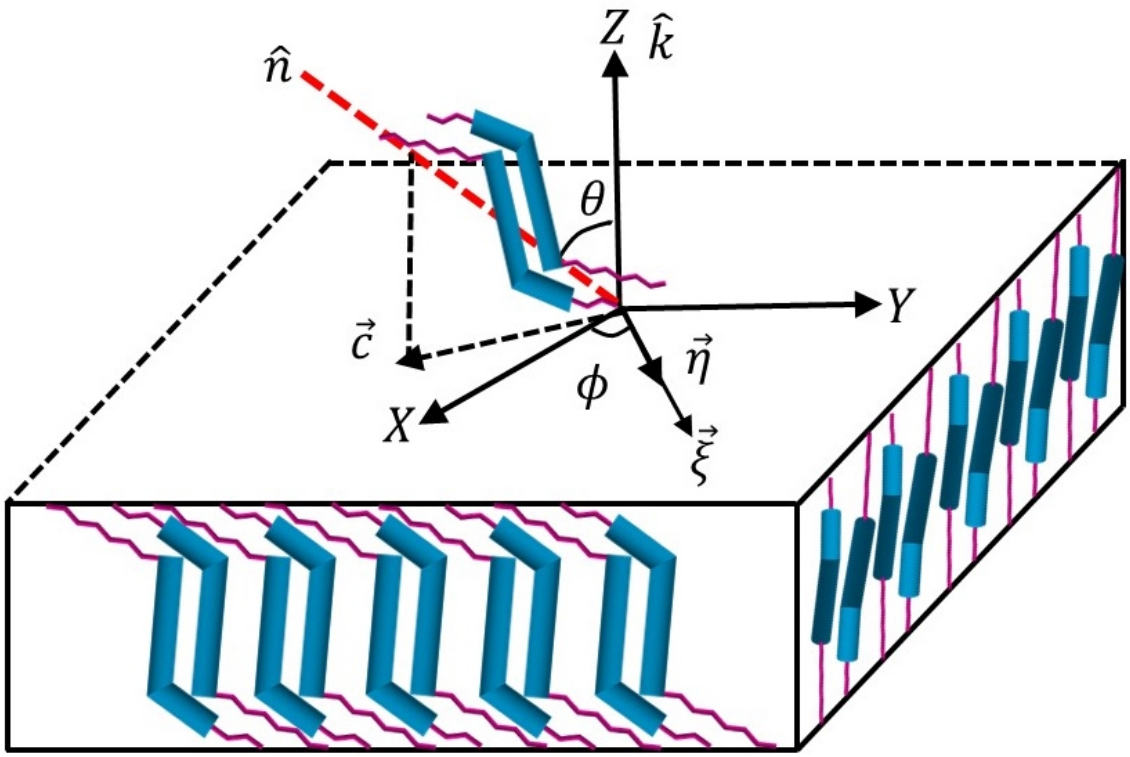

Figure 4.13: The zigzag configuration of BCHS molecules in a layer of tilted smectic phase. The order parameters $\vec{\xi}$, $\vec{\eta}$ and $\vec{c}$ denote the tilt, axial-vector the tilt, axial-vector order and c-director in the plane of the layer.

The quadratic coupling of the electric field due to the dielectric anisotropy of the layers could lead to a structural transition in this system. The bent-shape of the molecules led to large biaxiality of the layers characterized by three principle dielectric constants $\epsilon_1 < \epsilon_2 < \epsilon_3$, where ϵ_3, ϵ_1 denote the principle dielectric constant parallel to the director and perpendicular to the tilt plane, respectively. The intermediate value ϵ_2 corresponds to the principal component in the tilt plane, respectively. To account for the observed electric field effects, we assumed that in the smectic layers, the principle dielectric constant parallel to the director is maximum while that along the axial-vector order parameter is minimum.

4.6.1 Effective dielectric anisotropy in the SmC_A phase

For a planar-aligned sample in the higher-temperature SmC_A phase, the smectic layers were assumed to have a bookshelf geometry between the glass plates. The planar

anchoring of the molecules on the substrates favors the tilt plane of the molecules in the layer to be parallel to the glass plates and perpendicular to the applied electric field (Figure 4.14 bottom). Then, due to the dielectric anisotropy of the SmC_A layers, the applied electric field tended to reorient the molecules such that the layers has a maximum projection of its dielectric indicatrix along the field. Beyond a threshold field, the decrease in the intensity as found experimentally was attributed to the orientational transition of the molecules in the layers. With increasing field, the reorientation of the molecules about their long axes as well as the reorientation of the director about the layer normal occurred simultaneously.

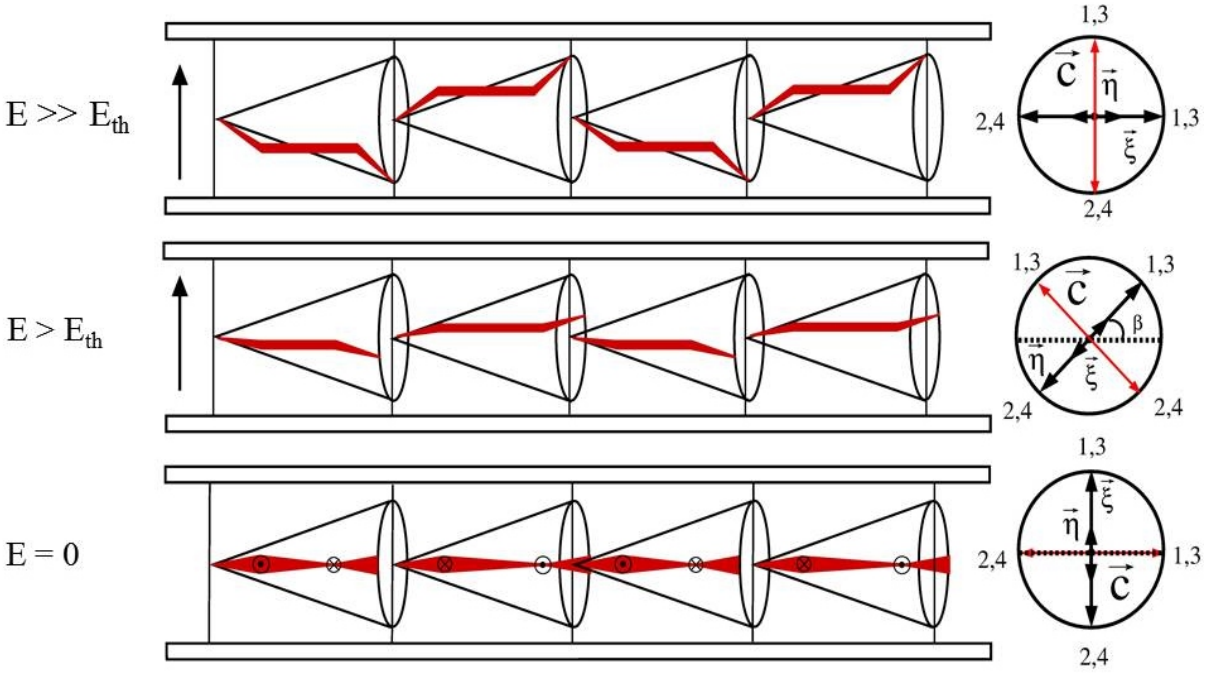

Figure 4.14: The schematic representation of the molecular organization at the mid-plane of the cell in the smectic layers in bookshelf geometry between two glass plates at different electric fields. The circles on the right side represent the orientation of the vectors $\vec{\xi}$, $\vec{\eta}$ and $\vec{c}$ (red arrow) in successive layers viewed along the layer normal. The number 1,2,3,...represent the sequence of the layers.

The dielectric tensor in 3D can be written as [19]

$$\epsilon_{ij} = A^{-1}\epsilon A$$

where

$$A = \begin{pmatrix} \cos\psi\cos\phi - \cos\theta\sin\phi\sin\psi & \cos\psi\sin\phi + \cos\theta\cos\phi\sin\psi & \sin\psi\sin\theta \\ -\sin\psi\cos\phi - \cos\theta\sin\phi\cos\psi & -\sin\psi\sin\phi + \cos\theta\cos\phi\cos\psi & \cos\psi\sin\theta \\ \sin\theta\sin\phi & -\sin\theta\cos\phi & \cos\theta \end{pmatrix}$$

The transpose of A is given by

$$A^{-1} = \begin{pmatrix} \cos\psi\cos\phi - \cos\theta\sin\phi\sin\psi & -\sin\psi\cos\phi - \cos\theta\sin\phi\cos\psi & \sin\theta\sin\phi \\ \cos\psi\sin\phi + \cos\theta\cos\phi\sin\psi & -\sin\psi\sin\phi + \cos\theta\cos\phi\cos\psi & -\sin\theta\cos\phi \\ \sin\psi\sin\theta & \cos\psi\sin\theta & \cos\theta \end{pmatrix}$$

$$\epsilon = \begin{pmatrix} \epsilon_1 & 0 & 0 \\ 0 & \epsilon_2 & 0 \\ 0 & 0 & \epsilon_3 \end{pmatrix}$$

Therefore, the dielectric tensor in 3D is given by,

$$\epsilon_{ij} = \begin{pmatrix} \epsilon_{11} & \epsilon_{12} & \epsilon_{13} \\ \epsilon_{21} & \epsilon_{22} & \epsilon_{23} \\ \epsilon_{31} & \epsilon_{32} & \epsilon_{33} \end{pmatrix}$$

where,

$$\epsilon_{11} = \epsilon_1(\cos\phi\cos\psi - \cos\theta\sin\phi\sin\psi)^2 + \epsilon_2(\cos\theta\sin\phi\cos\psi + \cos\phi\sin\psi)^2 + \epsilon_3\sin^2\theta\sin^2\phi$$

$$\epsilon_{12} = (\epsilon_1\cos^2\psi + \epsilon_2\sin^2\psi)\sin\phi\cos\phi + (\epsilon_1 - \epsilon_2)\cos\theta\cos 2\phi\sin\psi\cos\psi - \sin\phi\cos\phi[(\epsilon_1\sin^2\psi + \epsilon_2\cos^2\psi)\cos^2\theta - \epsilon_3\sin^2\theta]$$

$$\epsilon_{13} = (\epsilon_1 - \epsilon_2)\sin\theta\cos\phi\sin\psi\cos\psi - \sin\theta\cos\theta\sin\phi[\epsilon_1\sin^2\psi + \epsilon_2\cos^2\psi - \epsilon_3]$$

$$\epsilon_{21} = (\epsilon_1 \cos^2\psi + \epsilon_2 \sin^2\psi)\sin\phi\cos\phi + \cos\theta\cos 2\phi\sin\psi\cos\psi(\epsilon_1 - \epsilon_2) - \sin\phi\cos\phi[\cos^2\theta(\epsilon_1\sin^2\psi + \epsilon_2\cos^2\psi) + \epsilon_3\sin^2\theta]$$

$$\epsilon_{22} = \epsilon_1(\sin\phi\cos\psi + \cos\theta\cos\phi\sin\psi)^2 + \epsilon_2(\cos\theta\cos\phi\cos\psi - \sin\phi\sin\psi)^2 + \epsilon_3\sin^2\theta\cos^2\phi$$

$$\epsilon_{23} = (\epsilon_1 - \epsilon_2)\sin\theta\sin\phi\sin\psi\cos\psi + (\epsilon_1\sin^2\psi + \epsilon_2\cos^2\psi - \epsilon_3)\sin\theta\cos\theta\cos\phi$$

$$\epsilon_{31} = (\epsilon_1 - \epsilon_2)\sin\theta\cos\phi\sin\psi\cos\psi - \sin\theta\cos\theta\sin\phi(\epsilon_1\sin^2\psi + \epsilon_2\cos^2\psi - \epsilon_3)$$

$$\epsilon_{32} = (\epsilon_1 - \epsilon_2)\sin\theta\sin\phi\sin\psi\cos\psi + (\epsilon_1\sin^2\psi + \epsilon_2\cos^2\psi - \epsilon_3)\sin\theta\cos\theta\cos\phi$$

$$\epsilon_{33} = (\epsilon_1\sin^2\psi + \epsilon_2\cos^2\psi)\sin^2\theta + \epsilon_3\cos^2\theta$$

For a given layer, $\psi = 0$ and $\phi = \frac{\pi}{2}$ the dielectric tensor can be written as,

$$\epsilon^1_{ij} = \begin{pmatrix} \epsilon_2\cos^2\theta + \epsilon_3\sin^2\theta & 0 & -\epsilon_2\cos\theta\sin\theta + \epsilon_3\cos\theta\sin\theta \\ 0 & \epsilon_1 & 0 \\ -\epsilon_2\cos\theta\sin\theta + \epsilon_3\cos\theta\sin\theta & 0 & \epsilon_2\sin^2\theta + \epsilon_3\cos^2\theta \end{pmatrix}$$

For the adjacent layer, retaining anticlinic arrangement, $\psi = 0$ and $\phi = -\frac{\pi}{2}$ the dielectric tensor can be written as

$$\epsilon^2_{ij} = \begin{pmatrix} \epsilon_2\cos^2\theta + \epsilon_3\sin^2\theta & 0 & \epsilon_2\cos\theta\sin\theta - \epsilon_3\cos\theta\sin\theta \\ 0 & \epsilon_1 & 0 \\ \epsilon_2\cos\theta\sin\theta - \epsilon_3\cos\theta\sin\theta & 0 & \epsilon_2\sin^2\theta + \epsilon_3\cos^2\theta \end{pmatrix}$$

Thus, the dielectric tensor in the SmC_A phase can be written by averaging over adjacent layers as [20]

$$\epsilon^{12}_{ij} = \frac{\epsilon^1_{ij} + \epsilon^2_{ij}}{2}$$

$$\epsilon_{ij}^{12} = \begin{pmatrix} \epsilon_2 \cos^2\theta + \epsilon_3 \sin^2\theta & 0 & 0 \\ 0 & \epsilon_1 & 0 \\ 0 & 0 & \epsilon_2 \sin^2\theta + \epsilon_3 \cos\theta^2 \end{pmatrix}$$

Here, we assumed the Z-axis along with the layer normal, the Y-axis is normal to the glass plates of the cell, and the X-axis is in the plane of the glass plates orthogonal to both the Z- and Y-axis and θ is the tilt angle. However, in the presence of the applied field along the Y-axis, the field tend to align the tilt plane of the molecules due to the dielectric anisotropy of the layers. Whereas, the strong anchoring on the glass plates tend to retain the tilt plane of the molecules parallel to themselves. Beyond the threshold field, the tilt plane in successive layers made an angle β with the XZ-plane while retaining anticlinic organization in the SmC_A phase (Figure 4.14 middle). The angle β at the mid-plane of the cell (β_m) tended to the value of $\pi/2$ at a very high field (Figure 4.14 top). Therefore, in the presence of the electric field the dielectric tensor is given by,

$$\epsilon'_{ij} = B\epsilon_{ij}B^{-1}$$

where

$$B = \begin{pmatrix} \cos\beta & -\sin\beta & 0 \\ \sin\beta & \cos\beta & 0 \\ 0 & 0 & 1 \end{pmatrix}$$

And the transpose of matrix B is given by,

$$B^{-1} = \begin{pmatrix} \cos\beta & \sin\beta & 0 \\ -\sin\beta & \cos\beta & 0 \\ 0 & 0 & 1 \end{pmatrix}$$

And

$$\epsilon_{ij} = \begin{pmatrix} \epsilon_{xx} & 0 & 0 \\ 0 & \epsilon_{yy} & 0 \\ 0 & 0 & \epsilon_{zz} \end{pmatrix}$$

where

$$\epsilon_{xx} = \epsilon_2 \cos^2\theta + \epsilon_3 \sin^2\theta$$

$$\epsilon_{yy} = \epsilon_1$$

$$\epsilon_{zz} = \epsilon_2 \sin^2\theta + \epsilon_3 \cos^2\theta$$

where

$$\epsilon'_{ij} = \begin{pmatrix} \epsilon_{xx}\cos^2\beta + \epsilon_{yy}\sin^2\beta & \epsilon_{xx} - \epsilon_{yy}\sin\beta\cos\beta & 0 \\ \epsilon_{xx} - \epsilon_{yy}\sin\beta\cos\beta + \epsilon_{xx}\sin^2\beta + \epsilon_{yy}\cos^2\beta & 0 & 0 \\ 0 & 0 & \epsilon_{zz} \end{pmatrix}$$

Therefore the electric field energy is given by,

$$f_e = -\frac{1}{2}\vec{D}\cdot\vec{E}$$

$$= -\frac{1}{2}\epsilon_0 \cdot \epsilon'_{ij} \cdot \vec{E} \cdot \vec{E}$$

where

$$\vec{E} = \begin{pmatrix} 0 \\ E \\ 0 \end{pmatrix}$$

where

$$\begin{aligned}\epsilon_{xx} - \epsilon_{yy} &= \epsilon_2 \cos^2\theta + \epsilon_3 \sin^2\theta - \epsilon_1 \\ &= \epsilon_2 \cos^2\theta + \epsilon_3 \sin^2\theta - \epsilon_1(\sin^2\theta + \cos^2\theta) \\ &= (\epsilon_2 - \epsilon_1)\cos^2\theta + (\epsilon_3 - \epsilon_1)\sin^2\theta \\ &= \delta\epsilon \cos^2\theta + \Delta\epsilon \sin^2\theta = \widetilde{\Delta\epsilon}\end{aligned}$$

where $\Delta\epsilon = (\epsilon_3 - \epsilon_1)$ and $\delta\epsilon = (\epsilon_2 - \epsilon_1)$ are dielectric anisotropy and dielectric biaxiality of the sample in the SmC_A phase.

4.6.2 Fréedericksz type transition in the SmC_A phase

Therefore, the free energy per unit area of the sample cell in the presence of an applied electric field can be written as [21]

$$f = \frac{1}{2}K\left(\frac{d\beta}{dy}\right)^2 - \frac{1}{2}\epsilon_0 E^2\left[\widetilde{\Delta\epsilon}\sin^2\beta + \epsilon_1\right] \tag{4.7}$$

Here, K is a suitable elastic constant corresponding to the distortion of the tilt planes of the molecules across the sample cell and the last term corresponds to the free energy density in the presence of the electric field. $\widetilde{\Delta\epsilon}$ is the effective dielectric anisotropy of the sample in this configuration.
We define,

$$\beta = \beta_m \cos\left(\frac{\pi y}{d}\right)$$

$$\frac{d\beta}{dy} = -\beta_m \frac{\pi}{d}\sin\left(\frac{\pi y}{d}\right)$$

Assuming β is small near the threshold,

$$\sin\beta \simeq \beta \simeq \beta_m \cos\left(\frac{\pi y}{d}\right)$$

The free energy density,

$$f_e = -\frac{1}{2}\epsilon_0 E^2\Big[\widetilde{\Delta\epsilon}\beta_m^2\cos^2(\frac{\pi y}{d}) + \epsilon_1\Big] + \frac{1}{2}k\beta_m^2\Big(\frac{\pi}{d}\Big)^2\sin^2\Big(\frac{\pi y}{d}\Big) \tag{4.8}$$

Therefore, the total free energy can be written as,

$$F = \int_{-\frac{d}{2}}^{\frac{d}{2}} f_e dy$$

$$F = \int_{-\frac{d}{2}}^{\frac{d}{2}}\Big[-\frac{1}{2}\epsilon_0 E^2\epsilon_1 - \frac{1}{4}\epsilon_0\widetilde{\Delta\epsilon}E^2\beta_m^2\Big\{\cos\Big(\frac{2\pi y}{d}\Big) - 1\} + \frac{1}{4}k\beta_m^2\Big(\frac{\pi}{d}\Big)^2\{1-\cos\Big(\frac{2\pi y}{d}\Big)\Big\}\Big]dy$$

$$= -\frac{1}{2}\epsilon_0 E^2\epsilon_1 d - \frac{1}{4}\epsilon_0\widetilde{\Delta\epsilon}E^2\beta_m^2 d + \frac{1}{4}k\beta_m^2\Big(\frac{\pi}{d}\Big)^2 d$$

$$F = -\frac{1}{2}\epsilon_0 E^2\epsilon_1 d - \frac{1}{4}\beta_m^2 d\Big\{\epsilon_0\widetilde{\Delta\epsilon}E^2 - k\Big(\frac{\pi}{d}\Big)^2\Big\}$$

The free energy density in Equation 4.7 is analogous to that of a planar-aligned Nematic sample under electric field and predicts a Fréedericksz type transition above a threshold field for $\widetilde{\Delta\epsilon} > 0$. The threshold field is given by,

$$\boxed{E_{th} = \frac{\pi}{d}\sqrt{\frac{k}{\epsilon_0\widetilde{\Delta\epsilon}}}} \tag{4.9}$$

The Frèedericksz voltage is given by

$$\boxed{V_{th} = \pi\sqrt{\frac{k}{\epsilon_0\widetilde{\Delta\epsilon}}}} \tag{4.10}$$

Assuming that the elastic constant $K \sim 10^{-10}\ N$ in the anticlinic SmC_A phase and $\widetilde{\Delta\epsilon} \sim 0.2$, the calculated threshold fields from the above equation was quite close to

the experimentally measured thresholds field in the SmC_A phase. We also calculated the β-profile across the thickness of the sample cell by assuming the strong anchoring condition, β=0 at both the bounding glass plates. The minimization of free energy with respect to β gave a non-linear Euler-Lagrange equation, which was solved using Mathematica.

$$k\Big(\frac{d^2\beta}{dy^2}\Big) + \epsilon_0\widetilde{\Delta\epsilon}E^2\sin\beta\cos\beta = 0$$

Multiplying both sides by $\frac{d\beta}{dy}$,

$$k\Big(\frac{d^2\beta}{dy^2}\Big)\frac{d\beta}{dy} + \epsilon_0\widetilde{\Delta\epsilon}E^2\sin\beta\cos\frac{d\beta}{dy} = 0$$

$$\frac{d}{dy}\Big[\frac{1}{2}k\Big(\frac{d\beta}{dy}\Big)^2 + \frac{1}{2}\epsilon_0\widetilde{\Delta\epsilon}E^2\sin^2\beta\Big] = 0$$

$$\frac{1}{2}k\Big(\frac{d\beta}{dy}\Big)^2 + \frac{1}{2}\epsilon_0\widetilde{\Delta\epsilon}E^2\sin^2\beta = constant$$

Using the boundary condition, $\beta = 0$ at y $= \pm\frac{d}{2}$ and $y = 0$at $\beta = \beta_m$ First integral is given by,

$$k\Big(\frac{d\beta}{dy}\Big)^2 + \epsilon_0\widetilde{\Delta\epsilon}E^2\Big(\sin^2\beta - \sin^2\beta_m\Big) = 0$$

$$\frac{d\beta}{dy} = \sqrt{\frac{\widetilde{\Delta\epsilon}E^2}{k}\Big(\sin^2\beta_m - \sin^2\beta\Big)}$$

We integrate over half of the thickness of the liquid crystal cell.

$$\int_0^{\beta_m}\frac{1}{\sqrt{(sin^2\beta_m - sin^2\beta)}}d\beta = \frac{\pi}{d}\Big(\frac{E}{E_{th}}\Big)\int_{-d/2}^{0}dy$$

$$\int_0^{\beta_m} \frac{1}{\sqrt{(sin^2\beta_m - sin^2\beta)}} d\beta = \frac{\pi}{2}\Big(\frac{E}{E_{th}}\Big)$$

R.H.S,

$$\int_0^{\beta_m} \frac{1}{\sqrt{\big(sin^2\beta_m - sin^2\beta\big)}} d\beta$$

$$\int_0^{\beta_m} \frac{1}{\sin\beta_m \sqrt{(1 - \frac{sin^2\beta}{sin^2\beta_m})}} d\beta$$

Let's assume that

$$\sin u = \frac{\sin\beta}{\sin\beta_m}$$

the above equation become

$$\int_0^{\pi/2} \frac{1}{\sqrt{1 - \sin^2 u \sin^2\beta_m}} d\beta$$

which is the elliptic integral of the first kind and defined as

$$\int_0^{\pi/2} \frac{1}{\sqrt{1 - k^2 \sin^2 u}} du = K(\sin\beta_m)$$

where $k = \sin\beta_m$

$$\Rightarrow \boxed{\frac{\pi}{2}(\frac{E}{E_{th}}) = K(\sin\beta_m)} \tag{4.11}$$

Using the above elliptical integral of the first kind, we calculated the β profile across the thickness of a liquid crystal cell of thickness d using Mathematica. We assumed the strong anchoring $\beta = 0$ at both boundary glass plates. Figure 4.15a shows the profile of β across the cell for different fields beyond the threshold value. The β-profile depicts, the tilt planes of the molecules in successive layers reorient above threshold field, keeping anticlinic arrangement in successive layers. For a given field, β attained

the maximum value β_m at the mid-plane of the cell, and its value increased with increasing field. Figure 4.15b shows the variation of β_m with an increasing applied field.

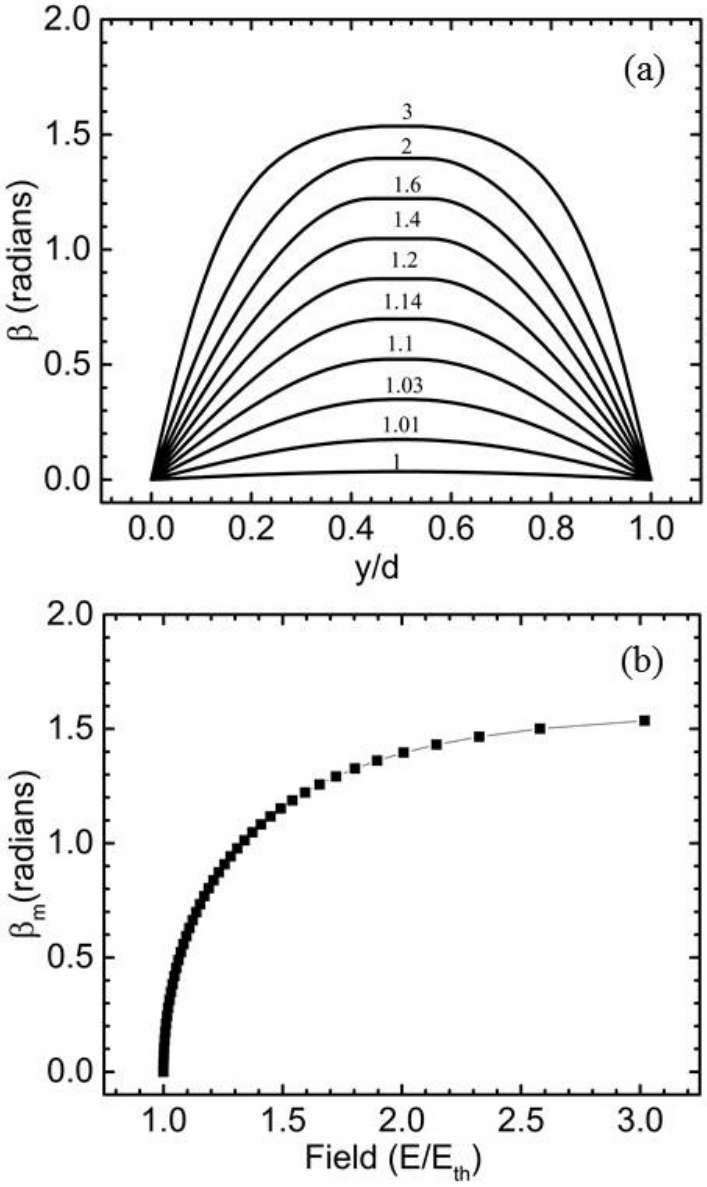

Figure 4.15: (a) The variation of β across the sample cell at different normalized electric fields. (b) The variation of the maximum value of β at the mid plane (β_m) as a function of the $\frac{E}{E_{th}}$.

4.7 Theoretically predicted changes in effective birefringence

Similar to the dielectric tensor, the refractive tensor in 3D for a planar-aligned sample in the SmC_A phase can be written by averaging over the adjacent layer as:

$$n_{ij}^{12} = \frac{n_{ij}^{1} + n_{ij}^{2}}{2}$$

$$n_{ij}^{12} = \begin{pmatrix} n_2 \cos^2\theta + n_3 \sin^2\theta & 0 & 0 \\ 0 & n_1 & 0 \\ 0 & 0 & n_2 \sin^2\theta + n_3 \cos^2\theta \end{pmatrix}$$

In the presence of an applied field, the tilt plane of the molecules make an angle β to the horizontal plane XZ. Then, for a given point at a distance r, the elliptic equation is given by

$$\frac{r^2 \cos^2\beta}{n_x^2} + \frac{r^2 \sin^2\beta}{n_y^2} = 1$$

$$r = \frac{n_x n_y}{\sqrt{n_y^2 \cos^2\beta + n_x^2 \sin^2\beta}}$$

Therefore, the local effective birefringence at a given point is given by,

$$(\Delta n)_{eff} = n_z - r$$

$$(\Delta n)_{eff} = n_z - \frac{n_x n_y}{\sqrt{n_y^2 \cos^2\beta + n_x^2 \sin^2\beta}}$$

The effective path difference is given by

$$\Delta\phi = \frac{2\pi}{\lambda}\int_{-d/2}^{d/2}(n_z - r)dy$$

$$= \frac{2\pi}{\lambda}\int_{-d/2}^{d/2}\left(n_z - \frac{n_x n_y}{\sqrt{n_y^2\cos^2\beta + n_x^2\sin^2\beta}}\right)dy$$

Changing the variable from y to β,

$$dy = \frac{dy}{d\beta}d\beta$$

$$= \frac{d}{\pi}\frac{1}{E'}\frac{1}{\sqrt{sin^2\beta_m - sin^2\beta}}$$

where

$$E' = \frac{E}{E_{th}}$$

$$\Delta\phi = \frac{4d}{\lambda}\frac{1}{E'}\int_0^{\beta_m}\left(n_z - \frac{n_x n_y}{\sqrt{n_y^2\cos^2\beta + n_x^2\sin^2\beta}}\right)\frac{1}{\sqrt{1-\frac{\sin^2\beta}{\sin^2\beta_m}}}\frac{1}{\sin\beta_m}d\beta$$

$$\Delta\phi = \frac{4d}{\lambda}\frac{1}{E'}\int_0^{\beta_m}\left(n_z - \frac{n_x}{\sqrt{1+\frac{(n_x^2-n_y^2)\sin^2\beta}{n_y^2}}}\right)\frac{1}{\sqrt{1-\frac{\sin^2\beta}{\sin^2\beta_m}}}\frac{1}{\sin\beta_m}d\beta$$

where

$$\left\{\sin u = \frac{\sin\beta}{\sin\beta_m}\right\}$$

$$\Delta\phi = \frac{4d}{\lambda}\frac{1}{E'}\int_0^{\pi/2}\left(n_z - \frac{n_x}{\sqrt{1+\nu k^2\sin^2 u}}\right)\frac{1}{\sqrt{1-k^2\sin^2 u}}du$$

$$\Delta\phi = \frac{4d}{\lambda}\frac{1}{E'}\int_0^{\pi/2} n_z\frac{1}{\sqrt{1-k^2\sin^2 u}}du - \int_0^{\pi/2}\frac{n_x}{\sqrt{1+\nu k^2\sin^2 u}}\frac{1}{\sqrt{1-k^2\sin^2 u}}du$$

$$\Delta\phi = \frac{4d}{\lambda}\frac{1}{E'}\left[n_z\int_0^{\pi/2}\frac{1}{\sqrt{1-k^2\sin^2 u}}du - \int_0^{\pi/2} n_x\frac{1}{\sqrt{1+\nu k^2\sin^2 u}}\frac{1}{\sqrt{1-k^2\sin^2 u}}du\right]$$

where

$$\nu = \frac{n_x^2 - n_y^2}{n_y^2}$$

$$\boxed{\Delta\phi = \frac{4d}{\lambda}\frac{1}{E'}\left[n_z\frac{EllipticK\left[\frac{k^2}{k^2-1}\right]}{\sqrt{1-k^2}} - n_x\frac{EllipticK\left[\frac{k^2(1+\nu)}{k^2-1}\right]}{\sqrt{1-k^2}}\right]} \tag{4.12}$$

Therefore, the effective birefringence of the sample is given by,

$$\Delta n = \frac{\lambda\Delta\phi}{2\pi d} \tag{4.13}$$

$$\boxed{\Delta n = \frac{2\left[n_z\frac{EllipticK\left[\frac{k^2}{k^2-1}\right]}{\sqrt{1-k^2}} - n_x\frac{EllipticK\left[\frac{k^2(1+\nu)}{k^2+1}\right]}{\sqrt{1-k^2}}\right]}{\pi E'}} \tag{4.14}$$

where the principle refractive indices are given by,

$$n_x = n_2\cos^2\theta + n_3\sin^2\theta = 0.7n_2 + 0.3n_3$$

$$n_y = n_1$$

$$n_z = n_2 \sin^2\theta + n_3 \cos^2\theta = 0.3n_2 + 0.7n_3$$

We also calculated the effective birefringence of the sample based on the calculated profile of β. For a given value of β, using the above principle refractive indices and the experimentally measured tilt angle, we calculated the effective birefringence changes with applied field of a planar-aligned sample in the higher-temperature SmC_A phase.

We calculated the effective birefringence changes with an applied field for compound 4OC18 in the higher-temperature SmC_A phase as shown in Figure 4.16. The estimated molecular length of compound 4OC18 is about 53 Å and the calculated effective layer spacing in the SmC_A phase is about 42.6 Å. Therefore, the calculated tilt angle from the XRD data is about 36.5 degrees. To calculate the effective birefringence of compound 4OC18, we assumed the principle refractive indices of a layer as, $n_3 = 1.75$, $n_2 = 1.52$ and $n_1 = 1.56$. The principle refractive indices of a layer are given as:

$$n_x = 0.65n_2 + 0.35n_3 = 1.6$$
$$n_y = n_1 = 1.56$$
$$n_z = 0.35n_2 + 0.65n_3 = 1.6695$$
$$\nu = 0.05259$$

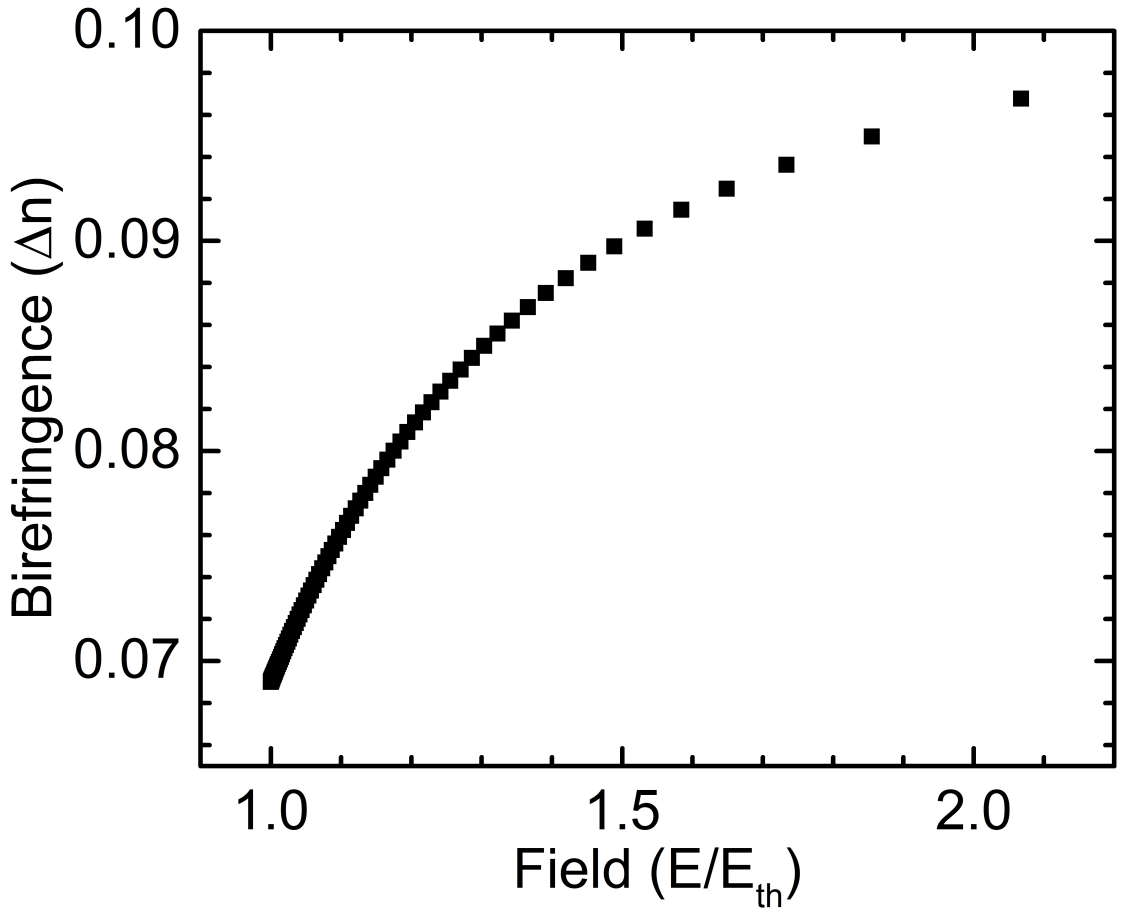

Figure 4.16: The theoretically estimated effective birefringence of compound 4OC18 of a planar-aligned sample of thickness 5 μm in higher-temperature SmC_A phase as a function of E/E_{th} at a constant temperature.

The molecular length and the layer spacing in the higher-temperature SmC_A phase of the compound A14 were about 53 Å and 44.3 Å, respectively. Therefore, the tilt angle in the higher-temperature phase was given by, $\theta = \cos^{-1}\frac{d}{l}$, where d is the layer spacing, calculated from XRD data and l is the molecular length, calculated by ChemDraw in minimized energy configuration. Therefore, $\theta = cos^{-1}(\frac{44.3}{53})$, $\theta = 33.29$ degree.

For the calculation of the birefringence changes with applied field of compound

A14, we assumed the principle refractive indices of a layer as,

$$n_3 = 1.7, n_2 = 1.5 and n_1 = 1.48$$

$$n_x = 0.7n_2 + 0.3n_3 = 1.56$$

$$n_y = n_1 = 1.48$$

$$n_z = 0.3n_2 + 0.7n_3 = 1.64$$

$$\nu = 0.11103$$

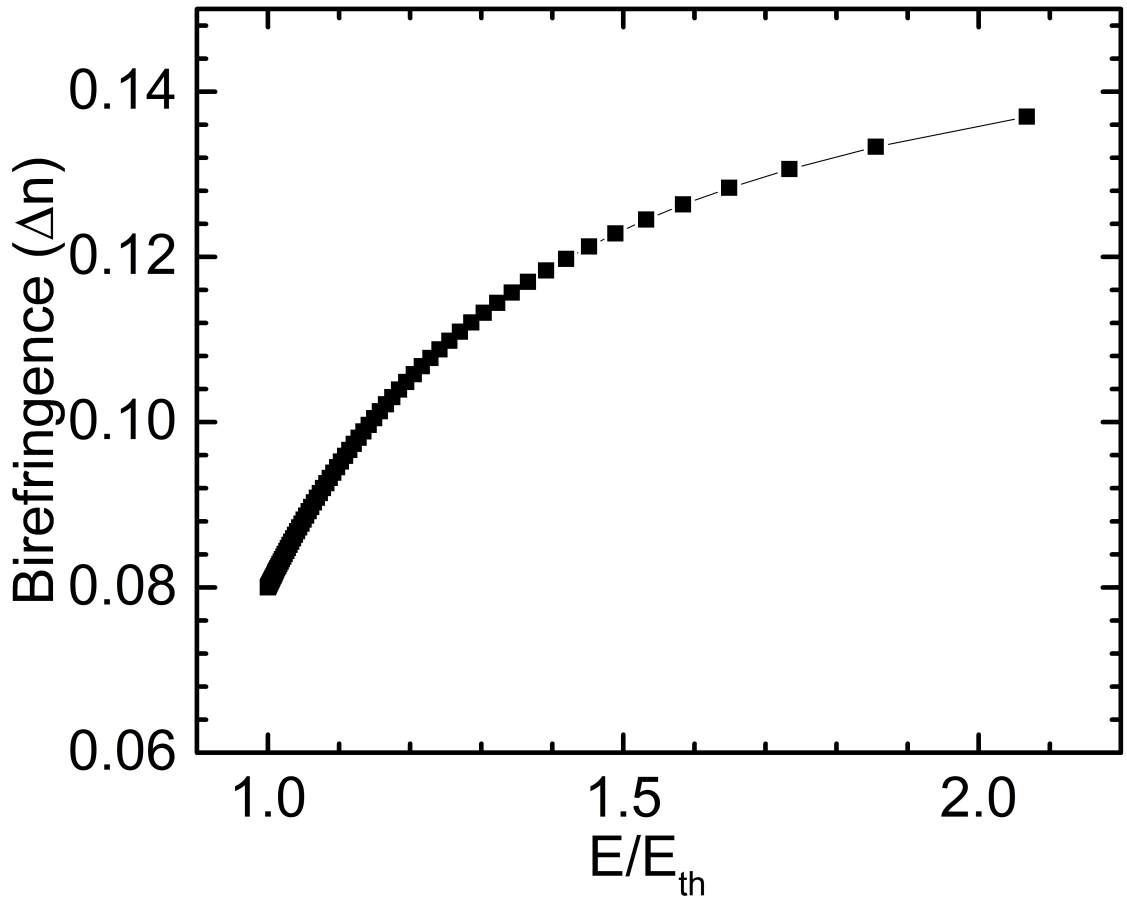

Figure 4.17: The theoretically calculated effective birefringence of compound A14 of a planar-aligned sample of thickness 5 μm in the higher-temperature SmC_A phase as a function of E/E_{th} at a constant temperature.

With these parameters and equations, we had calculated the estimated effective birefringence changes of the sample using Mathematica under the application of an AC electric field. Figure 4.17 shows the variation of the effective birefringence of

compound A14 in the higher-temperature phase SmC_A phase with an applied field.

4.8 Comparison with experimental data

For comparison with the experimental data, theoretically calculated effective birefringence for both compounds as a function of the applied field is shown in Figure 4.18. The model accounts for the observed threshold behavior in the changes of the effective birefringence of the samples with a field in the higher-temperature SmC_A phase. The theoretical values compared well with the experimental data near the threshold field, though it deviate significantly at higher fields. In this model, we assumed the perfect alignment of the sample with the bookshelf geometry of the layers. However, in the experimental liquid crystal cell, the alignment was far from perfect, and there were multiple domains with defects in the texture. The deviations between the experimental and theoretical values possibly arose because of the presence of these defects in the texture. The onset of electro-hydrodynamic instability at high fields (above 10 $V/\mu m$) also led to further complications in the measurements of the birefringence of the sample.

The existence of the Frèedericksz transition in the SmC phase was reported [22] earlier for a sample consisting of rod-like molecules with positive dielectric anisotropy. This kind of transition was also observed in anticlinic liquid crystals consisting of chiral molecules [23, 24]. However, due to bent-core nature of the molecules, the effective dielectric anisotropy ($\widetilde{\Delta\epsilon}$) could be positive even with negative dielectric anisotropy ($\Delta\epsilon < 0$) with a strong dielectric biaxiality ($\delta\epsilon > 0$) as can be seen from Equation 4.7, the effective dielectric anisotropy depends on dielectric anisotropy ($\Delta\epsilon$) and dielectric biaxiality ($\delta\epsilon$) and tilt angle for the studied samples.

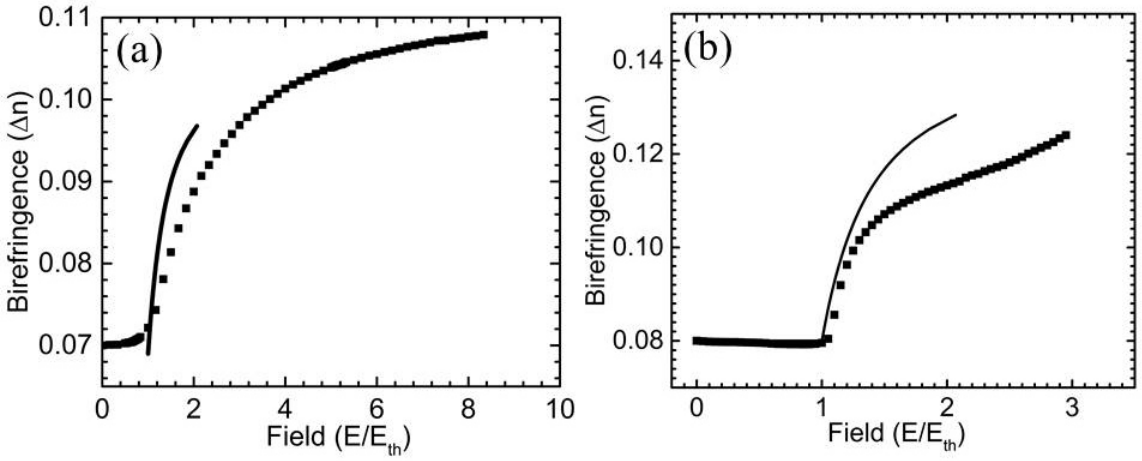

Figure 4.18: The effective birefringence of (a) compound 4OC18 and (b) compound A14 for a planar-aligned sample in the higher-temperature SmC_A phase with increasing amplitude of the applied electric field of frequency 1 kHz. The data points are experimental values whereas the solid line shows the theoretically calculated value of the effective birefringence using our model.

4.9 Conclusions

In summary, we have presented the experimental and theoretical results for the field effects on the structure of the observed mesophases of two compounds (4OC18 and A14) consisting of BCHS molecules. Experimental results clearly demonstrated that the layers in both the smectic phases did not possess any net electric polarization. In spite of the absence of polarization in the layers, both the phases exhibited an electro-optic response which is quadratic in the field. The electro-optic response arose from the field-induced reorientation of the molecules in the layers. For both the compounds, a field-induced Fréedericksz type transition was observed in the SmC_A phase. A simple theoretical model to account for the observed electro-optic behavior in the higher-temperature SmC_A phase of the studied compounds was developed. The coexisting degenerate structures in the SmC_I phase at zero fields reorient under field tending to restore a uniform fan texture.

Bibliography

[1] P. Sathyanarayana, S. Radhika, B. K. Sadashiva, and S. Dhara, *Soft Matter*, **8**, 2322 (2012).

[2] M. Alaasar, *Liq. Cryst.*, **43**, 2208-2243 (2016).

[3] S. Radhika, H. T. Srinivasa, and B. K. Sadashiva, *Liq. Cryst.*, **38**, 785 (2011).

[4] M. Alaasar, S. Poppe, C. Kerzig, C. Klopp, A. Eremin, and C. Tschierske, *J. Mater. Chem. C*, **5**, 8454-8468 (2017).

[5] D. D. Sarkar, R. Deb, N. Chakraborty, and V.S. R. Nandiraju, *Liq. Cryst.*, **39**, 1003-1010 (2012).

[6] E.R. Cioanca, E. L. Epure, I. C., G. Lisa, D. Wilson, N. Hurduc, and D. Scutaru, *Mol. Cryst. Liq. Cryst.*, **537**, 51-63 (2011).

[7] D. Malkar, B.K. Sadashiva, and A. Roy, *Soft Matter*, **12**, 4960 (2016).

[8] M. Monika, V. Prasad, and N.G. Nagaveni, *Liq. Cryst.*, **42**, 1490–1505 (2015).

[9] E. N. Keller, E. Nachaliel, D. Davidov, and Christine Böffel, *Phys. Rev. A*, **34**, 4363-4369 (1986).

[10] W. H. de Jeu, *Physical Properties of liquid crystal Materials*, Gordon and Breach, Science Publishers Ltd. (1980).

[11] K. Miyasato, S. Abe, H. Takezoe, A. Fukuda, and E. Kuze, *Jpn. J. App. Phys.*, **22**, L661-L663 (1983).

[12] D. Malkar, M. Monika, V.Prasad, and A. Roy, *Phys. Rev. E*, **101**, 012701 (2020).

[13] I. Dierking, *Textures of Liquid Crystals.*, WILEY-VCH Verlag GmbH and Co. KGaA, Weinheim Ltd. (2003).

[14] S. Chandrasekhar, *Liquid Crystals*, (Cambridge University Press, Cambridge, 1992).

[15] A. Jakli, and A. Saupe, *One- and two-dimensional fluids: physical properties of smectic, lamellar, and columnar liquid crystals*, CRC Press (2006).

[16] H. Takezoe, and L. Eremin, *Bent-shaped liquid crystals: structures and physical properties*, CRC Press (2017).

[17] A. Roy, N. V. Madhusudana, P. Toledano, and A. M. Figueiredo Neto, *Phys. Rev. Lett.*, **82**, 1466-1469 (1999).

[18] V. L. Lorman, A. A. Bulbitch, and P. Toledano, *Phys. Rev. E*, **49**, 1367-1374 (1994).

[19] H. Goldstein, C.P. Poole, J.L Safko *Handbook of Liquid Crystals*, (Addison-Wesely, **3**rd **ed.** 2001).

[20] J. W. Goodby, P. J. Collings, T. Kato, C. Tschierske, H. F. Gleeson, and P. Raynes, *Handbook of Liquid Crystals*, (Germany, **4** 2014).

[21] P. G. de Gennes, and J. Prost, *The Physics of Liquid Crystals*, (Clarendon, Oxford, 1994).

[22] G. Pelzl, P. Kolbe, Preukschas, S.Diele, and D. Demus, *Mol. Cryst. Liq. Cryst.*, **53**, 167-180 (1979).

[23] B. Wen, S. Zhang, S. S. Keast, M. E. Neubert, P. L. Taylor, and C. Rosenblatt, *Phys. Rev. E*, **62**, 8152-8128 (2000).

[24] T. Qian, and P. L. Taylor *Phys. Rev. E*, **60**, 2978-2984 (1999).

Chapter 5

THE deVries SmA-PHASE OF BCHS MOLECULES

5.1 Introduction

The rod-like molecules often exhibit smectic phases in which the molecules self-organized in stacks of fluid layers [1]. A variety of smectic phases had been observed for such molecules and the molecular organization in the most common smectic phases had been discussed in chapter 1. In their smectic phases, the rod-like molecules rotate almost freely about their long axis (Figure 5.1) giving rise to a uniaxial local symmetry about the director $\hat{n}$ [2].

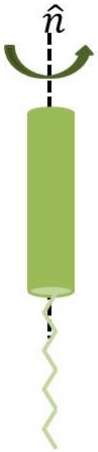

Figure 5.1: A freely rotating rod-like molecule about its long axis.

In the conventional SmA phase [3], the average orientation direction of the long axes of the molecules, *i.e.*, the director $\hat{n}$ is parallel to layer normal as shown in Figure 5.2a and the layer spacing is about the length of the molecules. In the SmC phase [4, 5, 6, 7, 8], the director $\hat{n}$ makes an angle θ with respect to the layer normal known as the tilt angle (see Figure 5.2b). If a sample undergoes a transition from the SmA to SmC phase, the tilt angle increased from zero with decreasing temperature below

the transition point. In calamitic liquid crystals consisting of rod-like molecules, the transition from the SmA to SmC phase is typically second-order or weakly first-order in nature and the variation of tilt angle with temperature is continuous or discontinuous, respectively across the transition. The tilt of the molecules reduced the layer spacing in the SmC phase as, $d_C = d_A \cos\theta$ where d_C and d_A represent the layer spacing in the SmC and SmA phases respectively, and θ is the tilt angle.

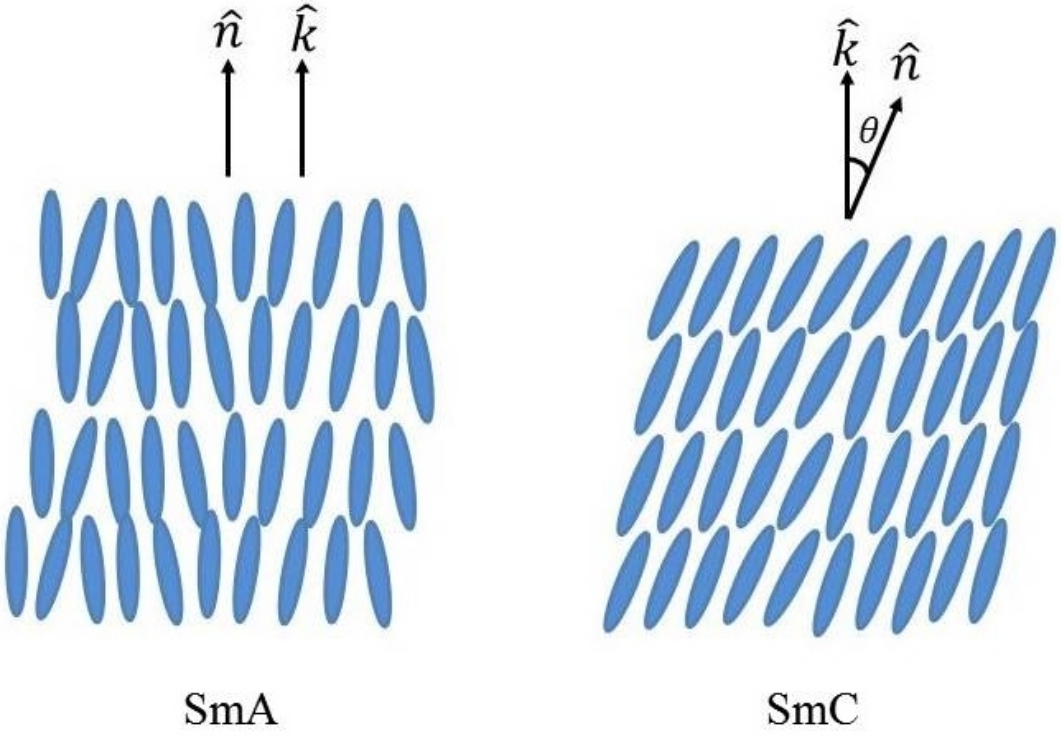

Figure 5.2: Molecular organization of rod-like molecules in (a) the SmA phase and (b) the SmC phase.

Thus, a large decrease in layer spacing is generally associated with the SmA to the SmC transition. In general, the layer contraction across the SmA to SmC phase transition is about 5-10% [9]. Far below the transition temperature, the contraction of the layers in the SmC phase compared to the SmA phase could be more than 10%. The layer shrinkage across the transition from the SmA phase to the SmC phase gives rise to so-called chevron defects in planar-aligned samples. A bookshelf geometry of the layers as shown in Figure 5.3a is obtained for a uniform planar-aligned sample in the SmA phase. When the sample is cooled to the SmC phase, layers take a chevron structure [10] as shown in Figure 5.3b, because of the decrease in the layer spacing

across the transition. The presence of the chevron defects in the tilted smectic phases restricts the commercialization of ferro- and antiferroelectric liquid crystals.

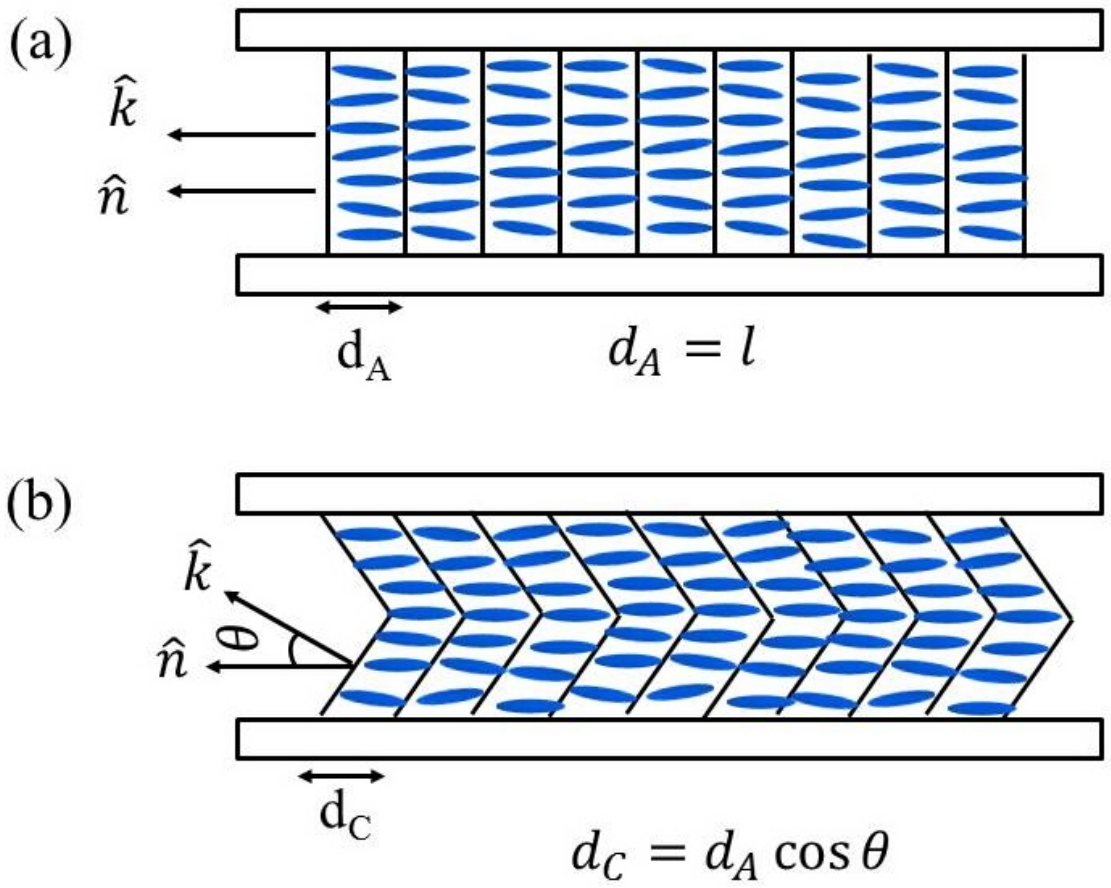

Figure 5.3: Schematic representation of the occurrence of the chevron defects on the transition from the SmA phase to SmC phase.

Diele et al. first reported that for some compounds, the thickness of smectic layers did not change significantly across the transition from the SmA to SmC phase over the full range of the SmC phase [9, 11, 12, 13, 14]. There were other reports, where the layer spacing in the SmA phase was found to be about 1.7 Å less than the length of the molecules [15]. The length of the molecules in these studies was estimated from the molecular formula assuming all the trans-conformation of the terminal chains. This lower value of the layer spacing in the SmA phase was accounted for by the interpenetration of the ends of the molecules in successive layers [16]. In some studies, the lower layer spacing in the SmA phase was also interpreted to arise because of the kinked structure of the terminal end chains of the molecules which decreases the molecular

length. In 1974 at the International liquid crystal conference (ILCC), deVries argued that the lower layer spacing in the SmA phase arises because the molecules are tilted in this SmA phase similar to that in the SmC phases but without long-range correlation between the tilt directions in the layers. Later on, deVries reported some other compounds where the layer spacing in the SmA phase was much smaller than the molecular length and explained these effects based on the random tilt correlation of the molecules in successive layers [17]. In 1977, de Vries found a different kind of A-C transition in the compound n-pentyl-4(4'-n-decyloxybenzylideneamino)-cinnamate [18]. He observed that the layer spacing, therefore tilt angle, did not change significantly across the A-C transition as shown in Figure 5.4. Further, the observed layer spacing in the SmA phase was found to be less than the molecular length. This lower value of layer spacing could be accounted for by assuming a non-zero tilt of about 15 degrees of the molecular long axes in the SmA phase. The SmA phase with the above characteristic properties is now known as the "deVries SmA" phase. In the same year 1977, de Jeu et al. also found the same behavior of the SmA phase in which the layer spacing was much lower than the molecular length and adopted deVries theory to explain their results. In the conventional SmA phase, however, the tilt angle is zero as the molecules are on average parallel to the layer normal with the layer spacing about the same as the molecular length. In this thesis, this conventional SmA phase is referred to as the SmA phase.

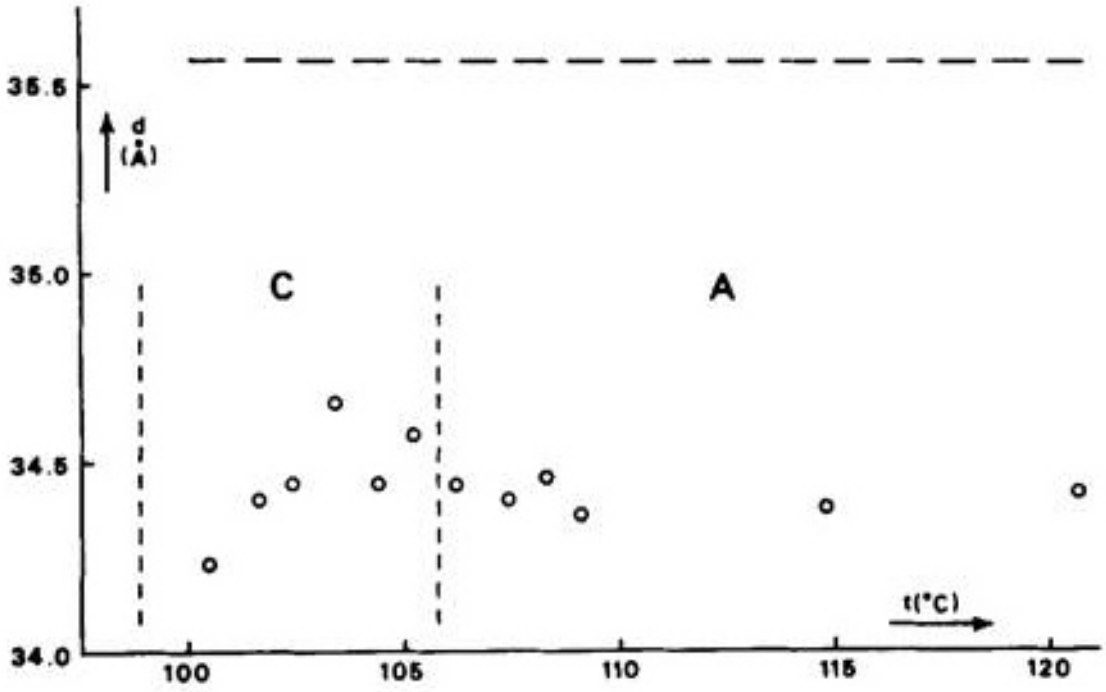

Figure 5.4: The layer spacing variation as a function of temperature for compound n-pentyl-4(4'-n-decyloxybenzylideneamino)-cinnamate. The horizontal and vertical dash lines show molecular length and the transitions between observed mesophases respectively.

The tilted nature of the molecules in layers and the uniaxial nature of the deVries SmA phase about the layer normal suggested that the tilt directions of the molecules are random in the layers. There are two possible configurations for the uncoupling of the tilt direction of the molecules in the smectic layers: non-correlated model and diffusive cone model. At the macroscopic level, both the models could be explained the nature of the deVries SmA phase.

Non-Correlated Model

In this model [14], it was assumed that the molecules are uniformly tilted in a preferred direction in each layer. But the correlation in the tilt directions between the layers is short range. Figure 5.5a shows a schematic representation of the non-correlated model. The short-range correlations between the tilt directions in successive layers give rise to the uniaxial deVries SmA phase though the molecules are tilted uniformly within the individual layers.

Diffusive Cone model

In this model [19, 20, 21], the molecules in each layer have approximately same tilt angle but with random azimuthal tilt directions, *i.e.*, the molecules are randomly orientated over the cone surface as shown in Figure 5.5b. Thus, there is no long-range tilt correlation between the molecules in each layer. Therefore, the average orientation direction of the long axes of the molecules in a layer, *i.e.*, the director $\hat{n}$ still remains parallel to the layer normal, giving rise to the uniaxial deVries SmA phase.

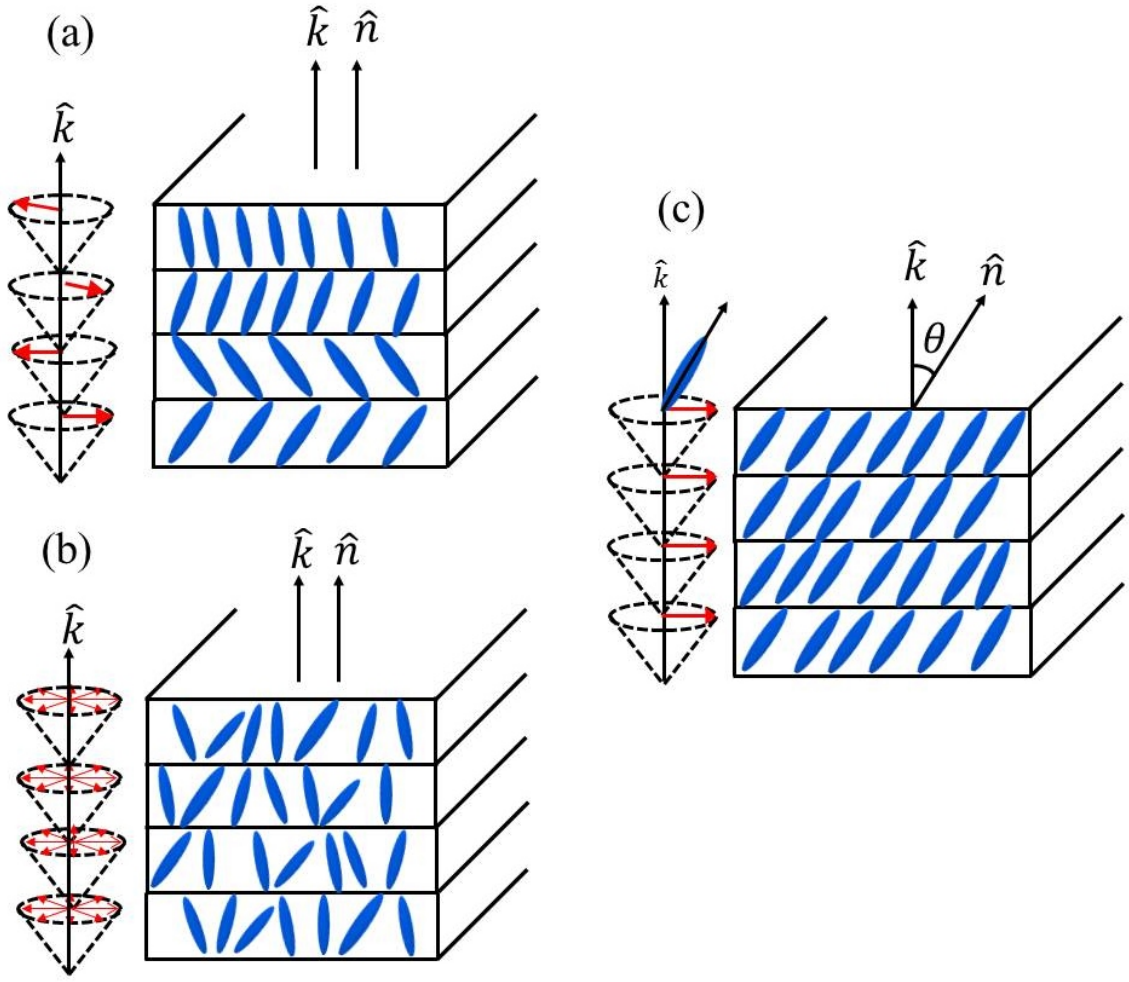

Figure 5.5: Schematic representation of (a) the non-correlated (b) the diffusive cone model for deVries SmA phase, and (c) SmC phase with a uniform tilt of the molecules in the layers. The red arrows show the tilt direction of the molecules in the indiviual layer.

Whereas in the SmC phase, the molecules are tilted uniformly in the smectic layers as shown Figure 5.5c. Across the transition from the deVries SmA phase to the SmC

phase, the tilt directions of all the molecules get correlated with a common azimuthal direction in each layer. Therefore, no significant layer contraction occurs across the deVries SmA phase to the SmC transition. Therefore, the deVries SmA phase can be characterized as [22]:

- The layer spacing is lower than the molecular length but the optic axis is paralle to the layer normal.
- There is no significant layer contraction across the deVries SmA to SmC transition in contrast to that of SmA to SmC transition.
- An increase in the birefringence is generally associated with the transition from the deVries SmA to the SmC phase.

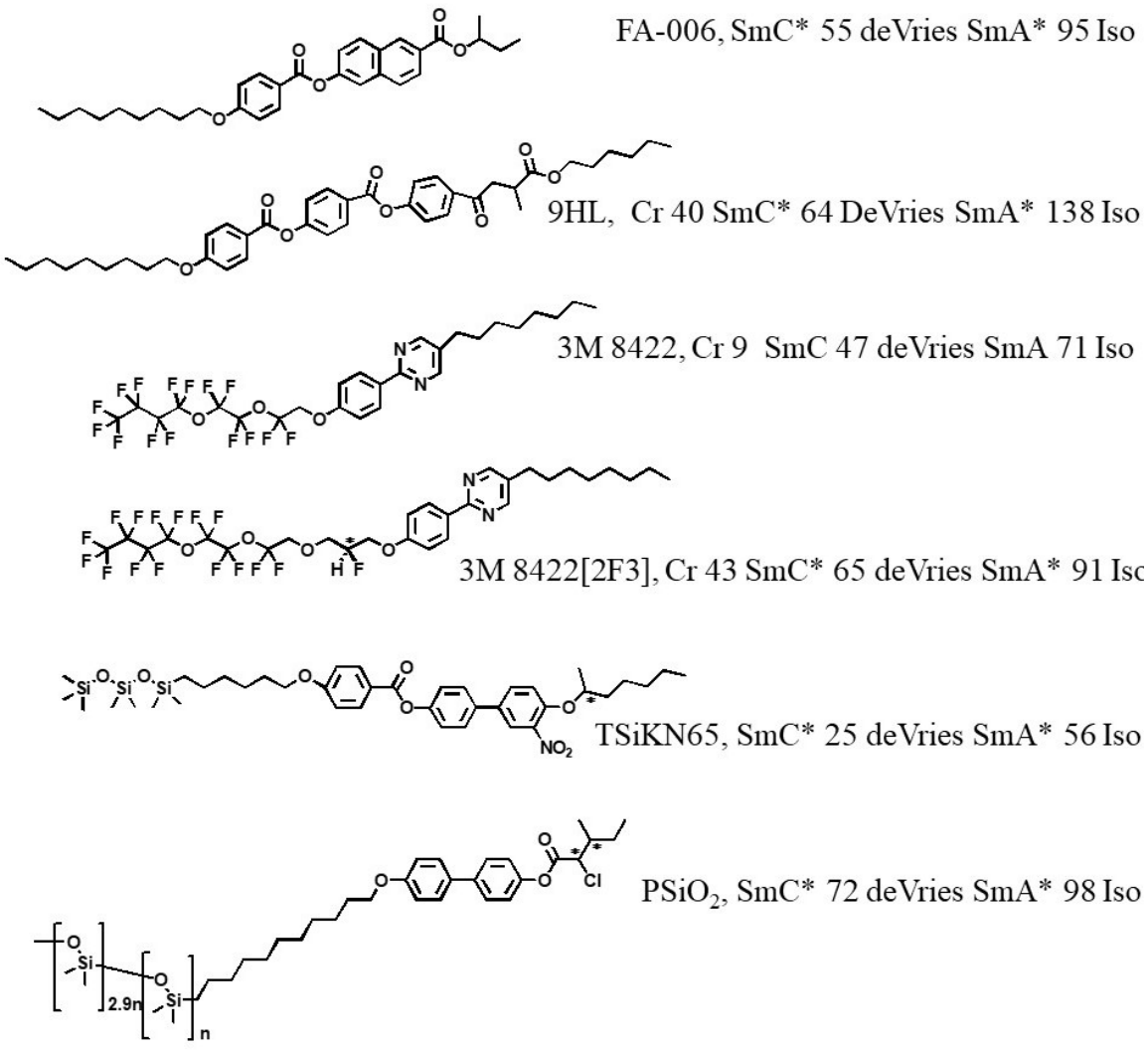

Figure 5.6: Some examples of LC compounds showing deVries SmA phase.

Figure 5.6 shows some examples of common LC compounds showing deVries SmA phase. These compound are generally made of rod-like molecules and show a phase sequence Cr→ SmC→ deVries SmA→ Iso. In general, the LC compounds containing unconventional structure elements like the fluorinated tails, for example in 3M 8422 [23, 24, 25], 3M 8422[2F3] [26, 27], the trisiloxane moiety in TSiKN65 [28, 29, 30, 31, 32], and the polysiloxane chain in the $PSiO_2$ [33, 34] copolymer show the deVries SmA phase. Whereas, 9HL [35, 27, 36, 37] and FA [38, 39] also show the deVries SmA phase though they do not contain any unconventional elements unlike other examples of LC compounds shown in Figure 5.6. There is no report yet on the compound consisting of an achiral BCHS molecules showing the deVries SmA phase.

In this chapter, we describe experimental studies on the liquid crystal phases of a azo-substituted compound consisting of BCHS molecules [40, 41, 42]. In particular, we report for the first time the observation of the deVries SmA phase in addition to the SmA and the SmC phases of a compound consisting of BCHS molecules. More interestingly, a first-order transition from the SmA phase to the deVries SmA phase was observed with decreasing temperature. This transition had not been reported earlier in the literature. The deVries SmA phase undergoes a second-order transition to the SmC phase on further decrease in temperature. This chapter is divided into two parts: we will describe the experimental studies and results on the compound in the first part and the model structures of these phases will be presented in the second part.

5.2 Experimental Studies

5.2.1 Sample

This is the ninth homologue of a series of azo-substituted compounds consisting of BCHS molecules. The azo-group materials now grab special attention due to their photochromic nature. The liquid crystals containing azo-groups can be exploited for optoelectronic devices. The molecular formula of the compound studied is 4-(((3-((4-(Decyloxy)benzoyl)oxy)phenyl)

imino)methyl)phenyl4-(-(4-(n-nonyloxy)phenyl)diazenyl)benzoate [42]. This compound is denoted as A9 for further discussion in the thesis. The molecular structure of compound A9 and the observed phase sequence on cooling from the isotropic phase are shown in Figure 5.7.

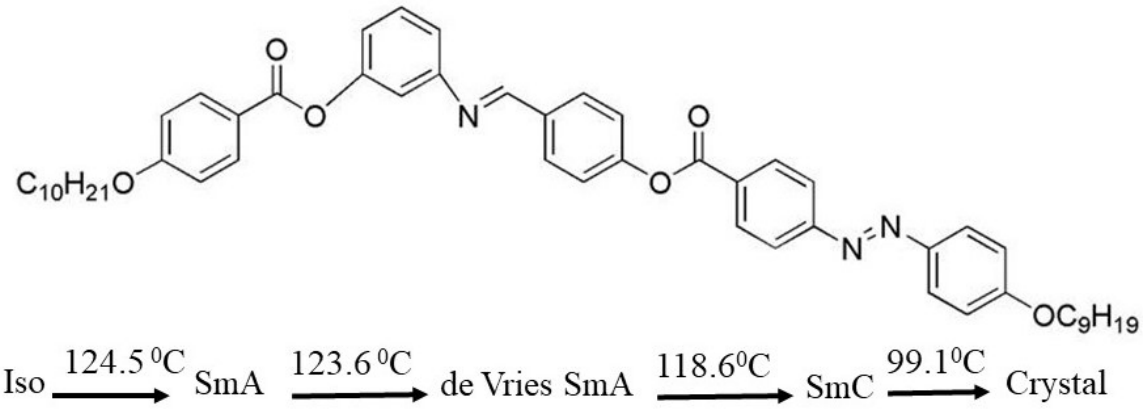

Figure 5.7: The molecular structure and the phase sequence of compound A9 on cooling from the isotropic phase. The transition temperatures are obtained from the DSC thermogram except the transition temperature from the de-Vries SmA phase to SmC phase which was obtained from the POM studies

The experimental studies were performed for both planar and homeotropic alignment of the molecules with respect to the glass substrate. For the planar-aligned sample, we used commercially available liquid crystal cells (Instec Inc.) of different thicknesses. For the homeotropic-alignment of the molecules, we used homemade ODSE coated cells. The method of construction of liquid crystal cells was described in detail in chapter 2. In general, BCHS molecules did not align homeotropically even with ODSE coated glass plates. However, for the compound A9, homeotropic-alignment was observed in ODSE coated liquid crystal cells. The sample was filled into the liquid crystal cell in the isotropic phase. It was found that the compound A9 also aligned homeotropically between a clean glass plate and a cover-slip without any special surface treatment when the sample was cooled slowly from the isotropic phase. Figure 5.8 shows the energy minimized configuration of the BCHS molecule of compound A9. The estimated end-to-end molecular length from the structure is about 51.7 Å.

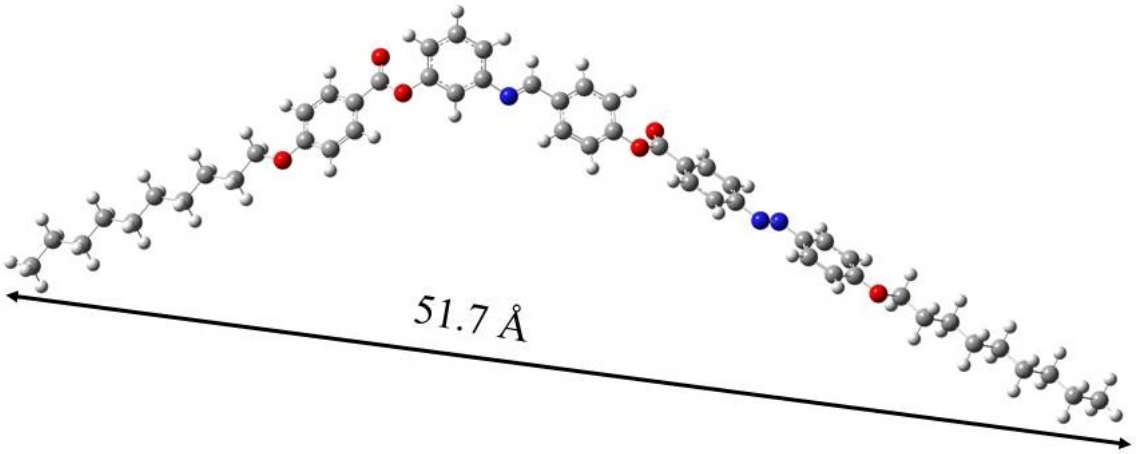

Figure 5.8: The molecular structure of compound A9 in the minimized energy configuration.

This energy minimized configuration was determined by using Gaussian-09 software.

5.2.2 Differential Scanning Calorimetry Investigations

The DSC studies on the sample were performed at a given heating/cooling rate to detect the transition between the phases. Figure 5.9 shows the DSC thermogram of compound A9 at a heating/cooling rate of 3 ^{0}C/min.

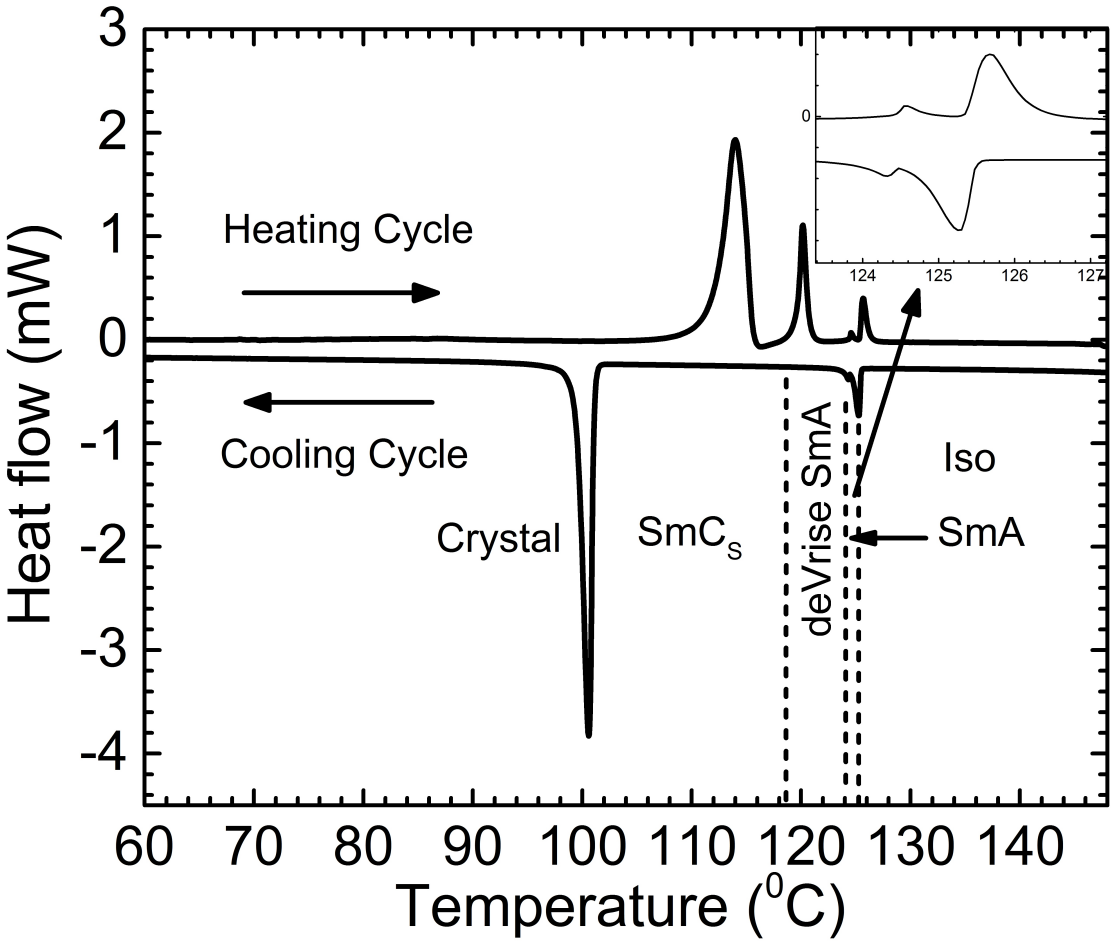

Figure 5.9: The DSC thermogram of compound A9 on heating and cooling the sample at a rate of 3 ^{0}C/min. The vertical dashed lines indicate the transition temperatures between the observed phases. The inset shows the magnified view of the peaks associated with the transition between the SmA and the deVries SmA phases. The DSC thermogram detected the weak first-order transition between the SmA and the deVries SmA phase.

The DSC thermogram detecte the transition peaks corresponding to the transition between the isotropic liquid and SmA, and SmA to deVries SmA phases in addition to a intense peak associated with the crystallization. A sharp peak was observed at the transition from the isotropic phase to the SmA phase with enthalpy change (3.75 kJ/mole), indicating a first-order transition. At a lower temperature, a very small peak was observed corresponding to a transition from the SmA phase to the deVries SmA phase with very small enthalpy change. The inset of Figure 5.9 on the upper right clearly shows the transition from the SmA phase to the deVries SmA phase. The small enthalpy change of about 0.12 kJ/mole indicated a very weak first-order phase

transition. A first-order transition between the SmA and deVries SmA phase was expected as there was no symmetry change between these two phases. However, DSC studies did not show any evidence of the transition from the deVries SmA phase to the SmC phase. This phase transition was, however, observed at 118.6 ^{0}C in polarizing optical microscopy (POM) studies. The absence of the transition peak in the DSC thermogram indicates that the transition from the deVries SmA to SmC phase is a second-order phase transition in nature. The transition from the deVries SmA phase to the SmC phase was expected to be second-order as the random tilt directions in the deVries SmA phase get uniformly aligned in the SmC phase. On further cooling, a sharp peak with large enthalpy change 33.54 kJ/mole appeared which correspond to the crystallization. Thus, the DSC studies clearly detected the weak first-order transition from the SmA phase to the deVries SmA phase.

5.2.3 X-ray Diffraction Investigations

The X-ray diffraction (XRD) studies were performed to characterize the lamellar order and to determine the layer spacing in the observed smectic phases. The XRD data was collected with an exposure time of 30 minutes in each smectic phase on cooling the sample from the isotropic phase. The XRD studies were performed on an unoriented sample filled in Lindemann capillary tubes with inner and outer diameter of about 0.8 mm and 1 mm, respectively. The Figure 5.10 shows the XRD intensity profile as a function of wave-vector of magnitude q in the observed smectic phases.

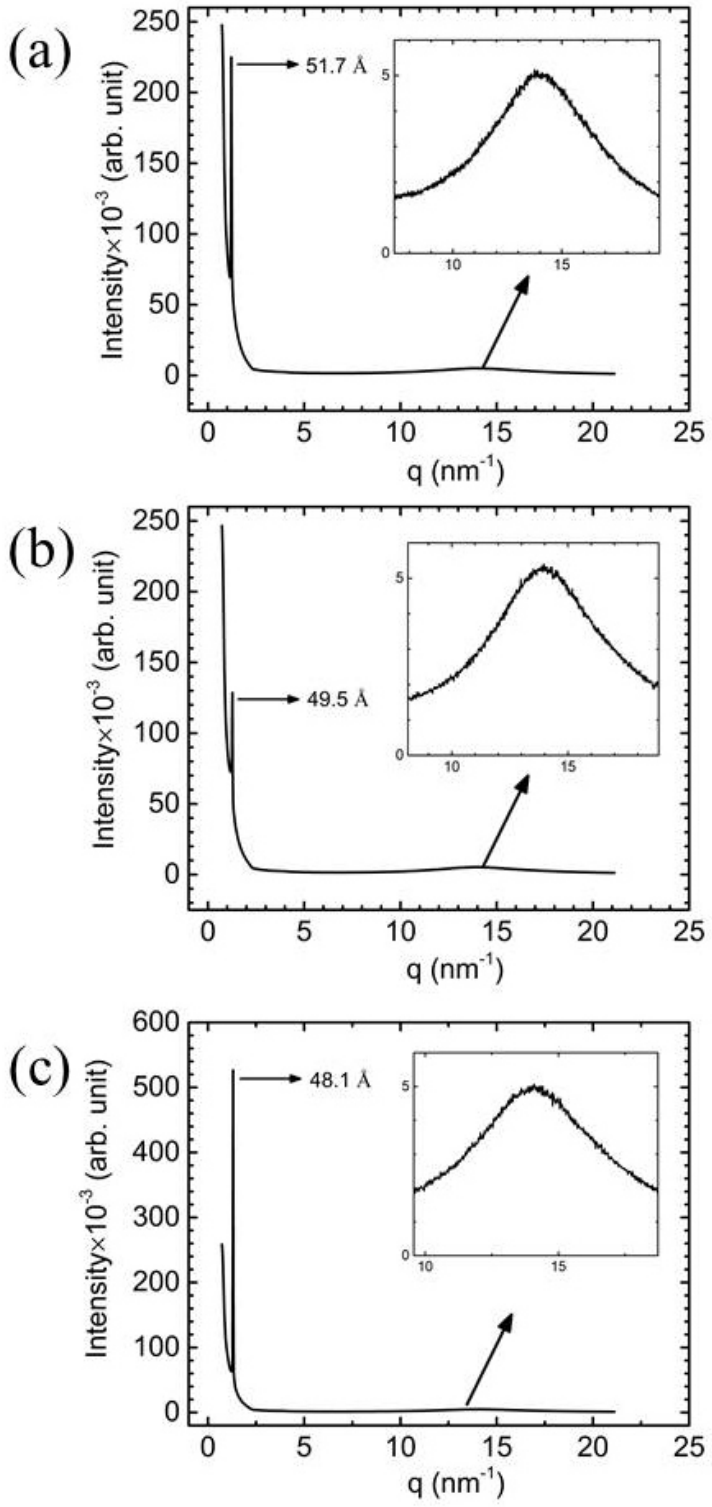

Figure 5.10: The XRD intensity profile of the compound A9 in the observed smectic phases (a) the conventional SmA phase at 124 ^{0}C (b) the deVries SmA phase at 122 ^{0}C and (c) SmC_S phase 116 ^{0}C.

In all the observed smectic phases, a sharp peak was observed in the small-angle

region in addition to a diffused peak in the wide-angle region. This XRD intensity profile is the characteristic of smectic phases. The sharp small-angle peak signified one-dimensional lamellar order and the presence of diffused wide-angle peak indicated the fluid-like order of the molecules within the layers. From the position of the small-angle peak in the SmA phase, the layer spacing could be determined as 51.7 Å at 124 ^{0}C. The observed layer spacing in this phase is the same as the molecular length (51.7 Å), indicating that the molecules are parallel to the layer normal. Upon cooling the sample to the deVries SmA phase, again, a sharp peak in the XRD profile was observed with layer spacing 49.5 Å at 122 ^{0}C. The observed layer spacing in the deVries SmA phase was smaller than the molecular length which indicated that the molecules are tilted with respect to the layer normal. In the SmC phase, the small-angle peak gives the spacing as 48.1 Å at 116 ^{0}C. The smaller layer spacing in the SmC phase again shows the tilted nature of the molecules in the layers. The d-spacing corresponding to the diffused wide-angle region peaks in the SmA, deVries SmA, and SmC phases are 4.5 Å, 4.45 Å, and 4.43 Å, respectively giving the lateral correlation length of the molecules in the layers. Thus, the XRD studies confirmed the lamellar order of all the observed smectic phases.

We also studied the variation of layer spacing (tilt angle) as a function of temperature in the observed smectic phases on cooling the sample from the SmA phase. The tilt angle θ of the molecules was calculated using the formula $d = l\cos\theta$ where d and l are the observed layer spacing and molecular length, respectively. The variation of layer spacing (tilt angle) with temperature for compound A9 is shown in Figure 5.11.

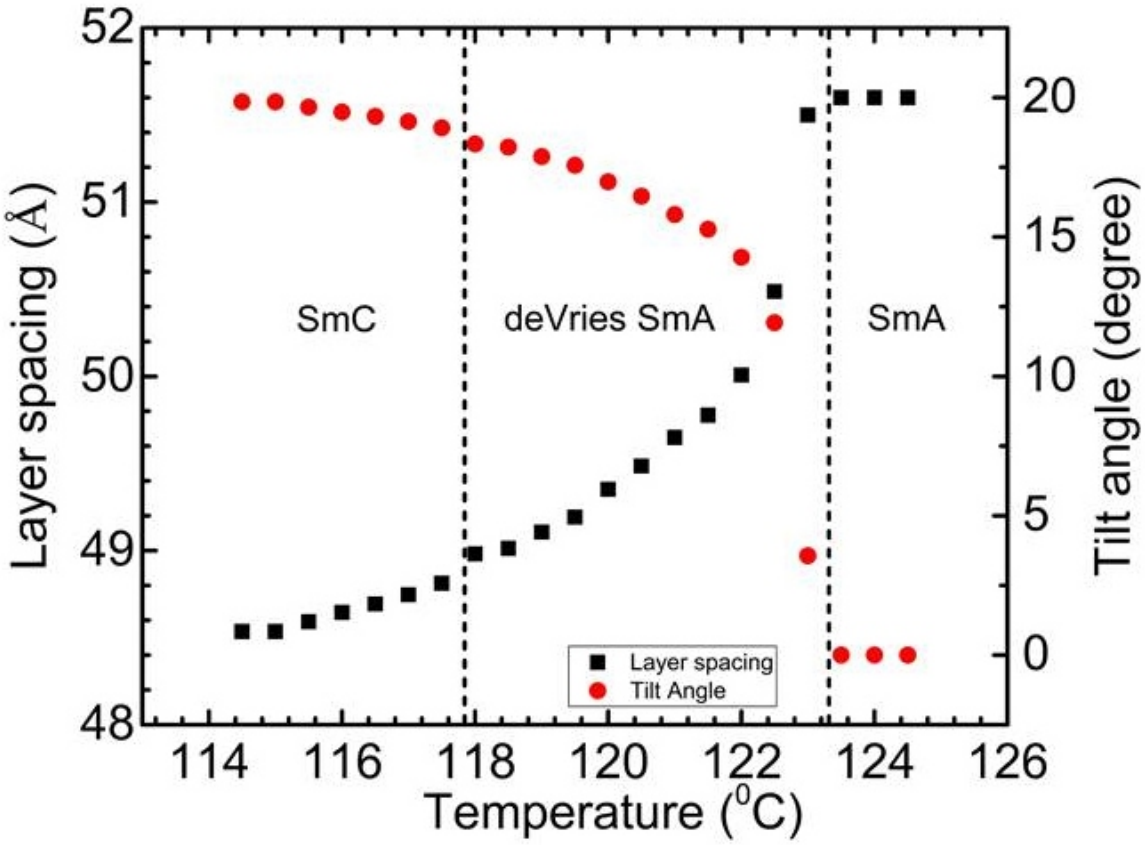

Figure 5.11: The variation of the layer spacing (tilt angle) of compound A9 as a function of temperature on cooling from the SmA phase. The layer spacing (tilt angle) is calculated from XRD data. The vertical dash lines show the transition between the observed smectic phases.

The layer spacing (tilt angle) remains constant in the SmA phase as the molecules are parallel to the layer normal. Upon cooling the sample to the deVries SmA phase, a gradual decrease (increase) in the layer spacing (tilt angle) was observed. This gradual decrease in the layer spacing indicates the tilt of the molecules with respect to the layer normal, *i.e.*, the tilt angle of the molecules increased with decreasing temperature in the deVries SmA phase. On the further decrease in temperature, a minimal change in the layer spacing was observed across the transition from the deVries SmA phase to the SmC phase. This was expected as the molecules are already tilted with respect to the layer normal in the deVries SmA phase. Only the tilt directions of the molecules get correlated on going to the SmC phase. This negligible layer contraction across the deVries SmA-SmC transition is a characteristic feature of the deVries SmA phase as reported in many other studies. Thus, the XRD studies confirmed the existence of the

SmA, deVries SmA, and SmC phases for the compound A9. This is the first report of a compound showing the transition from the SmA phase to the deVries SmA phase exhibited by BCHS molecules.

5.2.4 Polarized Optical Microscopy Investigations

The polarized optical microscopy (POM) investigations of the samples were carried out using OLYMPUS BX50. The temperature of the sample was controlled using a microscope hot stage and a temperature controller (LINKAM(T95HS) with the temperature stability of 0.1 ^{0}C. The sample was filled into the liquid crystal cells which were pretreated for planar or homeotropic alignment. For some studies, the sample was sandwiched between a clean glass plate and a cover-slip without any pretreatment of the glass plates. The sample was slowly cooled from the isotropic phase to the desired phase to promote better alignment between the plates. The POM textures of a planar-aligned sample in the different smectic phases are shown in the Figure 5.12.

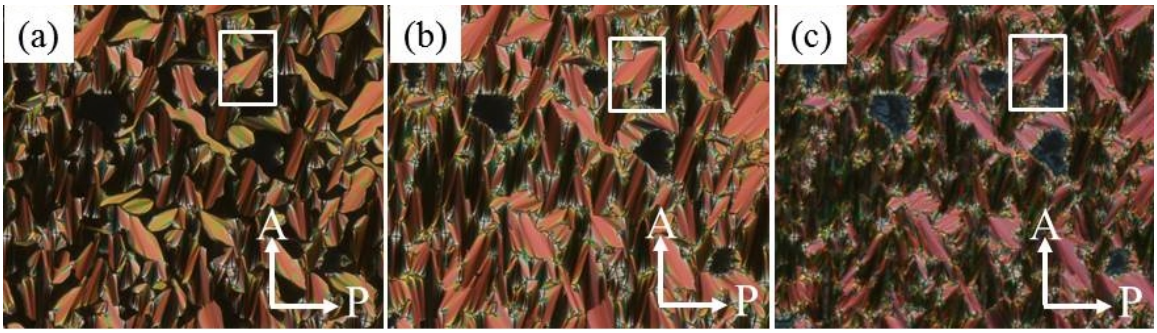

Figure 5.12: The POM textures of a planar-aligned sample of thickness 5 μm between crossed polarizers (a) a focal-conic fan texture in the SmA phase with the coexisting isotropic phase (b) the focal-conic fan textures in the deVries SmA phase with the dark regions showing the homeotropically-aligned deVries SmA phase (b) the broken focal-conic fan texture in the SmC phase and the dark region shows the schlieren texture which got clear on lowering the temperature of the sample.

The planar-aligned sample was cooled to the SmA phase at a rate of 1 ^{0}C/min between crossed polarizers. A smooth focal-conic fan texture (Figure 5.12a), which is the characteristic of the SmA phase, was observed with the coexistence of some isotropic regions. As the temperature range of stability of the SmA phase was narrow

for this sample, some coexisting isotropic phase is also observed throughout the range of the SmA phase. The dark brushes in the fan region appeared parallel or perpendicular to the polarizer when the layer normal was parallel or perpendicular to the polarizer. This implied that the optic axis was along with the layer normal which was consistent with the structure of the SmA phase. The bright orange birefringence color in the fan region for 5 μm thick sample at 124 ^{0}C gives the birefringence value as 0.08 estimated using the Michel-Levy interference chart.

On further cooling the sample to the deVries SmA phase, the focal-conic fan texture remains same though some changes in the birefringence color was observed. The birefringence color in the fan region changed to pale orange in the deVries SmA phase at about 122 ^{0}C as shown in Figure 5.12b. The dark extinction brushes in the focal-conic fan region indicated that the optic axes are parallel to the layer normal as in the SmA phase. In spite of XRD evidence of tilted molecules in the layers, this smectic phase appeared uniaxial about the layer normal confirming the deVries SmA phase. The color change from bright orange in the SmA phase to pale orange in the deVries SmA phase indicated that the birefringence in the deVries SmA phase was lower than that in the SmA phase. This decrease in birefringence in the deVries SmA phase compared to the SmA phase was expected because of the tilted uniaxial organization of the molecules with respect to the layer normal in the former phase.

A broken focal-conic fan texture typical in the SmC phase is observed on further decreasing the temperature. The extinction brushes in the broken focal-conic fan texture appears at an angle with respect to the layer normal when it was parallel or perpendicular to the polarizer indicating that the optic axis is at some angle with respect to the layer normal consistent with the structure of the SmC phase. The change in birefringence color from pale orange to violet with a birefringence value 0.1 was observed in the SmC phase. This color change indicates an increase in the birefringence of the SmC phase compared to that in the deVries SmA phase. The increase in the birefringence across the deVries SmA phase to SmC phase was expected as it goes from a random tilted organization to an ordered tilted organization in the SmC phase. This increase in birefringence starting from the deVries SmA to SmC

phase is also a characteristic feature of the deVries SmA phase as reported in the literature [43, 44].

The sample sandwiched between a non-treated glass slide and a cover-slip was used for POM studies of a homeotropically-aligned sample. A dark homeotropic texture was observed between crossed polarizers in the SmA phase at 124.5 ^{0}C on cooling from the isotropic phase. The texture remained dark on rotating the sample with respect to the polarizers indicating the uniaxial nature of the SmA phase about the layer normal. As both the isotropic and SmA phases with homeotropic alignment appeared dark between crossed polarizers, the analyzer was slightly uncrossed to distinguish the transition between these phases. Figure 5.13 shows the POM photomicrographs of a homeotropically-aligned sample on cooling from the isotropic phase at a rate of 0.1 ^{0}C/min. Figure 5.13a shows the nucleation of the SmA droplets in the isotropic phase. On decreasing the temperature, homeotropic domains of the deVries SmA phase grow in the SmA phase along with some coexisting isotropic phase (Figure 5.13b). As the range of the SmA phase for the compound A9 is narrow, the isotropic phase was found to coexist with the SmA phase over the whole temperature range of the latter. At lower temperatures, the uniform dark texture of the deVries SmA phase was observed as shown in Figure 5.13c. The texture did not change upon rotating the sample between crossed polarizers indicating the uniaxial nature of deVries SmA phase. These observations along with the XRD results clearly confirmed the existence of the deVries SmA phase. Upon further cooling, a schlieren texture (Figure 5.13d) was observed indicating a transition to the SmC phase. The schlieren texture clearly arises because of the uniform tilted organization of the molecules in the layers. Careful observations revealed the presence of only unit strength defects in the schlieren texture. The presence of the unit strength defects indicates the synclinic arrangement of the molecules in successive layers as in the SmC phase. The transition from the SmC to the crystal phase is observed at 98 ^{0}C on further cooling of the sample.

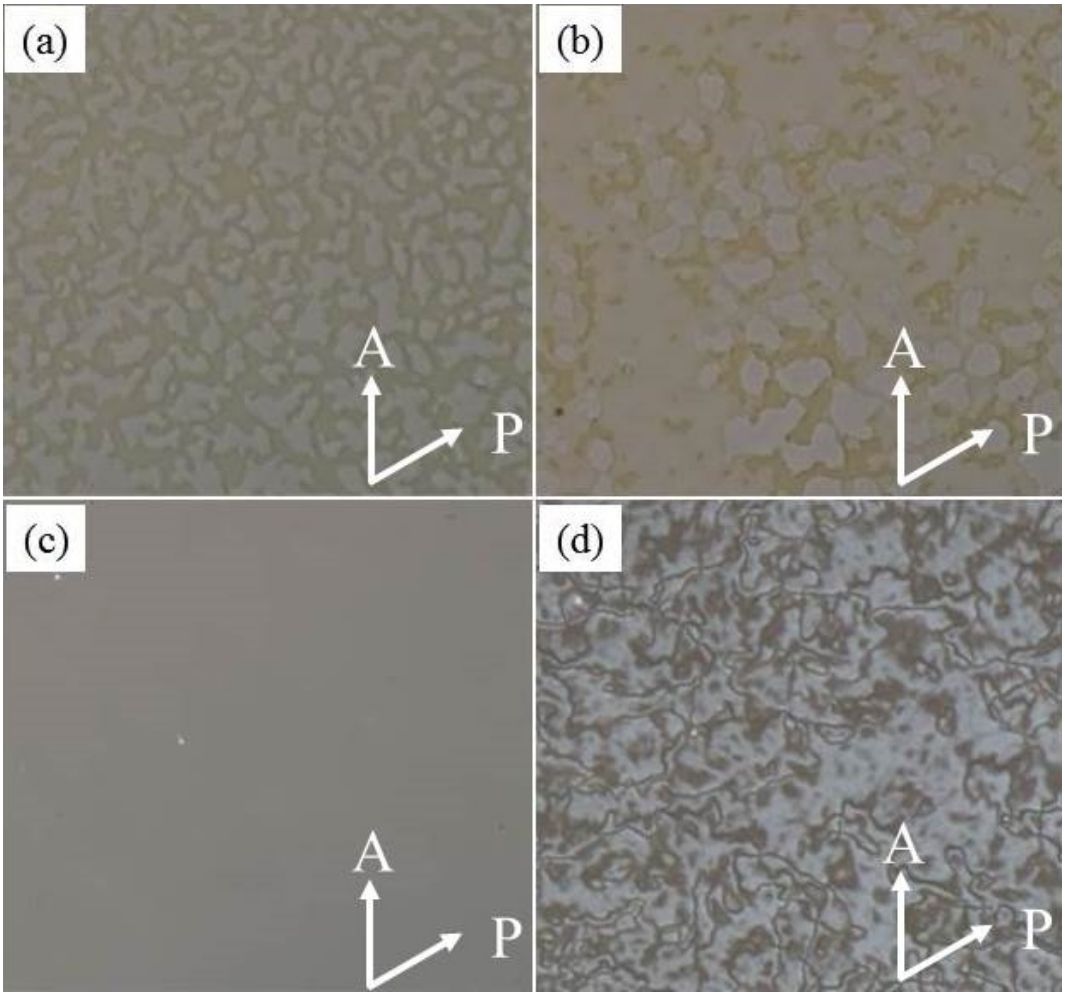

Figure 5.13: The POM textures of a homeotropically-aligned sample between slightly uncrossed polarizers (a) the growth of SmA domains in the isotropic phase (b) the growth of deVries SmA domains in the SmA regions along with some coexisting regions of the isotropic phase (c) a uniform homeotropically-aligned region deep in the deVries SmA phase (d) the schlieren texture in the SmC phase. The POM textures were taken with a 20X objective lens on cooling the sample from the isotropic phase at a rate of 0.1 ^{0}C/min .

The XRD and POM studies together confirmed the existence of the deVries SmA phase in addition to the higher-temperature SmA phase and a lower-temperature SmC phase for the compound A9. A first-order transition from the SmA phase to the deVries SmA phase is observed for the first time. The deVries SmA phase undergoes a second-order transition to the SmC phase.

5.2.5 Polarization Switching Current Measurements

The polarization reversal current measurements were performed to determine the existence of spontaneous electric polarization in the layers. The current measurements were carried out using a homemade experimental setup as described in section 2.11. A triangular wave voltage technique [45] was used to determine the polarization state of the layers in the observed smectic phases. A planar-aligned sample of thickness 5 μm was cooled from the isotropic phase to the deVries SmA phase between crossed polarizers. A focal-conic fan texture was observed in the deVries SmA phase as shown in Figure 5.12b. A triangular wave voltage of frequency 80 Hz was applied to a planar-aligned sample. The current response of the sample in the deVries SmA and SmC phases are shown in Figure 5.14a and Figure 5.14b, respectively.

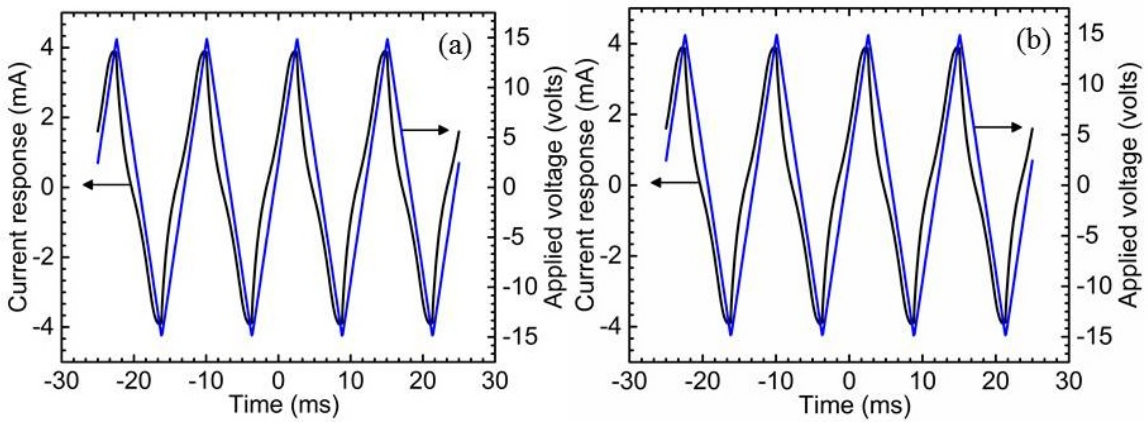

Figure 5.14: The current response of a planar-aligned sample of compound A9 in the (a) deVries SmA phase at 122 ^{0}C and (b) SmC phase at 114 ^{0}C.

The observed current response in both of these phases arise mainly from the dielectric and conductive contributions of the sample. The current peaks associated with the polarization reversal were not observed in both the phases which confirmed the absence of spontaneous polarization in the layers. These experimental results indicate that the BCHS molecules organized themselves in the layers with no net electric polarization. This result was consistent with the proposed structures of the observed smectic phases as discussed later in this chapter.

5.2.6 Steady-state electro-optic responses

The steady-state electro-optic response of a planar-aligned sample under an AC field was measured to determine the field-induced reorientation or change in the birefringence of the sample. The experimental technique used to measure the optical response is described in section 2.10. A planar-aligned sample of thickness 5 μm was used for the measurements. The steady-state optical response was recorded by applying a triangular wave voltage of amplitude 50 volts and frequency 230 Hz in the respective phases. The optical responses of the sample in the deVries SmA phase and SmC are shown in Figure 5.15.

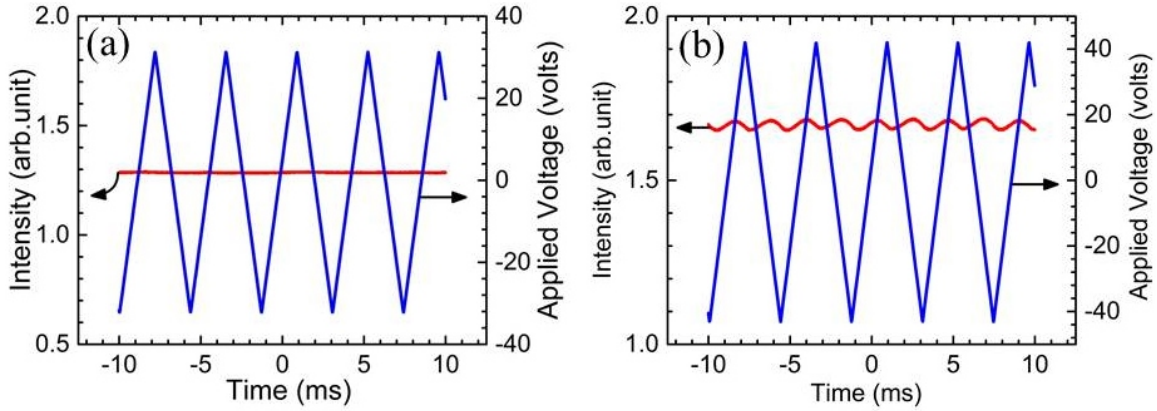

Figure 5.15: The optical responses of the compound A9 of a planar-aligned sample of thickness 5 μm as a function of an applied voltage in (a) the deVries SmA at 122 ^{0}C and (b) the SmC_S phase at 116 ^{0}C.

A flat DC intensity response is observed against the application of the triangular wave voltage in the deVries SmA phase. This implies that there was no field-induced reorientation or change in the birefringence of the sample in the deVries SmA phase. This result supported the "diffused cone" model rather than the "non-correlated" model proposed for the deVries SmA phase. In the diffused cone model, the molecules are tilted randomly within each layer and the field-induced change in orientations of the molecules of the layers are expected to be less effective. On the other hand, for the non-correlated model of deVries SmA phase, the molecules are tilted uniformly in each layer but the tilt directions from layer to layer are uncorrelated. As the molecules in each layer are already tilted uniformly, a larger influence of the field was expected in

this case. The absence of field-induced change in the optical response indicates the diffusive cone model structure of the observed deVries SmA phase.

In the SmC phase, a triangular wave voltage of amplitude 42 volts and frequency 230 Hz was applied to the sample to study the optical response. The optical response of the sample in the SmC phase is shown in Figure 5.15b. A small electro-optic response with twice the frequency of the applied voltage (2f response) was observed in the SmC phase. Clearly, the 2f response arises due to the quadratic coupling of the applied electric field with the orientational order. The 2f optical response in the SmC phase arises from the slight reorientation of the director in the planar-aligned sample due to the quadratic coupling of the field with the effective dielectric anisotropy of the sample. Thus, the experimental results of this section indicates the diffusive cone model structure of the observed deVries SmA phase.

5.2.7 Dielectric and Transmitted Optical Intensity Measurements

The simultaneous measurement of effective dielectric constant and the transmitted optical intensity between crossed polarizers of a planar-aligned sample was performed to determine the dielectric property and to detect the transition between the observed phases. The measurements were performed on a homemade experimental setup as described in section 2.8. The capacitance of the sample cell was determined using impedance analysis as described in section 2.6. The real part of the effective dielectric constant is measured by taking the ratio of the capacitance of the sample cell to that of an empty liquid crystal cell. The measurements were performed as a function of temperature on cooling the sample from the isotropic phase. Figure 5.16 shows the variation of the dielectric constant as a function of temperature for a planar-aligned sample of thickness 5 μm.

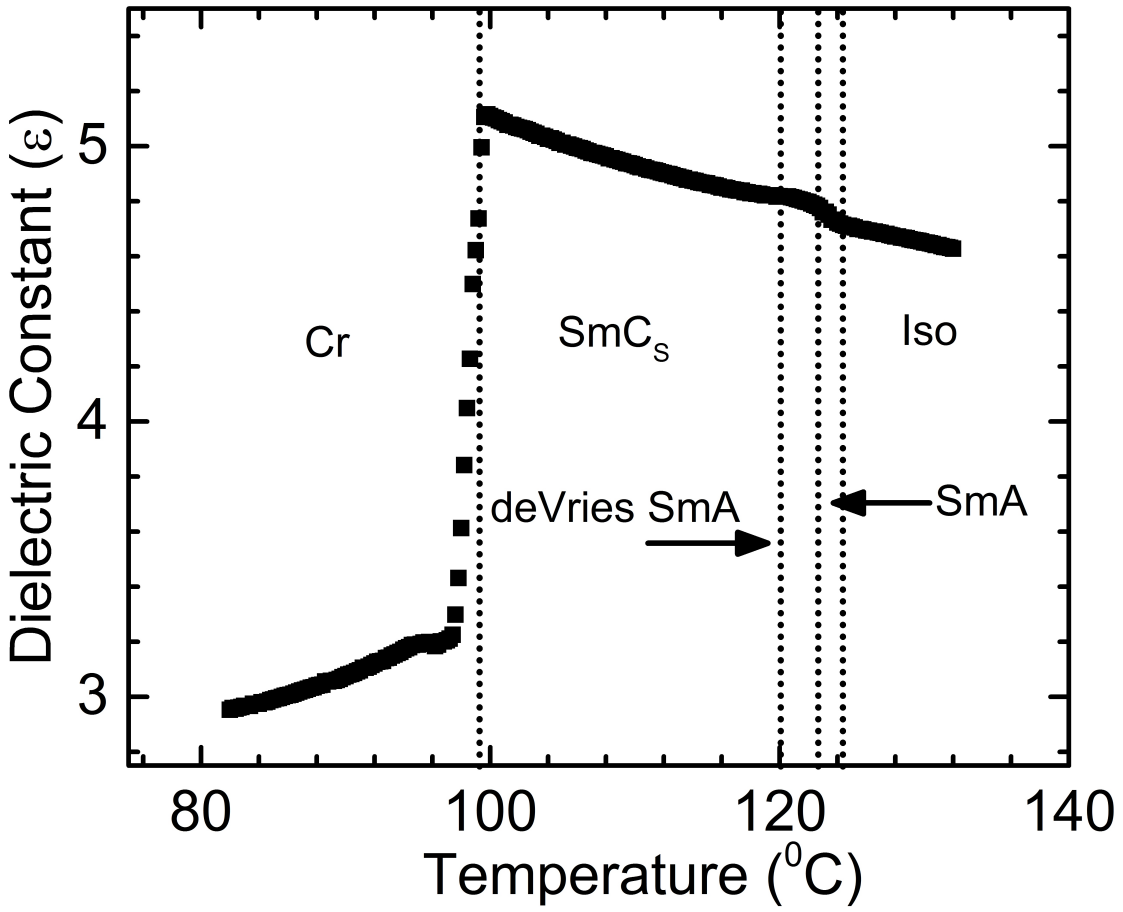

Figure 5.16: The variation of the real part of the effective dielectric constant as a function of temperature. The data was recorded on cooling the sample from the isotropic phase.

The dielectric constant increased slightly at the isotropic to the SmA phase transition point. No significant changes in the dielectric constant were observed across the transitions between the smectic phases. At the SmA to deVries SmA and deVries SmA, to SmC transition points, some changes in the slope of the dielectric constant data were observed. The dashed lines in Figure 5.16 indicate the transitions between the observed phases. Upon further cooling, a sharp decrease in the dielectric constant was observed as the sample goes to the crystal phase.

The variation of transmitted intensity with temperature on cooling the sample is shown in Figure 5.17.

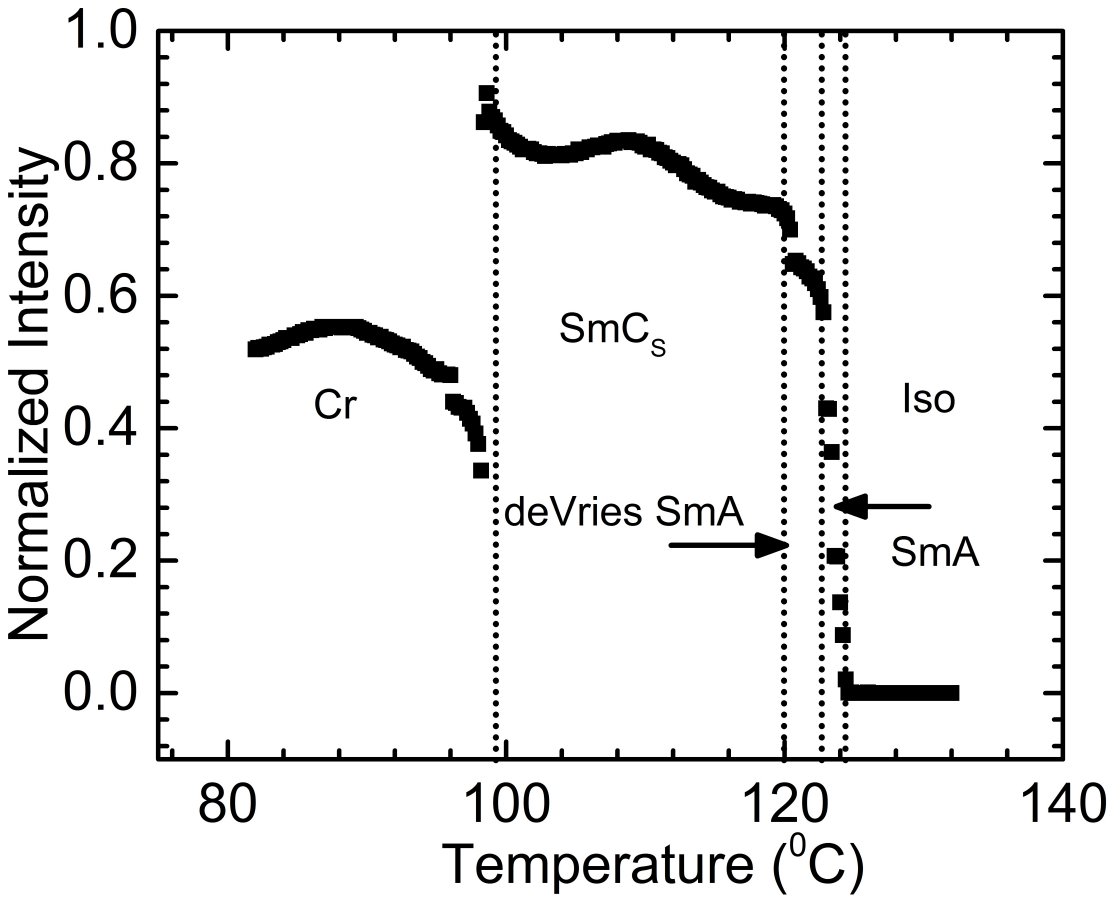

Figure 5.17: The temperature variation of the transmitted intensity passing through a planar-aligned sample of thickness 5 μm between crossed polarizers. The data was collected on cooling the sample from the isotropic phase.

The intensity increased sharply at the isotropic to the SmA transition temperature. There is a small jump in intensity at the SmA to deVries SmA transition temperature indicating a first-order transition. The intensity in the deVries SmA phase is higher than in the SmA phase due to the disappearing of the isotropic regions with decreasing temperature. A sharp increase in the intensity is observed at the deVries SmA-SmC transition temperature clearly detecting this transition. The simultaneous measurement of transmitted intensity along with the dielectric constant detected the transitions between the observed phases.

5.3 The proposed model structures

We now propose the possible organizations of BCHS molecules in these observed smectic phases. As the BCHS molecules have a rigid bent-core structure with one arm relatively longer than the other, these molecules are highly asymmetric in shape [46, 47, 48, 49, 50, 51]. One end of the molecule is bent giving a strong longitudinal head-tail asymmetry in addition to the transverse shape anisotropy. The experimental results suggested that the BCHS molecules adopt a zigzag shape [40, 52] as shown in Figure 5.18 for more efficient packing in the smectic layers.

The zigzag shape could be easily achieved by tilting the flexible terminal chain appropriately. These zigzag-shaped molecules aligned in the layers with their heads pointing up or down with equal probability. This organization of the molecules in the layers is entropically favored and the layers do not possess any net electric polarization as observed experimentally. In the higher-temperature SmA phase, the XRD results indicated that the layer spacing in the SmA phase is equal to the molecular length where the molecular length was determined as the end to end distance of the BCHS molecule. Therefore, the molecules in the SmA phase arrange themselves in the layers with long axes parallel to the layer normal. The BCHS molecules rotate freely about their long axes giving a uniaxial SmA phase as confirmed by POM studies. In the higher-temperature SmA phase, the density of molecules in the layer was lower and hence the larger inter-particle separation allowed the free rotation of the BCHS molecules about their long axes. Figure 5.18a shows the schematic representation of the organization of BCHS molecules in the SmA phase.

Clearly, in the SmA phase, both the core rod-like part and the terminal bent arms are tilted with respect to the layer normal. The average orientation direction of the long axes of the molecules, *i.e.*, the director $\hat{n}$, is parallel to the layer normal $\hat{k}$ (see Figure 5.18a).

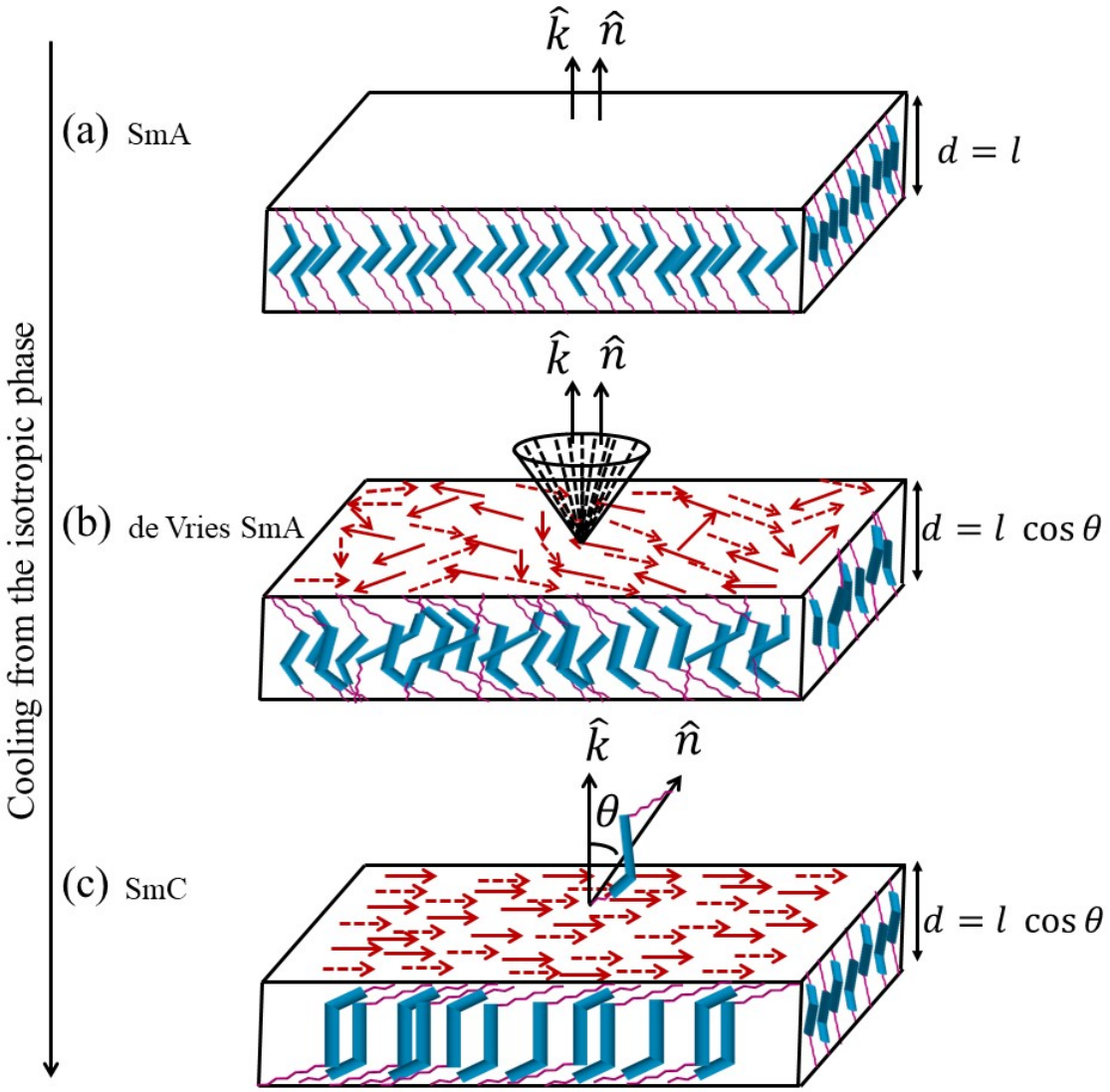

Figure 5.18: The molecular configuration of a BCHS molecule in a layer on cooling from the isotropic phase (a) the long axes of the molecules are parallel to the layer normal $\hat{k}$ (b) the molecules are randomly tilted in a given layer with respect to the layer normal. In Figure 5.18b, the red solid and dashed arrows show the direction of the c-vector in a given layer. The black dotted line shows the random distribution of the molecules over the surface of the cone and, (c) molecular configuration in SmC_S phase, all the solid and dashed arrows are aligned in the same direction indicating the uniform tilt of the molecules in layers.

At lower temperatures in the deVries SmA phase, the density increased in the layers which tend to align the core rod-like part of the molecules along the layer normal giving an effective tilt of the long axes of the molecules with respect to the layer normal. This arrangement reduced the effectively excluded volume between the molecules in the layer

and is favored entropically. This effective tilt of the long axes of the molecules reduces the layer spacing in the deVries SmA phase compared to the SmA phase as observed in the XRD studies. The terminal end parts of the BCHS molecules were at an angle with respect to the layer normal with no long-range correlation in the tilt direction. This, in turn, gives rise to no long-range correlation in the tilt directions of the long axes of the molecules in a layer. Thus, this model supported the diffusive cone model structure of the deVries SmA phase of BCHS molecules as found experimentally. The schematic representation of the organization of the BCHS molecules in the deVries SmA phase is shown in Figure 5.18b. In the deVries SmA phase, the long axes of molecules are tilted with respect to the layer normal and distributed over the surface of a cone in a given layer as shown in Figure 5.18b. The director $\hat{n}$ still remains parallel to the layer normal $\hat{k}$ giving rise to an uniaxial deVries SmA phase.

At even lower temperatures in the SmC phase, a further increase in density hindered the free rotation of the molecules in the layer. The better packing of the zigzag molecules then promoted the long-range correlation of the tilt directions in the layers (see Figure 5.18c). Therefore, the director $\hat{n}$ makes an angle θ with respect to the layer normal $\hat{k}$ in the SmC phase. As the molecules in the deVries SmA phase are already tilted, the layer spacing does not change significantly across the transition from the deVries SmA phase to the SmC phase as observed in XRD studies. The transition from the deVries SmA phase to the SmC phase belongs to the XY universality class and is expected to be a second-order transition as found experimentally.

5.4 Conclusions

In this chapter, we studied a lower homologue of a series of azo-substituted compound (A9) consisting of BCHS molecules. The higher homologue (A14) as described in chapter 3, show two pseudo-polar tilted smectic phases. This lower homologue of the compound (A9) shows different phase behavior than the compound A14. The compound A9 shows the following phase sequence on both increasing/decreasing temperature. Crystal (99.1 ^{0}C) $\rightarrow$ SmC (118.6 ^{0}C)$\rightarrow$ deVries SmA (123.6 ^{0}C) $\rightarrow$ SmA (124.5

^{0}C) $\rightarrow$ Isotropic. This is the first report of a compound consisting of BCHS molecules exhibits the deVries SmA phase. More interestingly, a first-order transition between the SmA phase to deVries SmA is observed in addition to a second-order transition between the deVries SmA phase to the SmC phase. We proposed model structures of the observed smectic phases consisting of BCHS molecules. The rigid bent structure of the molecules is responsible for the stability of the observed phases. The experimental results suggested the diffusive cone model structure for the deVries SmA phase.

Bibliography

[1] S. Chandrasekhar, *Liquid Crystals*, (Cambridge University Press, Cambridge, 1992).

[2] Z.Luz and S. Meiboom, *J. Chem. Phy.*, **59**, 275 (1973).

[3] P. G. de Gennes and J. Prost, *The Physics of Liquid Crystals*, (Clarendon, Oxford, 1993).

[4] W. L. McMillan, *Phys. Rev. A*, **4**, 1238 (1971).

[5] A. Wulf, *Phys. Rev. A*, **11**, 365 (1975).

[6] B. W. van der Meer and G. Vertogen, *J. Phys (Paris), Colloq.,* **C3–222**, 365 (1979).

[7] A. Poniewierski and T. J. Sluckin, *Mol. Phys.*, **73**, 199 (1991).

[8] A. S. Govind and N. V. Madhusudana, *Europhys. Lett.*, **55**, 505 (2001).

[9] S. Diele, P. Brand, and H. Sackmann, *Mol. Cryst. Liq. Cryst.*, **16**, 015-116 (1972).

[10] T. P. Rieker, N. A. Clark, G. S. Smith, D. S. Parmar, E. B. Sirota, and C. R. Safinya, *Phys. Rev. Lett.*, **59** 2658– 2661 (1987).

[11] J. Doucet, A.M. Levelut, and M. Lambert, *Mol. Cryst. Liq. Cryst.*, **24**, 317 (1973).

[12] R. Bartolino, J. Doucet, and G. Durand, *Ann. Phys.*, **3**, 389-395 (1978).

[13] A. de Vries, *Mol. Cryst. Liq. Cryst.*, **11**, 361-383 (1970).

[14] Adriaan De Vries, *Mol. Cryst. Liq. Cryst.*, **41**, 27-31 (1977).

[15] A. de Vries, *Mol. Cryst. Liq. Cryst.*, **20**, 119 (1973).

[16] A. de Vries, *Mol. Cryst. Liq. Cryst.*, **11**, 361 (1972).

[17] A. de Vries, *J. Phys. (Paris) Lett.*, **35**, L-135 (1974).

[18] W.H. de Jeu and J.A. de Poorter, *Phys. Rev. Lett.,* **61A**, 114 (1977).

[19] A. de Vries, *J. Chem. Phys.,* **71**, 25-31 (1979).

[20] A. de Vries, A. Ekachai, and N. Spielberg, *Mol. Cryst. Liq. Cryst. Lett.*, **49**, 143-152 (1979).

[21] A. de Vries *Advances in Liquid Crystal Research and Applications,Ed.: L. Bata), Pergamon, Oxford,* 71-80 (1980).

[22] Sven T. Lagerwall , Per Rudquist, and Frank Giesselmann, *Mol. Cryst. Liq. Cryst.*, **510**, 148-157 (2009).

[23] U. Dawin, J. P. F. Lagerwall, H.-J. Werner, M. Radcliffe, and F. Giesselmann, *presented at the 32nd Arbeitstagung FlJussigkristalle, Halle, Germany,* 4363 (2004).

[24] G. S. Iannacchione, C. W. Garland, P. M. Johnson, and C. C. Huang, *Liq. Cryst.*, **26**, 51–55 (1999).

[25] M. D. Radcliffe, M. L. Brostrom, K. A. Epstein, A. G. Rappaport, B. N. Thomas, R. F. Shao, and N. A. Clark, *Liq. Cryst.*, **26**, 789–794 (1999).

[26] J. P. F. Lagerwall, F. Giesselmann, and M. D. Radcliffe, *Phys. Rev. E*, **66**, 031703 (2002).

[27] M. Krueger, and F. Giesselmann, *Phys. Rev. E*, **71**, 041704 (2005).

[28] J. Naciri, J. Ruth, G. Crawford, R. Shashidar, and B. R. Ratna, *Chem. Mater.*, **7**, 1397–1402 (1995).

[29] M. Spector, P. Heiney, J. Naciri, B. Weslowski, D. Holt, and R. Shashidhar, *Phys. Rev. E*, **61**, 1579–1584 (2000).

[30] J. V. Selinger, P. J. Collings, and R. Shashidhar, *Phys. Rev. E*, **64**, 1579–1584 (2001).

[31] O. Panarina, Y. Panarin, J. Vij, M. Spector, and R. Shashidhar, *Phys. Rev. E*, **67**, 051 709 (2003).

[32] P. Collings, B. Ratna, and R. Shashidhar, *Phys. Rev. E*, **67**, 021705 (2003).

[33] M. Rossle, R. Zentel, J. Lagerwall, and F. Giesselmann, *Liq. Cryst.*, **31**, 883–887 (2004).

[34] M. Rossle, L. Braun, D. Schollmeyer, R. Zentel, J. P. F. Lagerwall, and F. Giesselmann, R. Stannarius, *Liq. Cryst.*, **32**, 533–538 (2005).

[35] S. Bezner, M. Krueger, F. Giesselmann, *presented at the 32nd Arbeitstagung FlJssigkristalle, Halle, Germany*, (2004).

[36] M. Kaspar, V. Hamplova, S. Pakhomov, A. Bubnov, F. Guittard, H. Sverenyak, I. Stibor, P. Vanek, and M. Glogarova, *Liq. Cryst.*, **24**, 599–605 (1998).

[37] F. Giesselmann, P. Zugenmaier, I. Dierking, S. T. Lagerwall, B. Stebler, M. Kaspar, V. Hamplova, and M. Glogarova, *Phys. Rev. E*, **60**, 598-602 (1999).

[38] A. Mochizuki, *in Proceedings of the 9th International Display Research Conference, Kyoto, Japan,* **34**, p.30 (1989).

[39] Y. Takanishi, Y. Ouchi, H. Takezoe, A. Fukuda, A. Mochizuki, and M. Nakatsuka, *J. Appl. Phys.*, **29**, L984–L986, (1990).

[40] D. Malkar, B. K. Sadashiva and A. Roy, *Soft Matter*, **12**, 4960 (2016).

[41] D. Malkar, M. Monika, V. Prasad, and A. Roy, *Phy. Rev. E*, **101**, 012701 (2020).

[42] M. Monika, V. Prasad, and N. G. Nagaveni, *Liq. Cryst.*, **42**, 1490–1505 (2015).

[43] J. Fernsler, D. Wicks, D. Staines, A. Havens, and Nathan Paszek, *Liq. Cryst.*, **39**, 1204–1215 (2012).

[44] J. P. F. Lagerwall and F. Giesselmann, *Chem. Phys. Chem,* **7**, 20 (2006).

[45] K. Miyasato, S. Abe, H. Takazoe, A. Fukuda, and E. Kuze, *Jpn. J. App. Phys.*, **22**, L661 (1983).

[46] P. Sathyanarayana, S. Radhika, B. K. Sadashiva, and S. Dhara, *Soft Matter*, **8**, 2322 (2012).

[47] M. Alaasar, *Liq. Cryst.,* **43**, 2208 (2016).

[48] S. Radhika, H. T. Srinivasa, and B. K. Sadashiva, *Liq. Cryst.*, **38**, 785 (2011).

[49] M. Alaasar, S. Poppe, C. Kerzig, C. Klopp, A. Eremin, and C. Tschierske, *J. Mater. Chem. C*, **5**, 8454 (2017).

[50] D. D. Sarkar, R. Deb, N. Chakraborty, and V. S. R. Nandiraju, *Liq. Cryst.*, **39**, 1003 (2012).

[51] E. R. Cioanca, E. L. Epure, I. Carlescu, G. Lisa, D. Wilson, N. Hurduc, and D. Scutaru, *Mol. Cryst. Liq. Cryst.*, **51**, 537 (2011).

[52] E. N. Keller, E. Nachaliel, D. Davidov, and C. Böffel, *Phys. Rev. A*, **34**, 4363-4369 (1986).

Chapter 6

Binary Mixtures of Rod-Like And Bchs Molecules

6.1 Introduction

The phase behavior of mixtures of molecules with different shapes is an important field in the research of liquid crystals. Previously, the phase behavior of the binary mixtures of different kinds of the molecules, for exmaple rod-like and BC banana shaped molecules [7, 8, 9], rod-like and disc-like, and BC banana shaped and disc-like molecules had been studied in detail.

In this chapter, we report the experimental studies on rod-like and BCHS molecules. There are no reports yet on the binary mixture of compounds made of BHCS molecules with other kind shapes of the molecules. However, recently there are some report on the binary mixtures of rod-like and other kind of hockey-stick shaped molecules [10, 11, 12]. We referred these kinds of the molecules as meta hockey-stick shaped molecules as described in section 1.5.

In the previous chapter 3, the liquid crystal phases exhibited by some BCHS molecules had been discussed [24, 25]. The long-chain homologue of the BCHS molecules was found to exhibit two pseudo-polar tilted smectic phases characterized by an axial-vector order parameter in addition to tilt order [19, 23, 24, 25]. The BCHS molecules have a rigid bent-core making the molecules highly asymmetric. The bent structure of the molecules introduced a shape anisotropy about their long axis which tend to hinder the free rotation of the molecules about their long axes in their condensed liquid crystal phases [26, 27, 28]. These effects and the close packing of the molecules in the layers give rise to the observed pseudo-polar tilted smectic phases. On the other hand, the rod-like molecules are nearly symmetric about their axes and they rotate

almost freely about their long axes in their liquid crystal phases [5, 29, 30]. Thus, the phase behavior of binary mixtures of these two types of molecules could illuminate the structure-property relation of these systems. In this chapter, we studied the phase diagram of the binary mixtures of rod-like and BCHS molecules. The physical properties of the binary mixtures were studied a variety of experimental techniques such as differential scanning calorimetry (DSC), X-ray diffraction (XRD), polarizing optical microscopy (POM), dielectric, and transmitted optical intensity studies. It was found that the calamitic smectic phases exhibited by the rod-like molecules progressively transformed to the pseudo-polar tilted smectic phases with increasing concentration of BCHS molecules in the mixtures. The layer spacing of the smectic phases of the mixture can be tuned by varying the concentration of the BCHS molecules.

6.2 Experimental Studies

6.2.1 Sample

The compounds used for the binary mixtures are 4OC18 and 8OCB. The compound 4OC18 consists of the BCHS molecules and the phase behavior of this compound is discussed in detail in section 3.2. The compound 8OCB consists of rod-like molecules and is commercially available. The 8OCB molecules carry a strong longitudinal dipole moment due to the nitrile (CN) group attached to one end of the molecule. The molecular structures of compounds 4OC18 and 8OCB are shown in Figure 6.1. The estimated molecular lengths of compounds 8OCB and 4OC18 are 21.7 Å and 53 Å, respectively.

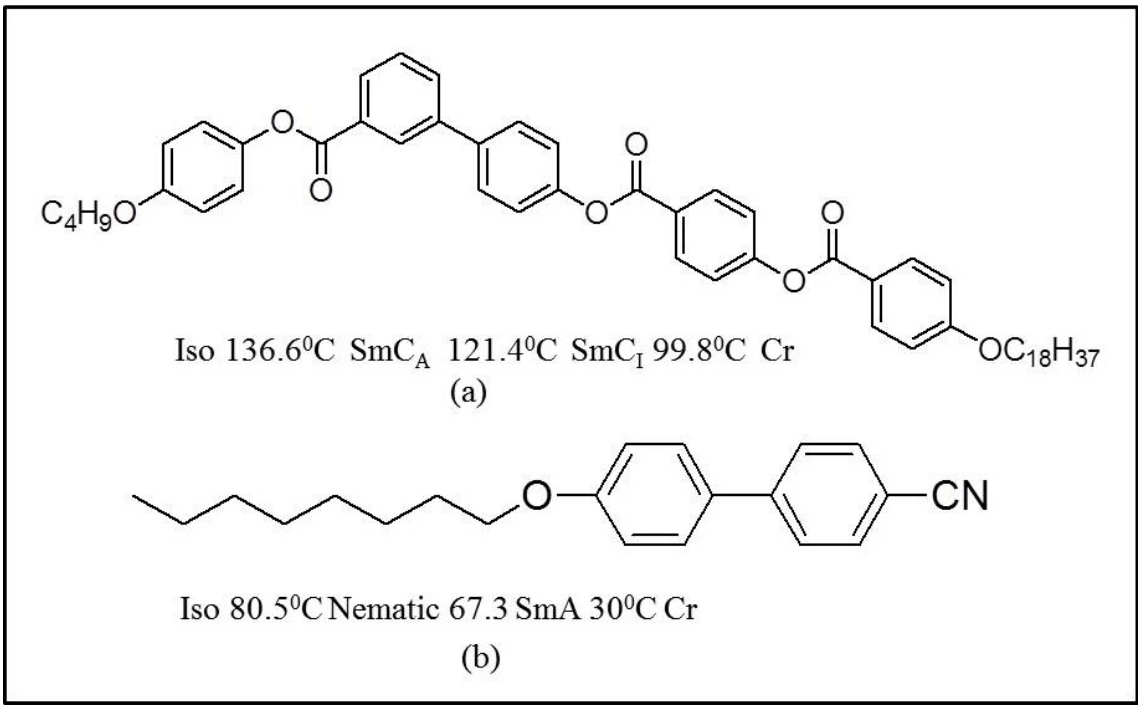

Figure 6.1: Molecular structures of (a) the compound 4OC18 consisting of BCHS molecules (b) the compound 8OCB consisting of rod-like molecules. The transition temperatures were taken from DSC.

The molecular structure of compounds in 4OC18 and 8OCB in the minimized energy configuration is shown in Figure 6.2. The molecular structures in the minimized energy configuration were achieved by using Gaussian-09 Software.

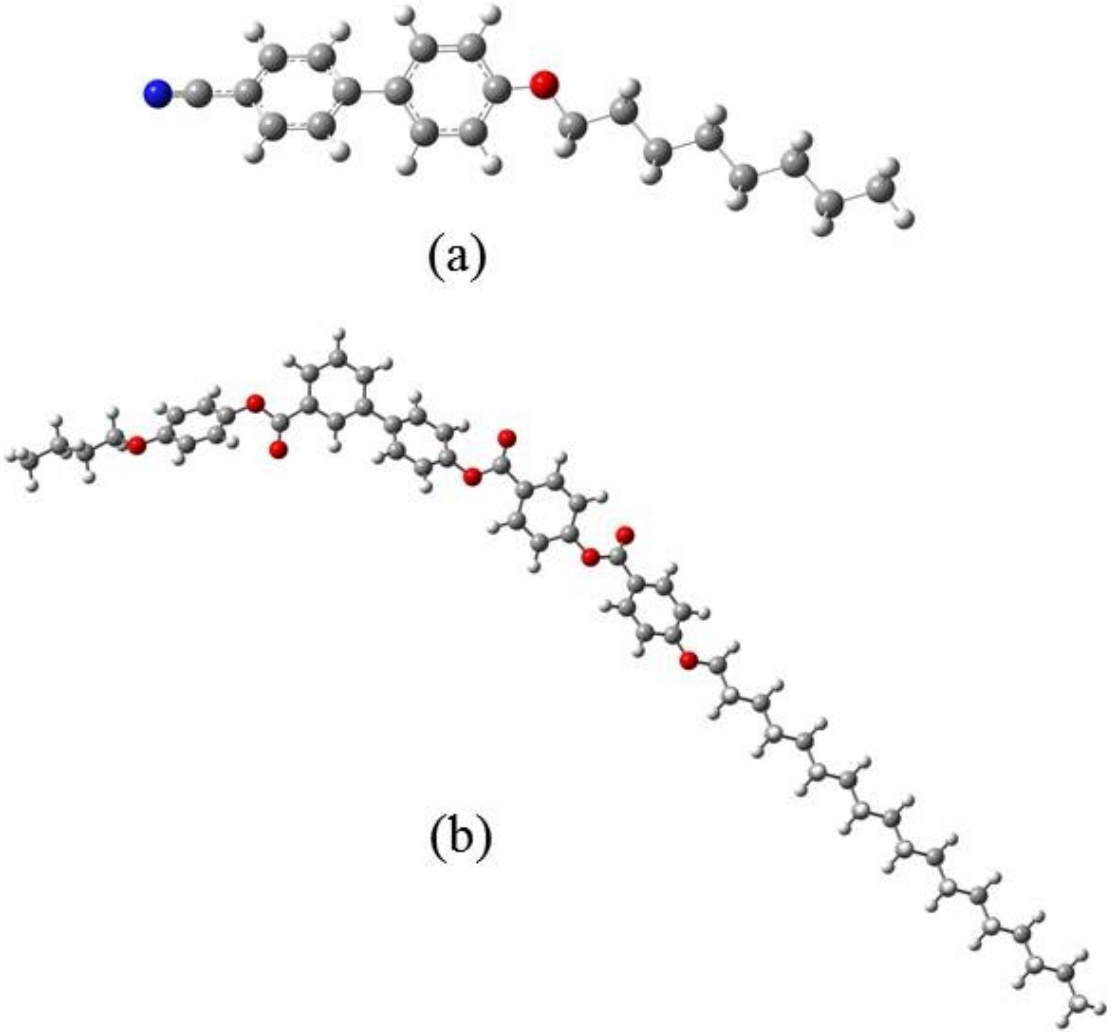

Figure 6.2: The molecular structure of a rod-like (8OCB) and a BCHS (4OC18) molecules in the minimized energy configuration.

The mixtures of the desired concentrations were prepared by weighing each component in small glass cups. The mixtures were heated to 10 ^{0}C above the isotropic temperature using a hot plate. Then, the mixtures were physically mixed by stirring with a clean glass rod at intervals of 10 minutes and maintained at the same temperature for 30 minutes before filling the sample into liquid crystal cells. The commercially available PI coated liquid crystal cells were used to get the planar-alignment of the molecules between the glass plates of the cells. The homeotropic-alignment was obtained by sandwiching the sample between an untreated clean glass plate and a clean cover-slip. The samples were studied on cooling the sample from the isotropic phase between crossed polarizers.

The molar percentage of BCHS molecules in the binary mixture was calculated as:

$$n\% = \frac{\frac{W_{BC}}{M_{BC}}}{\frac{W_{BC}}{M_{BC}} + \frac{W_R}{M_R}} * 100 \tag{6.1}$$

where M_{BC} = molecular weight of compound 4OC18 (854.6 gm/mole)
W_{BC} = weight of 4OC18 sample in gm
M_R = molecular weight of compound 8OCB (307.4 gm/mole)
W_R = weight of 8OCB sample in gm

6.3 Results and Discussions

The compound 4OC18 consisting of BCHS molecules exhibited two pseudo-polar tilted smectic phases as described in chapters section 3.2. The compound 8OCB consisting of rod-like molecules exhibits the Nematic and the SmA_d phases between its crystal and the isotropic liquid phase. In the SmA_d phase, the molecules form a lamellar structure in which their long axes are on average parallel to the layer normal as in the SmA phase. But the layer spacing in the SmA_d phase lies between l and $2l$, where l is the molecular length. As the 8OCB molecules consist of strong dipole moments, the strong dipole-dipole interaction between the molecules are thought to gives rise to an intercalated structure in the SmA_d phase [31]. The phase diagram of the binary mixtures of these two compounds is studied with a varying molar percentage of BCHS molecules. We studied 2, 4, 8, 17, 20, 25, 30, 60, 73 mol% of BCHS molecules in the mixtures. In this thesis, the mixtures with the above molar percentages are denoted as $M2$, $M4$, $M8$, $M13.6$, $M17$, $M20$, $M25$, $M30$, $M60$, and $M73$, respectively. The experimental studies on three representative mixtures $M8$, $M25$, and $M73$ will be discussed in detail.

Figure 6.3 shows the phase diagram in the temperature-molar percentage plane of binary mixtures of rod-like and BCHS molecules.

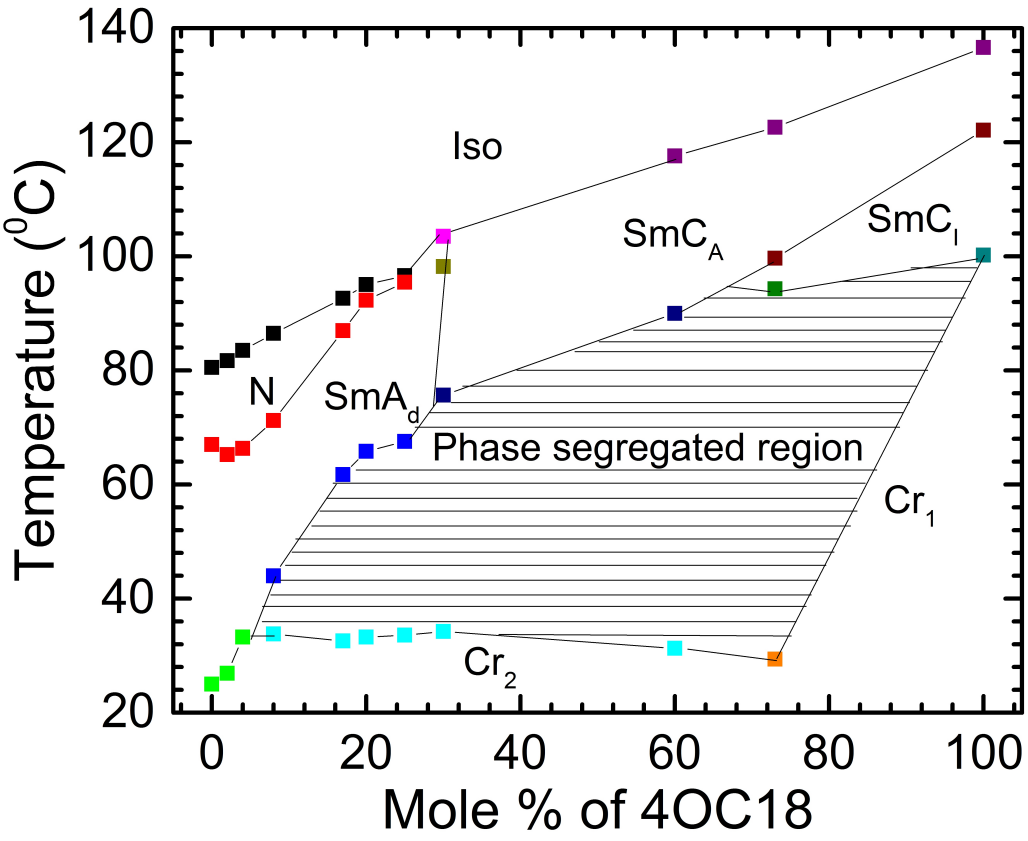

Figure 6.3: Phase diagram of the binary mixtures of rod-like and BCHS molecules.

The phase diagram was constructed based on POM observations and DSC studies. For mixtures rich in rod-like molecules, the Nematic and the SmA_d mesophases are observed. Whereas, the mixtures rich in BCHS molecules exhibit two pseudo-polar tilted smectic phases are obsereved. These observations indicate that the axial-vector order arises due to the hindered rotation of BCHS molecules about their long axes in the smectic layers. For pure 8OCB, the isotropic to Nematic transition temperature (T_{NI}) and Nematic to SmA_d transition temperature (T_{NA}) are 80 ^{0}C and 67.3 ^{0}C, respectively. Both T_{NI} and T_{NA} increased with increasing concentration of BCHS molecules indicating that the guest BCHS molecules in the mixtures enhanced the orientational order of the host rod-like molecules. The T_{NI} increased linearly with increasing molar percentage of 4OC18 as shown in the Figure 6.4.

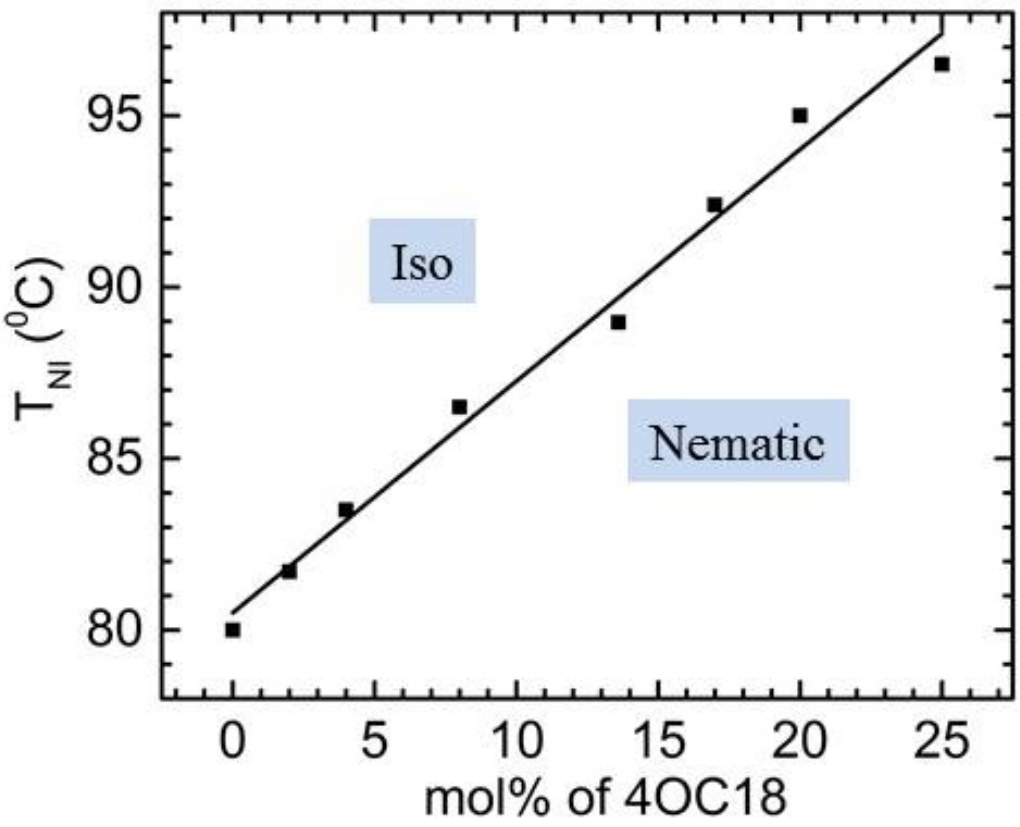

Figure 6.4: The variation of the $I - N$ transition temperatures as a function of molar percentages of BCHS molecules. The data points show the experimental values and the solid line shows the fitted line.

The temperature range of stability of the Nematic phase decreased with increasing concentration of BCHS molecules which promote the lamellar order. The Nematic phase was unstable above 25 mol% of BCHS molecules. Further, an increase in the concentration of BCHS molecules promoted the pseudo-polar tilted smectic phases. Above 30 mol% of BCHS molecules, the SmA_d phase becomes unstable and the pseudo-polar SmC_A phase become stable. The incorporation of the BCHS molecules in the uniaxial SmA_d layers of the rod-like molecules introduced biaxiality in the layers due to hindered rotation of BCHS molecules about their long axes and beyond a particular molar percentage, the tilted pseudo-polar SmC_A phase was stabilized. At even higher concentration (about 73 mol%) of BCHS molecules, the lower-temperature SmC_I phase was also stabilized in addition to the higher-temperature SmC_A phase. Though, both the compounds were found to be mixed homogeneously at all concentrations at high

temperatures in their fluid phases, the phase segregation was observed at lower temperatures driven by the crystallization of the compound 4OC18. The phase segregated regions of crystals and SmA_d appeared at about 8 mol% of BCHS molecules. The temperature range of the phase segregated region increased upon increasing the molar percentage of BCHS molecules.

6.4 Differential Scanning Calorimetry

The DSC studies on the mixtures were performed to detect the transition between the different phases. The DSC thermogram of the compound 8OCB is shown in Figure 6.5. The compound 8OCB shows the Nematic and SmA_d phases on heating and cooling between the isotropic liquid and crystal phases. A small peak corresponding to the transition between the isotropic and Nematic phase is detected. The phase transition from the Nematic to the SmA_d phase is associated with a very weak peak with an enthalpy change of 0.11 J/g. The inset in Figure 6.5 shows the magnified view of the transition peak between these two phases on heating and cooling of the sample. The small change in enthalpy shows a very weak first-order phase transition from the Nematic to the SmA_d phase.

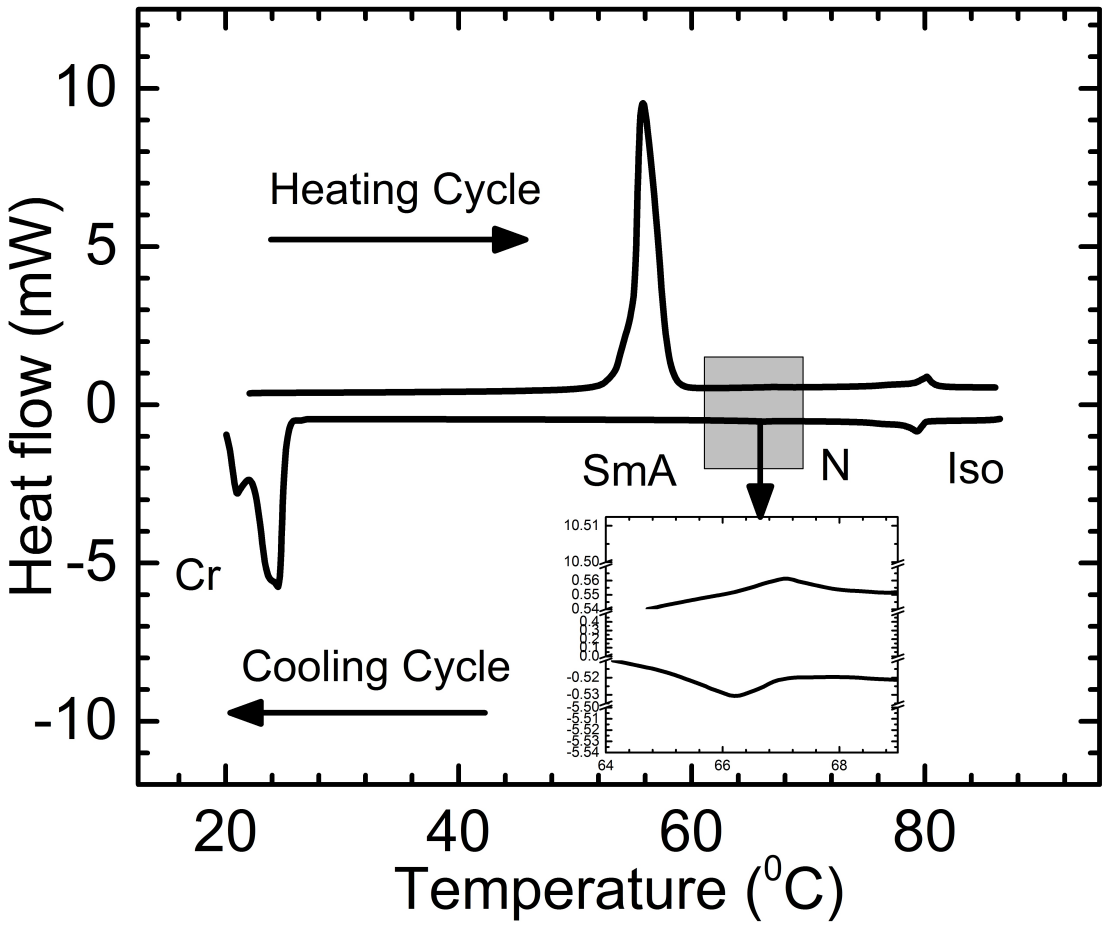

Figure 6.5: The DSC thermogram of the compound 8OCB on heating/cooling at a rate of 3 ^{0}C/min. The inset shows a weak transition peak between the Nematic and SmA_d phases on heating and cooling the sample.

On the other hand, the compound 4OC18 shows two pseudo-polar tilted smectic phases between its isotopic liquid and the crystal phase as described in subsection 3.2.1. The DSC thermogram of compound 4OC18 on heating and cooling is shown in Figure 6.6. An enthalpy change of 0.07 kJ/mol was associated with the transition between the SmC_A and SmC_I phase indicating a weak first-order phase transition. The inset of Figure 6.6 shows a clear phase transition between the higher-temperature SmC_A and the lower-temperature SmC_I phase on heating and cooling the sample.

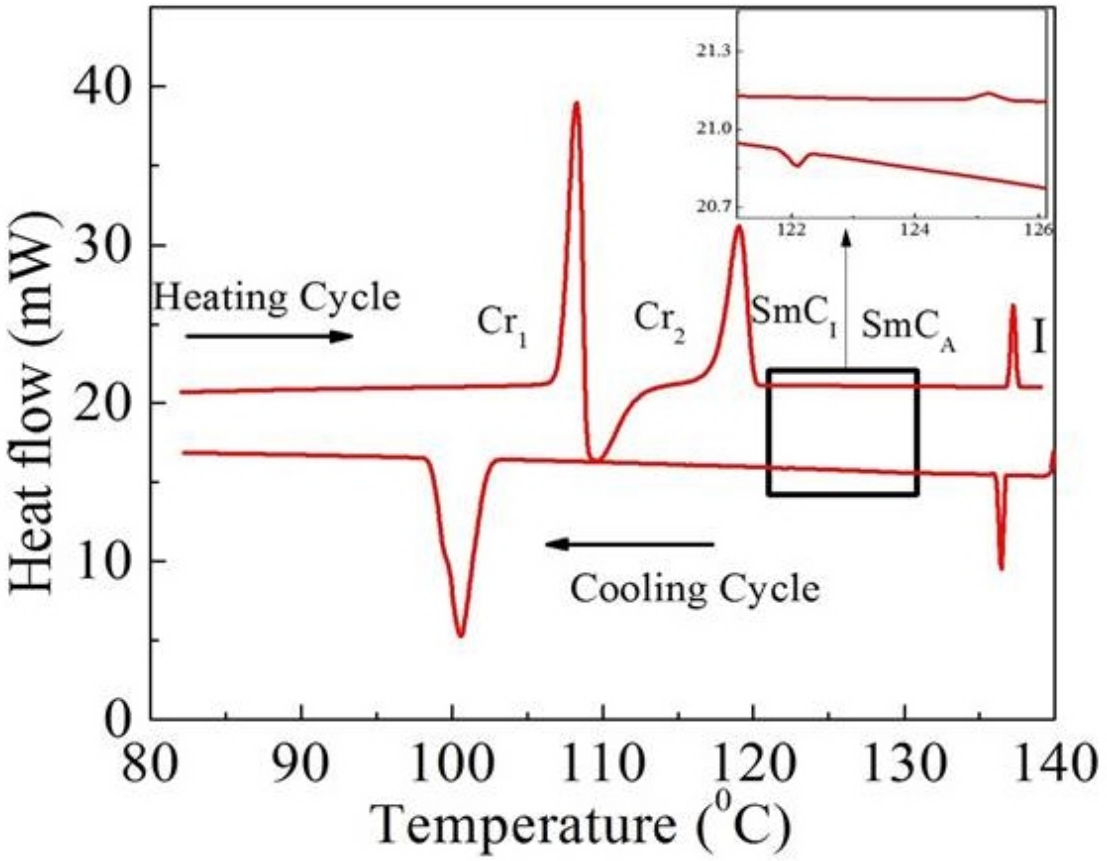

Figure 6.6: The DSC thermogram of the compound 4OC18 upon heating and cooling at a rate of 5 ^{0}C/min. The inset shows the magnified region corresponding to the transition between SmC_A and SmC_I phases.

The DSC thermograms of some of the representative mixtures on cooling are shown in Figure 6.7. As there was a phase segregation at lower temperatures, DSC thermograms of some mixtures are shown only on cooling from their isotropic phase. The vertical lines showed the phase transitions between the different phases.

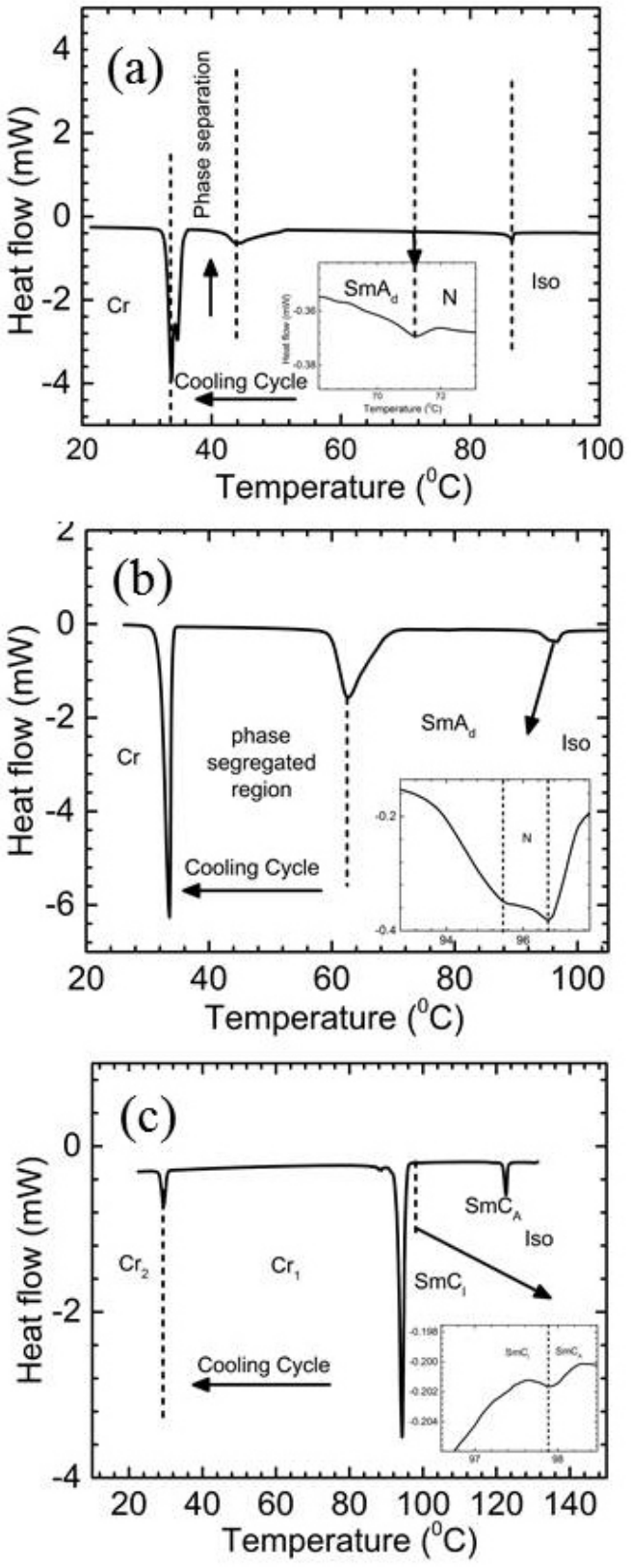

Figure 6.7: The DSC thermograms of $M8$, $M25$, and $M73$ on cooling the sample from the isotropic phase. The insets show the magnified view of weak first-order transition peaks between the mesophases.

For the mixture with 8 mol% of BCHS molecules ($M8$), the transition peaks from the isotropic to Nematic, and Nematic to SmA_d phases were observed (Figure 6.7a). For a higher molar percentage of compound 4OC18 (25 mol %), the transition temperatures from the isotropic to Nematic, and Nematic to SmA_d phases increased but with a decrease in the temperature range of stability of the Nematic phase (Figure 6.7b). The enhancement of the clearing temperature indicates that the BCHS molecules promoted the orientation order in the mixtures. The mixture rich in BCHS molecules (73 mol%) exhibited pseudo-polar tilted smectic SmC_A and SmC_I phases as shown in Figure 6.7c. This clearly indicated that the pseudo-polar tilted smectic phases are the characteristic of the BCHS molecules.

The transition temperatures and corresponding enthalpy changes across the transitions between the mesophases for the mixtures studied are listed in Table 6.1. The transition temperatures in ^{0} C and the corresponding enthalpy changes in J/g between the parentheses are shown in the table. The DSC studies clearly shows that the clearing temperature and the range of the Nematic phase increases and decreases, respectively with increasing the molar percentages of BCHS molecules. Above 8 mol% of BCHS molecules, the phase segregation appeared at lower temperatures driven by the crystallization of compound the 4OC18. At the higher molar percentage of BCHS molecules, two phases were observed to coexist at lower temperatures of the mixtures. A crystal phase corresponding to the compound 4OC18 and SmA_d/crystal phase corresponding to the compound 8OCB were observed in the mixtures at the higher molar percentage of BCHS molecules. The temperature range of the phase segregated region increased with increasing the molar percentage of BCHS molecules in the mixture which again decreased with a very high concentration of BCHS molecules corresponding to pure compound 4OC18.

Table 6.1: The transition temperatures and corresponding enthalpy changes are in ^{0}C and kJ/gm, respectively for the observed mesophases.

sample	**phase sequence of the binary mixtures**
8OCB	Iso 80 (-2.06) N 66.7 (-0.12) SmA_d 30.5(-61.68)Cr
M2	Iso 81.7 (-2.03) N 65.3 (-0.038) SmA_d 26.8 (-63.17) Cr
M4	Iso 83.5 (-1.66) N 66.3 (-0.11) SmA_d 33.34 (-61.07) Cr
M8	Iso 86.5 (-1.35) N 71.2 (-0.063) SmA_d 43.9 (-13.7) phase segregated region 33.8 (-53.3) Cr
M17	Iso 92.4 (-0.92) N 87(-0.41) SmA_d 61.7(-27.63) phase segregated region 32.03 (-44.96) Cr
M20	Iso 95 (-0.39) N 93 (-0.19) SmA_d 65.6 (-33.96) phase segregated region 33 (-40.12) Cr
M25	Iso 96.5 (-2.98) N 95.9 (-0.23) SmA_d 63.32 (-26.04) phase segregated region 29.5 (-29.8) Cr
M30	Iso 101.6(-4.05) SmA_d 88 (0.006) SmC_A 75.8 (-42.4) phase segregated region 34.1 (34.18) Cr
M60	Iso 117.4 (-4.75) SmC_A 89.7 (54.2) phase segregated region 31.1 (-13.46) Cr
M73	Iso 122.5 (-4.03) SmC_A 98 (-0.002) SmC_I 94.2 (-55.23) Cr_1 29.6 (-6.16) Cr_2
4OC18	Iso 136.6 (-8.86) SmC_A 121.4 (-0.07) SmC_I 99.8 (-105.2) Cr

6.5 POM Investigations

The POM investigations on the samples were performed to characterize the different phases and to detect transitions between them. The commercially available PI coated liquid crystal cells were used for the planar-alignment of the samples. The homeotropic-alignment of the sample was achieved by sandwiching it between a clean glass-slide

and a cover-slip. Figure 6.8 shows POM textures of the planar-aligned sample in the Nematic and SmA_d phases of pure compound 8OCB on cooling from the isotropic phase between crossed polarizers. The textures indicate good homogeneous planar-alignment of 8OCB molecules in the PI coated cells. Similarly, well-aligned homeotropic dark textures between crossed polarizers were obtained in the Nematic and SmA_d phase of pure compound 8OCB.

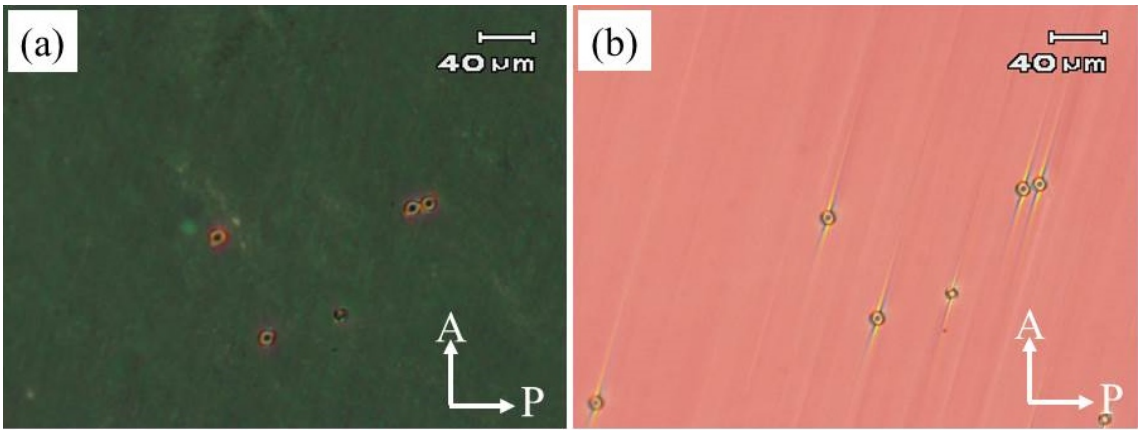

Figure 6.8: POM textures of a pure compound 8OCB of a planar-aligned sample of thickness 5 μm in (a) Nematic phase (b) SmA_d phase.

POM textures in the SmC_A and the SmC_I phases of pure compound 4OC18 are shown in Figure 6.9. As discussed in subsection 3.2.3, schlieren textures due to the tilted organization of the molecules in the layers are observed in the SmC_A and SmC_I phases for a homeotropically-aligned sample. For a planar-aligned sample, a focal-conic fan texture is observed in the SmC_A phase whereas, an irregular band texture is observed in the SmC_I phase.

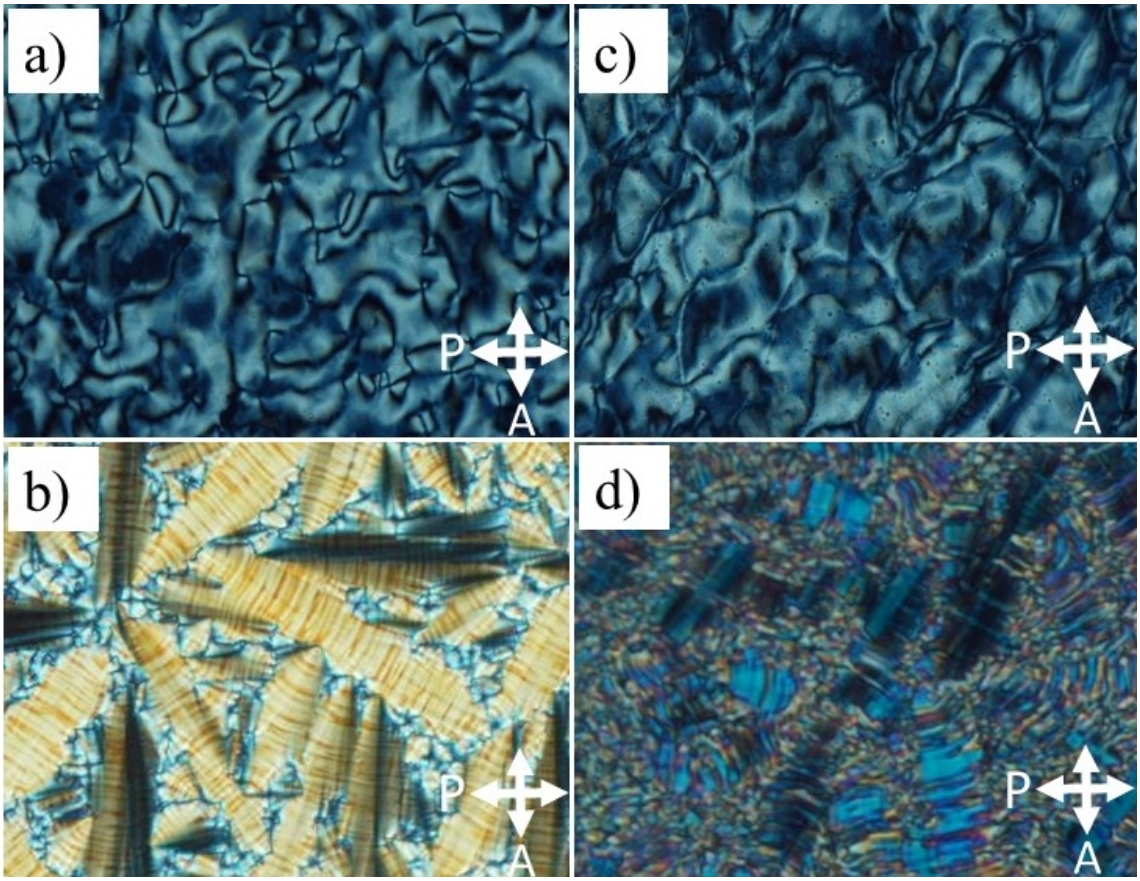

Figure 6.9: POM textures of compound 4OC18 in (a) SmC_A phase (c) SmC_I phase for a homeotropically aligned sample. The planar-aligned sample of thickness 5 μm in (b) SmC_A phase (d) SmC_I phase.

For POM studies of the binary mixtures, the sample was equilibrated in the isotropic phase for about 5-10 minutes to allow the sample to mix homogeneously to avoid the phase segregation effects at the lower temperatures. POM textures of the mixtures were studied on cooling the sample from the isotropic phase. The POM studies of three representative mixtures 8 mol% ($M8$), 25 mol% ($M25$), and 73 mol% ($M73$) are discussed here. Figure 6.10 shows the homeotropically-aligned sample of $M8$ between the crossed polarizers on cooling from the isotropic phase.

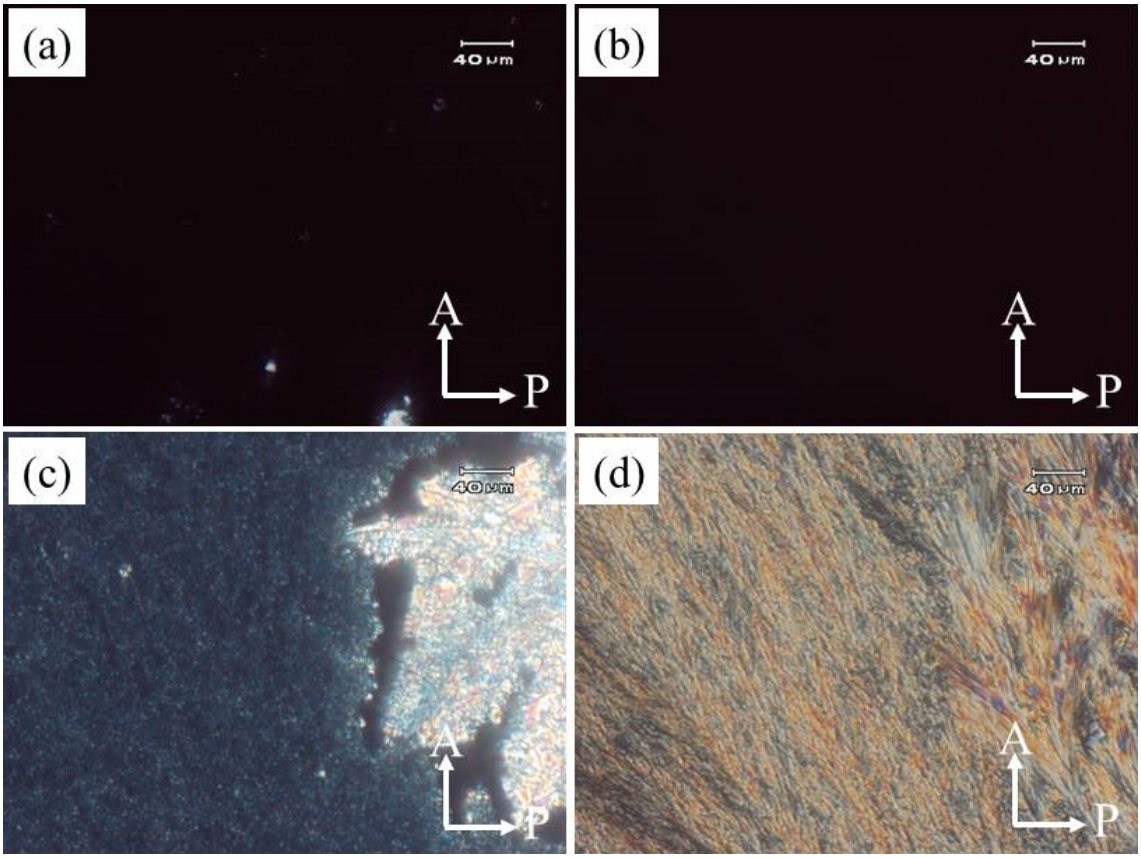

Figure 6.10: POM textures for the homeotropically-aligned sample of $M8$ in (a) Nematic phase at 73 ^{0} (b) SmA_d phase at 53 ^{0}C (c) phase segregated region at 45 ^{0} (d) crystal phase at 33 ^{0}.

A dark texture between crossed polarizers (Figure 6.10a) was observed in the Nematic phase which remained dark on rotating the sample confirmed homeotropic-alignment of the molecules. Some fluctuations in the light intensity in the dark background were observed due to the thermal fluctuations of the director in the Nematic phase. On further cooling, the sample undergoes a transition to the SmA_d phase, again showing a dark texture (see Figure 6.10b). The dark texture indicated the uniaxial nature of the SmA_d phase of the mixture. However, in this phase, the fluctuations in the light intensity arising from thermal fluctuations were not visible due to the more ordered and layered structure of the molecules in the SmA_d phase. On further, decreasing the temperature, the phase separation into the crystal and SmA_d phases was observed at about 44 ^{0}C as shown in Figure 6.10c. The sample proceeded to the crystal phase coexistence (see Figure 6.10d) at 34.6 ^{0}C.

The textures of a planar-aligned sample ($M8$) of thickness 5 μm in different phases are shown in Figure 6.11.

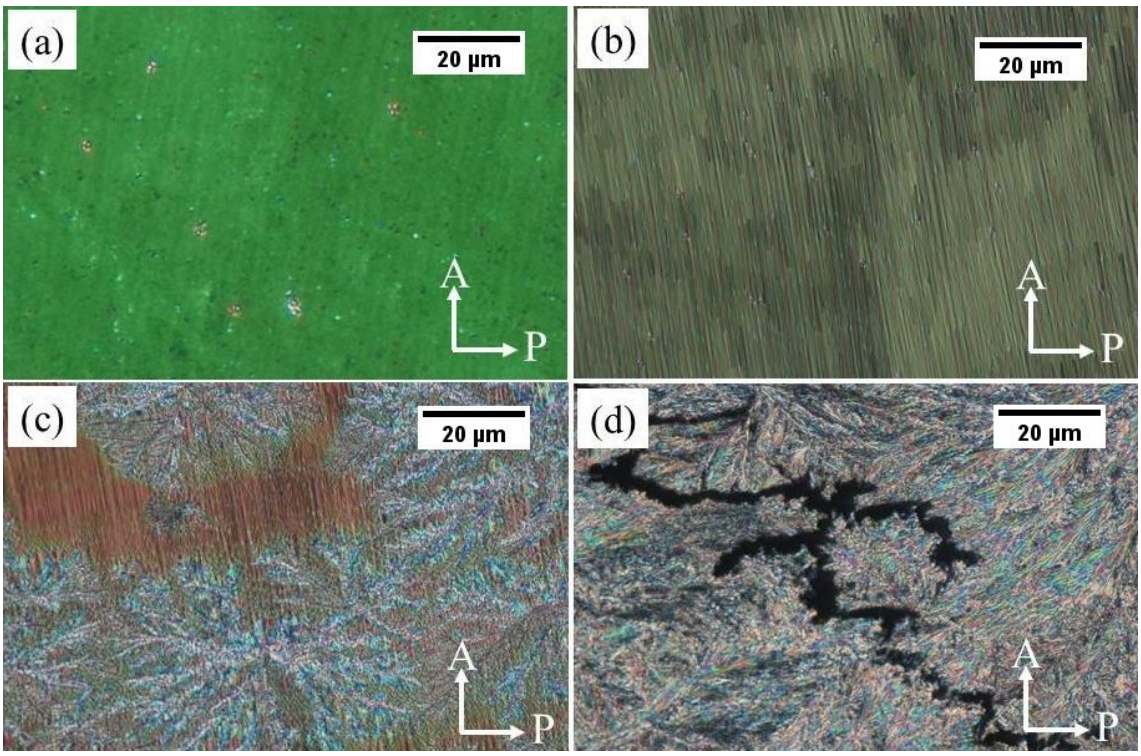

Figure 6.11: Planar-aligned sample of thickness 5 μm under POM on cooling from the isotropic phase in (a) Nematic phase at 73 ^{0}C (b) the SmA_d phase at 53 ^{0}C (c) phase segregated region at 45 ^{0}C (d) crystal phase at room temperature.

A well-aligned sample along the rubbing direction is obtained in the Nematic and SmA_d phases which were confirmed by rotating the sample between crossed polarizers. The maximum and minimum intensity were observed when the rubbing direction was making an angle 45 or 0/90 degrees, respectively with respect to the polarizer. The observed texture was similar to the typical textures of the Nematic and SmA_d phase. At lower temperatures, the textures with phase segregated regions were observed as shown in Figure 6.11c. The 8OCB rich regions shows the planar-aligned texture as that of SmA_d, whereas, 4OC18 rich regions shows the crystalline phase. Upon further lowering the temperature, the entire sample became crystal as shown in Figure 6.11d.

POM textures for the homeotropically-aligned sample of the mixture $M25$ are shown in Figure 6.12.

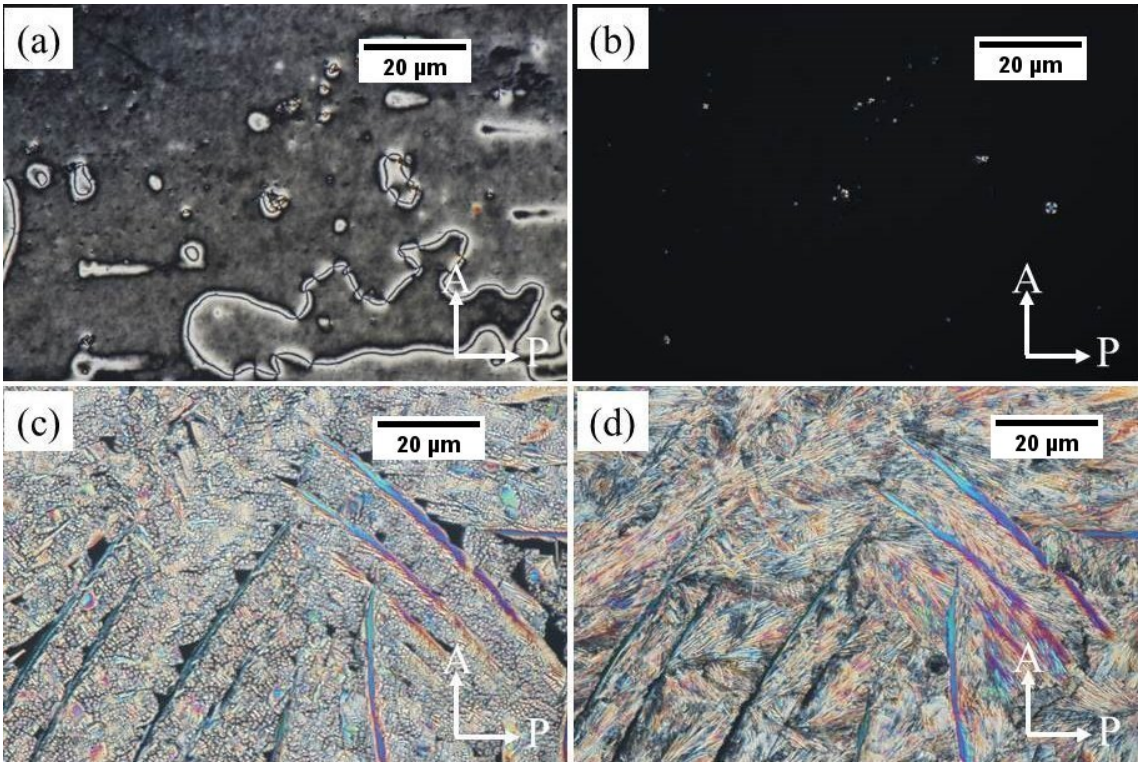

Figure 6.12: POM textures of a homeotropically-aligned sample of $M25$ in (a) the Nematic phase at 100 ^{0}C (b) the SmA_d phase at 94 ^{0}C (c) phase segregated region at 664 ^{0}C (d) crystal phase at room temperature.

A schlieren texture corresponding to the Nematic phase appeared at 96.5 ^{0}C as shown in Figure 6.12a. The Nematic phase in this mixture had a very narrow temperature range stability. On cooling the sample, the SmA_d phase with a completely well aligned homeotropic texture (see Figure 6.12b) was observed around 95.9 ^{0}C. Phase segregation effects appeared at about 63 ^{0}C (see Figure 6.12c). Upon further cooling, the whole sample crystallizes at about 29 ^{0}C.

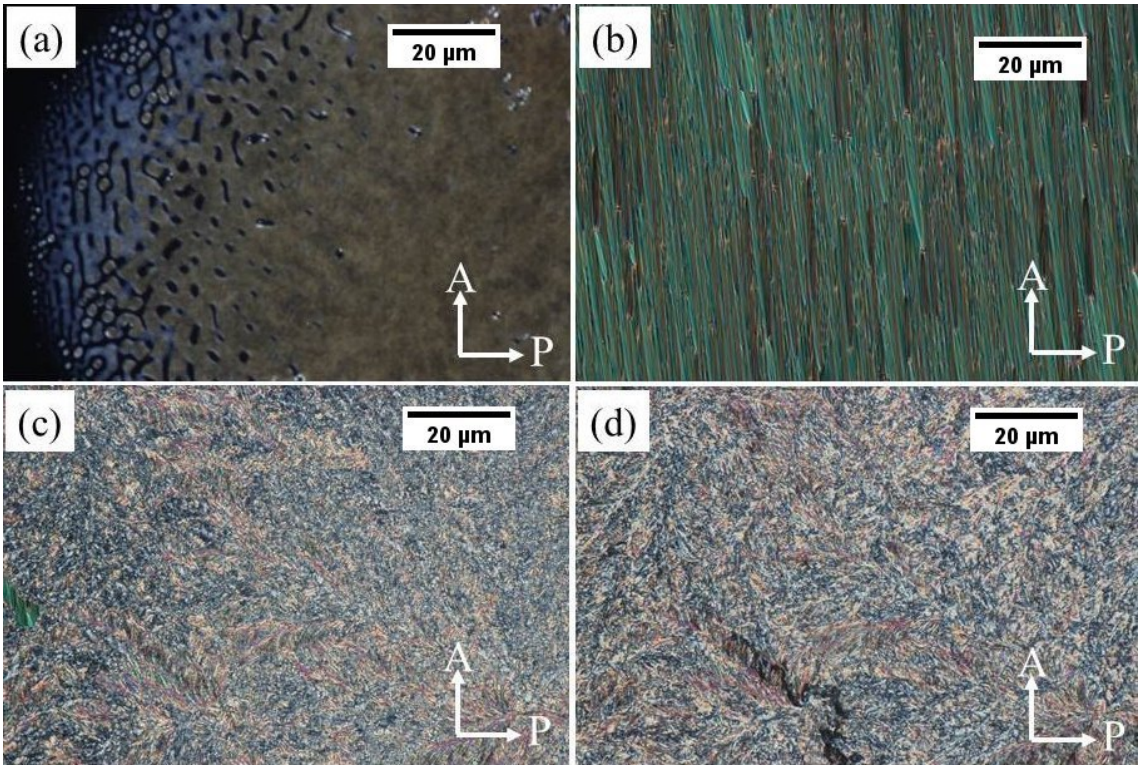

Figure 6.13: POM textures of $M25$ of a planar-aligned sample on cooling from the isotropic phase between the crossed polarizers (a) Nematic phase at 100 ^{0}C (b) SmA_d phase at 94 ^{0}C (c) phase segregated region at 64 ^{0}C and (d) the crystal phase at room temperature.

The textures of the homeotropically-aligned sample of the mixture $M73$ are shown in Figure 6.14.

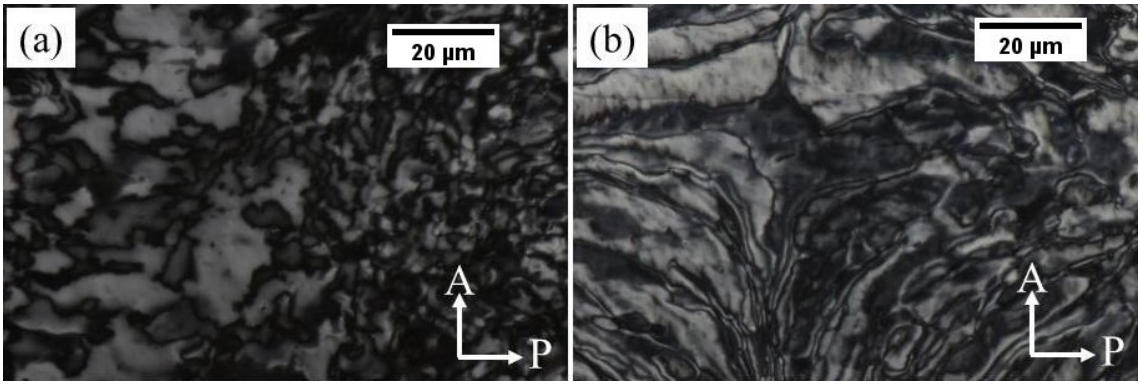

Figure 6.14: POM textures of a homeotropically-aligned sample of M73 between crossed polarizers in (a) the SmC_A phase at 122 ^{0}C and (b) the SmC_I phase at 100 ^{0}C.

A hazy schlieren texture (Figure 6.14a) is observed in the higher-temperature SmC_A

phase at about 122.5 ^{0}C. The schlieren texture clearly indicated the tilt organization of the molecules in the layers in contrast to the SmA_d phase. Upon further cooling of the sample, again, a schlieren texture with domain walls separating coexisting structures (Figure 6.14b) is observed similar to that of the lower-temperature SmC_I phase of the pure compound 4OC18.

For a planar-aligned sample of the mixture $M73$, a focal-conic fan texture (Figure 6.15a) is observed in the SmC_A phase as typically observed in the SmC_A phase. The black brushes in the fan region appeared parallel to the layer normal when it was parallel/perpendicular to the polarizer which indicates that one of the optic axes was parallel to the layer normal. At lower temperatures, coexisting domain structures parallel to the layers appeare in the fan region similar to the texture observed in the SmC_I phase of pure compound 4OC18. Thus, at a high molar percentage of the BCHS molecules, the mixtures exhibit the pseudo-polar tilted smectic phases.

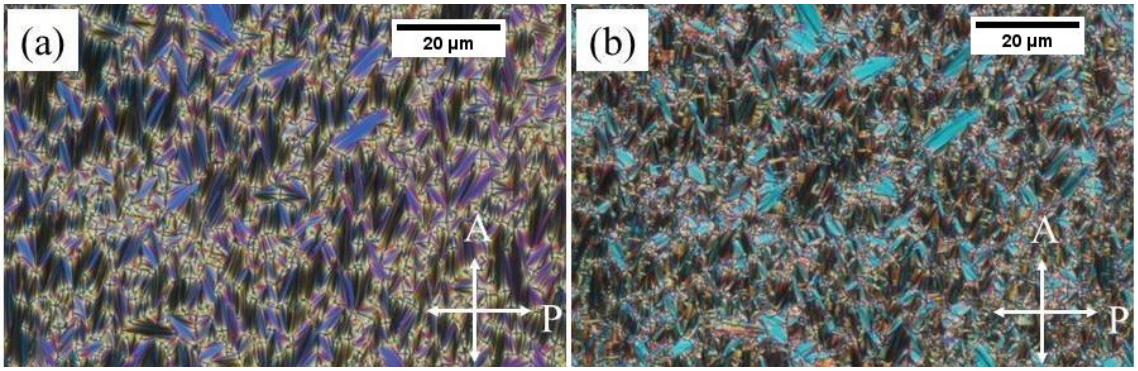

Figure 6.15: POM textures of a planar-aligned sample of $M73$ of thickness 5 μm in (a) the SmC_A phase at 122 ^{0}C and (b) the mC_I phase at 100 ^{0}C.

6.6 Dielectric and optical transmittance measurements

The simultaneous measurements of the dielectric constant and the transmitted optical intensity of the mixtures as a function of temperature were performed to detect the transition between the observed phases. The electro-optic studies were performed on a homemade setup, as described in section 2.8. The data was collected on cooling the sample from the isotropic phase between crossed polarizers. The variation of the real

part of dielectric constant and the transmitted optical intensity of a planar-aligned sample of thickness 5 μm with temperature for a pure compound 8OCB is shown in Figure 6.16.

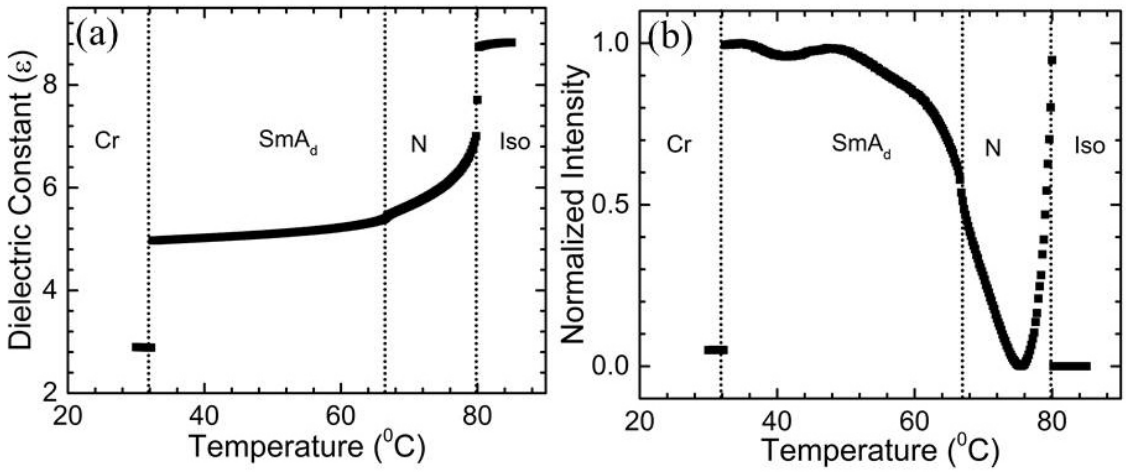

Figure 6.16: The variation of (a) dielectric constant and (b) the optical intensity of Compound 8OCB of a planar-aligned sample as a function of temperature.

For the binary mixtures, the sample was equilibrated in the isotropic phase for 10 minutes before collecting data. The commercially available liquid crystal cells of thickness 5 μm for a planar-alignment of the sample were used for the measurements. The results of three representative mixtures $M8$, $M25$, and $M73$ are discussed here.

The real part of the effective dielectric constant and the transmitted optical intensity passing through a planar-aligned sample of mixture $M8$ is shown in Figure 6.17.

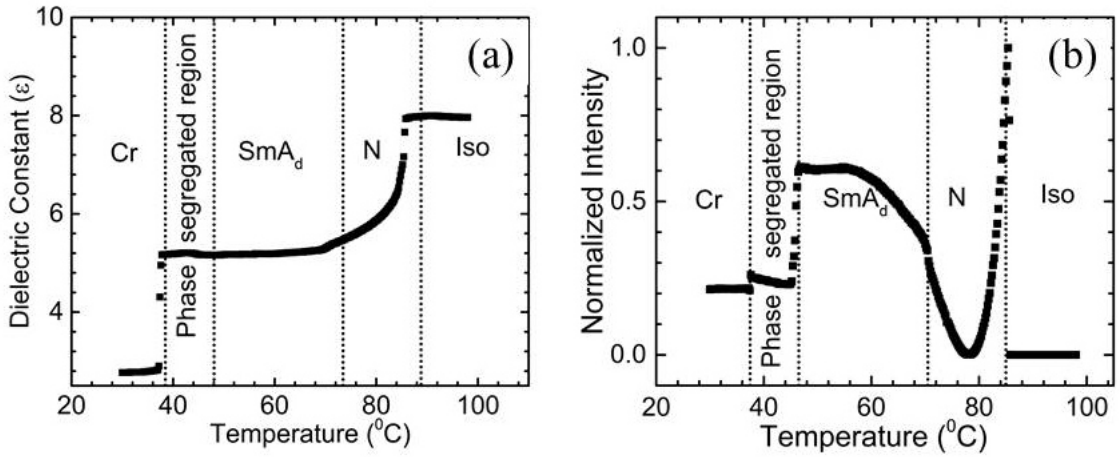

Figure 6.17: The variation of (a) dielectric constant and (b) the optical intensity of M8 of a planar-aligned sample of thickness 5 μm as a function of temperature. The was collected on cooling the sample from the isotopic phase.

The sharp decrease in the dielectric constant at 86.5 ^{0}C on cooling from the isotropic phase indicates the transition to the Nematic phase. The dielectric constant of the sample decreased to 5.5 at lower temperatures in the Nematic phase. For a uniform planar-alignment in the Nematic phase, the perpendicular component of the dielectric constant ($\epsilon_\perp$ mostly contributed to the measurement. The mixture $M8$ was rich in 8OCB which had positive dielectric anisotropy in the Nematic and SmA_d phase. Thus, the measured dielectric constant decreased in the Nematic phase compared to that in the isotropic phase. A kink in the dielectric constant data at around 69 ^{0}C indicates the transition to the SmA_d phase. At lower temperatures in the SmA_d phase, the dielectric constant get saturated to a value of about 5.0. Upon further cooling, a sharp drop in the dielectric constant at 38 ^{0}C indicates the transition to the crystal phase.

The temperature variation of the transmitted optical intensity through a planar-aligned sample of thickness 5 μm between crossed polarizers is shown in Figure 6.17b. A sharp increase in the optical intensity at the isotropic to Nematic temperature (T_{NI}) is observed due to the stiff increase in the birefringence of the sample in the Nematic phase. At lower temperatures, the increasing birefringence of the sample gives rise the characteristic oscillatory behavior of the optical intensity. A small discontinuity of the optical signal at around 69 ^{0}C indicates the transition to the SmA_d phase. A sharp decrease in the transmitted intensity at about 47 ^{0}C clearly indicates the onset of

phase segregation at lower temperatures though it was not detected from the dielectric measurements. The crystallization of the sample at 37.6 ^{0}C is also detected in the optical measurement.

The variation of the real part of effective dielectric constant and the optical intensity with temperature for the mixture $M25$ on cooling from the isotropic phase are shown in Figure 6.18.

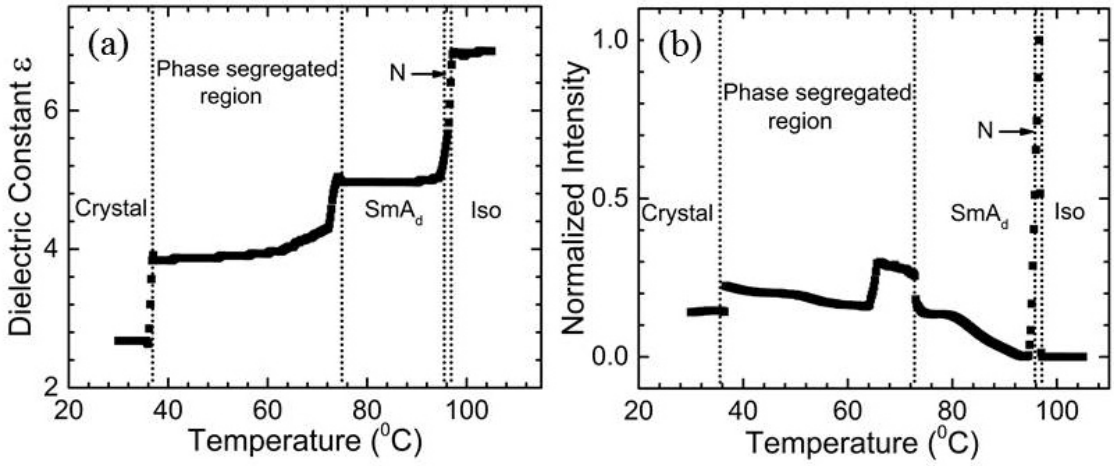

Figure 6.18: The variation of (a) the real part of the dielectric constant and (b) the optical intensity of $M25$ of a planar-aligned sample of thickness 5 μm as a function of temperature.

Both the dielectric constant and transmitted optical intensity data detected the transitions from the isotropic to Nematic and Nematic to the SmA_d phase. The Nematic phase is stable over a narrow temperature range. A slope discontinuity in the dielectric data was observed at the transition point from the Nematic phase to the SmA_d phase. The dielectric constant is about 4.5 in the SmA_d phase. A sharp decrease in the dielectric constant value is observed at the onset of phase segregation. Similarly, the temperature variation of the transmitted optical intensity passing through a planar-aligned sample (Figure 6.18b) clearly detected all the transitions.

The mixture of $M73$ was rich in BCHS molecules. For this mixture, POM studies revealed a focal-conic fan texture for a planar-aligned sample. The variation of the real part of effective dielectric constant with temperature for a planar-aligned sample is shown in Figure 6.19a.

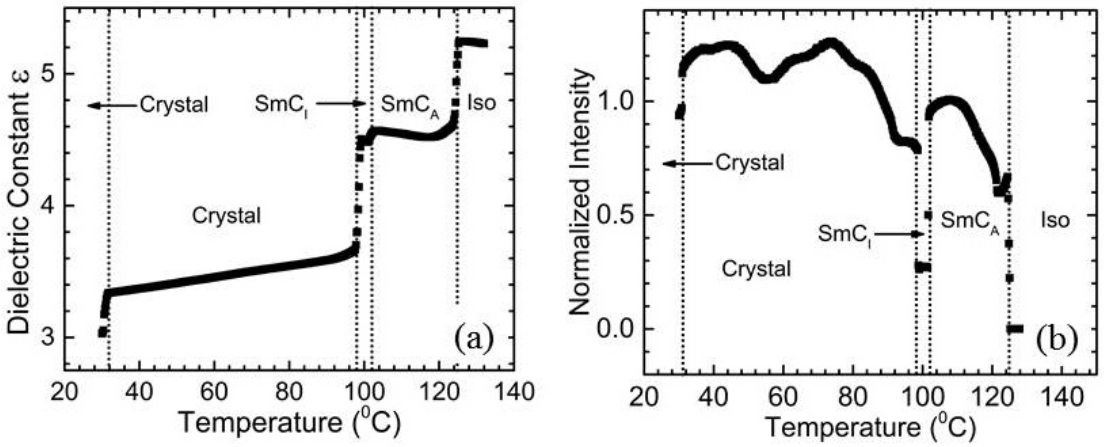

Figure 6.19: The variation of (a) dielectric constant and (b) the transmitted optical intensity passing through a planar-aligned sample of thickness 5 μm of $M7$3 on cooling from the isotropic phase.

The dielectric constant of the sample decreases on cooling from the isotropic phase to the higher-temperature SmC_A phase. The dielectric constant in the SmC_A phase is found to be about 4.6. At the transition from the SmC_A to the SmC_I phase, a further decrease in the dielectric constant was observed. The dielectric constant again decreases as the phase segregation appeared at about 99 ^{0}C. The measurements of optical intensity also detected all the transitions as shown in Figure 6.19b.

The dielectric and optical transmittance studies for a pure compound 4OC18 consisting of BCHS molecules are already discussed in subsection 4.3.1. The variation of the real part of the effective dielectric constant and optical transmittance of a planar-aligned sample as a function of temperature are shown in Figure 6.20.

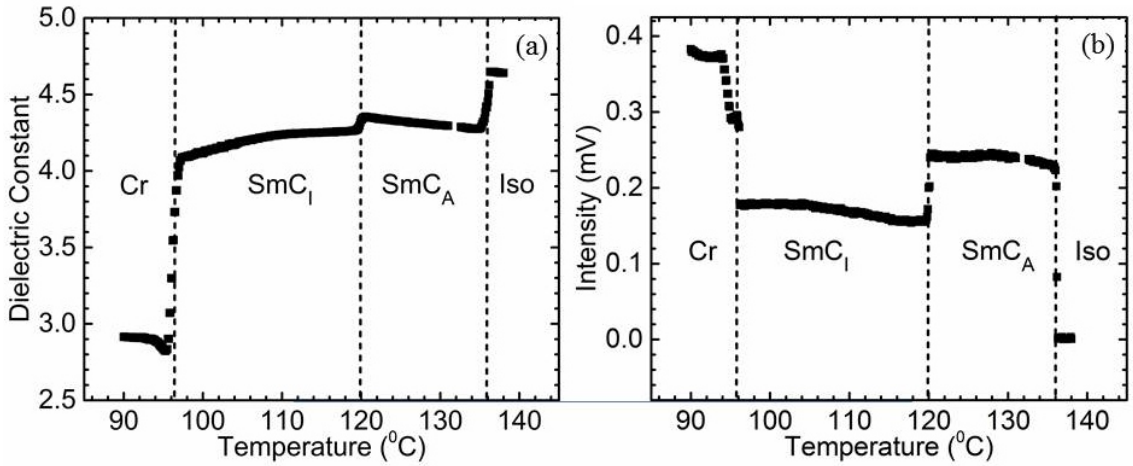

Figure 6.20: The variation of (a) the real part of the effective dielectric constant and (b) the transmitted optical intensity passing through a planar-aligned sample of thickness 5 μm of compound 4OC18 on cooling from the isotropic phase.

The dielectric and optical transmittance measurements detected all the transitions between the observed phases on cooling the sample from the isotropic phase. As discussed earlier, the BCHS molecules give rise to an axial-vector order without any net electric polarization in the smectic layers and hence the pure compound 4OC18 had relatively small dielectric constant with low dielectric anisotropy compared to that of the pure compound 8OCB. The rod-like molecules of the compound 8OCB has a strong dipole moment parallel to their long axes due to the presence of the nitrile group (-CN) at one end of the molecule. Thus, the pure compound 8OCB has a large dielectric constant parallel to the director with large positive dielectric anisotropy in its Nematic and SmA_d phases. Thus, the effective dielectric constant of the mixtures decreased upon increasing the molar percentage of BCHS molecules.

6.7 X-ray diffraction Investigations

The XRD studies were performed on the samples to further characterize the liquid crystal phases. The XRD intensity profiles in the Nematic and SmA_d phases of a pure compound 8OCB are shown in Figure 6.21.

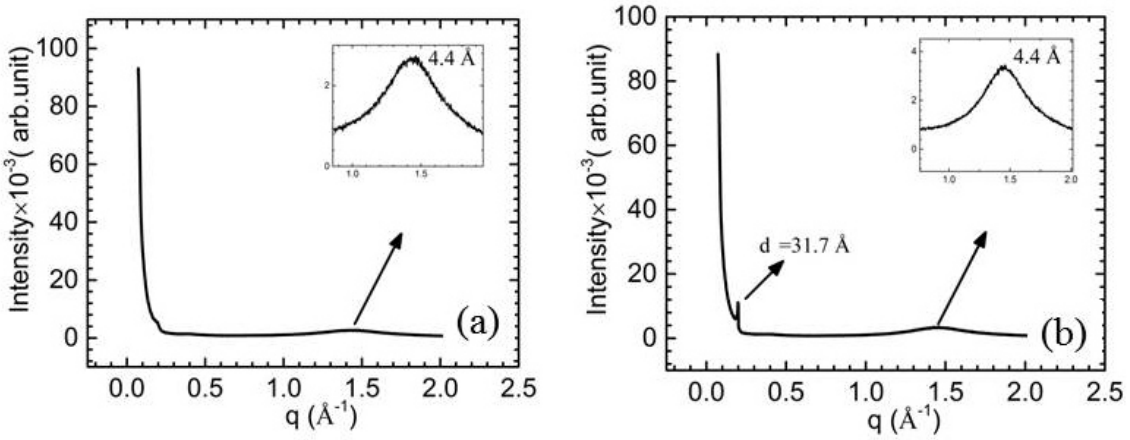

Figure 6.21: The XRD intensity profile of the pure compound 8OCB in (a) the Nematic phase at 70 ^{0}C (b) the SmA_d phase at 48 ^{0}C with layer spacing 31.7 Å.

The intensity profile in the Nematic phase (Figure 6.21a) showed only a diffused peak in the wide-angle region indicating no long-range positional order of the molecules. A sharp peak in the small-angle region in the SmA_d phase indicates the lamellar order of the molecules. The small-angle region peak in the SmA_d phase gives the effective layer spacing as 31.7 Å. The molecular length l of the 8OCB molecule estimated from the molecular formula was about 21.7 Å. Clearly, the observed layer spacing in the SmA_d phase lies between l and $2l$ and the XRD studies show that the molecules have an intercalated structure in the SmA_d phase. The additional diffused peak at a wide-angle region in the SmA_d phase indicates a fluid lamellar structure with lateral average d-spacing between the molecules as 4.4 Å.

Figure 6.22 shows the intensity profile as a function of wave-vector of a pure compound 4OC18 in the SmC_A and SmC_I phases. The small-angle region peaks in both the phases gave the layer spacing as 42.6 AA Å and 43.1 Å, respectively. The XRD studies showed that the molecules are tilted with respect to the layer normal in both the mesophases as discussed in subsection 3.2.2. The d-spacing in the wide-angle peak region in both the observed mesophases are about 4.6 Å in both phases.

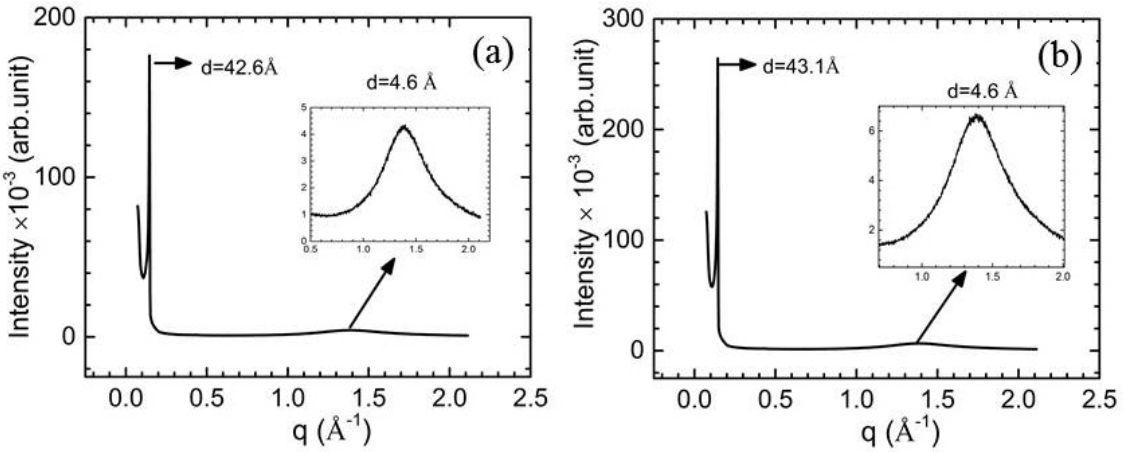

Figure 6.22: The intensity profile of the pure compound 4OC18 in (a) higher-temperature SmC_A phase with a layer spacing 42.6 Å at 126 ^{0}C and (b) the lower temperature SmC_I phase with layer spacing 43.1 Å at 115 ^{0}C.

For the XRD studies of the mixtures, the samples were heated 5 ^{0}C above the clearing temperature and equilibrated at that temperature. The XRD data was collected with an exposure time of about 30 minutes on cooling the sample to the desired phase from the isotropic phase. The XRD intensity profiles as a function of wave-vector q in the different phases for 8 mol% ($M8$) of 4OC18 in the mixture are shown in Figure 6.23.

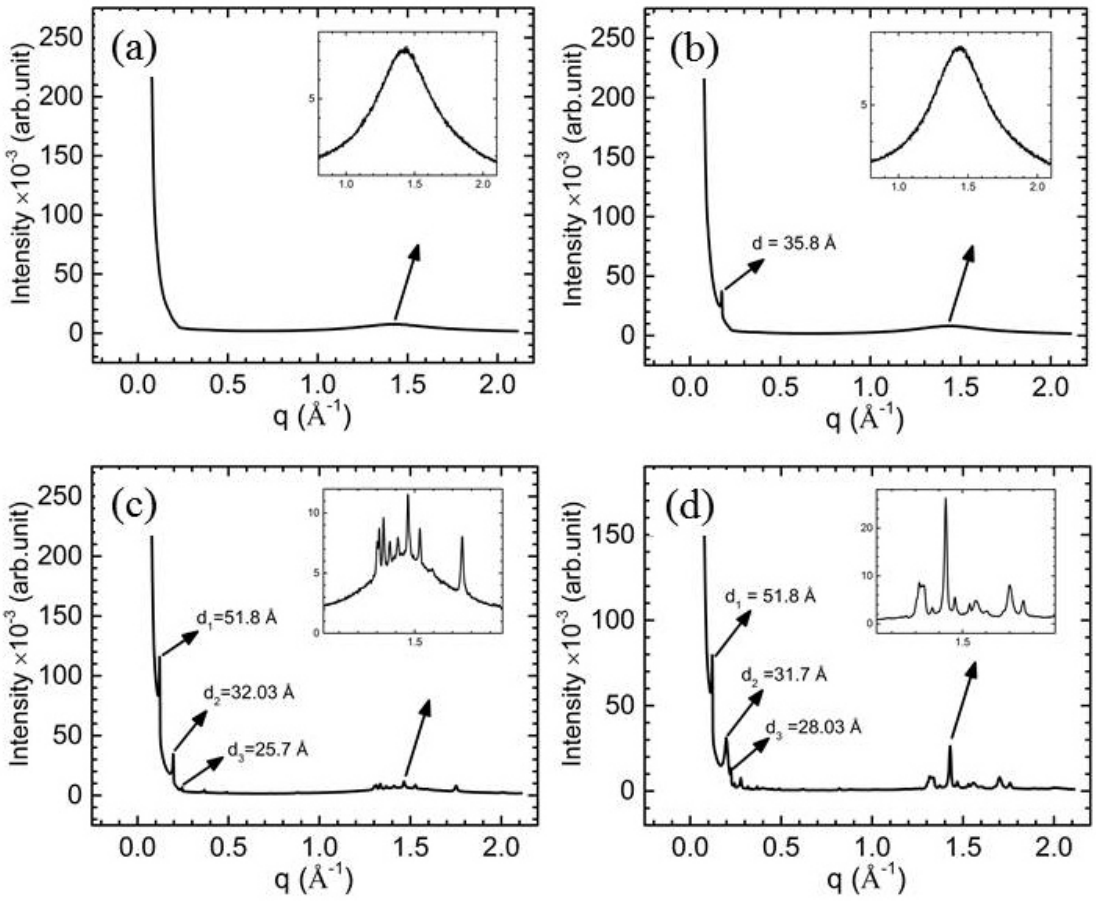

Figure 6.23: The XRD intensity profile of $M8$ as a function of wave-vector q in (a) Nematic phase at 81 ^{0}C (b) SmA_d phase at 64 ^{0}C (c) phase segregated region at 48 ^{0}C and (d) coexisting crystal phases at room temperature. The insets show the diffusive peaks in the wide-angle region.

For the mixture $M8$, the XRD profile in the Nematic phase shows only a diffusive peak at the wide-angle region which is a characteristic of the absence of long-range positional order. In the SmA_d phase, a sharp peak in the small-angle region confirmed the lamellar order with the layer spacing of about 35.8 Å. At lower temperatures in the coexistence range, we observed multiple sharp peaks in the small-angle region as well as in the wide-angle region confirming the crystallization of the sample. The XRD studies in conjunction with the POM studies confirmed the phase segregation with coexisting crystal phase and LC phase. At even lower temperatures, the XRD and POM studies confirmed the coexisting crystal phases at room temperature.

Figure 6.24 shows the XRD intensity profile for 25 mol% of 4OC18 in the mixture

($M25$).

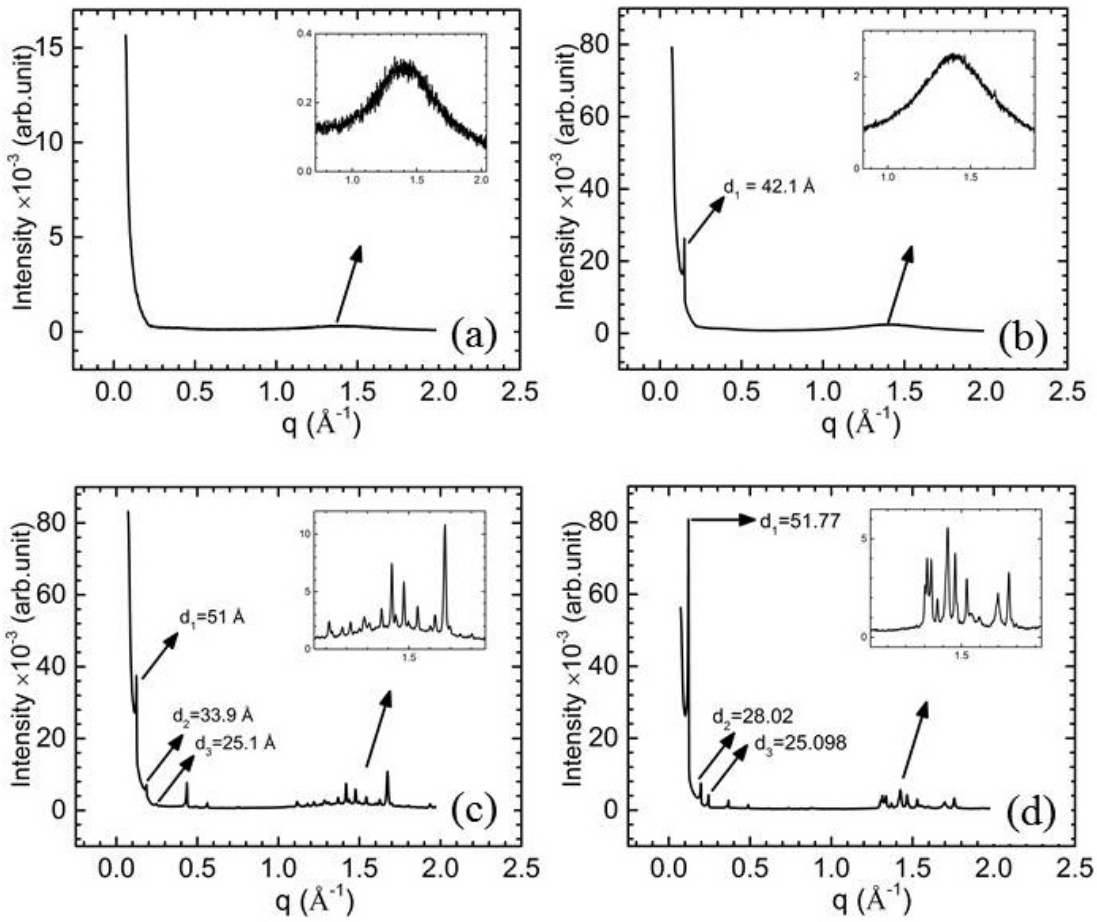

Figure 6.24: The intensity profile for $M25$ in (a) the Nematic phase at 100 ^{0}C (b) the SmA_d phase at 94 ^{0}C (c) phase segregated region at 64 ^{0}C (d) crystal phases at room temperature.

For$M25$, the XRD profile in the Nematic phase again showed a diffusive peak in the wide-angle region. The layer spacing in the SmA_d phase is found to be about 42.1 Å. Thus, an increase in the layer spacing in the SmA_d phase was observed with increasing the molar percentage of BCHS molecules. Upon further cooling of the sample to the phase segregated region, the XRD profiles clearly indicated the coexistence of crystal and other phases.

At even higher molar percentage of the BCHS molecules in the mixtures, the calamitic Nematic and SmA_d phases were not observed. Instead the pseudo-polar tilted smectic phases get stabilized. The XRD intensity profile of 73 mol% of BCHS molecules in the mixture ($M73$) is shown in Figure 6.25.

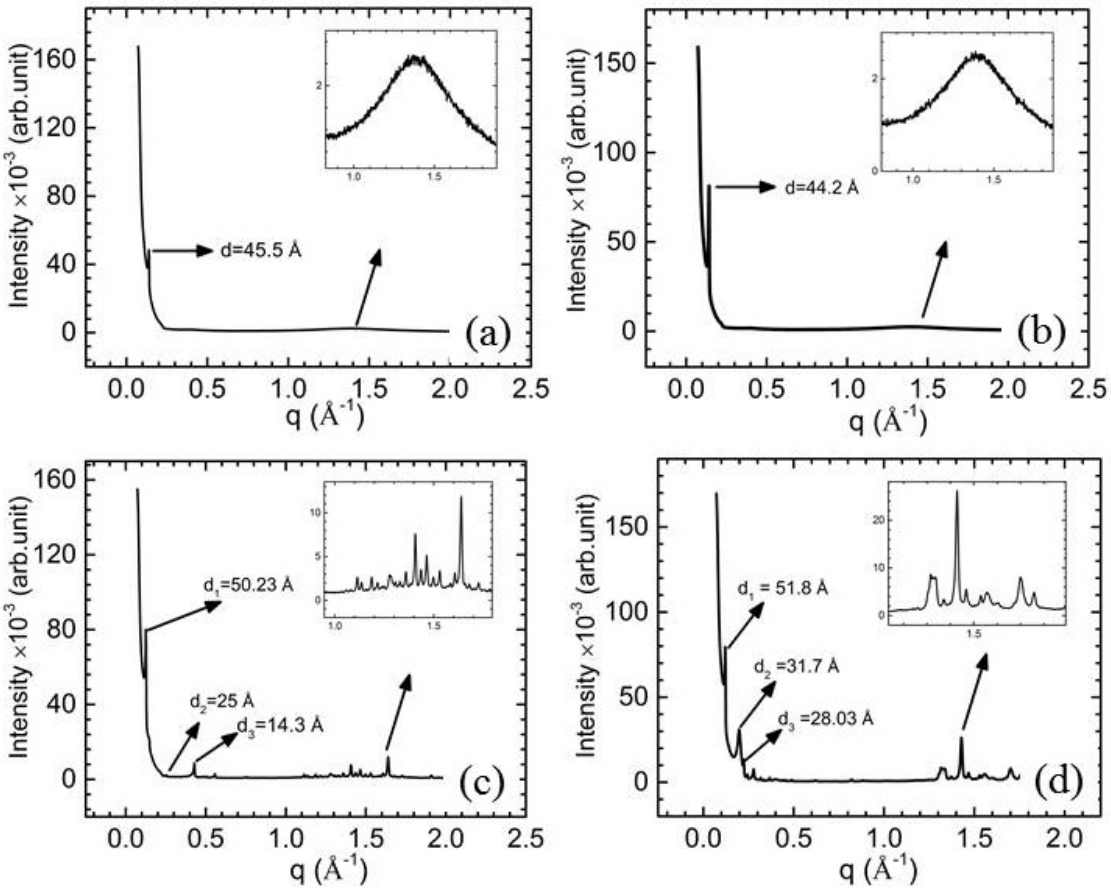

Figure 6.25: The intensity profile of $M73$ in (a) SmC_A phase at 122^0 C (b) SmC_I phase at 100 ^{0}C (c) crystal phase at 98 ^{0}C and (d) crystal phase at room temperature.

A sharp peak in the small-angle region in the SmC_A phase gives the layer spacing about 45.5 Å (Figure 6.25a). Interestingly, the observed layer spacing in the SmC_A phase was about double the molecular length of the rod-like molecules. At lower temperatures in the SmC_I phase, the layer spacing was found to be about 44.2 Å. Even at lower temperatures, the coexisting crystal phases were observed as shown in Figure 6.25. The layer spacing in the observed smectic phases of the mixtures obtained from the XRD results is shown in the Table 6.2.

Table 6.2: The layer spacing in different phases of respective binary mixtures

Sample	**Mesophases**	**Temperature**	**Layer spacing**
8OCB	SmA_d	65	31.7
M2	SmA_d	65	32.6
M4	SmA_d	66	33.4
M8	SmA_d	70	35.8
M17	SmA_d	86	40.1
M20	SmA_d	93	41.03
M25	SmA_d	97	42.1
M30	SmA_d	100	43.1
	SmC_A	87	42.6
M60	SmA_A	112	46.1
M73	SmC_A	122	45.5
	SmC_I	100	44.3
4OC18	SmC_A	126	42.6
	SmC_I	115	43.1

We also determined the variation of layer spacing in the observed smectic phases as a function of the molar concentration of the BCHS molecules in the mixtures (Figure 6.26).

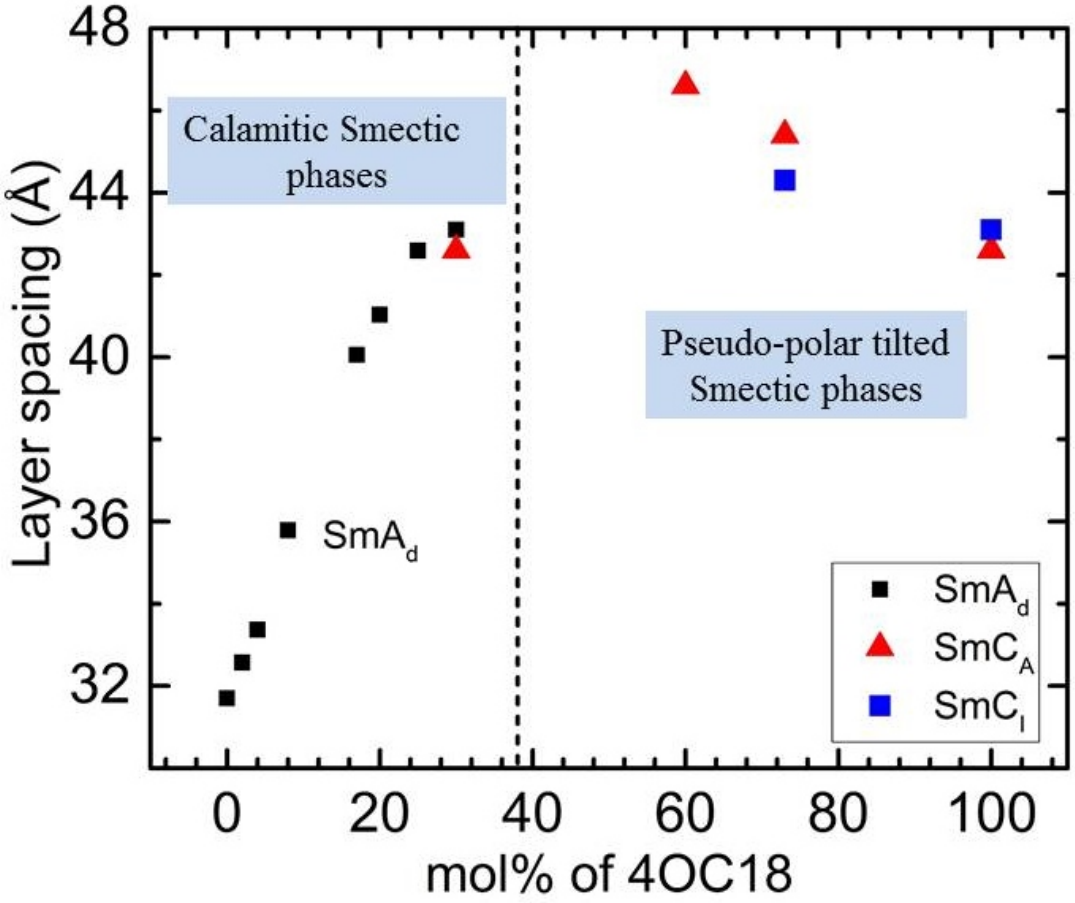

Figure 6.26: The variation of layer spacing in the calamitic and pseudo-polar tiled smectic phases with different molar concentrations of the BCHS molecules in the mixture. The vertical dashed line separates the stability regions of the uniaxial calamitic and pseudo-polar tilted smectic phases exhibited by rod-like and BCHS molecules respectively.

As can be seen from Figure 6.26, the layer spacing in the SmA_d phase increases with the increasing molar percentage of BCHS molecules. The layer spacing in the SmA_d phase of pure compound 8OCB is about 31.7 Å which lies between l and $2l$ where l = 21.6 Å being the molecular length of the rod-like molecule. Thus, the molecules in the layers have an intercalated organization, giving the layer spacing between l and $2l$. The XRD results show that the layer spacing in the SmA_d phase of the mixtures increases towards $2l$ with increasing the molar percentage of BCHS molecules. Thus, the BCHS molecules tend to decrease the overlap of the intercalated rod-like molecules in the layers. Above a certain concentration of BCHS molecules, the SmC_A phase was stabilized and the layer spacing in the SmC_A phase decreased towards the value

corresponding to pure 4OC18 with an increasing molar percentage of BCHS molecules in the mixtures. The vertical line shows the phase transition between the uniaxial SmA_d, which is rich in rod-like molecules, to biaxial smectic C phase, which is rich in BCHS molecules. The decrease in the layer spacing in the SmC_A phases arose due to an increase in the tilt angle of the BCHS molecules with respect to the layer normal. The model structures of the different phases of the mixtures are discussed below.

6.8 Molecular organizations in different phases

Based on our experimental results, we proposed a model for the organization of the rod-like and BCHS molecules in the different smectic phases exhibited by their binary mixtures. The pure compound 8OCB consisting of strongly polar rod-like molecules gives rise to the SmA_d phase with an intercalated layer structure. In the intercalated layer structure, the molecules arranged themselves with their dipole moments on average antiparallel with a large overlap of their molecular cores giving the layer spacing between l and $2l$. The layer spacing in the SmA_d phase of pure compound 8OCB is 31.7 Å as obtained from the XRD studies whereas the molecular length obtained from the molecular formula is 21.6 Å. At the low molar percentage of BCHS molecules, the rod-like molecules have an intercalated layer structure as in their SmA_d phase and the BCHS molecules are dispersed in these intercalated layers with their aliphatic chain and aromatic core parts matching with the corresponding chain and core parts of the rod-like molecules in the layers as shown in Figure 6.27a.

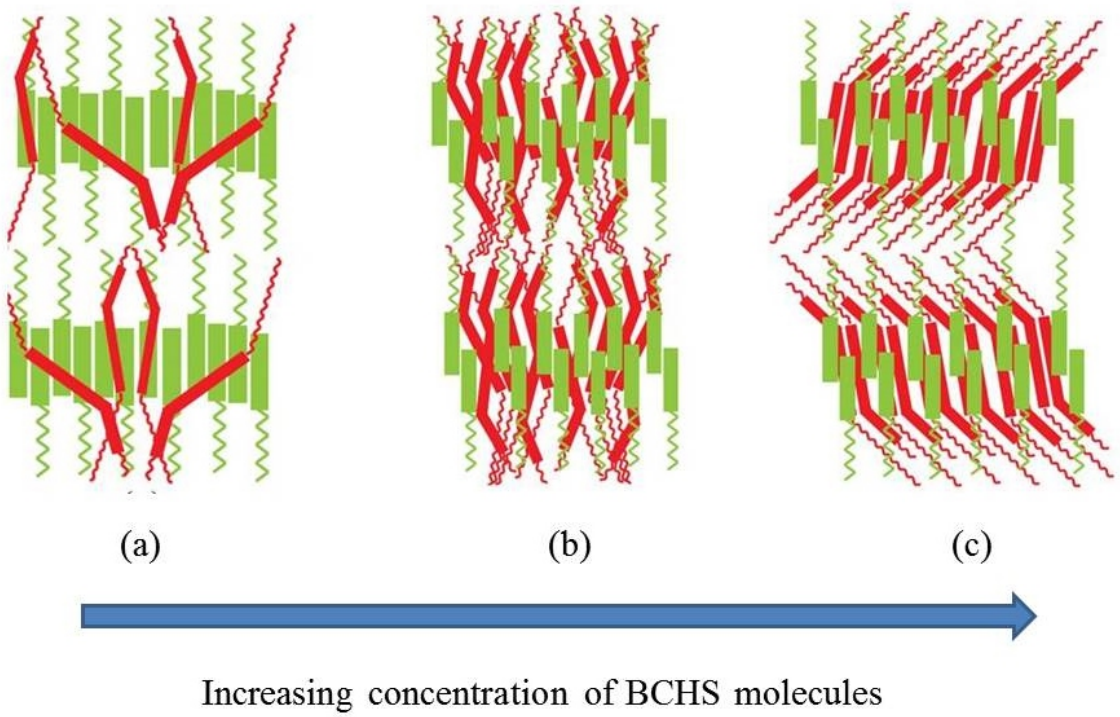

Figure 6.27: Molecular representation in different smectic phases with varing concentration of BCHS molecules (a) at a lower concentration of BCHS molecules (b) at an intermediate concentration of BCHS molecules and (c) higher concentration of BCHS molecules in the mixtures.

The molecular length of BCHS molecule as estimated from the molecular formula is about 53 Å which is about 2.5 times the length of the rod-like 8OCB molecules. Thus, the long axes of the BCHS molecules are tilted considerably with respect to the layer normal to match the core and chain parts of the respective molecules yet the BCHS molecules have a uniaxial distribution about the layer normal. But, the increasing molar percentage of BCHS molecules in the mixture tended to increase the layer spacing in their SmA_d phase so as to accommodate the BCHS molecules in the layers as well as to reduce the tilt of the BCHS molecules retaining the uniaxial distribution about the layer normal. The molecular organization in the SmA_d phase for this intermediate concentration of the BCHS molecules is shown in Figure 6.27b. In this case, the layer spacing was considerably larger due to the reduction in the intercalated depth of rod-like molecules in the smectic layers. At the higher molar percentage of BCHS molecules in the mixture, the BCHS molecules adopt a zigzag configuration in the layers giving rise to the pseudo-polar tilted smectic phases. The molecular

organization in the pseudo-polar tilted smectic phases of a mixture rich in the BCHS molecule is shown in Figure 6.27c. Upon further increase in the molar percentage of BCHS molecules, the layer spacing slightly decreased due to the increasing tilt of the BCHS molecules in the layers.

6.9 Conclusions

The liquid crystal phases exhibited by mixtures consisting of rod-like and BCHS molecules were studied in this chapter. The compounds 8OCB and 4OC18 consisting of rod-like and BCHS molecules, respectively were mixed homogeneously at all molar concentrations in their fluid phases. The phase diagram in the temperature and molar percentage parameter plane was constructed. The mixtures rich in rod-like molecules showed the Nematic and SmA_d phases. Interestingly, XRD results show that the layer spacing of the SmA_d phase can be tuned by changing the molar percentage of BCHS molecules in the binary mixture. The mixtures rich in BCHS molecules exhibit pseudo-polar tilted smectic phases. These results indicated that the pseudo-polar tilted smectic phases were the characteristic phases of BCHS molecules. We proposed simple model structures of different phases to account for our experimental observations. At lower temperatures and higher molar concentrations of both the components, the observed phase segregation was triggered by the crystallization of 4OC18. At the phase segregated regions, coexisting crystal phase rich in the compound 4OC18 and the smectic or crystal phase rich in the compound 8OCB was observed.

Bibliography

[1] K.C.Lim, and J.T.Ho, *Phys. Rev. Lett.*, **40**, 944 (1978).

[2] M. J. Bradshaw, E. P. Raynes, J. D. Bunning, and T. E. Faber *J. Physique*, **46**, 1513 (1985).

[3] T. Niori, T. Sekine, J. Watanabe, T. Furukawa, and H. Takezoe, *J. Mater. Chem.*, **6**, 1231 (1996).

[4] H. Takezoe and Y. Takanishi, *Jpn. J. App. Phys.*, **45**, 597 (2006).

[5] S. Chandrasekhar, *Liquid Crystals*, (Cambridge University Press, Cambridge, 1992).

[6] P. G. de Gennes, and J. Prost, *The Physics of Liquid Crystals*, (Clarendon, Oxford, 1994).

[7] R. Pratibha, N. V. Madhusudana, and B. K. Sadashiva, *Science*, **288**, 2184 (2000).

[8] R. Pratibha, N. V. Madhusudana, and B. K. Sadashiva, *Phys. Rev. E*, **71**, 011701 (2005).

[9] I. I. Smalyukh, R. Pratibha, N. V. Madhusudana, and O. Lavrentovich, *Eur. Phys. J. E*, **1**, 179 (2005).

[10] F. C. Yu, and L. J. Yu, *Liq. Cryst.*, **35**, 799–813 (2008).

[11] B. Das, S. Grande, W. Weissflog, A. Eremin, M. W. Schröder, G. Pelzl, S. Diele, and H. Kresse, *Liq. Cryst.*, **30**, 529-539 (2003).

[12] A. Chakraborty, M. K. Das, B. Das, U. Baumeister, and W. Weissflog, *J. Mater. Chem. C*, **1**, 7418 (2013).

[13] V. Novotna', M. Glogarova', V. Kozmi'k, J. Svoboda, V. Hamplova', M. Kaa'para and D. Pociechac, *Soft Matter*, **9**, 5647-653 (2012).

[14] A. Chakraborty, S. Chakraborty, and M. K. Das, *Phys. Rev. E*, **91**, 032503 (2015).

[15] S. Chakraborty, A. Chakraborty, M. K. Das, W. Weissflog *J. Mol. Liq.*, **219**, 608–613 (2016).

[16] S. Chakraborty, A. Chakraborty, M. K. Das, W. Weissflog *Phase Transitions*, doi:10.1080/01411594.2019.1642476 (2019).

[17] P. Sathyanarayana, S. Radhika, B. K. Sadashiva, and S. Dhara, *Soft Matter*, **8**, 2322 (2012).

[18] M. Alaasar, *Liq. Cryst.*, **43**, 2208-2243 (2016).

[19] S. Radhika, H. T. Srinivasa, and B. K. Sadashiva, *Liq. Cryst.*, **38**, 785 (2011).

[20] M. Alaasar, S. Poppe, C. Kerzig, C. Klopp, A. Eremin, and C. Tschierske, *J. Mater. Chem. C*, **5**, 8454-8468 (2017).

[21] D. D. Sarkar, R. Deb, N. Chakraborty, and V.S. R. Nandiraju, *Liq. Cryst.*, **39**, 1003-1010 (2012).

[22] E. R. Cioanca, E. L. Epure, I. C., G. Lisa, D. Wilson, N. Hurduc, and D. Scutaru, *Mol. Cryst. Liq. Cryst.*, **537**, 51-63 (2011).

[23] M. Monika, V. Prasad, and N. G. Nagaveni, *Liq. Cryst.*, **42**, 1490–1505 (2015).

[24] D. Malkar, B. K. Sadashiva, and A. Roy, *Soft Matter*, **12**, 4960 (2016).

[25] D. Malkar, M. Monika, V. Prasad, and A. Roy, *Phy. Rev. E*, **101**, 012701 (2020).

[26] J. W. Goodby, P. J. Collings, T. Kato, C. Tschierske, H. F. Gleeson, and P. Raynes, *Handbook of Liquid Crystals*, (Germany, **4** 2014).

[27] H. Takezoe and E. Alexey, *Bent-shaped liquid crystals: structures and physical properties*, CRC Press (2017).

[28] A. Jakli and A. Saupe, *One- and two-dimensional fluids: physical properties of smectic, lamellar, and columnar liquid crystals*, CRC Press (2006).

[29] Z.Luz and S. Meiboom, *J. Chem. Phy.*, **59**, 275 (1973).

[30] W. H. de Jeu, Physical Properties of liquid crystal Materials, Gordon and Breach, Science Publishers Ltd. (1980).

[31] A. J. Leadbetter, R. Richardon, and C. N. Colling, *J. Phy. Colloq.*, **36**, C1 (1975).

Summary

In first chapter, we discussed the backgrounds of liquid crystals in detail which helped us to understand the upcoming chapters in this thesis.

Second chapter contained the experimental techniques, which had been used to characterize the liquid crystals compounds presented in the thesis.

Chapter three contained the experimental studies on two LC compounds (4OC18 and A14) exhibited by BCHS molecules. Both compounds showed the same phase behavior between the isotropic liquid and crystal phases. These kind of compounds show pseudo-polar tilted smectic phases which had been designed as SmC_A, SmC_I corresponding to the higher and lower temperatures, respectively. These phases are characterized by an in-plane axial-vector order parameter in addition to tilt order in the smectic layers. The BCHS molecules adopted a zigzag configuration in these pseudo-polar smectic-C phases. To explain the molecular configuration of the BCHS molecules in the tilted smectic phases, a simple theoretical model was developed in chapter 3. On the basis of studied compounds which contain BCHS molecules, we could generalized this theoretical model to explain the molecular organization of the compound showing the similar kind of phase behavior.

Chapter 4 described the field effects on the observed mesophases of the studied compounds in chapter 3. The layers in both the mesophases of both compounds showed the absence of net electric polarization. However, both the mesophases of the studied compounds showed field-induced response. To understand the field effect, a model was presented which explained how the birefringence of the sample changed with applied electric field. We had explained the field effects in the higher temperature SmC_A phase in detail. For the lower temperature SmC_I phase, due to the coexistence of different stable degenerate structures, it was difficult to estimate the effective birefringence in

zero-field. This constrained the calculation of the effective birefringence changes with applied electric field. Therefore, the given model could be generalized to explain the field effect on the pseudo-polar tilted smectic phases exhibited by BCHS molecules.

In chapter 4 and chapter 5, we studied two azo-substituted compounds of an *A*-series. The higher homologue (n>10) of this series showed the pseudo-polar tilted smectic phases whereas the lower homologue (n<10) of the same series showed the Sm*A* to deVries Sm*A* phase transition. The higher homologue (A14) showed the optical response under applied field whereas the lower homologue did not respond. These azo-substituted compounds did not show any photo isomerization in the visible light. In chapter5, we have investigated a compound A9 which shows Sm*A* to deVries Sm*A* transition. The molecular organization of the molecules in the deVries Sm*A* phase could also be explained by the diffusive cone model.

In chapter 6, we have investigated the phase diagram of binary mixtures of rod-like and BCHS molecules. The binary mixtures of these two different shapes of the molecules showed some interesting results as the BCHS molecules have intermediate structure between the rod-like and symmetric bent-core banana-shaped molecules. The experimental studies on the binary mixtures showed that the layer spacing of the SmA_d phase can be tuned continuously by controlling the concentration of BCHS molecules in the mixtures.